5-1-2013

Modeling and condition monitoring of fully floating reciprocating compressor main bearings using data driven classification

Markus Holzenkamp

Rochester Institute of Technology

Modeling and Condition Monitoring of Fully Floating Reciprocating Compressor Main Bearings using Data Driven Classification

by

Markus Holzenkamp

A Thesis Submitted in Partial Fulfillment of the Requirements for the Degree of Master of Science in Mechanical Engineering

Kate Gleason College of Engineering
Department of Mechanical Engineering

May 2013

Committee Approval:

Dr. Jason Kolodziej, Assistant Professor Date

Thesis Advisor, Department of Mechanical Engineering

Dr. Stephen Boedo, Associate Professor Date

Committee Member, Department of Mechanical Engineering

Dr. Agamemnon Crassidis, Associate Professor Date

Committee Member, Department of Mechanical Engineering

Dr. Alan Nye, Professor Date

Department Representative, Department of Mechanical Engineering

An meine Eltern, Bernd und Edith Holzenkamp

Abstract

Condition monitoring reduces maintenance costs on industrial machinery by reducing downtime and allowing for need-based maintenance instead of schedule-based maintenance. Currently, condition monitoring is not as widely applied on reciprocating compressors as compared to rotating compressors. However, research for monitoring various components of reciprocating compressors such as inlet and outlet valves and piston rings is conducted. There is industry interest into expanding this research to the main bearings of the compressor. Previous research on bearings focuses on either rolling element bearings or traditional journal bearings with not much information available on low speed applications of fully floating ring journal bearings as are studied in this work.

The following work shows a detailed derivation of the forces acting on the main bearings during normal compressor operation based on kinematic relations and dynamic equivalence. The bearing is simulated using an adaptation of the mobility method for fully floating ring bearings found in previous research. It involves solving two simultaneous mobility calculations along with the ring speed to link the inner to the outer bearing. Experimental data of the crankshaft orbit is collected for comparison to the simulation.

Condition monitoring for three different fault types is investigated through seeded fault testing: Varying lubricant viscosity, oil feed hole obstruction, and grooves in the bearing land. Principle component analysis has been shown previously to be a successful method of feature selection for classification. This is applied to several sensors and the classification results are compared. A single axis position measurement of the crankshaft shows the most promising results compared to a traditional accelerometer on the bearing housing and a novel accelerometer on the crankshaft. The single axis measurement provides a cost efficient alternative method to the two axis orbit measurement typically used for traditional journal bearings.

Contents

List of Figures

List of Tables

Chapter 1

Introduction

1.1 Background: Reciprocating compressors and their role in industry

1.1.1 Operating Principles

Reciprocating compressors operate on the same basic principles today as when they were first developed in the 1890s. A crankshaft is turned by a power source and converts rotary motion into linear motion. As the crankshaft turns, the connecting rod moves a piston up and down. This piston moves in a cylinder which acts as the compression chamber for the operating fluid. Inlet valves open during the expansion stroke of the piston and outlet valves open when the desired operating pressure is reached during the compression stroke to allow the fluid into a storage reservoir.

Advances to the technology include improved separation of the lubrication necessary for the 'power' side of the compressor and the working fluid in the 'compression' side of the compressor. This is achieved through improved piston rings and seals as well as physical separation of the two components through the distance piece. Improved materials lead to longer lifetimes and higher efficiencies. However, with longer overall lifetimes, it became important to monitor the machines to keep them operating at optimal conditions.

Current Applications Reciprocating compressors are widely employed in the gas and fuel industries. They provide advantages when high flow is required, as they typically have larger flow rates compared to rotating compressors. As such, one of the main areas of employment for reciprocating compressors is on natural gas pipelines to provide the necessary transport pressure. They are also widely used in oil refineries to bring hydrogen gas to the required pressure for hydrocracking [1]. These are just some examples of applications for reciprocating compressors.

1.1.2 Literature Review: What is the current standard in condition monitoring

Overview

While reciprocating machinery is widely used in industry, the standard of condition monitoring is not at the same level as for turbo machinery. Due to this, turbo machines currently have lower maintenance cost compared to reciprocating machines. Better condition monitoring techniques could change this. An effective way to monitor reciprocating compressors is by evaluating their real time P-v diagrams. It is relatively easy to monitor pressure in the cylinder and if the crank angle can be monitored accurately, the pressure volume relationship can be calculated. This can then be compared to a theoretical diagram and deviations signal failure on a part of the compressor [2].

Other techniques that can be used to monitor the condition of a reciprocating compressor include vibration monitoring, rod drop monitoring and temperature monitoring. For vibration monitoring, two main categories should be considered: crankcase vibration and crosshead/distance piece vibration. Since most reciprocating compressors have a balanced opposing cylinder configuration, measuring the vibration of the

crankcase allows the detection of any failure that would upset this inherent balance. Catastrophic examples of such failures include a broken piston rod or the loss of a counterweight on the crankshaft. Measuring the vibration or acceleration of the crosshead/distance piece allows the detection of loose piston nuts, clearance problems and others failures that result in impact events to the crosshead. Rod-drop monitoring can show rider band wear but is very difficult to measure accurately. For temperature monitoring, typical measurements include cylinder discharge temperature, valve temperature, packing temperature, crosshead pin/big end bearing temperature and main bearing temperature. Cylinder discharge temperature can show leaks in rings and valves. Valve temperatures give away individual valve problems. Packing temperature can show packing leakage and bearing temperature can show a failing bearing [3].

In order to combine all these measurements into one complete health monitoring that is viable for industry, some sacrifices have to be made in sensor placement and sensor choice in order to achieve a balance between capabilities and cost. Additional to the measurements, a simulation of the compressor is desirable. This allows the comparison of actual versus expected values. This is in addition to conventional alarms that trigger when the measurements exceed a stored value. If an alarm triggers, the alarm value should be raised a small amount to confirm a trend through continuous triggering instead of an outlier [4]..

Methods

Specific research in the area of condition classification and monitoring has investigated a wide range of possible techniques. Yang, B.-S. et al. developed a techniques to determine whether a small reciprocating compressor is faulty. This technique was then implemented as part of the quality control process on the compressor assembly line. The classifier used vibration measurements in both horizontal and vertical direction to determine the condition of the compressor [5].

Ahmed, M., Gu, F., and Ball, A use a genetic algorithm to select features and then a probabilistic neural network to classify the condition of a reciprocating compressor. Seeded fault testing was used to obtain datasets for healthy and three types of failing conditions, valve leakage, intercooler leakage, and a loose drive belt. All three faults require the compressor to use more energy to generate the same pressure. The authors manage to achieve a 100 % correct classification rate when the genetic algorithm is used to select the features on which the neural network bases the classification [6].

Another technique that has been investigated is to monitor the condition of the compressor lubrication oil. Jiang, X. used atomic emission spectroscopy combined with ferrographic analysis to check the particle contents of the oil. Atomic emission spectroscopy is used to determine the concentration of metal elements due to wear, additives, and contaminants in the oil. Ferrographic analysis is used to detect the wear and failure mechanisms. The combination of the two methods is necessary to achieve complete monitoring as the spectroscopy only measure particles with a size smaller than 10 micrometers. Ferrographic analysis is then used to discover larger particles resulting from heavy wear. If the materials of certain mechanical components of the compressor are known, a higher than average concentration of elements of some material can indicate the wear of a specific component [7].

Bearing failure characteristics

In order to monitor the condition of bearings, several ranges of frequencies are of interest for rolling element bearings. The rotor vibration region and the prime spike region are the most important frequency bands to monitor in order to be able to accurately determine the condition of rolling element bearings. Rotor vibrations are in the range of to 3 times the rotational speed of the shaft. An increase in the vibration levels in this frequency range indicates a bearing failure due to some malfunction with the rotor or shaft loading. The underlying failure is not with the bearing so unless the real cause is corrected the bearing will continue to fail. Displacement or velocity measurements lend themselves the best to detect these frequencies. The prime spike region includes the frequencies between the element passing rate and up to seven harmonics of it. The element passing rate is defined by the rate at which the rolling elements of the bearing pass a certain point on the inner or outer race of the bearing. The vibrations in this range can be effectively measured as acceleration, velocity, or displacement. This frequency band detects failures in bearing races which contain approximately 90 percent of all bearing failures [8].

For journal bearings, failure characteristics are less clearly defined. However, several methods to monitor the condition of these type of bearings have been developed.

Condition monitoring techniques for journal bearings

Typically, bearing monitoring and condition determination have been done in two different ways. The first method is look at the dynamic load rating and the equivalent load experienced by the bearing to arrive at a prediction of fatigue and the second is to actively monitoring the bearing through some measurements. The first method has the weakness of not being able to account for varying operating conditions. The second method is very useful if usable features can be extracted from the measurements [9].

Vibration measurements are one of the most common types of data collected in order to perform condition monitoring on both rolling element and journal bearings. The collected data can then be processed in order to analyse it. G.Y. Lou et al. suggest a wavelet transform method as a novel way to process the signal. The wavelet transform has advantages over the classical Fourier Transform analysis and the time domain analysis in that the wavelet transform allows for the monitoring of the time evolution of the signal frequency spectrum. The time information is lost in the classical Fourier transform and the time domain does not analyse the frequency spectrum. They apply this method to perform condition monitoring successfully on a rolling element bearing [10].

Parnelli et al. looked at measuring the wear of a dimpled bushing through vibration measurement. The dimpled bushing is acting as a journal bearing in a planetary gear set and has an inside coating which will wear over time. The previously employed temperature measurements did not give a sufficient indication of bearing condition as the temperature would rise drastically moments before catastrophic failure while remaining nearly constant throughout the wear process. By analyzing frequency bands of high activity of the vibration signals collected of the bearing, a linear relationship between the wear and the band power of the signal was observed [11]. Other features extracted from vibration measurements for rolling element bearings include power spectrum, bi-spectrum, and bi-coherence [12].

Tandon and Parey give very good overview of condition monitoring in general and some techniques for journal bearings in particular. Using displacement sensors at a ninety degree angle from each other allows one to measure the shaft motion and obtain so called orbit plots. These give a good indication of the state of the bearing.

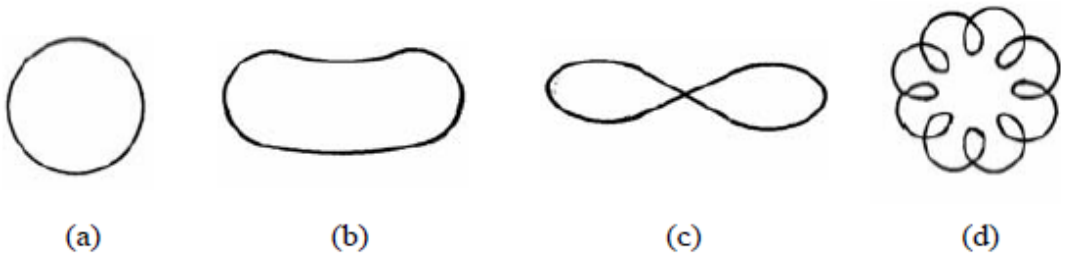

Figure 1.1: Typical orbit plots from two proximity probes for (a) normal condition, (b) misalignment, (c) severe misalignment, (d) rubbing [13]

Figure 1.1 shows some common faults in bearings and how they appear in the orbit plot. When dealing with multi-frequency signals, it is possible to clarify and filter the orbit plot through band filtering to look only at the frequency of interest [13].

Chen et al. developed a method to monitor and classify journal bearings including sensor fusion, phase spectra, holospectrum, purified orbit diagrams, and filtered orbit diagrams [14]. Of major interest to this research are the filtered orbit diagrams as well as using several sensor at the same time for classification. Filtered orbit plots are in theory very simple to obtain by applying a non-phase shifting band pass filter to the signal measuring the shaft motion. The frequency band of the filter can be chosen according to what fault is of interest. Table 1.1 shows general frequencies of interest in rotating machinery. Most of these also apply to reciprocating machinery such as the compressor in this research.

Frequency	Mechanical Interpretation
f_1	rotating frequency of the machine
f_2	second harmonic of the rotating frequency ($2f_1$)
f_3	third harmonic of the rotating frequency ($3f_1$)
f_4	forth harmonic of the rotating frequency ($4f_1$)
f_5	fifth harmonic of the rotating frequency ($5f_1$)
f_6	sixth harmonic of the rotating frequency ($6f_1$)
f_7	surge frequency (peak frequency $[0,0.4]f_1$)
f_8	oil whirl frequency (peak frequency $[0.4,0.51]f_1$)
f_9	rotating stall frequency (peak frequency $[0.7,0.9]f_1$)
f_{10}	loose bearing cap frequency (peak frequency $[0,0.3]f_1$)
f_{11}	pipe excitation frequency (peak frequency $[0.4,0.5]f_1$)
f_{12}	electrical power supply frequency (60Hz)

Table 1.1: Important frequencies in diagnostics [14]

1.2 Purpose of Research

Gaps in the literature There is comparatively less research into journal bearing compared to rolling element bearings. There is even less research into the fully floating ring journal bearing used as main bearings on this compressor. This research attempts to determine the feasibility of monitoring the main crankshaft bearings through a data driven classifier. Since the application of condition monitoring on reciprocating machinery is less common compared to turbo machinery, there is a large demand from industry to develop such systems. The application of condition monitoring can ultimately reduce operating costs and increase the competitiveness of reciprocating machinery.

Scope of thesis work The thesis work is based on several sequential steps. Step 1 is to develop a basic model to predict bearing movement from bearing specifications, compressor dimensions and compressor operating characteristics. Step 2 is to determine a way to measure the journal orbit in order to validate the model. Step 3 is to perform seeded fault testing on the bearing to obtain measurements for various conditions and compare to the simulated results. And step 4 is to develop a basic classification algorithm based on the measurements from the seeded fault testing.

Chapter 2

Modelling

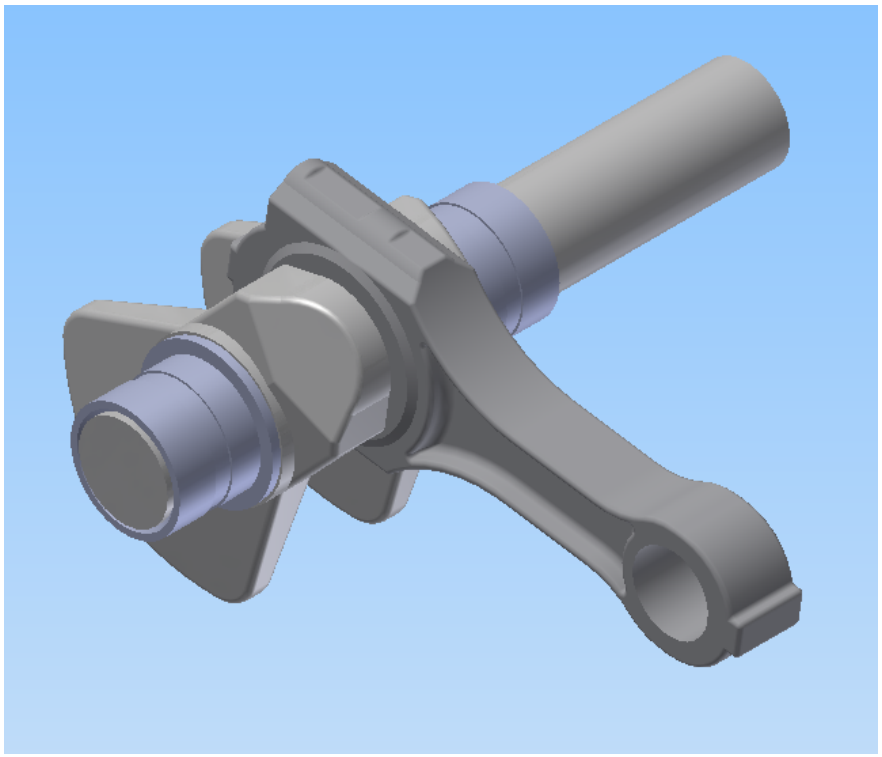

Figure 2.1: 3D model of the crankshaft, connecting rod, and main bearings

2.1 Modelling Approach

This is seen as a first model for the compressor main bearings as it follows very much from first principles. The mobility method is used to model the actual bearing performance while kinematic equivalence and point mass assumption are used to derive the forces acting on the bearing. The model does include gravitational effects due to the large size of the components. The model also includes the floating ring complication and can account for misalignment effects due to a offset sensor location. This allows for a better comparison to experimental data later on.

2.2 Bearing Model

In order to apply the mobility method to calculate the motion of the journal and ring in their respective clearance space, the forces acting on the bearing have to known. As such the compressor was modeled using conventional engine kinematics and dynamics where the forces are based on the geometric and masses of the individual components. Pressure forces acting on the piston are included in the form of experimental data collected at various crank angles. The mobility algorithm is modified to allow for simultaneous solution of both the journal to ring motion as well as the ring to sleeve motion.

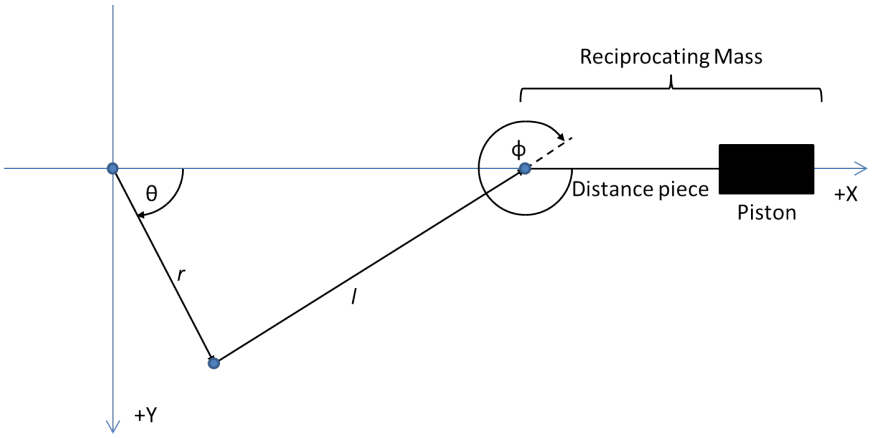

Figure 2.2: Simplified system schematic showing components relevant to the analysis

Simplified Model Most of what follows is based on [15, 16, 17]. Figure 2.2 shows the simplified system from which the free body diagrams are created. The concept of dynamic equivalence is applied to both the connecting rod and the crankshaft (Fig. 2.3 and 2.5). The solid body connecting rod is modelled as two point mass connected by a massless rod of length l. The masses are the rotating big end mass at the connection to the crankshaft and the reciprocating mass that is comprised of the piston, distance piece and the small end mass.

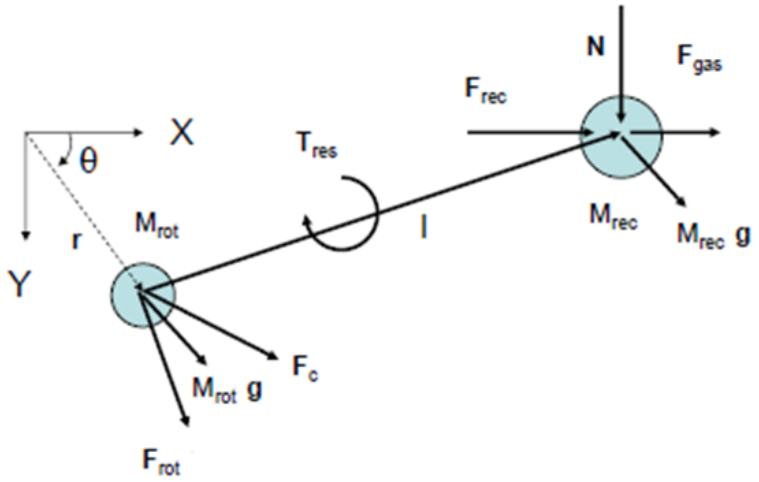

Figure 2.3: Dynamically equivalent model of the connecting rod

F_{rot} and F_{rec} are inertia forces from the motion of the connecting rod and are known from given masses

and accelerations determined through kinematics. N is the side-wall force from the cylinder on the piston. F_{gas} is the force due to the cylinder pressure. Gravitational effects are included for both the reciprocating and the rotating mass as seen on fig. 2.3 The main unknown of interest is the force from the big end bearing onto the connecting rod (F_c) as this is the link between connecting rod and crankshaft and so between what is occurring in the cylinder and the loads on the main bearing. T_{res} is typically negligible and is dropped from the following calculations.

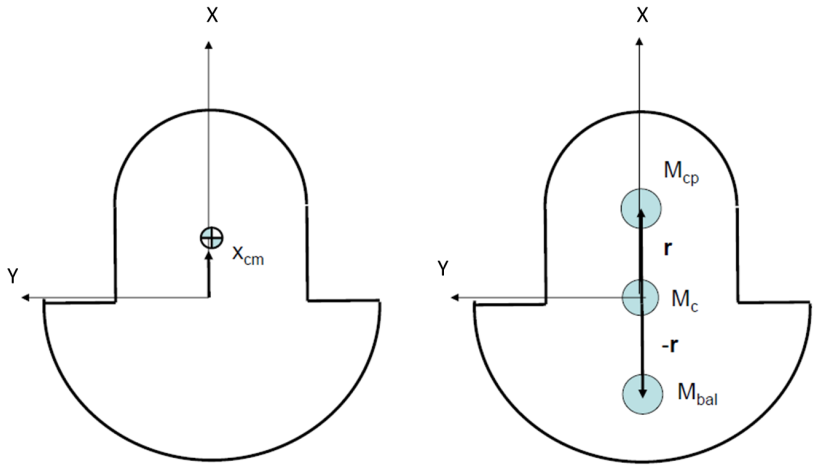

Figure 2.4: Determining dynamically equivalent masses for the crankshaft

The solid body crankshaft is modeled as three point masses (Fig. 2.4). The first, M_{cp}, is the mass of the crankpin at a distance $\vec{r}$ from the origin. The second, M_c, is the mass of the shaft acting at the axis of rotation. This means it does not contribute to the rotating inertia loads. Third is the mass of the counterweights located at a distance of $-\vec{r}$. Unlike the connecting rod, where the big end and small end mass were given, the concept of dynamic equivalence was applied to the crankshaft. In order to determine the overall mass (M_{crank}), inertia (J_{crank}), and location of the center of mass (x_{cm}), a 3D model was created from a drawing provided by Dresser-Rand. Equations 2.1 through 2.3 show how the equivalent masses are calculated.

$$M_{cp} = (M_{crank} x_{cm} r + J_{crank})/(2r^2) \tag{2.1}$$

$$M_{bal} = (J_{crank} - M_{crank} x_{cm} r)/(2r^2) \tag{2.2}$$

$$M_c = (M_{crank} r^2 - J_{crank})/r^2 \tag{2.3}$$

In the free body diagram of the dynamically equivalent model of the crankshaft (Fig. 2.5), F_{bal} is the inertia force of the counterweight, F_{cp} is the inertia force of the crankpin mass. $-F_c$ is the reaction force from the big end bearing onto the crankpin and R_m is the reaction force from both main bearings on the crankshaft. This is later divided by two to account for the two main bearings supporting the crankshaft. The fact that there are only two supports is convenient as it makes this problem statically determinate which allows for including static effects from the weight of the flywheel to calculate individual bearing loads as a combination of rotational effects and static effects. One thing to note is that the y-axis is defined positive downward in order to allow for the direction of rotation to be positive. This results in a positive value for acceleration due to gravity.

Kinematic Relations The position vectors for the reciprocating mass and crankpin are given by

$$\vec{s} = (r\cos\theta + l\cos\phi)\hat{i} \tag{2.4}$$

$$\vec{r} = r\cos\theta\hat{i} + r\sin\theta\hat{j} \tag{2.5}$$

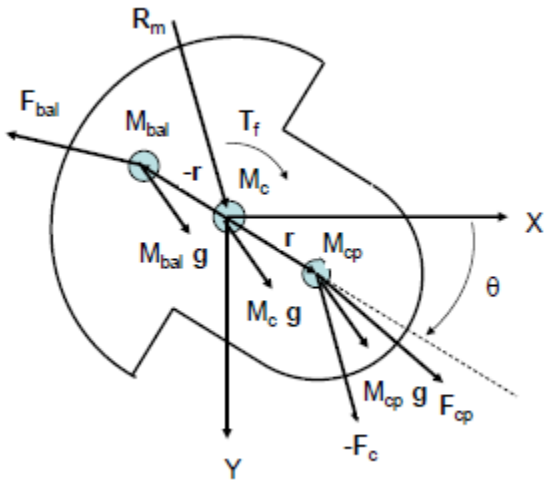

Figure 2.5: Dynamically equivalent model of the crankshaft

and the connecting rod vector is given by

$$\vec{l} = l\cos\phi\hat{i} + l\sin\phi\hat{j} \tag{2.6}$$

Defining an auxiliary connecting rod angle ϕ with

$$\sin\phi = -\frac{r}{l}\sin\theta \tag{2.7}$$

$$\cos\phi = \sqrt{1-\sin^2\theta} \tag{2.8}$$

one can find the connecting rod angular velocity

$$\dot{\phi} = -\frac{r\omega\cos\theta}{l\cos\phi} \tag{2.9}$$

where ω is the rotational speed of the crankshaft (assumed constant here).

In order to solve for the forces on the bearings, the acceleration vectors are needed. These are found by taking the second time derivative of the position vectors.

$$\ddot{\vec{s}} = -(r\omega^2\cos\theta + l\ddot{\phi}\sin\phi + l\dot{\phi}^2\cos\phi)\hat{i} \tag{2.10}$$

$$\ddot{\vec{r}} = r\omega^2\cos\theta\hat{i} - r\omega^2\sin\theta\hat{j} \tag{2.11}$$

where

$$\ddot{\phi} = \frac{r\omega^2\sin\theta + l\dot{\phi}^2\sin\phi}{l\cos\phi} \tag{2.12}$$

With the above set of equations, the complete motion of the compressor can be described if the crankshaft angle θ and rotational speed ω are known.

Forces Excluding flywheel loading effects for now, the big end conrod bearing force components (crankpin to sleeve) are found by

$$F_c^x = -m_{rec}\ddot{s} - m_{rot}\ddot{r}^x - F_{gas} \tag{2.13}$$

$$F_c^y = F_c^x tan\phi + m_{rot}\ddot{r}^y - m_{rot}\ddot{r}^x tan\phi - m_{rot}g^y \tag{2.14}$$

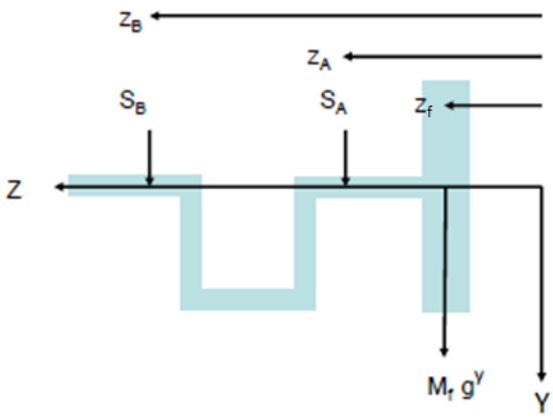

Figure 2.6: Free body diagram of the crankshaft used to determine static effects due to the flywheel

The resultant of the two main bearing forces is given by

$$R_m^x = F_c^x + m_{cp}\ddot{r}^x - m_{bal}\ddot{r}^x \tag{2.15}$$

$$R_m^y = F_c^y + m_{cp}\ddot{r}^y - m_{bal}\ddot{r}^y - (m_{cp} + m_{bal} + m_m)g^y \tag{2.16}$$

The model was then further refined since the two main bearings do not carry identical loads due to the asymmetric crankshaft design and the large flywheel. Figure 2.6 shows the simplified free body diagram that was used to determine the reaction forces due to the flywheel weight. Solving for static equilibrium from the free body diagrams yields

$$S_a = -M_f g^y (z_B - z_f)/(z_B - z_A) \tag{2.17}$$

$$S_b = -M_f g^y (z_A - z_f)/(z_B - z_A) \tag{2.18}$$

Now the main bearing loads to be used in the mobility code can be calculated. The focus is on the bearing closest to the flywheel as it experiences the greater load and as such is expected to carry a smaller film thickness. The negative sign is required as the mobility method expects forces to act from the journal onto the sleeve.

$$F_{bearing}^x = -R_m^x/2 \tag{2.19}$$

$$F_{bearing}^y = -S_a - R_m^y/2 \tag{2.20}$$

2.3 Mobility Method

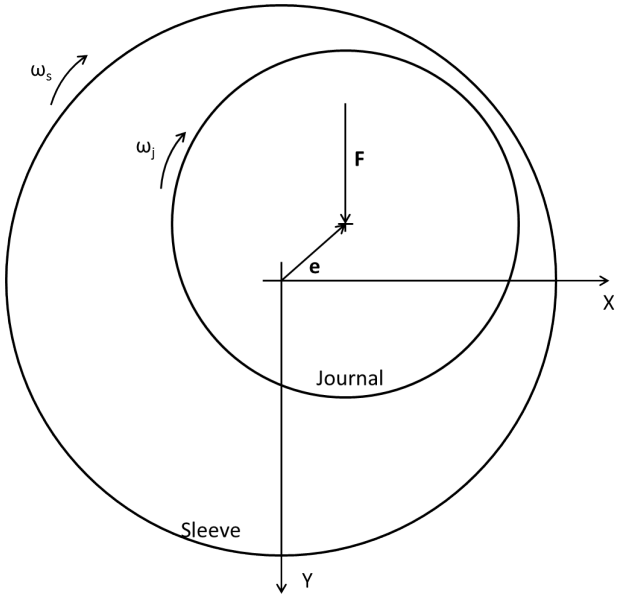

Figure 2.7: Schematic of a traditional journal bearing

Background The mobility method has been in use since the 1960s as a very fast method to predict journal bearing orbits first graphically and later on through numerical curve fits. Even though a full finite element solution is more accurate, the run time benefits of mobility, which runs up to 2000 times faster than a full solution, can outweigh the small loss in overall accuracy ($< 10\%$) [18]

Theory Journal mobility is defined as a dimensionless parameter that relates velocity and the force applied to the bearing. From this, several mobility maps have been created that can show numerically the path that a journal would take in a non rotating bearing with a constant downward force given the starting point of the journal center. The journal mobility is defined as a function of the eccentricity and the L/D ratio of the bearing. These are again defined below.

$$\vec{e} \equiv \textit{vector from sleeve center to journal center} \tag{2.21}$$

$$\epsilon = \frac{\vec{e}}{C} \equiv \textit{eccentricity vector normalized w.r.t. radial clearance} \tag{2.22}$$

$$L = \textit{bearing length} \tag{2.23}$$

$$D = \textit{bearing diameter} \tag{2.24}$$

$$\frac{d\vec{e}}{dt} = \frac{|F|(\frac{2C}{D})^2}{(\frac{LD\mu}{C})} M(\frac{L}{D}, \epsilon_x, \epsilon_y) \tag{2.25}$$

Equation 2.25 describes the motion of the journal by calculating the time derivative of the eccentricity. Integrating this equation over a specified time allows the plotting of the journal path. In order to extend this method to rotating bearings, the concept of reference frames is applied. Firstly, consider a point rotating in the bearing sleeve center at the same angular velocity as that of the journal. Relative to this point, the

bearing is experiencing pure squeeze film motion so equation 2.25 holds. Now consider a second point in the sleeve center that is non rotating, or in general, rotating at a different speed than point 1. Since the two observers are in relative motion to each other, the journal velocity vector relative to the second point is different by the cross product of angular velocity difference and the eccentricity vector.

$$\frac{d\vec{e}}{dt} = \frac{|F|(\frac{2C}{D})^2}{(\frac{LD\mu}{C})} M(\frac{L}{D}, \epsilon_x, \epsilon_y) + \vec{\omega}_{avg} \times \vec{e} \tag{2.26}$$

In this research, the Goenka mobility approximation is used in the Matlab code as it still is one of the most accurate and widely applicable methods to determine the mobility vector M.

Lastly, to convert from journal position to lubricant film thickness, the following equation is used.

$$h = C(1 - |\epsilon|) \tag{2.27}$$

The mobility method is explained in greater detail in J.F. Booker's paper on the numerical application of the mobility method [19].

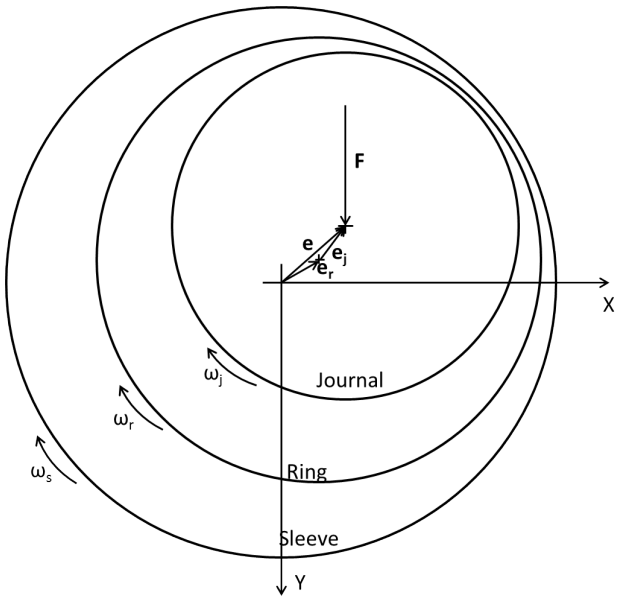

Figure 2.8: Schematic for a floating ring bearing showing individual eccentricity vectors

Floating Ring Integration The integration of the floating ring bearing is based on a derivation found in Rhode [20]. A floating ring bearing involves the simultaneous solution of two dynamically loaded fluid film bearings. The two bearings are linked by the equation of motion for the rotation of the ring (Eqn. 2.28)

$$I_r \frac{d\omega_r}{dt} = T_j - T_r \tag{2.28}$$

T_1 and T_2 are the fluid film torques exerted on the ring by the inner and outer film respectively. Since the torques are dependent on the ring speed, equation 2.28 needs to be integrated numerically to solve for the ring speed. This lends itself for integration with the mobility code and its iterative solution method. The torques for the inner film, T_1, and the outer film, T_2, are given by equations 2.29 and 2.30.

$$T_j = \frac{\omega_j - \omega_r}{(1-\epsilon_j^2)^{(1/2)}} \frac{2\pi R_j^3 L\mu}{C_j} + \frac{\vec{e_j} \times \vec{F}}{2} \bullet \hat{k} \tag{2.29}$$

$$T_r = \frac{\omega_r - \omega_s}{(1-\epsilon_r^2)^{(1/2)}} \frac{2\pi R_r^3 L\mu}{C_r} + \frac{\vec{e_r} \times \vec{F}}{2} \bullet \hat{k} \tag{2.30}$$

Plugging these two equations into 2.28 yields a differential equation that can be solved along with eqn. 2.26 for both the journal and the ring to find the full solution for the floating ring bearing.

One thing to note is that the bearing is a fully grooved bearing with even length lands. This has the effect that each land carries half the load. This produces different results compared to a non grooved bearing since the mobility vector depends on the L/D ratio, where L is the length of uninterrupted bearing surface.

Model Validation In order to validate model it was run with the same parameters as published in [20]. Since not enough data is given for the main bearing, the simulation was run for the connecting rod big end bearing. Figure 2.9 compares the simulated forces acting on the big end connecting rod bearing versus the published results. The results show very good agreement.

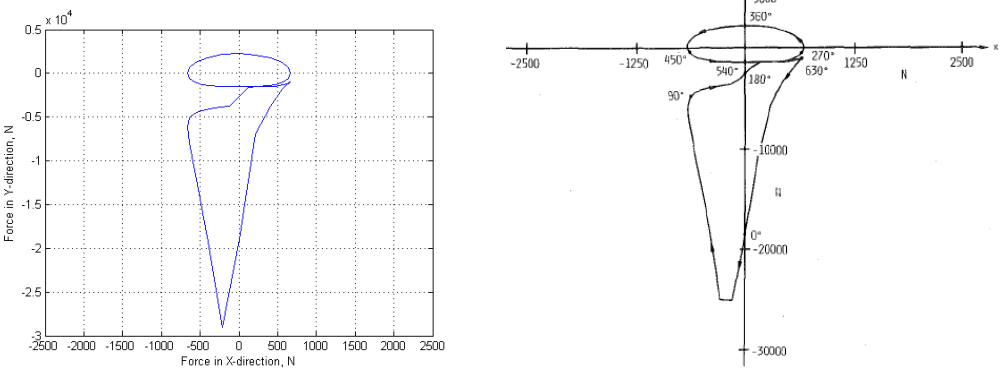

(a) Simulation result

(b) Published result

Figure 2.9: Polar plot of the force acting on the big end bearing in the connecting rod frame of reference

The next step is to compare the simulated minimum cyclic film thickness to the published results. As figure 2.10 shows, there is very good agreement between the results. As additional validation, two independent floating ring implementations are compared. These show very good agreement except for the minimum film thickness between the ring and the sleeve for small clearances between the journal and the ring. The clearances in this simulation are greater than those affected by the difference in implementation.

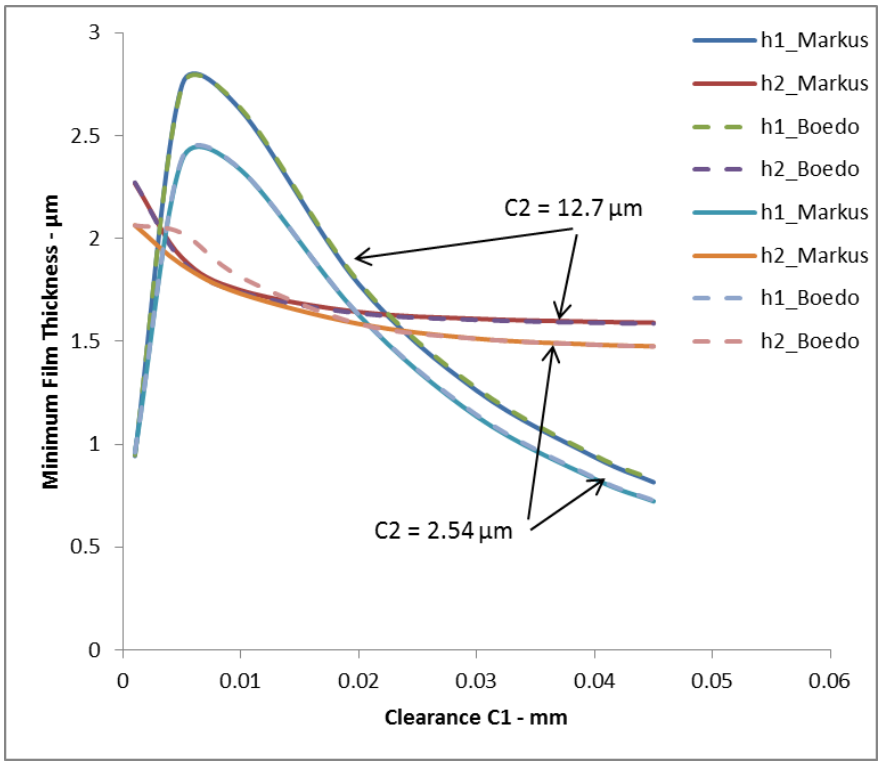

(a) Simulation result

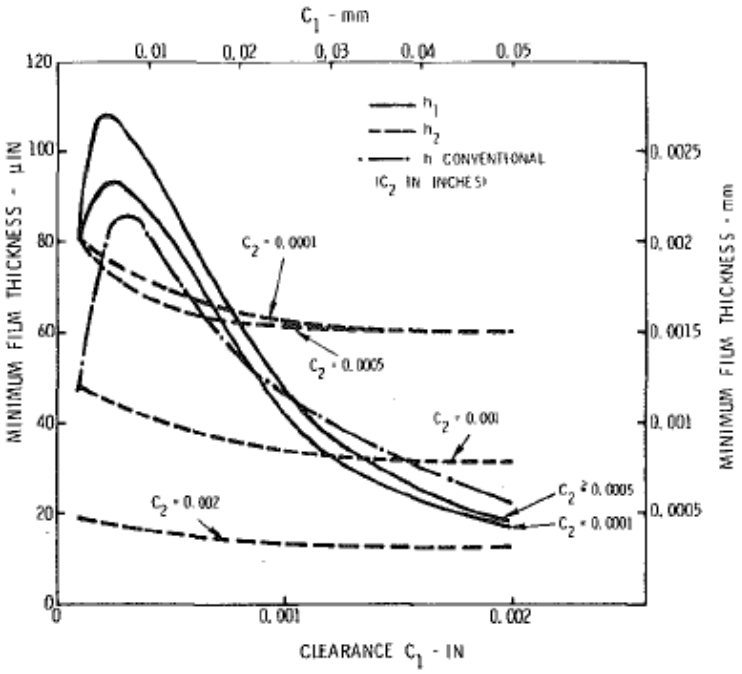

Fig. 4(*a*) Con-rod bearing film thickness: 209 rad/s—road load

(b) Published result

Figure 2.10: Minimum cyclic film thickness as a function of clearance between journal and ring

Reciprocating Mass (kg)	77.0
Rotating Mass (kg)	04.9
Crankpin Mass (kg)	12.4
Shaft Mass(kg)	0.16
Balance Mass(kg)	16.9
Flywheel Mass(kg)	106
Bearing Diameter (m)	0.06985
Bearing Length (full) (m)	0.06985
Bearing Length (1 land) (m)	0.03
Bearing Radial Clear. Journal to Ring (μm)	35-95
Bearing Radial Clear. Ring to Sleeve (μm)	35-65
Viscosity (Pa-s)	0.061 (SAE 30W @ 50 °C)
Ring Inertia ($kg * m^2$)	0.613e-10
Gravity g^y (m/s^2)	9.81

Table 2.1: Simulation parameters

2.4 Simulation Results

For consistencies sake, the bearing from the journal to the ring is referred to as the inner bearing while the bearing from the ring to the sleeve is referred to as the outer bearing from here on out.

Solving for the main bearing loads and then calculating the bearing motion for the inner bearing yielded the results shown in fig. 2.11. The parameters for the simulation are given Table 2.1. Several simulations were run to test the effect of radial clearance on film thickness. Standard SAE 30 oil was used as the lubricant. The results show the expected trends for the journal to ring bearing. The effect of changing the outer bearing clearance is very small, while changing the load results in visible changes at BDC. Changing the clearance for the inner bearing has the biggest effect on the film thickness.

The results for the outer bearing from ring to sleeve are less intuitive. The change of the inner clearance has a bigger effect on the outer bearing than vice versa. Again, the clearance of the outer bearing and the loading of the compressor show the biggest impact to the film thickness. It is notable that film thickness in the outer bearing increases with clearance in the inner bearing as shown by figure 2.13. The trends also show that under an increase in compressor loading reduces the film thickness in both the inner and outer film. For the inner bearing, the larger the clearance, the lower the minimum film thickness value.

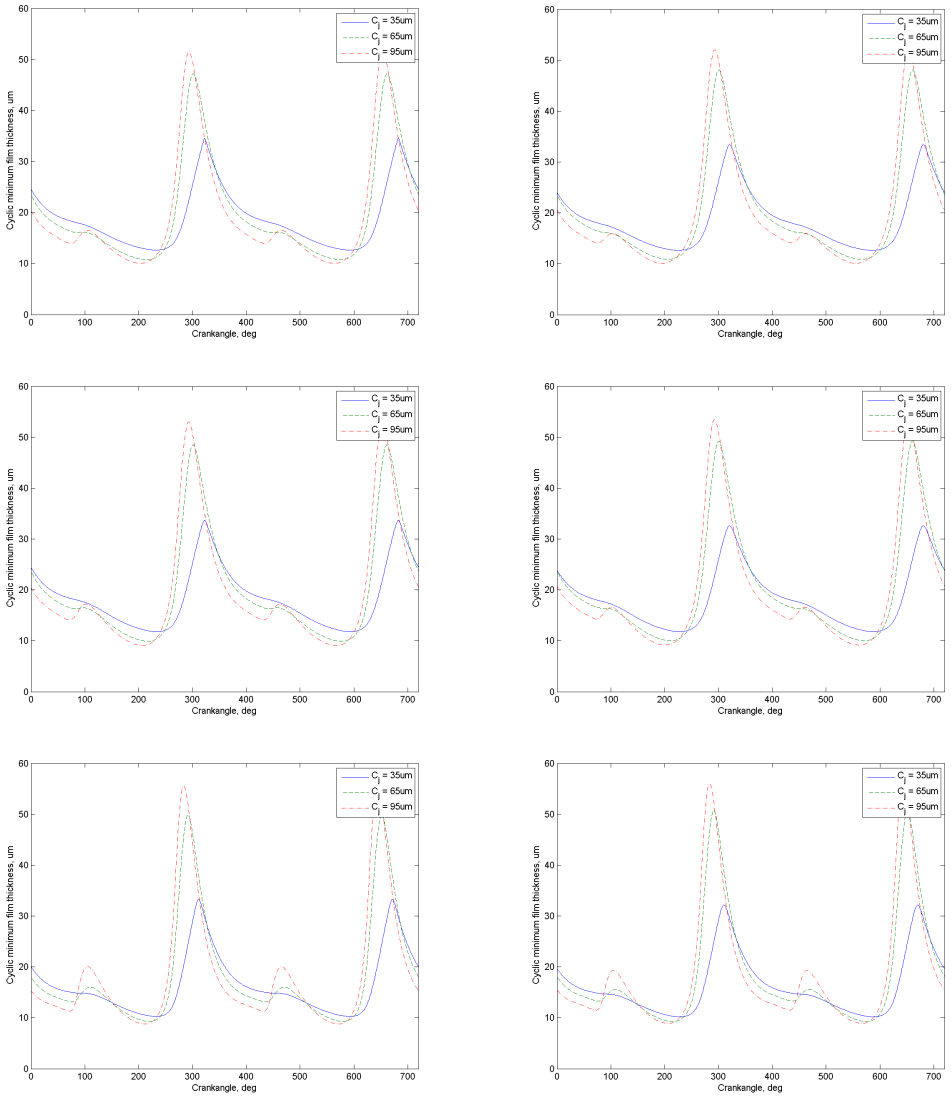

(a) Cr = 35um (b) Cr = 65um

Figure 2.11: Minimum film thickness between the journal and ring for a range of inner bearing clearances (Top: 0% Load, Middle: 50% Load, Bottom: 100% Load)

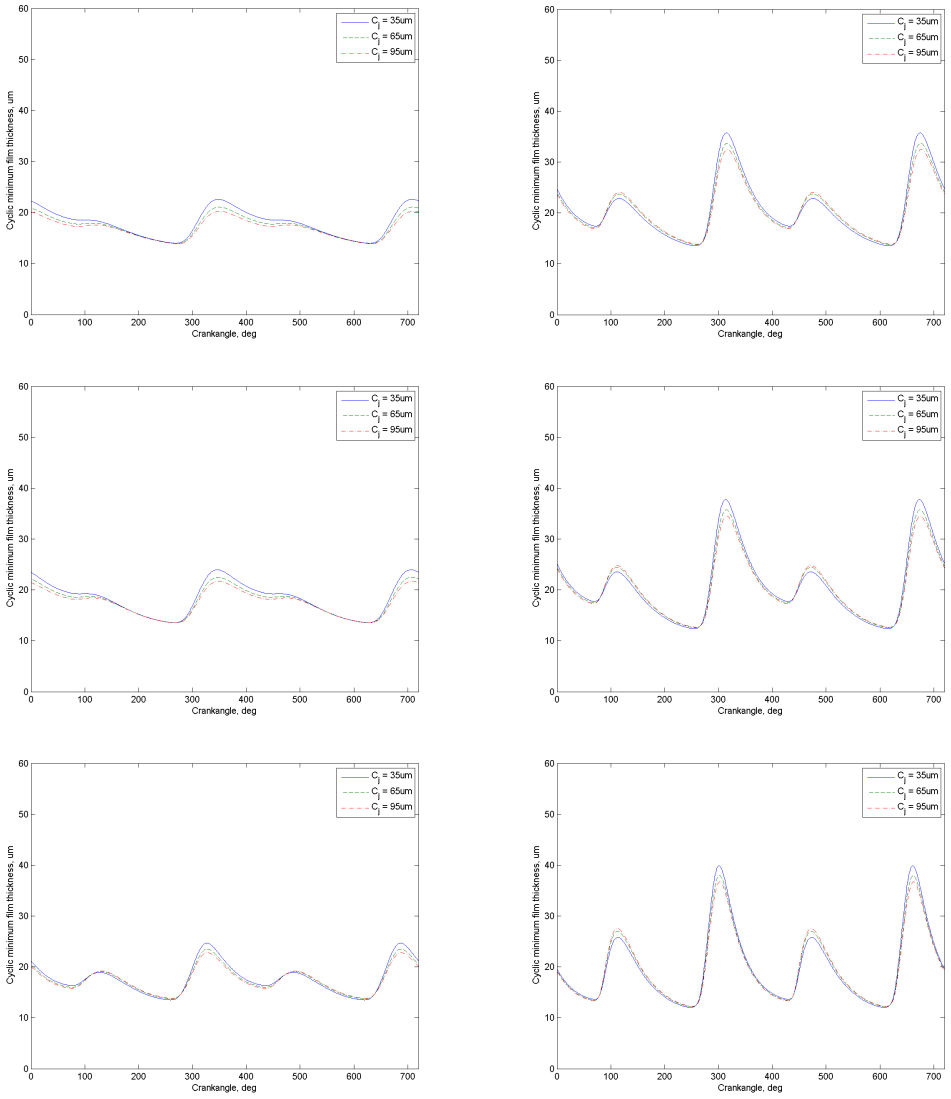

(a) Cr = 35um (b) Cr = 65um

Figure 2.12: Minimum film thickness between the ring and sleeve for a range of inner bearing clearances (Top: 0% Load, Middle: 50% Load, Bottom: 100% Load)

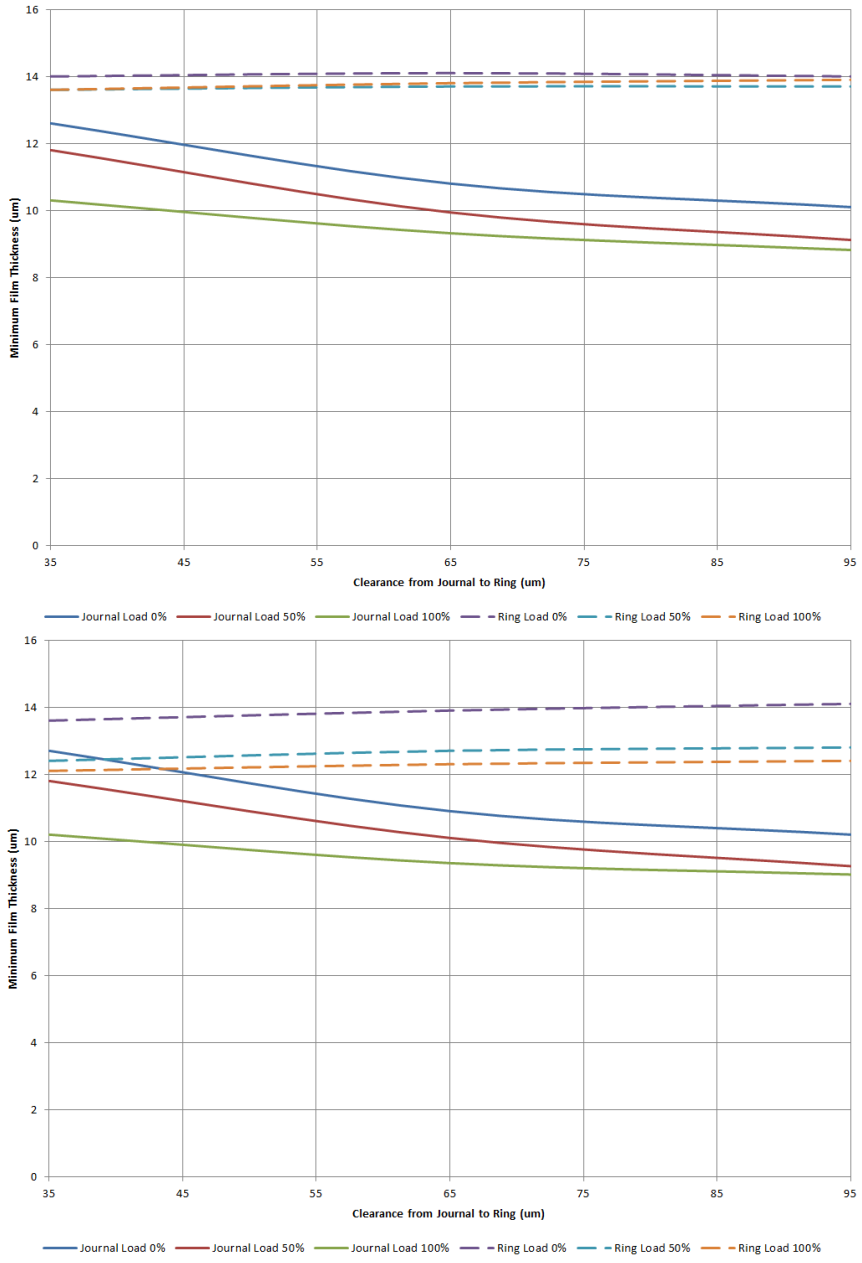

Figure 2.13: Minimum film thickness trends following inner bearing clearances and compressor loading conditions (Top: 35 microns ring clearance, Bottom: 65 microns ring clearance)

SAE	0 °C	20 °C	50 °C	100 °C
10	0.31	0.079	0.020	0.005
20	0.72	0.170	0.033	0.007
30	1.53	0.310	0.061	0.010
40	2.61	0.430	0.072	0.012
50	3.82	0.630	0.097	0.015

Table 2.2: Dynamic viscosity of engine oil(PA-S)

2.5 Modeling a faulty bearing

During the lifetime of a bearing there are many ways that it could fail. One common failure mode is degradation of the lubricant through contamination with either the operating fluid of the compressor or through foreign contaminants such as dirt and water. This can be simulated by changing the viscosity used in the simulation. The simulation of other failure modes is left for a future finite element analysis as the mobility method is limited in this regard.

Oil Viscosity Variation

To model degrading oil, the simulation was run with the typical clearances but various values for viscosity. The operations manual provided by Dresser-Rand specifies the required oil characteristics: Viscosity at 40 degrees C should be no more than 168.4 centistokes and no less than 10.2 centistokes at 100 degrees C. SAE 30 motor oil fits these characteristics fine and is currently used in the compressor as standard oil. To show how oil viscosity affects the bearing performance, the model was run with 35 micron clearance and with viscosity values ranging from SAE 10 to SAE 50 oils at 50 degrees Celsius. Table 2.2 shows the various viscosities for a range of temperatures. 50 degrees Celsius was chosen from thermocouple data measuring main bearing housing temperature.

Figure 2.14 shows the impact of viscosity on minimum film thickness. One can see that the higher the viscosity the higher the film thickness with overall less variation throughout a cycle. While this is theoretically a benefit to the bearing operation, it has negative effects such as increased power loss and in extreme cases issues with refilling the bearing in time and as such should be monitored. A lower viscosity results in thinner films which can lead to bearing wear. Figure 2.15 shows trends for the minimum film thickness based on lubricant variation. It still holds true that higher pressure loadings lead to thinner films regardless of viscosity.

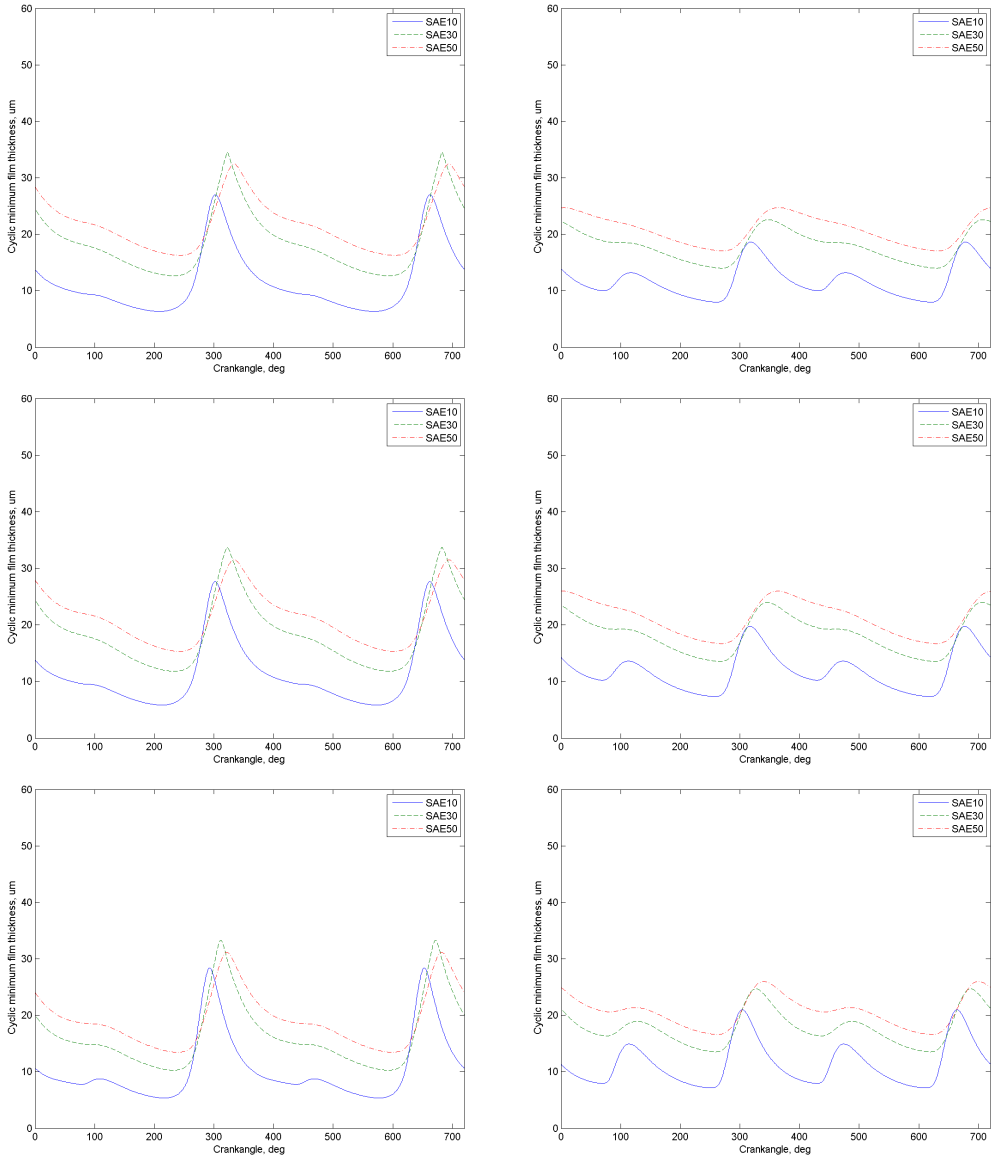

(a) Journal (b) Ring

Figure 2.14: Minimum film thickness for both the inner and outer bearing for a range of viscosities. Both the inner and outer clearance are set to 35 μm (Top: 0% Load, Middle: 50% Load, Bottom: 100% Load)

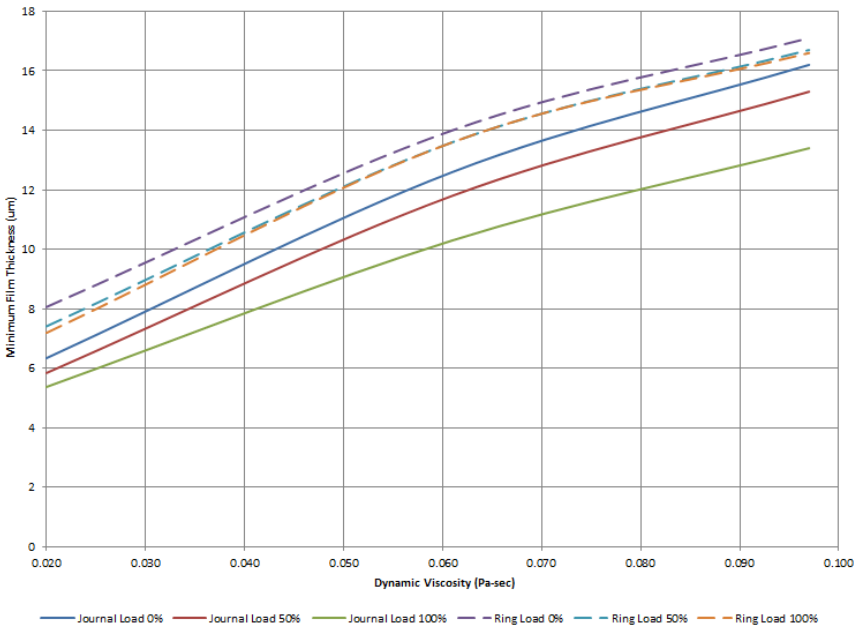

Figure 2.15: Minimum film thickness trends for various lubricant viscosities and compressor loading condition

Chapter 3

Methodology

3.1 Introduction

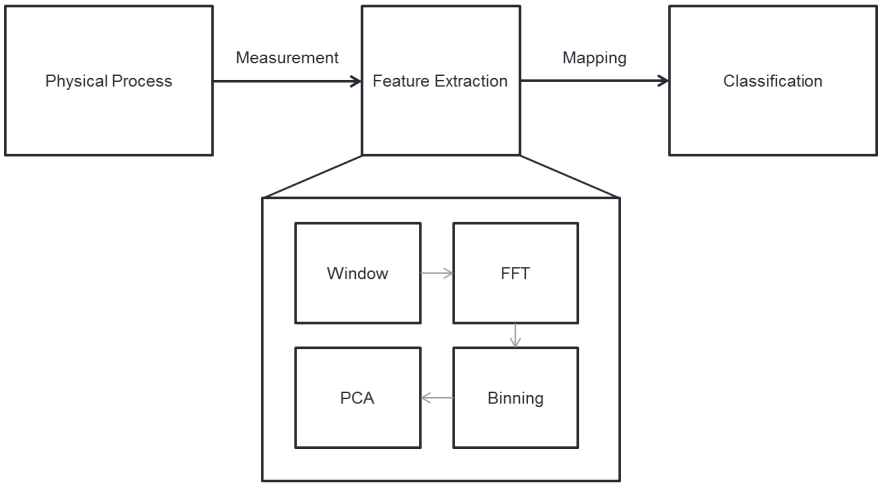

Figure 3.1: Signal processing and classification methodology

This chapter explains the process used in this research to automate the process of classifying the data collected during seeded fault testing (Fig. 3.1). The process is illustrated by following an example with simulated data throughout the different sections. The model described in chapter 2 is used to simulate the eccentricity in the x-direction for three different oil viscosities, SAE10, SAE30, and SAE50. In order to better approximate a real signal, white Gaussian noise is added to the simulated data with a signal to noise ratio of five dB. Additionally, a sinusoid of different amplitude for the different cases at the fifth resonant frequency was added to increase the frequency content in the signal (Eqn. 3.1). The resulting signal is shown in figure 3.2. Fifty seconds of data were simulated and split into one second intervals in order to generate fifty individual samples for each class.

$$x = awgn(x,5) + A*sin(30*theta) \tag{3.1}$$

where A equals fifteen for the SAE30 case, ten for SAE10, and five for SAE50.

The basic methodology is to convert the time domain signal into the frequency domain using a fast Fourier transform (FFT). Then the FFT is separated into frequency bins and a coordinate transformation is applied to orient the signal along its eigenvectors. From there the features are selected and a classifier based on the Bayesian classification approach is used to classify the data.

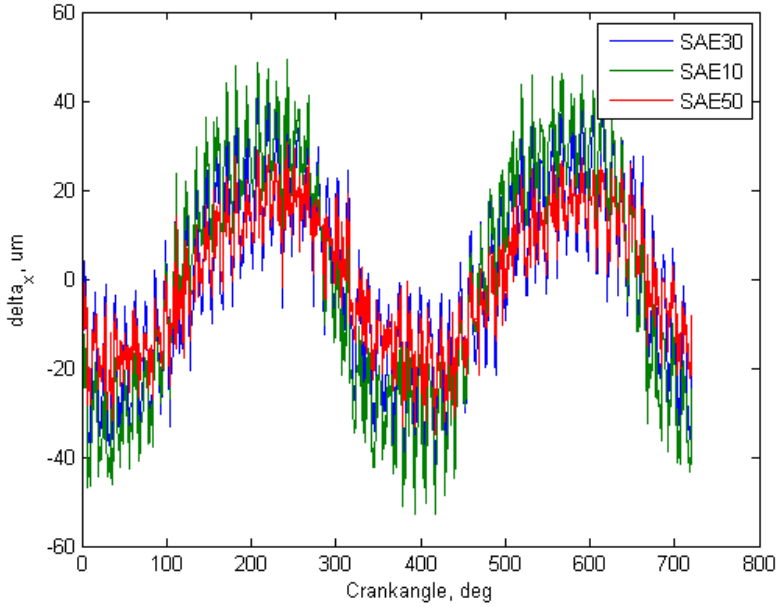

Figure 3.2: Raw x-direction eccentricity data from the simulation used to demonstrate the methodology

3.2 DFT and FFT

The discrete Fourier transform (DFT) converts a signal consisting of equally spaced samples into a list of coefficients of complex sinusoids in order of their frequencies. Effectively it converts a signal from the time domain into the frequency domain. The frequency content of a signal is often of interest in fault detection as many faults have characteristic frequencies associated with them. The basic definition of a DFT is

$$X_k = \sum_{n=0}^{N-1} x_n e^{-2\pi i k n/N} \tag{3.2}$$

where each X_k is the coefficient of a complex sinusoid ordered according to their frequencies. The signal is essentially transformed into the frequency domain from the time domain. The fast Fourier transform is a computation algorithm used instead of evaluating the DFT directly. Both transforms yield the same results. In the case of the example, the FFT shows the most frequency content at 6.4Hz as seen in figure 3.3. This correlates with the operating frequency of the compressor as is expected. A raw FFT does not lend itself to classification due the large number of data points. A sampling rate in the simulation of 2160Hz gives a Nyquist frequency or upper limit of alias-free frequencies of 1080Hz. The frequency resolution can be calculated by dividing the sampling rate by the number of points used to calculate the FFT.

$$freqRes = F_s/N_{FFT} \tag{3.3}$$

where

$$N_{FFT} = 2^P \tag{3.4}$$

where P is the smallest value such that

$$2^P > Signal\ Length \tag{3.5}$$

At the sampling rate used in the simulation, this gives a frequency resolution of 0.5Hz. Even when the frequency range of interested is limited from 1Hz to 350Hz, this results in 750 features. This is ineffective for classification many of those points are simply due to noise and not representative of any content.

In order to avoid any issues with signal end points not matching or incomplete periods in the signal, a basic Hamming window is applied over the entire signal length. Investigating the effect of changing window parameters is reserved for future work.

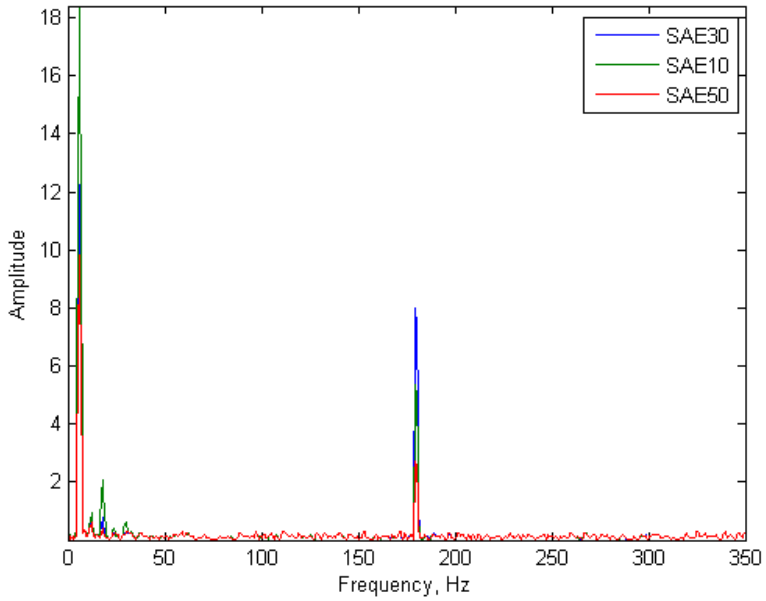

Figure 3.3: FFT of the eccentricity data used to demonstrate the methodology

3.3 FFT Binning

The first step in reducing the number of features is the binning process of the FFT. This reduces the resolution based on the number and size of the bins. Additionally, the frequencies are also limited to a range of interest. In this case, a range of 1 to 350 Hz with a bin size of 10 Hz are chosen. To compute the magnitude of a bin, the FFT is numerically integrated over the range of frequencies the bin covers using the trapezoidal rule.

$$\int_{f=x}^{y} FFT(f)df = (y-x)\frac{FFT(x)+FFT(y)}{2} \tag{3.6}$$

where x is the starting frequency and y is the end frequency of the bin. This can then be repeated to cover the entire FFT. Figure 3.4 shows the results for the three cases. There are now 35 bins for each case instead of 750 points as before. The difference in the signals is preserved.

3.4 Coordinate Transformation

Remapping a dataset in a different coordinate frame can reveal new insights about characteristic features. In this research, principle component analysis (PCA) is used to map the data along its eigenvectors. This serves as a way to identify patterns in the date and plot the data in a way that highlights these patters. PCA also gives the option to reduce the number of dimensions of a feature vector by mapping it to a space with a smaller dimensions through equation 3.7

$$Z = W^T Y^T \tag{3.7}$$

where Y is the original data and W is the mapping vector. The dimension of the mapping vector depends on how many eigenvectors are chosen and can range from one up to the original number of dimensions.

This process has been used successfully in previous research dealing with rotating machinery. Chirico and Kolodziej applied this technique to separate bearing faults in electro-mechanical activators [22] and De Boe and Golinval used PCA to localize a fault through an array of piezoelectronic sensors [23].

When applying PCA to a multi dimensional data set, covariance becomes an important factor in the analysis as it gives information about the relationship between different dimensions. Then the largest eigen-

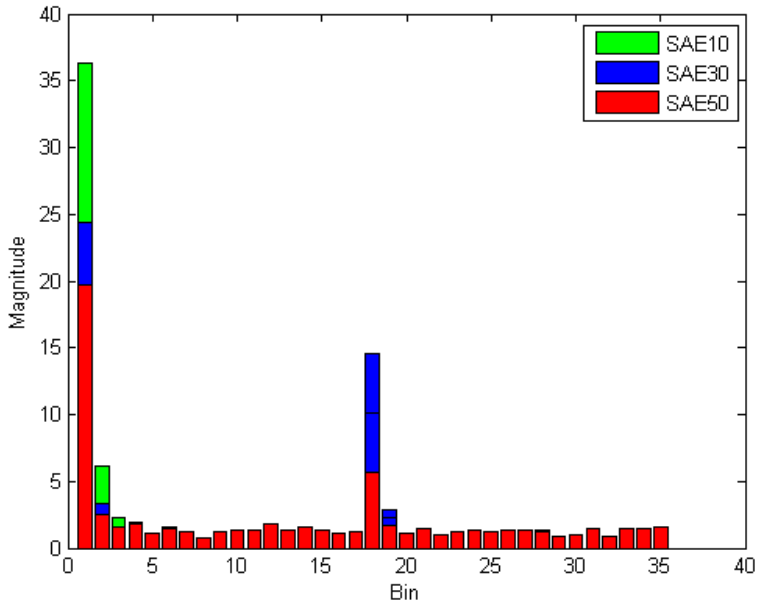

Figure 3.4: Binned FFT data used to demonstrate the methodology

values and the associated eigenvectors of the covariance matrix represent the principle components [24]. How much information is represented by a single eigenvalue can be estimated from the percentage that the eigenvalue represents of the sum of all eigenvalues. Figure 3.5 shows that in the case of the example, the first two eigenvalues reproduce 99% of the information in the system. In order to reduce the dimension of the dataset, the eigenvectors corresponding to the largest eigenvalues are chosen. The final feature vector is found by multiplying the eigenvector matrix with the data matrix.

Below is detailed step-through of the process:

1. Center the data at zero by subtracting the mean $\bar{x}_i$ from each dimension i.

$$y_i = x_i - \bar{x}_i \tag{3.8}$$

then,

$$Y = (y_1, y_2, \ldots, y_n) \tag{3.9}$$

2. Form the covariance matrix C by calculating the covariance between each dimension y_1 through y_n.

$$C = \begin{pmatrix} cov(y_1, y_1) & cov(y_1, y_2) & \ldots & cov(y_1, y_n) \\ cov(y_2, y_1) & cov(y_2, y_2) & \ldots & cov(y_2, y_n) \\ \vdots & \vdots & \ddots & \vdots \\ cov(y_n, y_1) & cov(y_n, y_2) & \ldots & cov(y_n, y_n) \end{pmatrix} \tag{3.10}$$

3. Determine the eigenvalues and eigenvectors of the covariance matrix.

4. Determine which eigenvectors to use and form a feature vector W where k is the maximum number of dimensions the final feature data set should contain.

$$W = (eig_1, eig_2, \ldots, eig_k) \tag{3.11}$$

5. Determine the final feature data set by multiplying the transpose of the feature matrix with the transpose of the adjusted data set from step 1 as shown by equation 3.7.

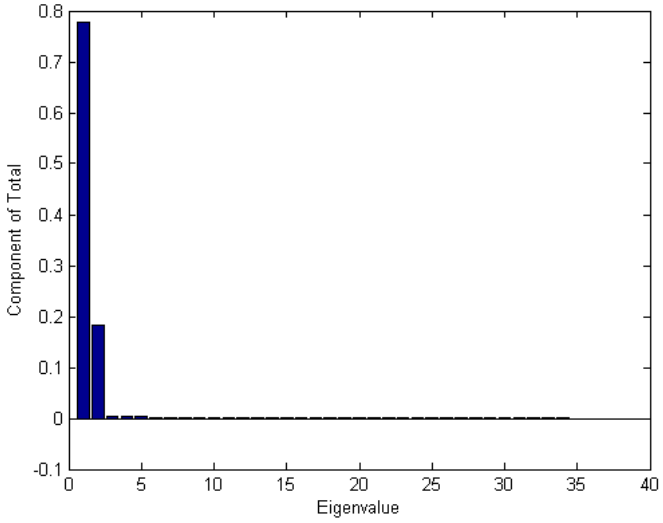

Figure 3.5: Percentage each eigenvalue represents of the total sum to determine fidelity loss by reducing features

Plotting the data in the new coordinate frame shows clear separation between the classes (Fig. 3.6). In this example a final dimension of two was chosen as the largest two eigenvalues nearly completely represent the system as seen in figure 3.5. This also allows for convenient plotting of the feature vector where each axis represents one dimension of the feature vector. From the binned FFT and the number of samples for each case, the data vector Y has a dimension of 50 by 35. Choosing two eigenvectors for the feature vector leads to dimensions of 35 by 2. Multiplying these according to equation 3.7 leads to a final feature vector with dimensions of 2 by 50, or 50 samples for each case with 2 features describing each sample, down from 35 features based on the binned FFT without losing information about the system. This shows the power of principle component analysis.

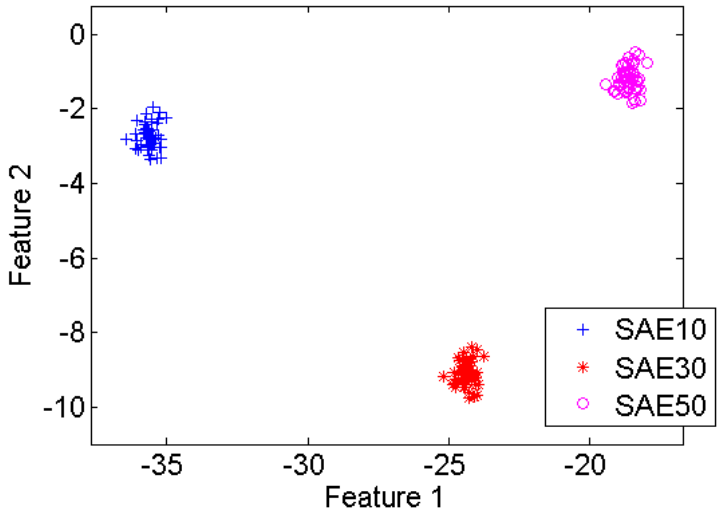

Figure 3.6: Plotting the data in the feature coordinate frame determined by PCA

3.5 Bayesian Classification

There are many different options for pattern classification. A classifier looks for certain patterns in recorded measurements and as a result of the classification process assigns the measured object to a class (Fig. 3.7). This work focuses on a statistical approach and specifically a Bayesian classifier.

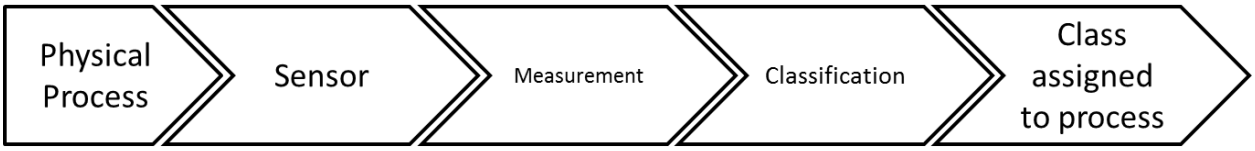

Figure 3.7: Basic pattern classification process

The Bayesian classifier is based on probability theory and Bayes theorem in particular. Using Bayes theorem, one can calculate the posterior probability of a class based on the feature vector.

$$P(w_k|z) = \frac{p(z|w_k)P(w_k)}{p(z)} \tag{3.12}$$

$P(w_k|z)$ is the posterior probability of a class. This is the result that determines what class is assigned to a feature. $p(z|w_k)$ is the conditional probability density function of the feature vector. For this work, a two dimensional Gaussian pdf is assumed (Eqn. 3.13).

$$f(x,y) = \frac{1}{2\pi\sigma_x\sigma_y\sqrt{1-\rho^2}} exp\left(-\frac{1}{2(1-\rho^2)}\left[\frac{(x-\mu_x)^2}{\sigma_x^2} + \frac{(y-\mu_y)^2}{\sigma_y^2} - \frac{2\rho(x-\mu_x)(y-\mu_y)}{\sigma_x\sigma_y}\right]\right) \tag{3.13}$$

The mean and standard deviations are determined from the actual feature vectors for each class that are obtained through seeded fault testing. $P(w_k)$ is known as the prior probability of a class and is based on knowledge about the system in question. In this research all classes are assumed to have equal prior probability. Finally, $p(z)$ is the unconditional probability density function of the feature vector. This can be calculated by

$$p(z) = \sum_{k-1}^{K}[p(z|w_k)P(w_k)] \tag{3.14}$$

Associated with each class of the classifier is a cost. This cost represents the risk involved when selecting a given class. As an example, it could have large consequences when a failing bearing is classified as healthy and the machine continues to run. This might lead to a catastrophic failure. However, there is also as cost involved if a healthy bearing is classified as failing when it still has significant life left and maintenance is performed too early. This cost is represented in the following equations as $C(w_i|w_k)$, where w_i is the class chosen by the classifier and w_k is the actual class. The expected cost or risk is given by

$$R(w_i|z) = E[C(w_i|w_k)|z] = \sum_{k=1}^{K}[C(w_i|w_k)P(w_k|z)] \tag{3.15}$$

The Bayesian classifier returns the class that minimizes this risk

$$w_{BAYES}(z) = min\sum_{k=1}^{K} C(w_i|w_k)P(w_k|z) \tag{3.16}$$

These classifiers can then be integrated into software packages to automate the process [25]. In this research, the prior probability and cost function are both set to unity to generate effectively a maximum likelihood classifier where only the posterior probability determines the class assigned to a feature. The resulting classification output for the example is shown in figure 3.8.

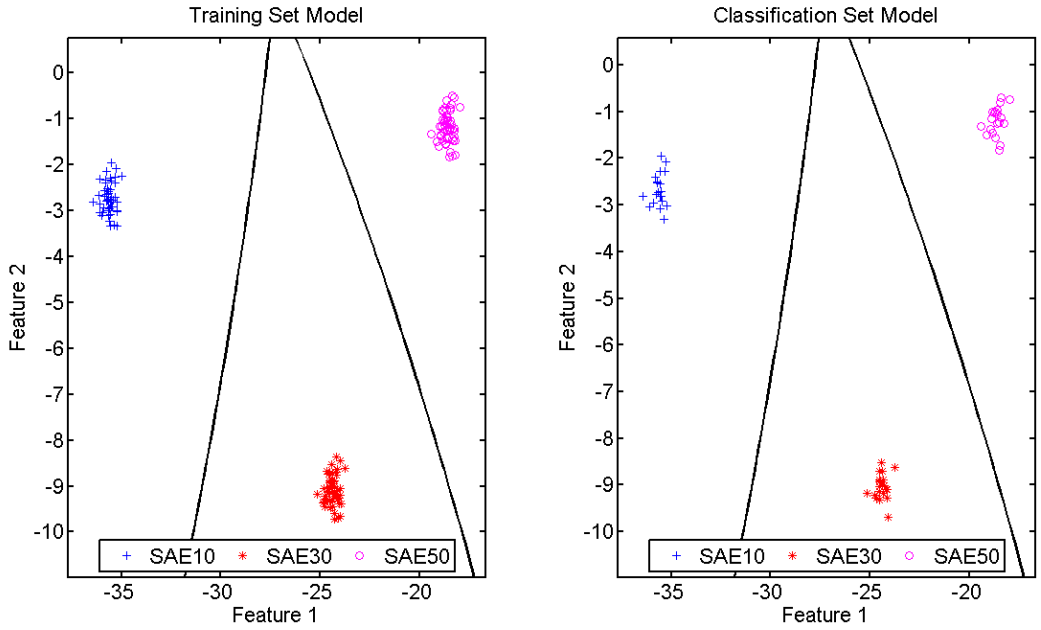

Figure 3.8: Final classifier output for simulated data with the training set on the left and the validation set on the right

Chapter 4

Simulation Classification

This methodology was then applied to two simulation cases: Varying oil viscosity and varying clearance. This allows for later comparison to experimental results. The oil viscosities used are values for SAE10, SAE30, and SAE50 oil at fifty degrees Celsius. These are the actual oils used in the experimental section so that the results may be compared against each other. The bearing clearances are measured from the original bearing in the compressor as well as two new bearings. Again, these are the actual bearings used in the experimental section to allow for comparison between simulation and experiment. Both the viscosity and the clearance simulation are run for all three loading conditions of the compressor (0%, 50%, and 100%). The simulated signal is the x-direction position of the crankshaft at the measurement location of the LVDT as described in chapter 5. This again allows for better comparison to experimental results. Additionally, random noise with a mean of 0 and a standard deviation of 5.5 is added to the signal to better replicate an actual measurement.

Oil Viscosity Table 4.1 shows the details of the oil viscosity simulation case study. Figure 4.1 shows the training and validation sets for the classifier. The classifier returns a 100% correct classification. Thicker oil has a smaller magnitude feature 1 and as the oil gets thinner the magnitude of feature 1 increases.

Legend Entry	SAE30	SAE10	SAE50
Inner Radial Clearance (mm)	0.035	0.035	0.035
Outer Radial Clearance (mm)	0.031	0.031	0.031
Oil Type	SAE30	SAE10	SAE50

Table 4.1: Case study details for varying viscosity

Clearance Variation Table 4.2 shows the simulation parameters for the clearance simulation case study. Figure 4.2 shows the training and validation sets for the new bearing classification. The classifier returns very good results and shows the same trends as the viscosity variation which is expected. The overall difference between the classes is smaller which comes from the smaller difference in clearances compared to the differences in viscosity.

Legend Entry	Original	New 1	New 2
Inner Radial Clearance (mm)	0.035	0.010	0.005
Outer Radial Clearance (mm)	0.031	0.013	0.020
Oil Type	SAE30	SAE30	SAE30

Table 4.2: Case study details for clearance simulation

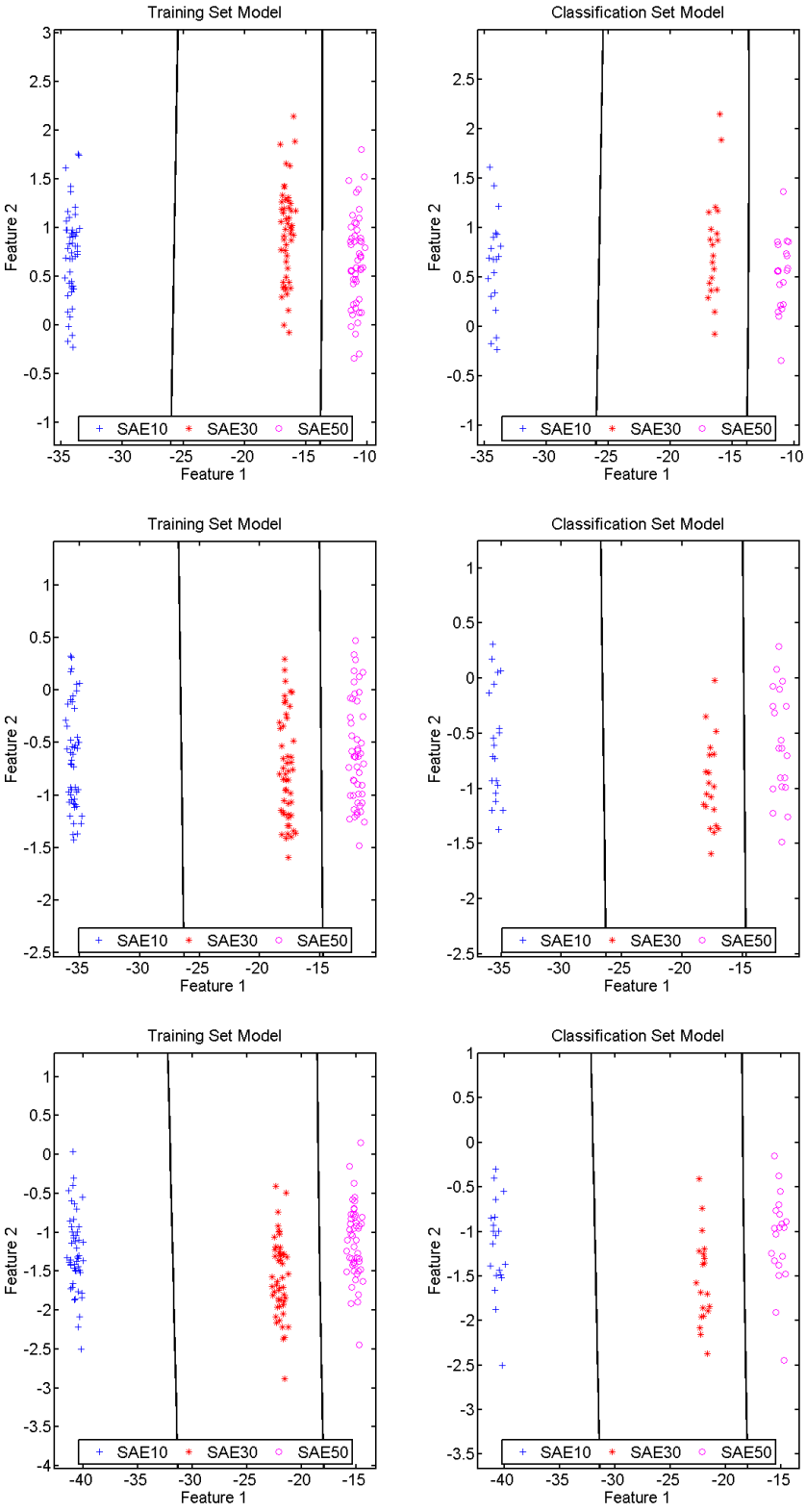

Figure 4.1: Classification training and validation sets for the varying viscosity (Top: 0% Load, Middle: 50% Load, Bottom: 100% Load)

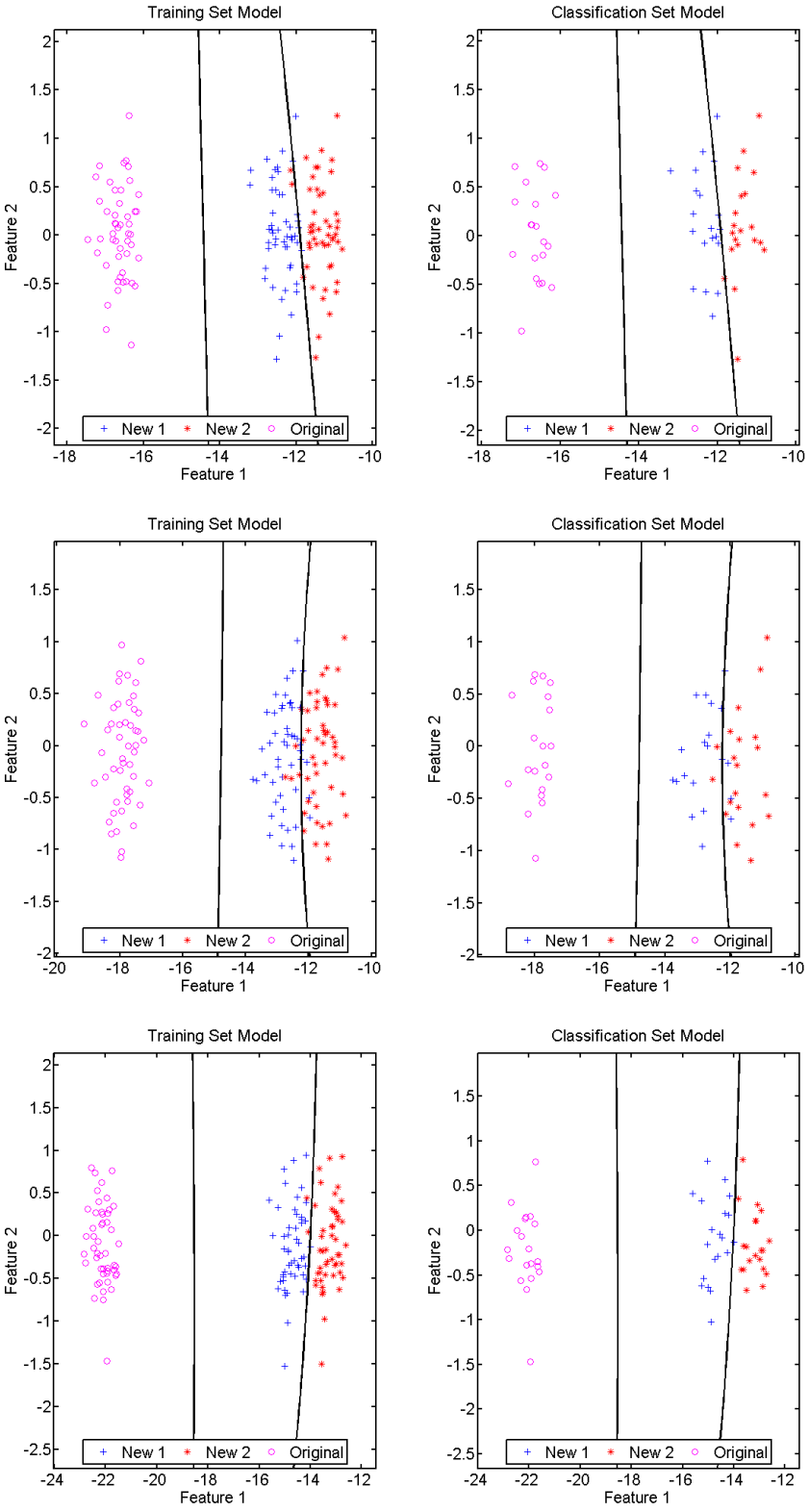

Figure 4.2: Classification training and validation sets for the clearance variation (Top: 0% Load, Middle: 50% Load, Bottom: 100% Load)

Chapter 5

Seeded Fault Testing

5.1 Design of Experiment

The goal is to test several variations of the same fault type in order to establish trends in the classification. Three different fault types are considered: Oil viscosity, circumferential grooves, and obstruction of the oil feed holes. For each type, two cases of varying severity are considered. The unmodified bearing with SAE30 oil is the baseline for all tests and is considered the healthy bearing from here on. To test the effects of viscosity changes, SAE10 and SAE50 oils are tested. To investigate grooving, the bearing is run with a single groove in one inner land as well as with symmetrical grooves in both inner lands. Lastly, the bearing is run with two degrees of oil feed hole obstruction. The first case is 75% blocked and the second case is 50% blocked.

For each condition, a steady state test is run to gather data for classification. The compressor is run for one hour to achieve a steady oil temperature. Data is collected from six accelerometers, two LVDTs, and a current sensor. Also recorded is the temperature of the oil and both main bearing housings. Additionally, start-up and shut-down data are collected for both the cold compressor as well as after steady state condition is reached.

5.2 Data Collection

5.2.1 Measuring bearing orbit

Background In order to validate the model created in Matlab, the actual orbital motion of the bearing is measured. Researching the available literature demonstrated several possible methods of measuring the bearing motion. Jeon et al. developed a cylindrical capacitive sensor [26] in order to reduce the error from imperfections in the measured object. In order to keep costs low and use off-the-shelf sensors, the measurements for this research are taken from two displacement sensors arranged ninety degrees apart, measuring the x and z movement of the crankshaft. Figure 5.1 shows a schematic of the layout. Since e_x and e_z are much smaller than R, the angles α and β can be assumed small in the analysis. This greatly simplifies the solution. If α and β were non-trivial the equations to solve would be:

$$e_x^2 + e_y^2 = R^2 + x^2 - 2Rx\cos b \tag{5.1}$$

$$e_x^2 + e_y^2 = R^2 + y^2 - 2Ry\cos a \tag{5.2}$$

Also,

$$R\cos b + e_y = x \tag{5.3}$$

$$R\cos a + e_y = y \tag{5.4}$$

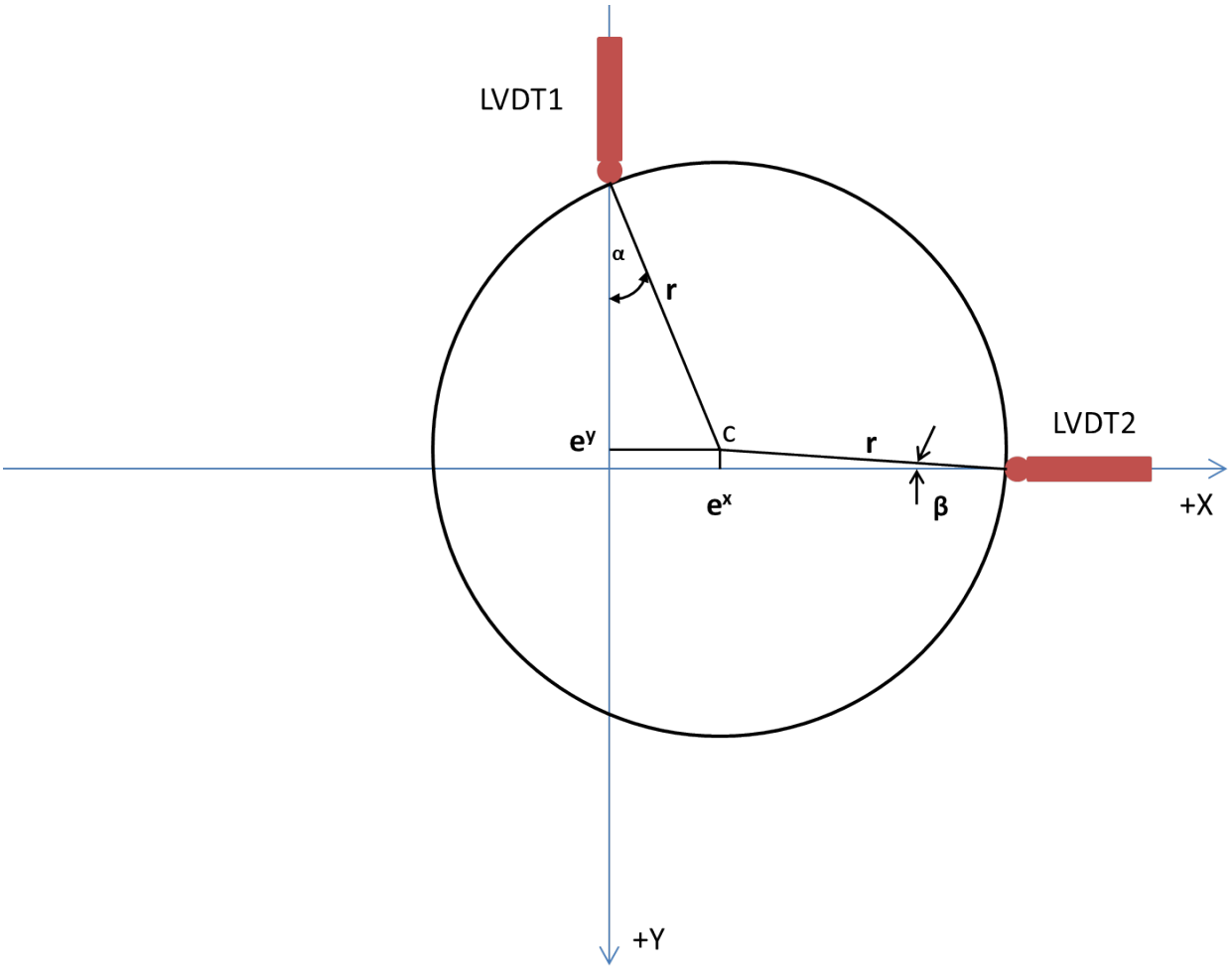

Figure 5.1: Approach and theory to measure the crankshaft orbit

Due to the small angle approximation, these simplify to

$$R + e_x = x \tag{5.5}$$

$$R + e_y = y \tag{5.6}$$

And since the sensors are calibrated to read zero when the compressor is at rest, the eccentricity vectors can be measured directly from the sensors without any additional calculation.

Sensor Technology Several sensor technologies from various vendors were considered for the actual measurements. The options included capacitive non-contact sensors, fiber-optic non-contact sensors, eddy current non-contact sensors, and finally a contact linear variable differential transformer (LVDT) sensor set-up. Table 5.1 shows a list of considered sensors and their specifications. Since the crankshaft is very heavy compared to any sensor pushback, the contact method with LVDTs was chosen for cost effectiveness while maintaining high accuracy.

The sensor model chosen for the initial measurements is the BBPM-315-020 LVDT from Macro Sensors. It has a range of $\pm$ 0.5mm with a repeatability of $<$ 0.15 microns. Along with the sensor, the LVC2500 signal conditioning module is used in order to deliver the 0-10Vdc output for the data acquisition system.

LVDT is an acronym for linear variable differential transformer. Figure 5.2 shows the construction of an LVDT. It consists of a coil assembly with one primary coil and two secondary coils on either side of the

Company	Sensor / Signal Conditioner	Method	Range	Accuracy / Repeatability	Output	Cost (Dollar)
Macro Sensors	BBPM-315-20 / LVC2500	LVDT	+/- 0.5mm	0.15 microns	+/- 10V	1,664
Bently Nevada	3300 XL 8mm probe	Eddy Current	2mm	–	4-20ma	1,960
Philtec	RC12	Fiber optic	0.5mm	1 percent	0-5V	3,290
RDP Electrosense	AC-AC LVDT	LVDT	+/- 0.5mm	0.15 microns	+/- 10V	2,240
Lion Precision	MFG3-3002 system / P016-6002 Probe	Capacitive	–	–	+/- 10V	4,680
Capacitec	220-SLC-4KHz-ENC / HPT-150E-A-L2-10-B Probe	Capacitive	250 microns	0.1nm	+/- 10V	5,260
Keyence	GT2-H12 / GT2-71MCP	LVDT	12mm	0.5 microns	4-20ma	1,645

Table 5.1: Possible sensor options to measure orbital motion. Both contact and non contact options were considered

primary. It has a magnetic core that can move axially within the coils. When applying an appropriate AC voltage to the primary coil, a magnetic flux is created that is coupled to the secondary coils through the core. As the core moves with the object whose displacement is to be measured, the voltages in the secondary coils start to differ from each other [27]. This difference is measured and converted to an easy to use DC voltage or current by the signal conditioning equipment.

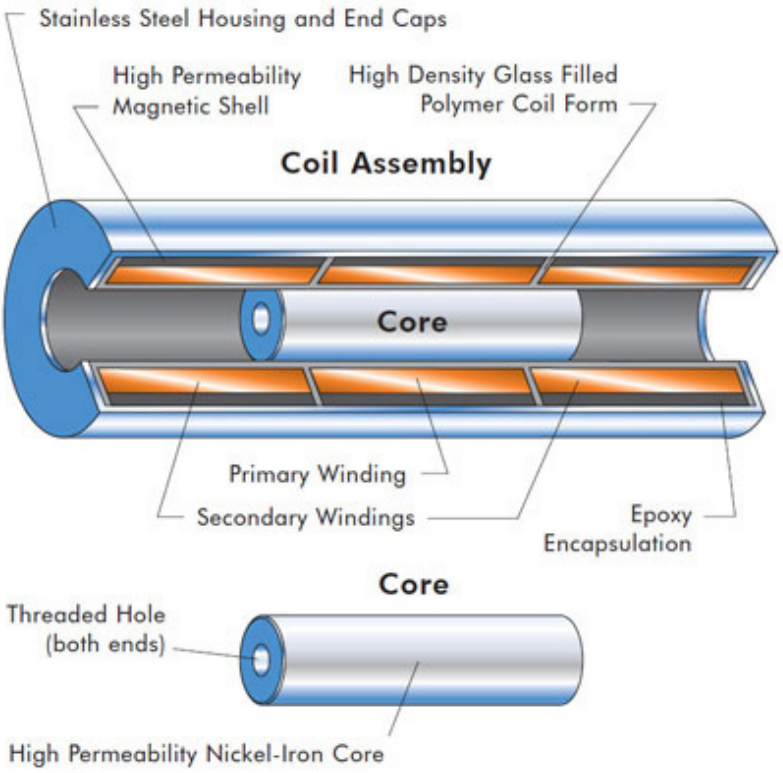

Figure 5.2: Cutaway view of an LVDT [27]

Sensor installation In order to ensure the correct mounting of the sensors radially in line with the crankshaft centerline as well as 90 degrees apart from each other, a special sensor mount was designed. Below are 3D images showing the final layout, followed by pictures of the manufactured bracket with sensors installed.

Data Collection To determine the validity of the measurements obtained from the LVDTs, they are compared to the Matlab model. Figure 5.5 a comparison of simulating the motion of the crankshaft at the measurement location with a brand new bearing installed and actual measurement data of that bearing. There is good agreement on the overall magnitude of the results with the characteristic straight line motion lining up well. There are differences between the model and the experiment in shape which can be explained by the overall movement and vibration of the compressor affecting the signal. These differences become more pronounced with increased pressure loading on the compressor.

To determine the sensitivity of the LVDTs and the signal path, a block of aluminum is drilled to hold the sensor in a fixed position at about the midpoint of the sensor range to ensure the signal collected represents a steady state. Then the data is normalized with respect to the mean and its standard deviation is determined (Fig. 5.6). Given the range of the sensor and its actual output range a scale factor is determined. Table 5.2 shows the results obtained.

Lastly, the data collected during compressor operation is compared against turning the crankshaft by hand (Fig. 5.7). This ensure that the data collected is representative of the compressor state and not simply

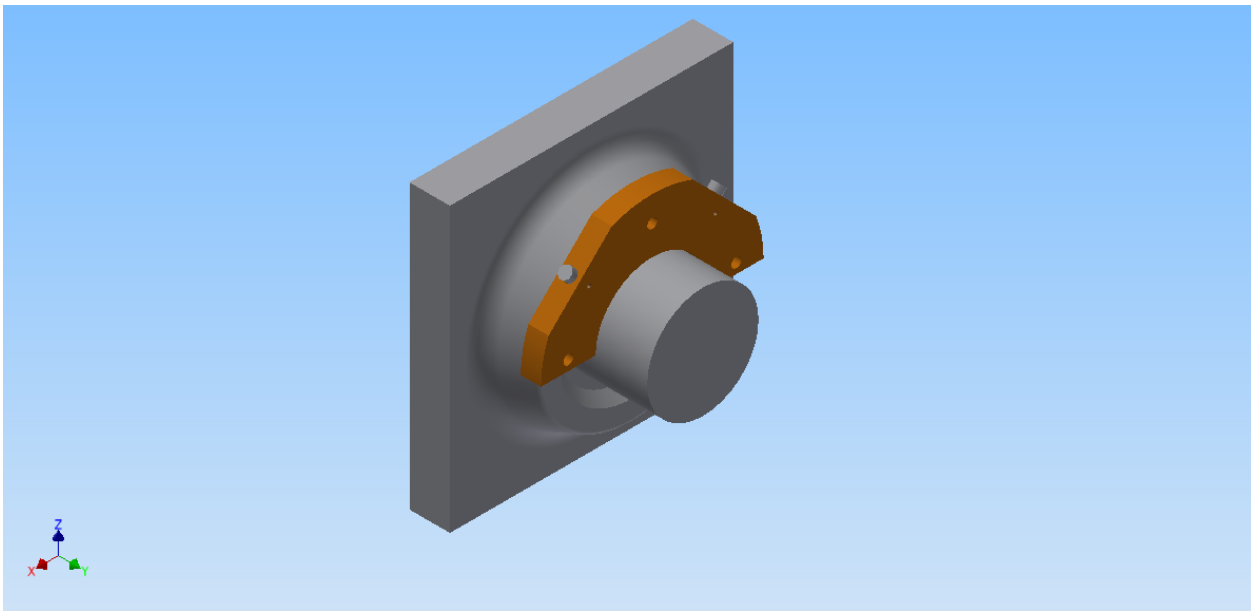

Figure 5.3: Isometric view of the sensor bracket shown in position on compressor cutout

Figure 5.4: Machined sensor bracket with LVDTs installed

a measurement of the crankshaft surface finish. Figure 5.7 shows the measurement of the LVDTs when the compressor is running at 0 load versus when turned by hand. As one can see there are differences in the signal indicating that the measured values are representative of the running compressor. The difference in experimental data to the one shown in figure 5.5 is due to a brand new bearing shown in the comparison to the simulation while a run-in bearing is shown in figure 5.7. There is also a coordinate transformation necessary to align the simulation with the experimental data while figure 5.7 shows raw data without processing.

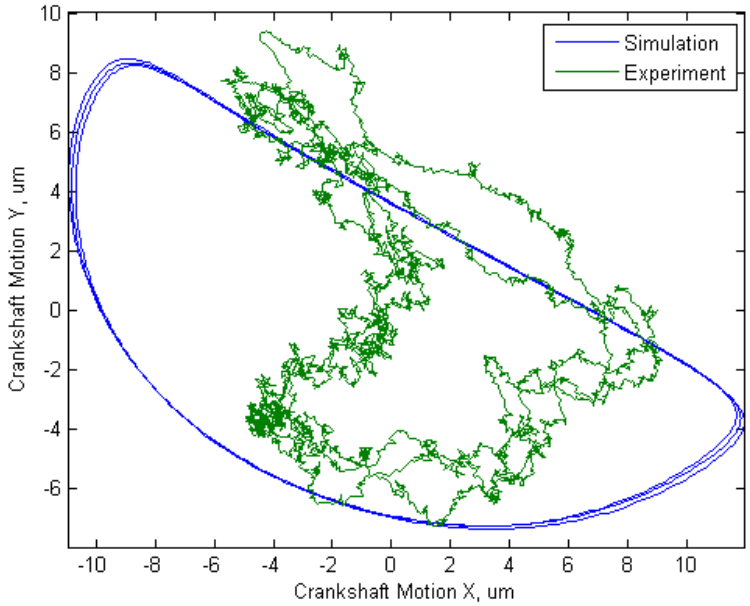

Figure 5.5: Comparison between simulation and experimental measurements of a new bearing at the 0% loading condition

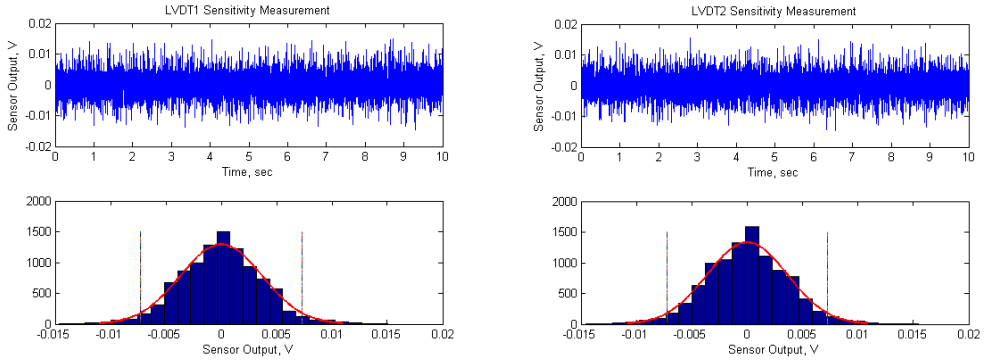

(a) LVDT 1

(b) LVDT 2

Figure 5.6: Sensitivity measurements for both LVDTs. Top shows time signal, bottom shows distribution of signal with the vertical line marking 2 standard deviations.

	LVDT 1	LVDT 2
Scale Factor (μm/V)	98.03	97.09
Standard Devitation (V)	0.0037	0.0036
Uncertainty, 2 Std (μm)	0.72	0.70

Table 5.2: LVDT sensitivity information

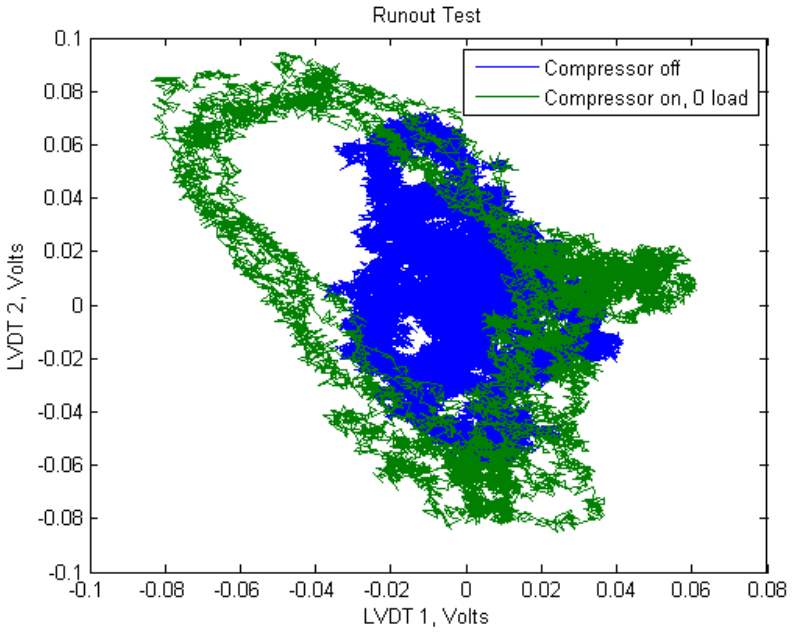

Figure 5.7: Measurement with the compressor on versus turning the crankshaft by hand

Location	Direction	Model	Sensitivity (mV/g)
Frame	-x	PCB 623C01	97
Frame	z	PCB 623C01	101
Crankcase	x	Wilcoxon Research 793-33	102
Crosshead	z	Wilcoxon Research 793-33	99
Bearing Housing	Radial	PCB 607A11	101
Crankshaft	Radial	PCB 66213LPZ2	100

Table 5.3: Accelerometer Detail

5.2.2 Vibration Measurements

Background Vibration measurements have long been used in condition monitoring and finding the Fast Fourier Transform of vibration measurements is a standard method to detect machine faults. Almost all references cited in the bearing monitoring section of the literature review use some form of vibration measurement.

Sensor Technology All vibration sensors installed on this compressor are of the piezoelectric type. When a force due an acceleration is applied to a mass inside the accelerometer (fig. 5.8), the piezoelectric material connected to the mass induces a charge proportional to the force. This charge is then conditioned to a voltage output and connected to the data acquisition system. More information can be found on the PCB website (www.pcb.com)

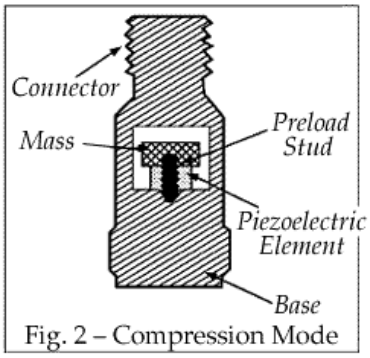

Figure 5.8: Piezoelectric Accelerometer Detail (from PCB)

Sensor Installation Part of the data acquisition capabilities are vibration sensors in the x, y, and z direction. In previous projects, accelerometers were installed on the frame base underneath the cylinder as basic characterization sensors (Fig. 5.9). With Dresser-Rand's Envision system, two more accelerometers are installed, one oriented in the x-direction on the crankcase and one oriented in the z-direction on the frame extension above the crosshead bearing (Fig. 5.10). Additionally to the traditional sensors on the outside of the compressor, an accelerometer is installed on the inside of the crankcase and attached directly to the bearing housing in a radial fashion. As a completely new sensor option, an accelerometer is installed on the crankshaft. It transmits its signal wirelessly at a fixed sampling rate of 2.6 kHz (Fig 5.11).

The X sensor is meant to pick up issues mostly in regard to big end bearing issues but also other failures in the crankshaft. The Z sensor is very effective at detecting faults in the crosshead bearing as well as small end bearing. Having two sensors in the same direction on the compressor can allow for finding the location of faults as these may cause vibration that dampen out when travelling through the machine. If one sensor picks up a stronger vibration in one frequency it shows that something is local to that area.

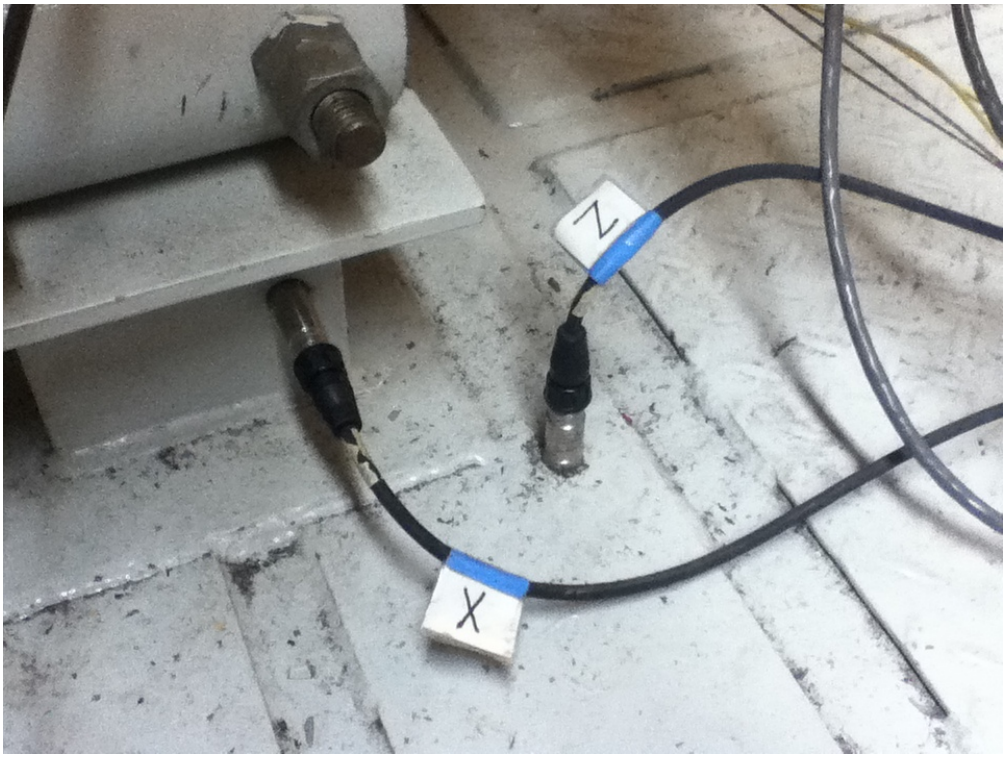

Figure 5.9: Frame accelerometer install location

X direction One can see that the signal from the frame sensor is a relatively smooth curve with the low frequency motion as the dominant feature (5.12). As the load increases, the overall amplitude increases as well. The signal from the crankcase sensor is more interesting. During the 0 load cycle, one can see the load reversal in the big end bearing at 180 and 360 degrees, or bottom dead center (BDC) and top dead center (TDC) respectively. Once the load switches to 50, the load reversal at TDC becomes far more pronounced due to the pressure on the crank side cylinder. Under 100 loading, the signal becomes more agitated. However, the peaks return to BDC as well as TDC since there is a symmetric pressure on both sides of the piston.

Z direction Figure 5.14 shows the vibration in the z direction for the frame sensor and the crosshead sensor. First, consider the crosshead sensor. Looking at the 0 loading condition, one can see peaks at TDC and BDC. This is due to the load reversing on the cross head pin. At 50 loading, the well-defined peak at BDC becomes less pronounced lasts for a longer range of crank angle. It is consistent with the time frame of the highest compression in the cylinder. Under 100 loading, the situation almost reverses from the 50 condition. Now the peaks move to BDC. As far as the frame mounted sensor goes, it is a similar situation as in the x direction. It is a fairly smooth signal with the notable feature being the 6Hz motion. One interesting fact to note is that there is a difference in this motion between the two mounting points. This shows that there is a pitching motion in the compressor. The cross head is closer to the center of rotation as it has the flatter signal response. The sinusoid is more pronounced in the frame sensor which shows that its mounting point moves more overall. This is most noticeable during the 0 loading cycle before pressure effects start to play a role.

Start-up measurements Bearings wear more heavily during start-up and shut-down phases as the compressor approaches steady state operating conditions from rest. As such it is important to be able to monitor the bearing during those phases and be able to give an overview of the operating characteristics. Similar measurements as the steady state condition are taken for a compressor start-up. Only the 0 loading condition is available as a built in safety feature in the compressor.

(a) Crankcase accelerometer

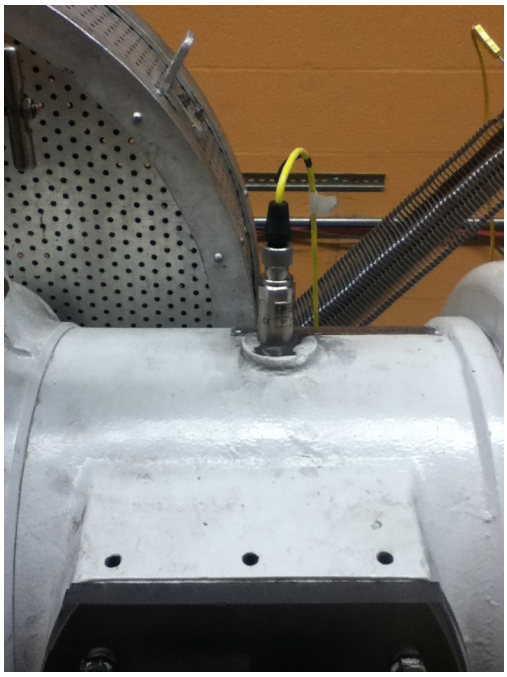

(b) Crosshead accelerometer

Figure 5.10: Crankcase and Crosshead accelerometer install location

(a) Bearing accelerometer

(b) Wireless accelerometer with transmitter box

Figure 5.11: Bearing housing accelerometer and wireless accelerometer install location

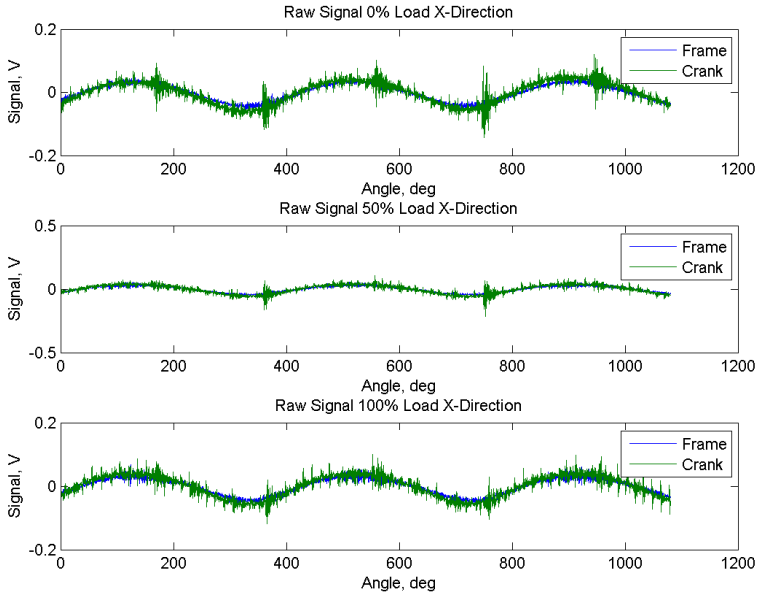

Figure 5.12: X direction raw signal comparison between the frame and crank accelerometer (Top: 0% Load, Middle: 50% Load, Bottom: 100% Load)

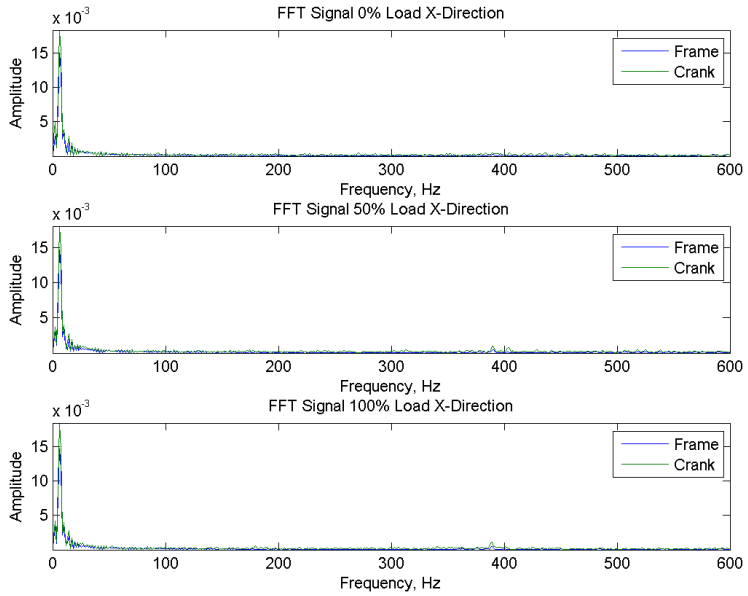

Figure 5.13: X direction FFT signal comparison between the frame and crank accelerometer (Top: 0% Load, Middle: 50% Load, Bottom: 100% Load)

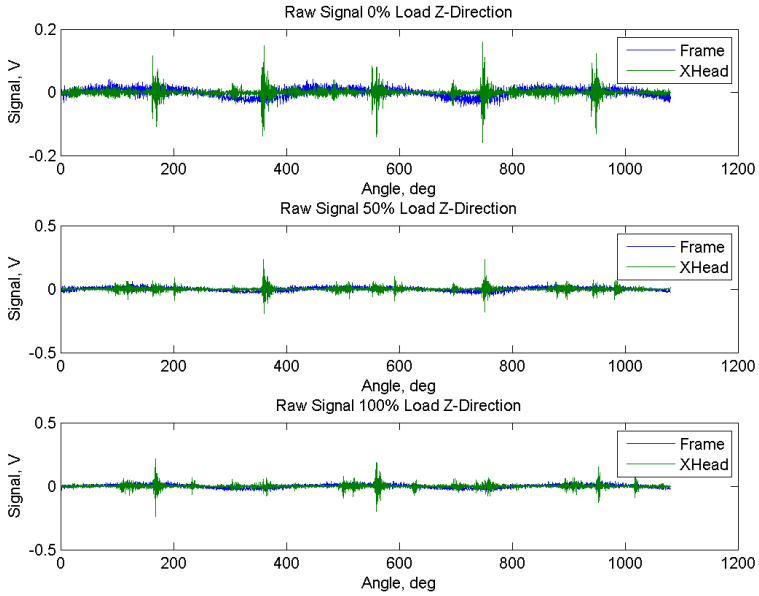

Figure 5.14: Z direction raw signal comparison between the frame and crosshead accelerometer (Top: 0% Load, Middle: 50% Load, Bottom: 100% Load)

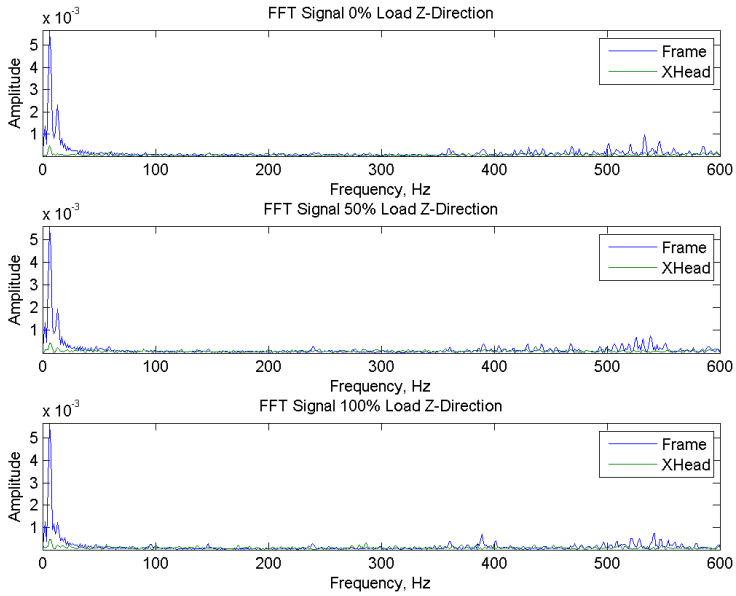

Figure 5.15: Z direction FFT signal comparison between the frame and crosshead accelerometer (Top: 0% Load, Middle: 50% Load, Bottom: 100% Load)

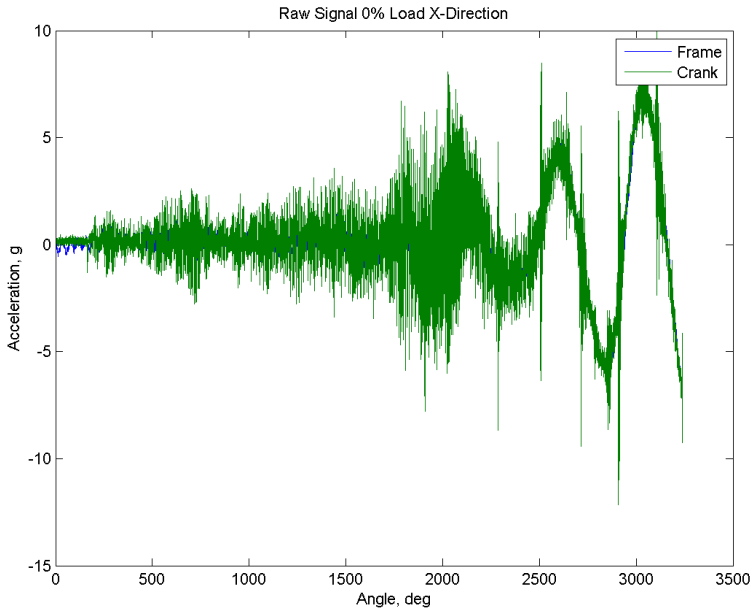

Figure 5.16: Start-Up: X direction raw signal comparison between the frame and crank accelerometer (Top: 0% Load, Middle: 50% Load, Bottom: 100% Load)

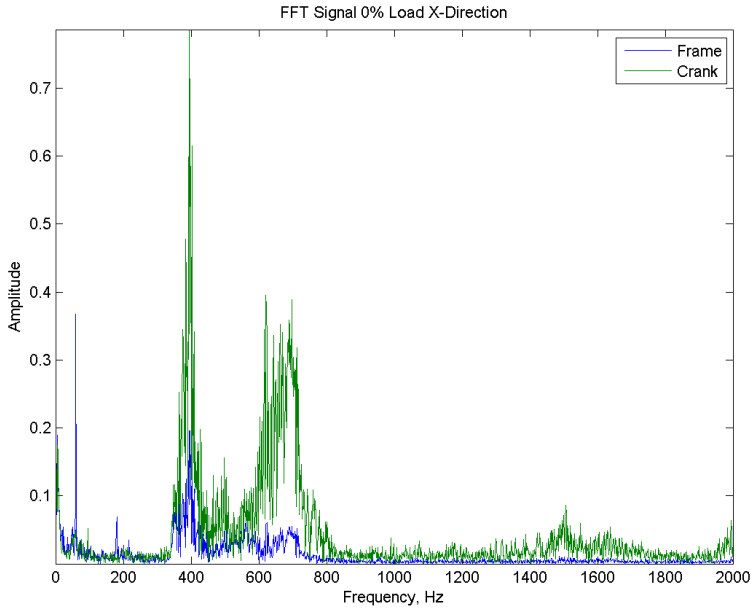

Figure 5.17: Start-Up: X direction FFT signal comparison between the frame and crank accelerometer (Top: 0% Load, Middle: 50% Load, Bottom: 100% Load)

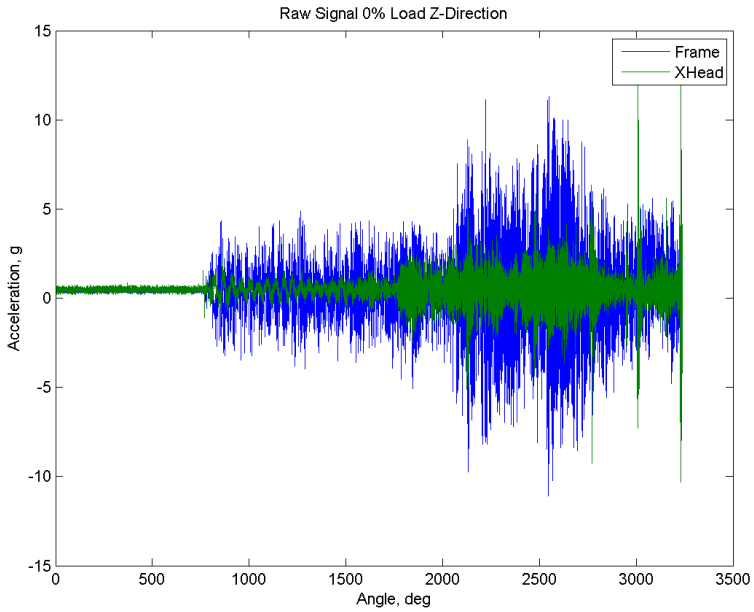

Figure 5.18: Start-Up: Z direction raw signal comparison between the frame and crosshead accelerometer (Top: 0% Load, Middle: 50% Load, Bottom: 100% Load)

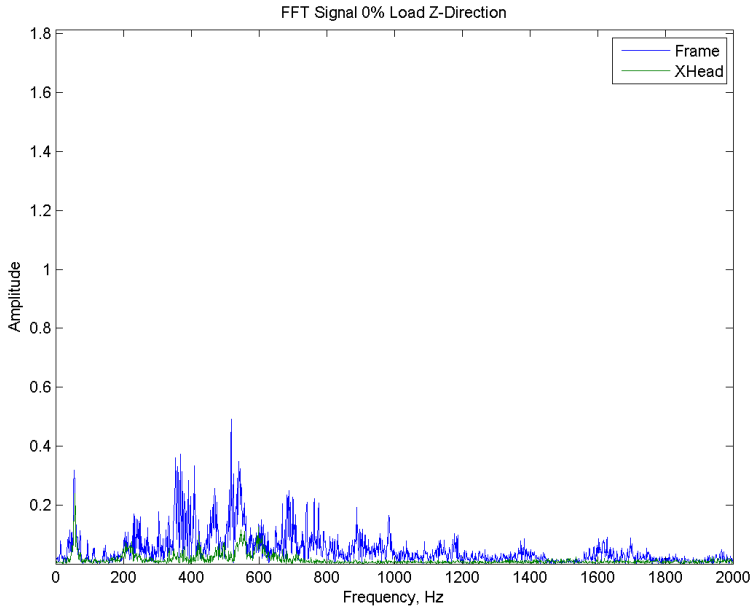

Figure 5.19: Start-Up: Z direction FFT signal comparison between the frame and crosshead accelerometer (Top: 0% Load, Middle: 50% Load, Bottom: 100% Load)

5.2.3 Current Measurements

Background Measuring the current that is drawn be the motor is a simple and cost effective way to monitor the general condition of the machine. While it can give a good overview, it can be hard to pinpoint specific failures by looking at just the current draw. Several faults can impact the power required, such as increased friction in the bearings, incorrectly adjusted belt tension, and too high or too low cylinder pressures.

Sensor Technology An AC current sensor works by combining a transformer with some signal condition to provide an output voltage proportional to the current passing through it. A typical set up is a toroidal transformer with many turns on the secondary coil and only one turn on the primary coil. This single coil is provided by the power line passing through the center of the secondary coil. The AC current in the primary coil produces a magnetic field which then induces a proportional current in the secondary coil. Since the turn to turn relationship is known, the current in the primary line can be measured by looking at the current output of the secondary coil as shown in figure 5.20.

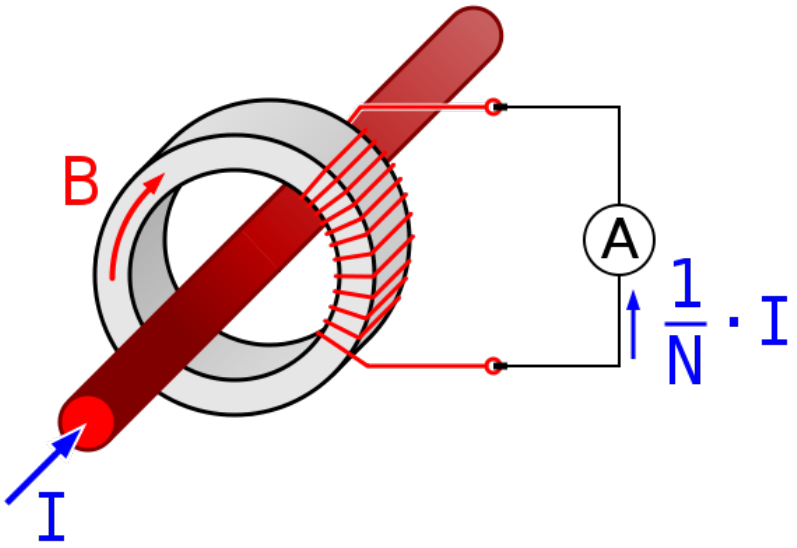

Figure 5.20: Theory behind current transformer sensors

Sensor Installation The sensor model used to collect data for this research is the Eaton EAC210SP. It features a measurable current range of 100 to 200 amps. In this application, it is run in the lowest setting of 100A as the start-up current of the motor reaches about 60A. The sensor is installed in the main wiring panel and covers one of the three phases of the power supply. Measuring only one phase is sufficient for general monitoring as all three phases show the same characteristics phase shifted by 120 degrees. Figure 5.21 shows the location of the sensor in the main wiring panel.

Data Collection As with the other sensors, both steady state and start-up date is collected for the current. Figure 5.22 shows the steady state current draw for the three loading cases. One can see that running the compressor at full pressure draws more power as expected. Figure 5.23 shows the FFT of the steady state data with the expected peak at 6.4Hz.

Figure 5.21: Install location for motor current sensor

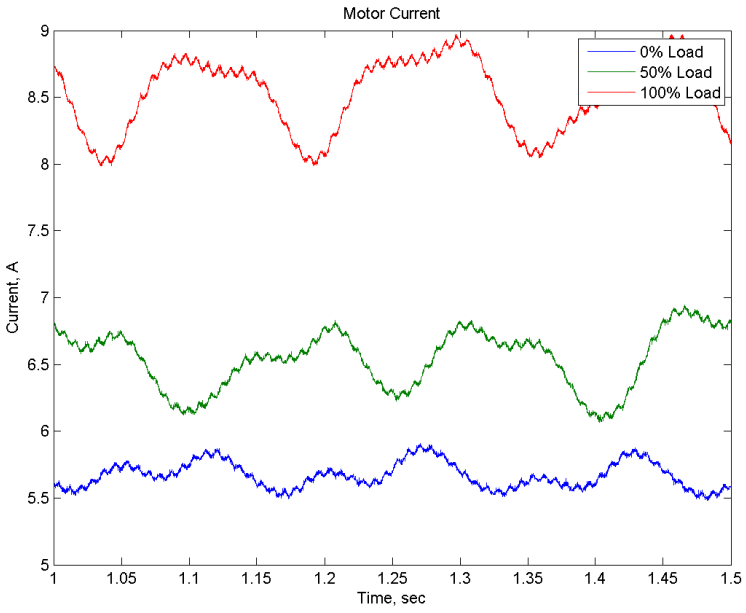

Figure 5.22: Steady state current draw for the three different loading conditions

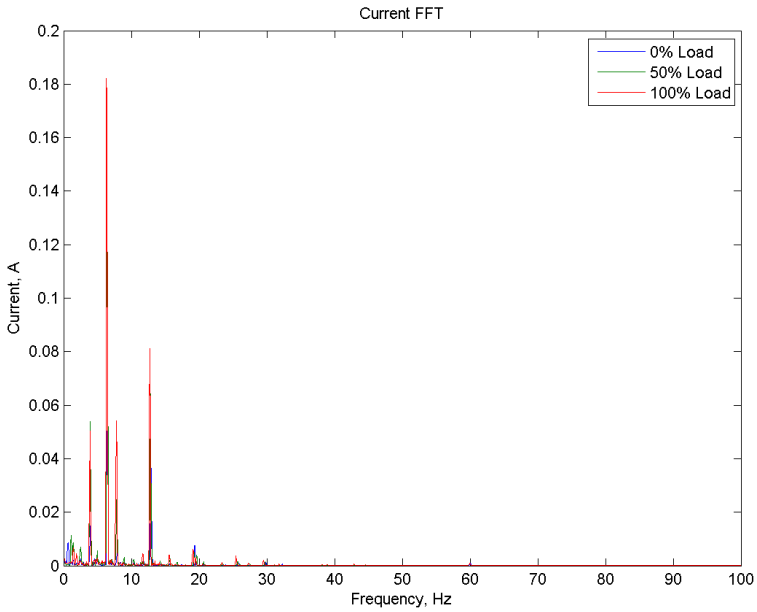

Figure 5.23: FFT of steady state current draw for the three loading conditions

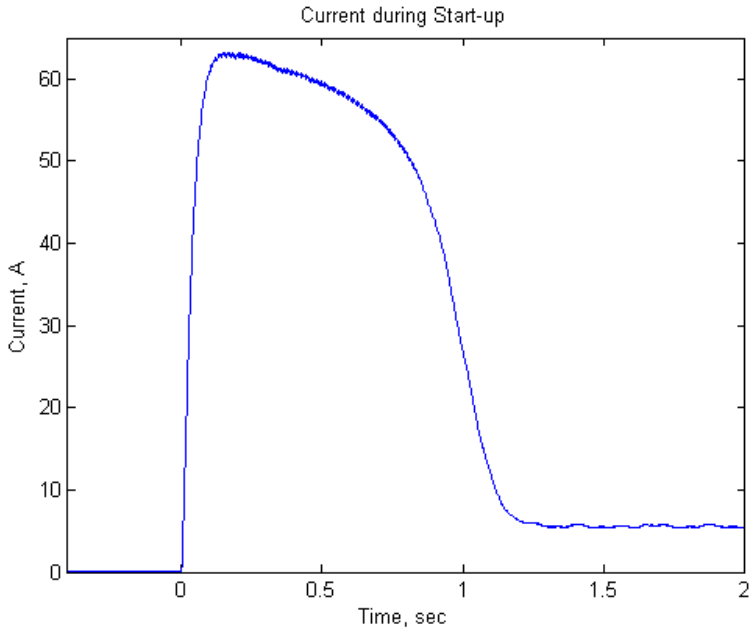

Figure 5.24: Current start-up data

5.3 Fault Seeding

5.3.1 Changing a Main Bearing

In order to change the bearings in the compressor, some significant work is required. As preparation, remove the drive belt guard, and loosen the drive motor and move it towards the compressor. This relives the tension in the drive belts so they can be easily taken off. Also drain the oil to avoid spilling later on and ease the work inside the crankcase (Fig. 5.25).

The steps dealing with the compressor directly are outlined in the manual but documented here again for completeness and future reference. After opening the maintenance cover on the crankcase, the connecting rod big end cap has to be removed and the connecting rod moved out of the way of the crankshaft. This is a good opportunity to check the crank pin bearing as it can be visually inspected at this time. Also inside the crankcase, the oil feeder tube has to be removed along with the thermocouple connected to the right main bearing housing (Fig. 5.26). Before removing the flywheel, disconnect the wireless sensor from the transmitter. Then remove the flywheel, using its attachment bolts as jacking bolts to remove it from the hub (Fig. 5.27). Use a hub puller to remove the flywheel hub from the crankshaft and take off the LVDT mounting bracket with LVDTs still attached before removing the drive key. Leaving the LVDTs in the bracket avoids having to readjust them after reassembly (Fig. 5.28). Use a hammer and brass block to avoid damaging the key when removing it from its keyway. Then the oil pump housing can be removed, again using its attachment bolts as jacking bolts (Fig. 5.29). Finally the crankshaft can be pulled out through the opening created by the oil pump housing (Fig. 5.30). Care has to be exercised when dealing with any bearing surface as they are precision machined parts and surface finish is critical to the operation of the compressor.

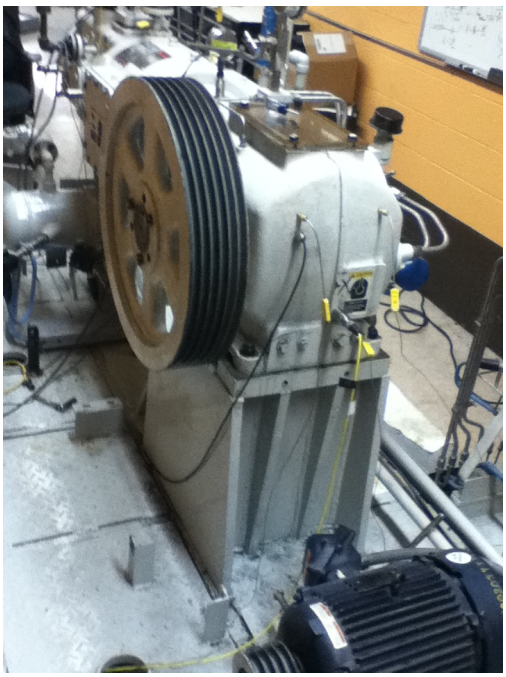

(a) Drive belts removed

(b) Oil feed tube inside crankcase

Figure 5.25: Preparing the compressor

When reassembling the compressor, it is important to ensure the dowel pin in the end of the crankshaft is lined up with the oil pump key way. Also make sure the connecting rod cap bolts are tightened to the correct torque (100 ft-lbs) to ensure proper operation of the crankpin bearing.

(a) Connecting rod removed from crankshaft

(b) Thermocouple removed from oil pump

Figure 5.26: Inside crankcase

(a) Unplug the wireless sensor

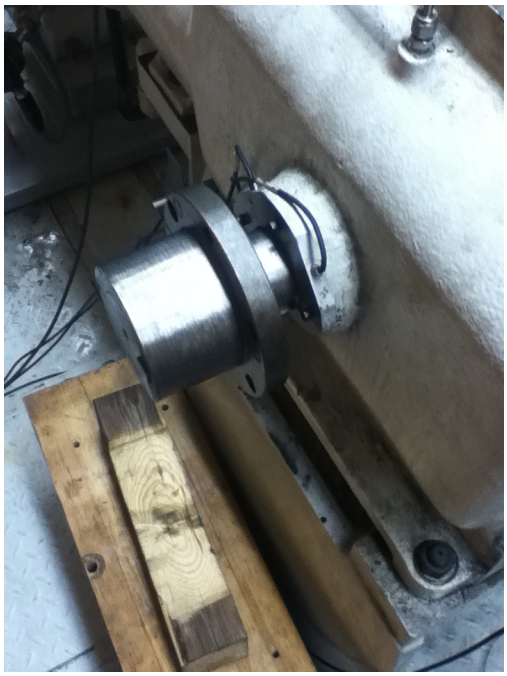

(b) Flywheel removed from hub

Figure 5.27: Removing the flywheel

(a) Flywheel hub removed from crankshaft

(b) LVDT bracket removed from compressor

Figure 5.28: Preparing crankshaft, Step 1

(a) Drive key removed from crankshaft

(b) Oil pump removed from crankcase

Figure 5.29: Preparing crankshaft, Step 2

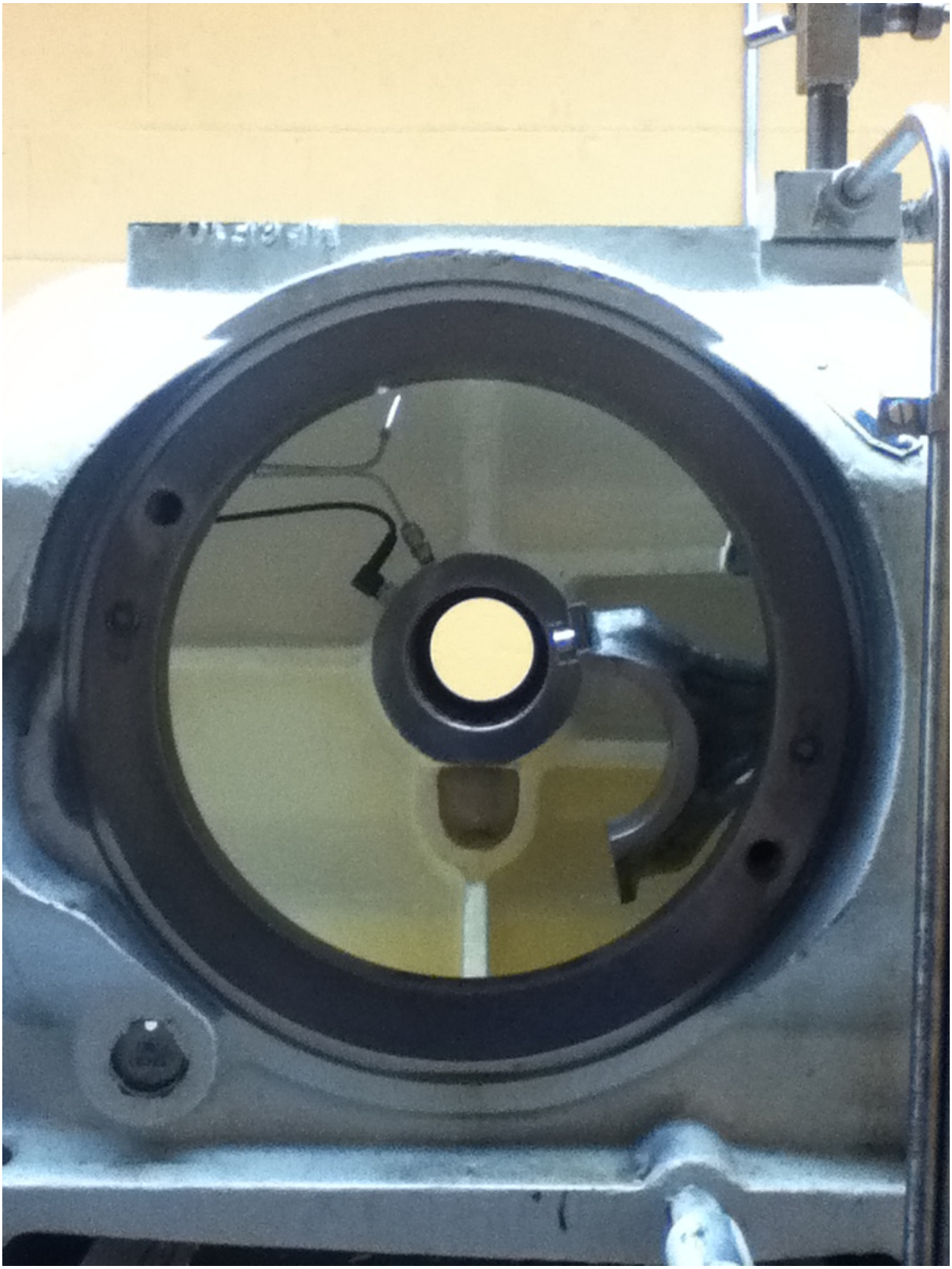

Figure 5.30: Crankshaft removed from crank case

Bearing	T1	T2	T3	T4	T5	Avg	std. dev.	Radial Clearance
1	69.906	69.911	69.909	69.904	69.914	69.909	0.004	0.012
2	69.898	69.896	69.900	69.890	69.898	69.896	0.003	0.005
3	69.891	69.903	69.903	69.901	69.895	69.899	0.005	0.006
4	69.915	69.903	69.885	69.912	69.915	69.906	0.011	0.010
Original Right	69.941	69.946	69.952	69.975	69.960	69.955	0.013	0.035
Original Left	69.946	69.937	69.986	69.959	69.998	69.965	0.026	0.059

Table 5.4: Dimensions for the inside diameter of the floating ring (mm)

Bearing	T1	T2	T3	T4	T5	Avg.	std. dev.	Radial Clearance
1	85.665	85.668	85.665	85.668	85.668	85.667	0.001	0.017
2	85.661	85.652	85.664	85.665	85.662	85.661	0.005	0.020
3	85.658	85.670	85.669	85.654	85.664	85.663	0.006	0.019
4	85.666	85.678	85.672	85.675	85.683	85.675	0.006	0.013
Original Right	85.654	85.640	85.647	85.633	85.614	85.638	0.015	0.031
Original Left	85.622	85.625	85.668	85.671	85.647	85.647	0.023	0.027

Table 5.5: Dimensions for the outside diameter of the floating ring (mm)

5.3.2 Measuring components

After the crankshaft was removed, its diameter is measured on a coordinate measurement machine (CMM) along with diameter of the original bearings. This information is used to re-run the model to improve the quality of the results. The diameter of the replacement bearings are also measured to understand the baseline condition before any modifications for faults are made. This information is shown in tables 5.4 and 5.5 for the inside and outside respectively. The bearing housing in the cast is measured with a calliper to get a basic understanding since no other measurement technique is accessible. From this information, the radial clearance can be determined. As can be seen from the tables, there is some run-in that occurs during the first hours of operation. Both the inner and outer clearance are significantly larger for the original bearings compared to the out of the box replacements.

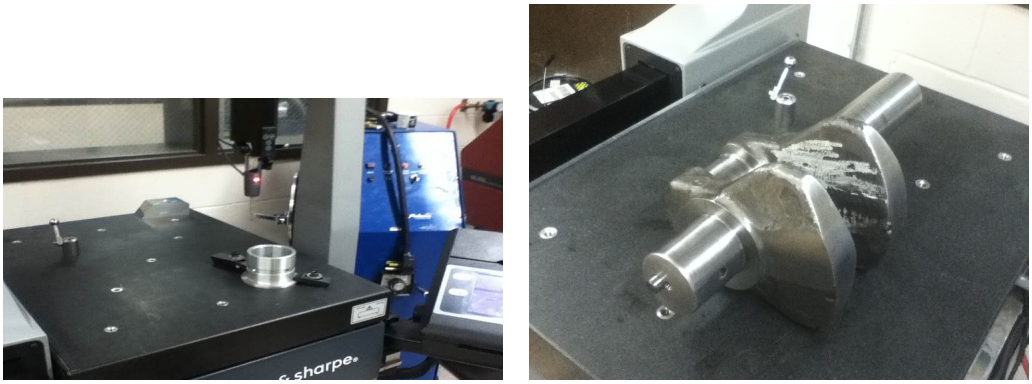

(a) Floating ring on CMM

(b) Crankshaft on CMM on table

Figure 5.31: Measuring components on CMM

5.3.3 Baseline Data

Before seeding any faults into the system, a comprehensive set of baseline measurements are taken (Fig. 5.32 through 5.39). These are used as the healthy condition for classification. In order to achieve a steady state operating condition, the compressor is run an hour from a cold start. The shift in between different loading conditions is due to the fact that the time vectors between trials is not the same. The peaks and valleys occur at the same crank angle for each loading condition as seen for example in Fig. 5.12.

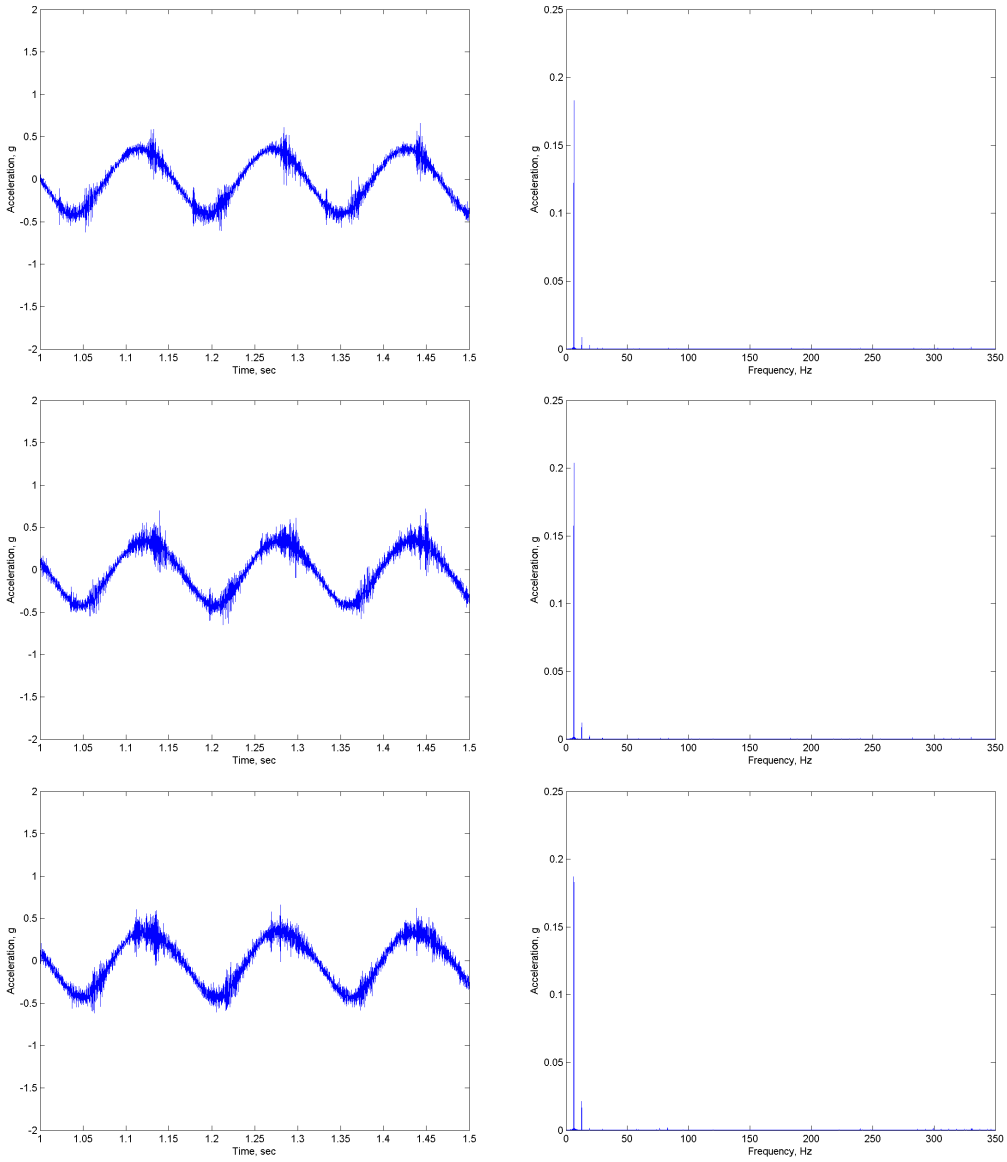

(a) Time Domain (b) Frequency Domain

Figure 5.32: X direction frame vibration for the baseline bearing (Top: 0% Load, Middle: 50% Load, Bottom: 100% Load)

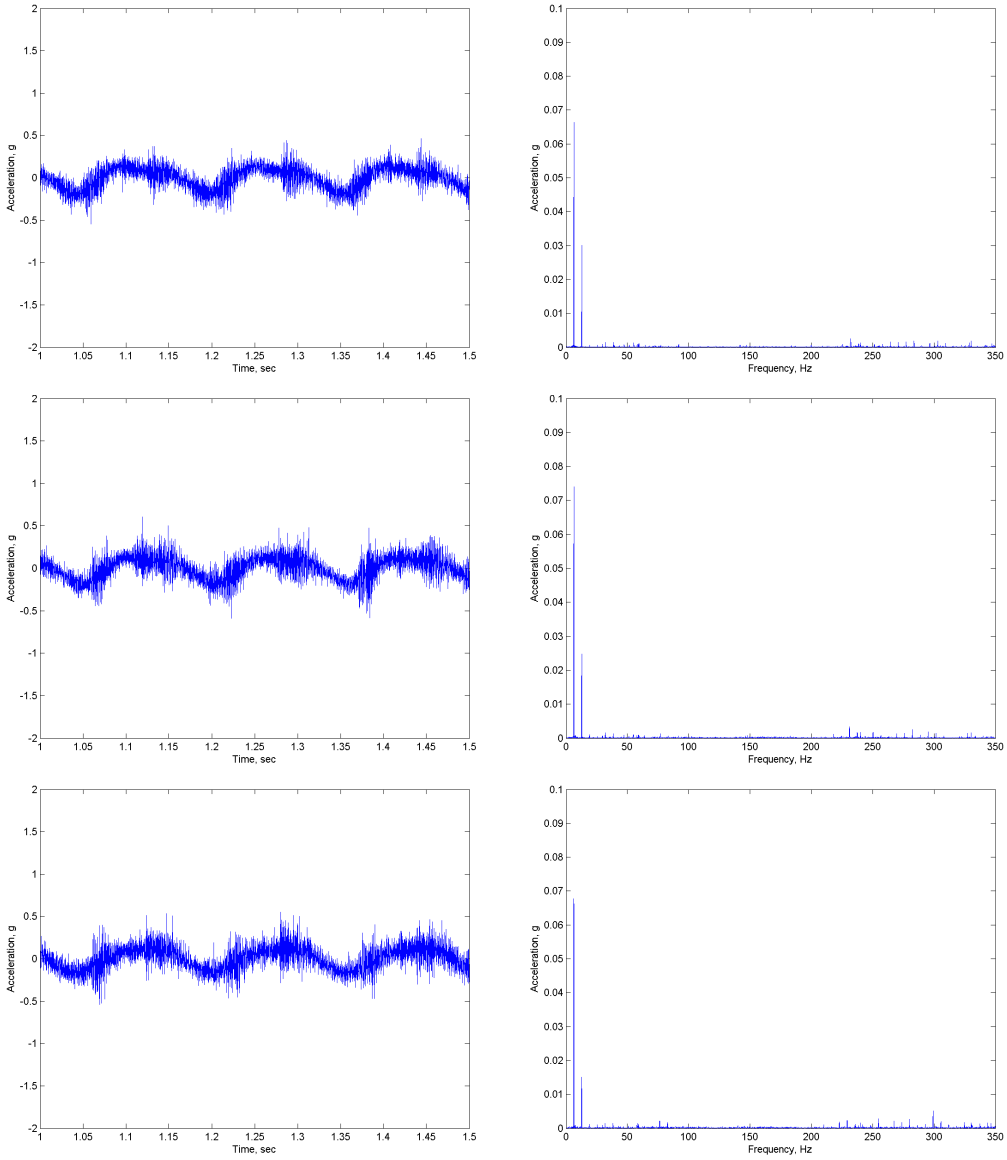

(a) Time Domain (b) Frequency Domain

Figure 5.33: Z direction frame vibration for the baseline bearing (Top: 0% Load, Middle: 50% Load, Bottom: 100% Load)

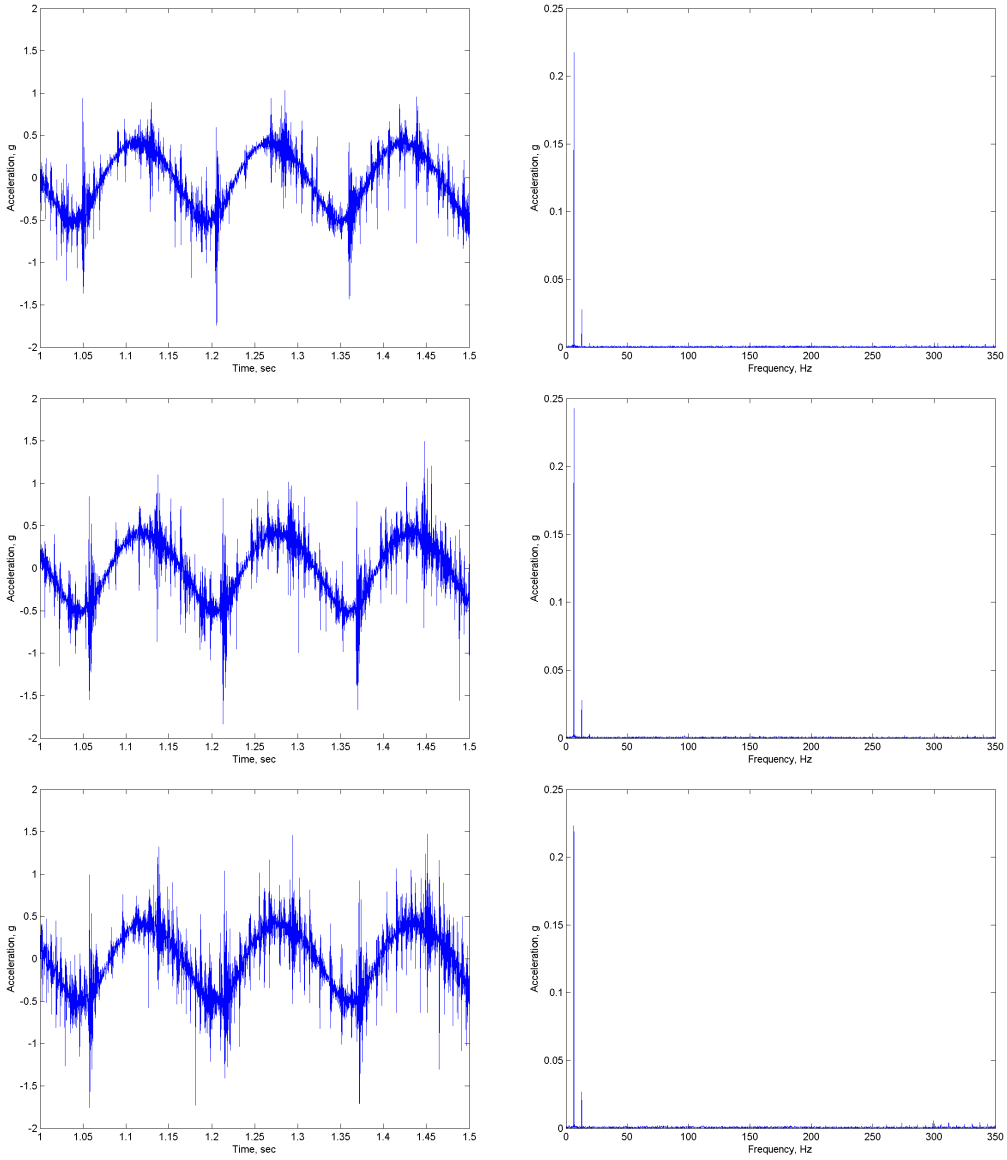

(a) Time Domain (b) Frequency Domain

Figure 5.34: X direction crankcase vibration for the baseline bearing (Top: 0% Load, Middle: 50% Load, Bottom: 100% Load)

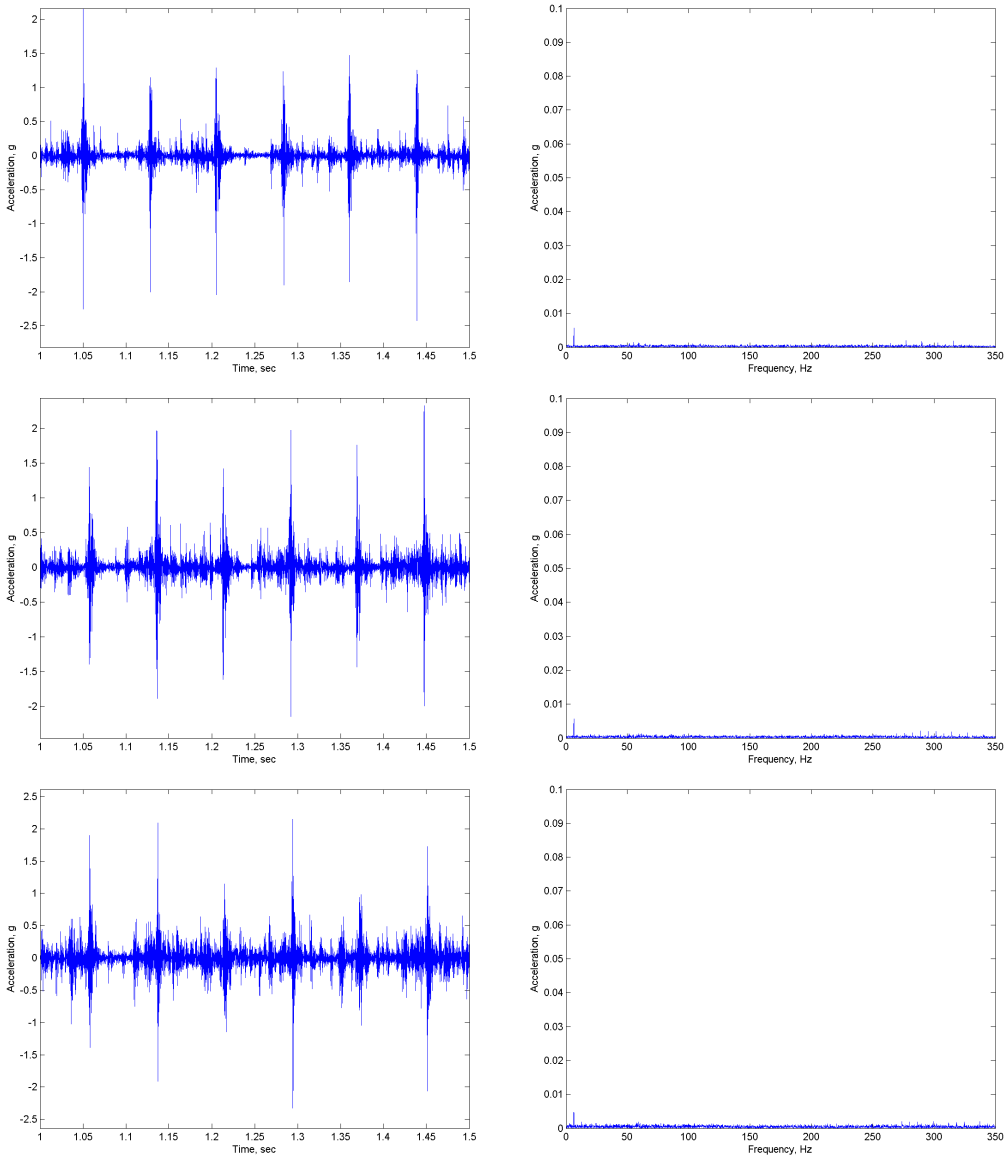

(a) Time Domain (b) Frequency Domain

Figure 5.35: Z direction crosshead vibration for the baseline bearing (Top: 0% Load, Middle: 50% Load, Bottom: 100% Load)

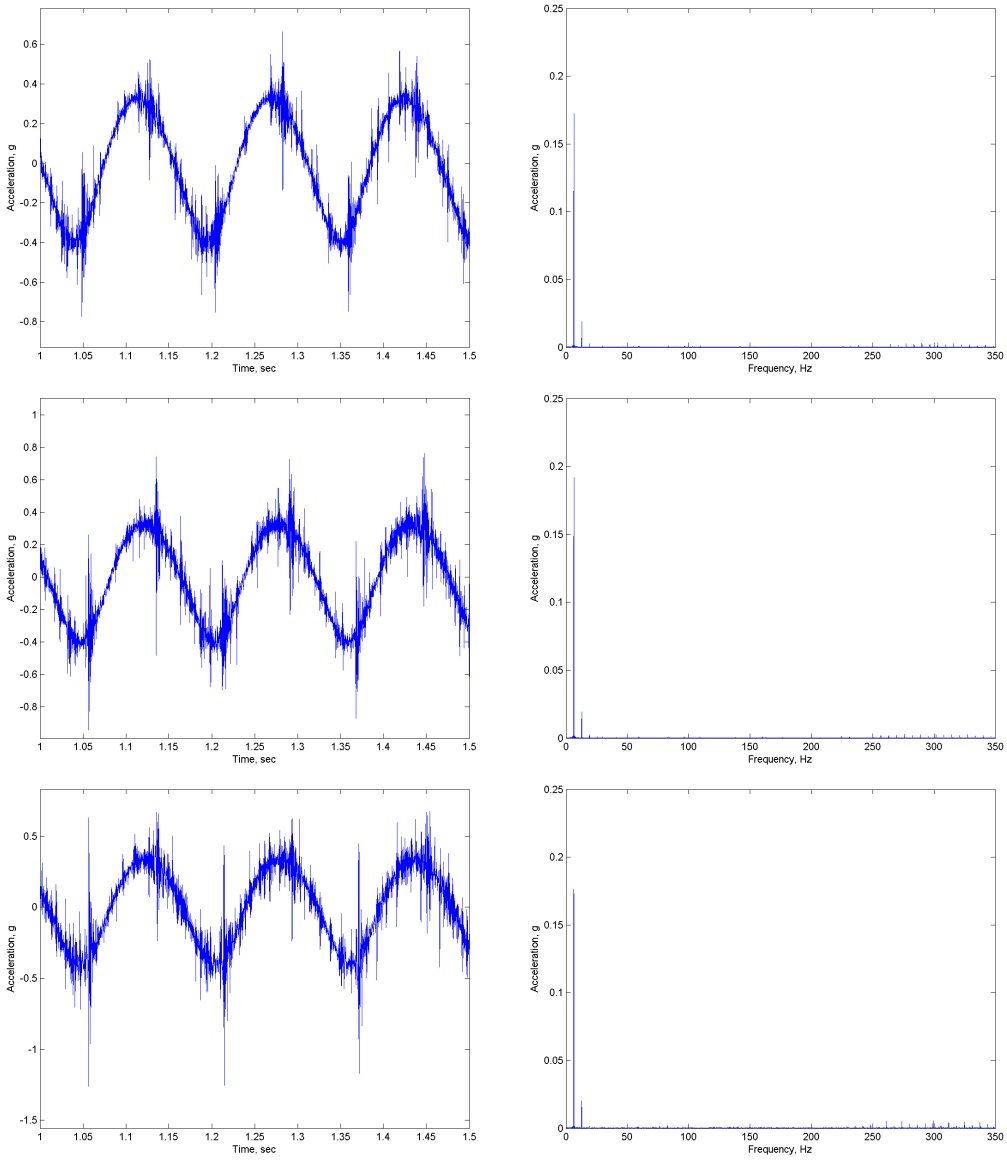

(a) Time Domain (b) Frequency Domain

Figure 5.36: Bearing housing vibration for the baseline bearing (Top: 0% Load, Middle: 50% Load, Bottom: 100% Load)

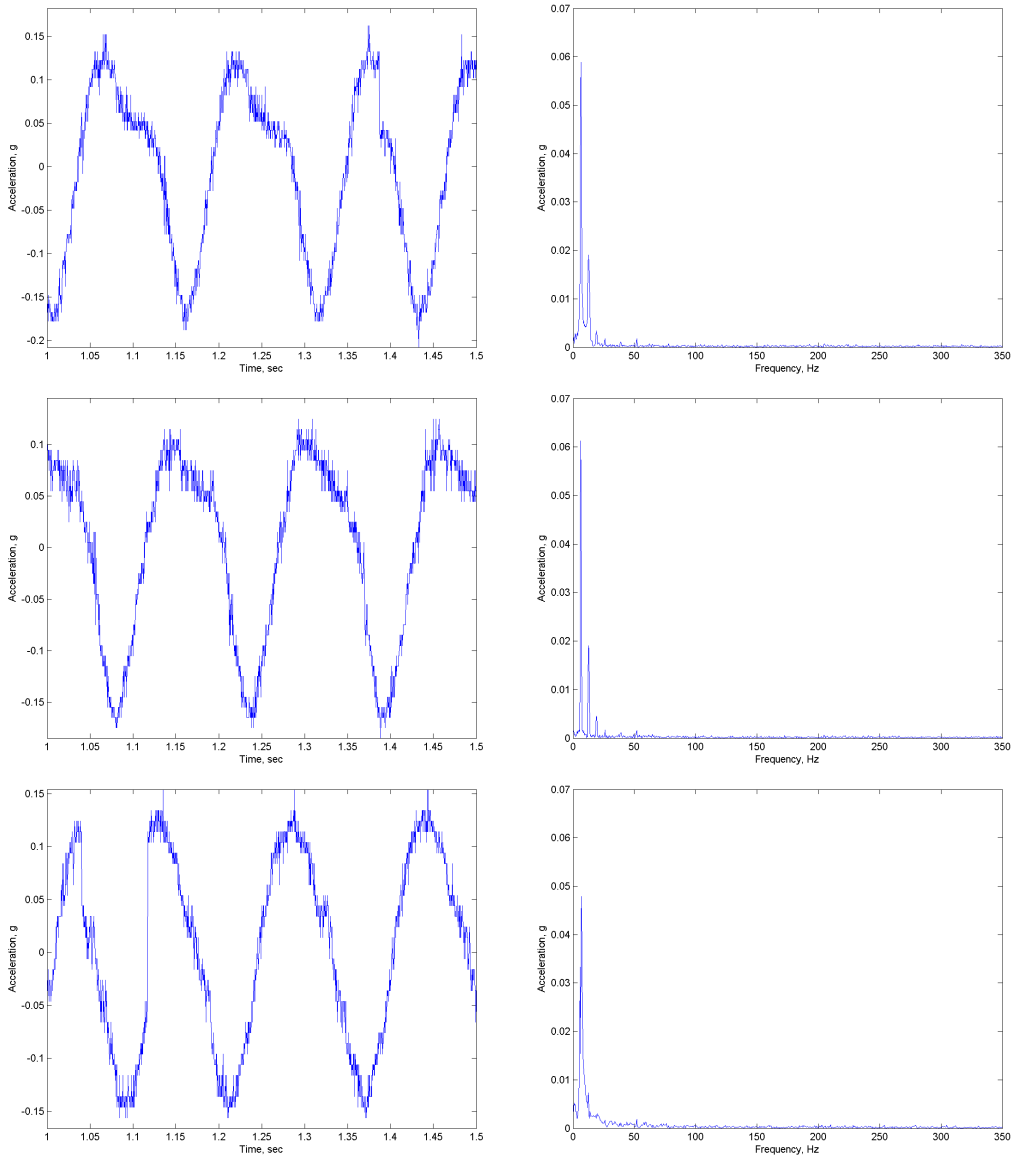

(a) Time Domain (b) Frequency Domain

Figure 5.37: Crankshaft vibration for the baseline bearing (Top: 0% Load, Middle: 50% Load, Bottom: 100% Load)

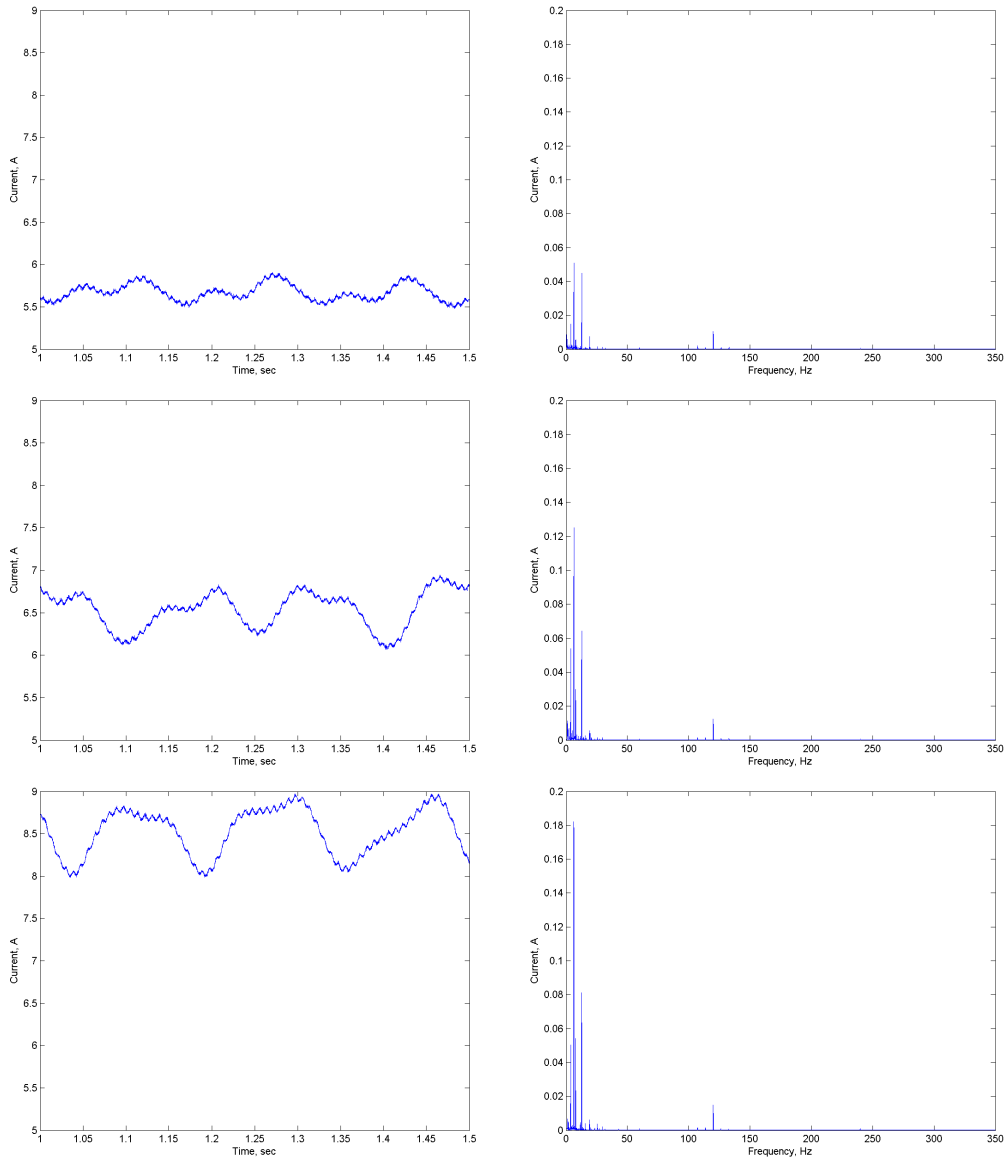

(a) Time Domain (b) Frequency Domain

Figure 5.38: Current draw for the baseline bearing (Top: 0% Load, Middle: 50% Load, Bottom: 100% Load)

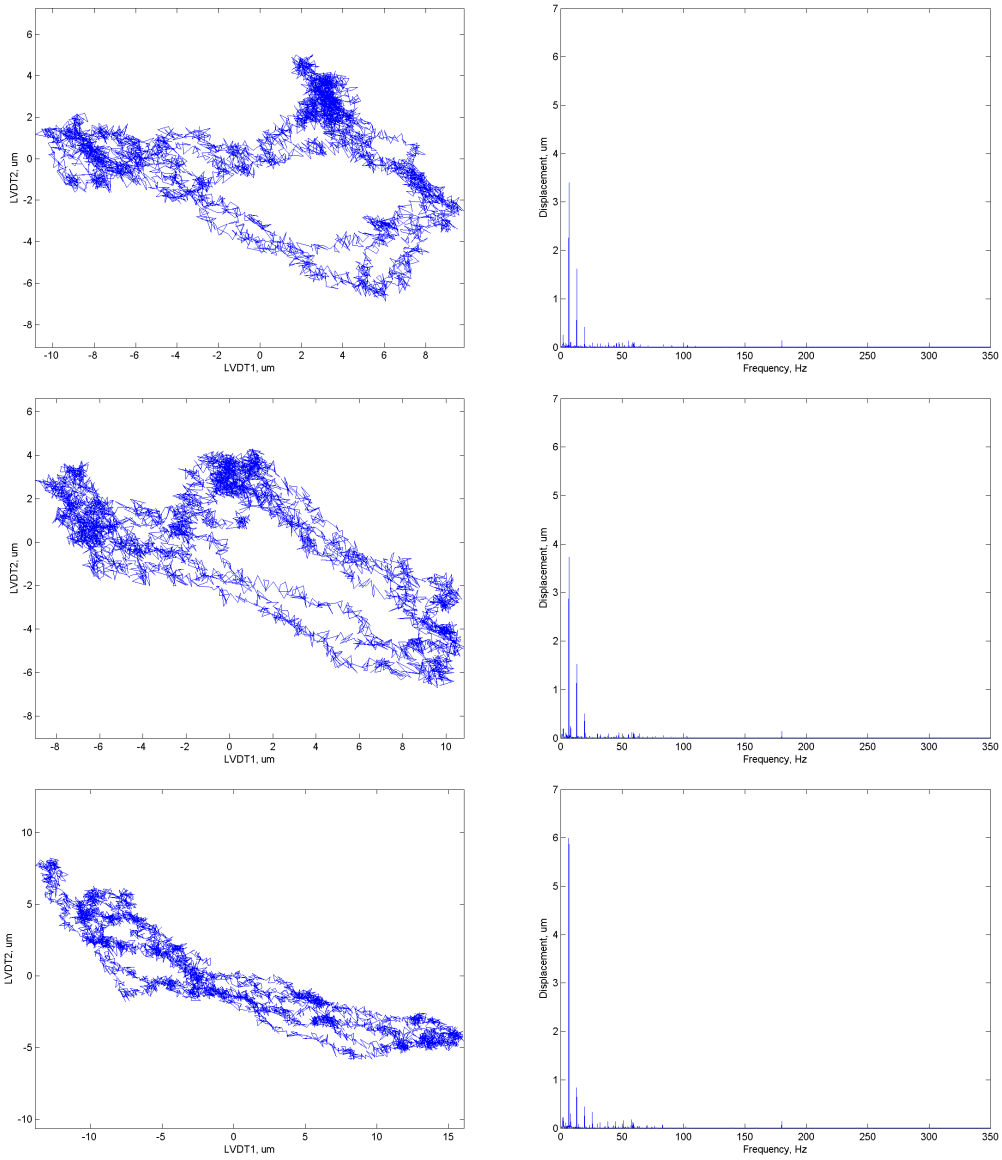

(a) Time Domain (b) Frequency Domain

Figure 5.39: Crankshaft orbit and LVDT FFT for the baseline bearing (Top: 0% Load, Middle: 50% Load, Bottom: 100% Load)

5.3.4 Bearing Modifications

Besides the oil viscosity changes, two different physical modifications are made to the bearing. The first is to investigate full circumferential grooves in the bearing land. Both, a single groove in one bearing land (Fig. 5.41)as well as symmetrical grooves in both lands are tested (Fig. 5.42). The other modification is to partially obstruct the oil feed holes in the bearing. Again, two cases are investigated: 75% obstructed (Fig. 5.59) and 50% obstructed (Fig. 5.60).

5.3.5 Grooved Bearing

The grooves machined into the bearing are very small in order to represent scratches that could occur from particulates in the oil. Both grooves are designed the same with a width of 0.5mm and a depth of 0.2mm. Roundness variation in the actual part causes the actual depth of the grooves to vary slightly over the circumference of the bearing. Figure 5.40 shows the orientation of the grooved bearing in the compressor.

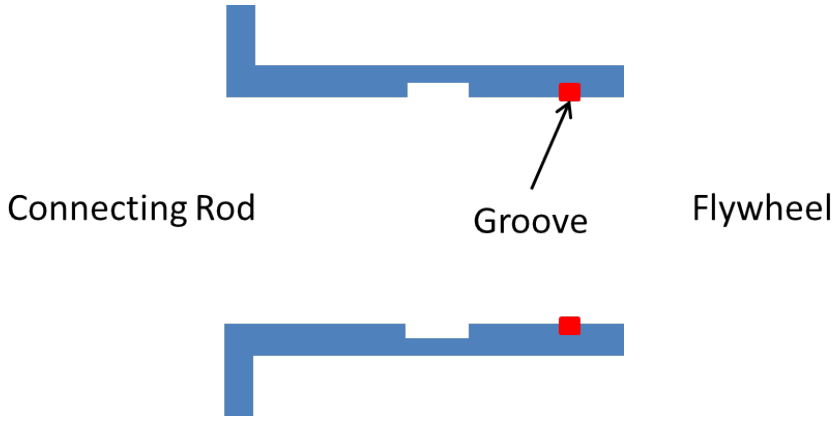

Figure 5.40: Schematic showing the orientation of the grooved bearing in the compressor

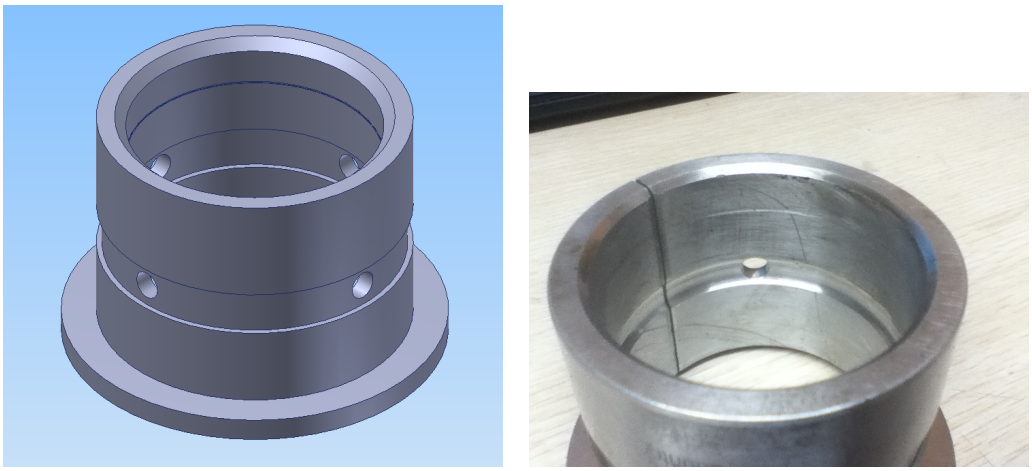

(a) 3D (b) implementation

Figure 5.41: Bearing with 1 groove

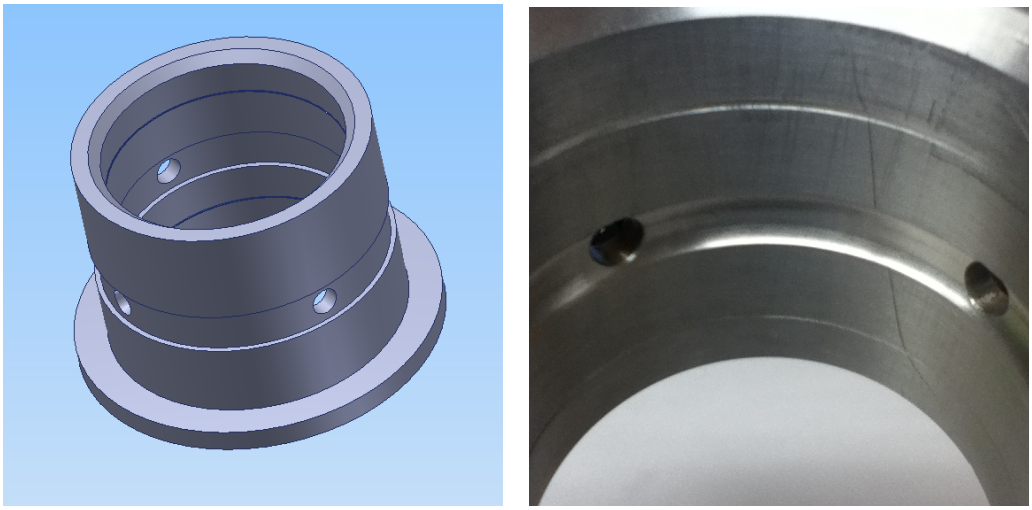

(a) 3D (b) implementation

Figure 5.42: Bearing with 2 grooves

1 Groove

As figures 5.43 through 5.50 show, this bearing runs very noisy. One can see much higher vibration values in both the time domain and frequency domain compared to the baseline. The measured bearing orbit is also very hard to identify over the noise. This is expected as the unsymmetrical load carrying capacity can lead to misalignment which impacts performance greatly.

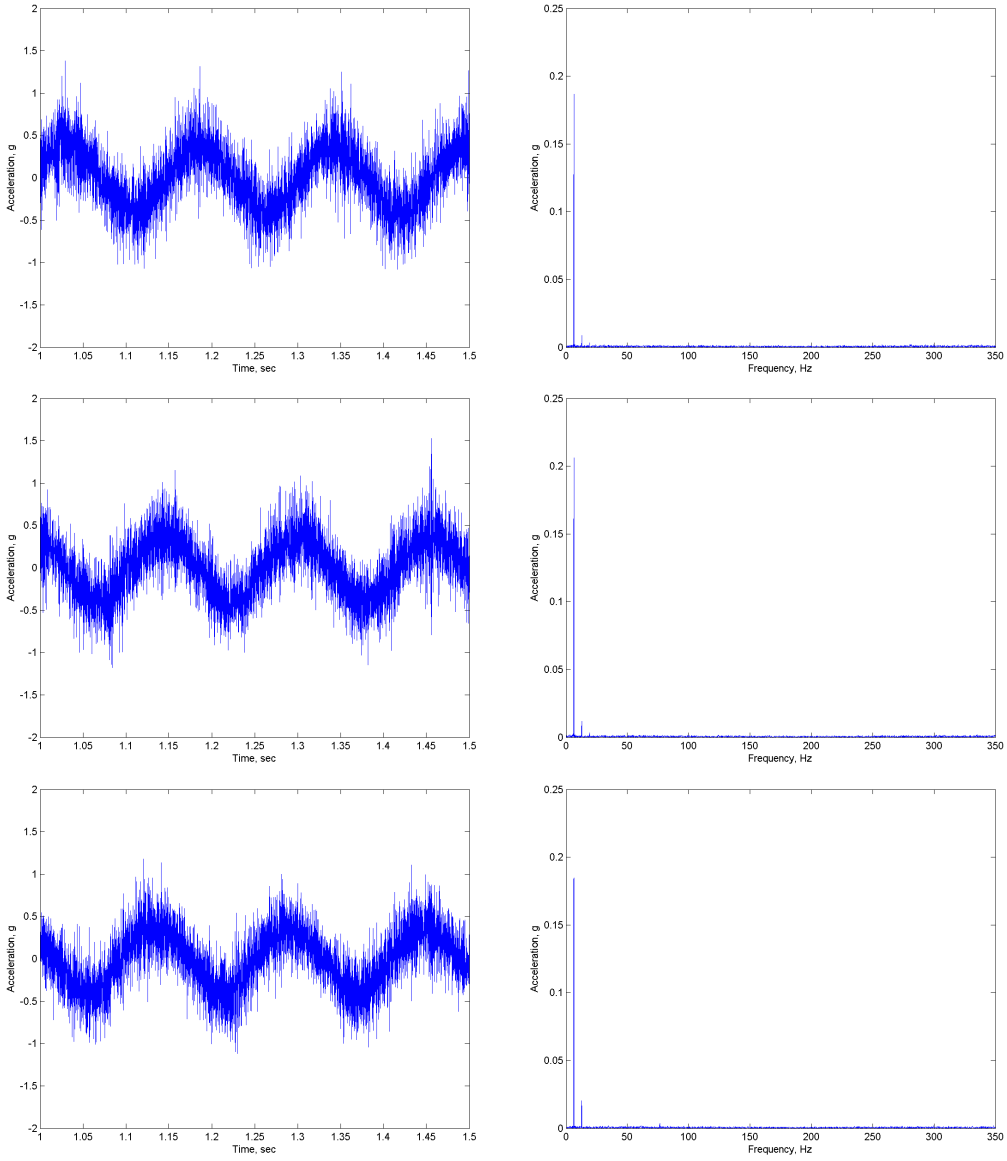

(a) Time Domain (b) Frequency Domain

Figure 5.43: X direction frame vibration for the grooved bearing (Top: 0% Load, Middle: 50% Load, Bottom: 100% Load)

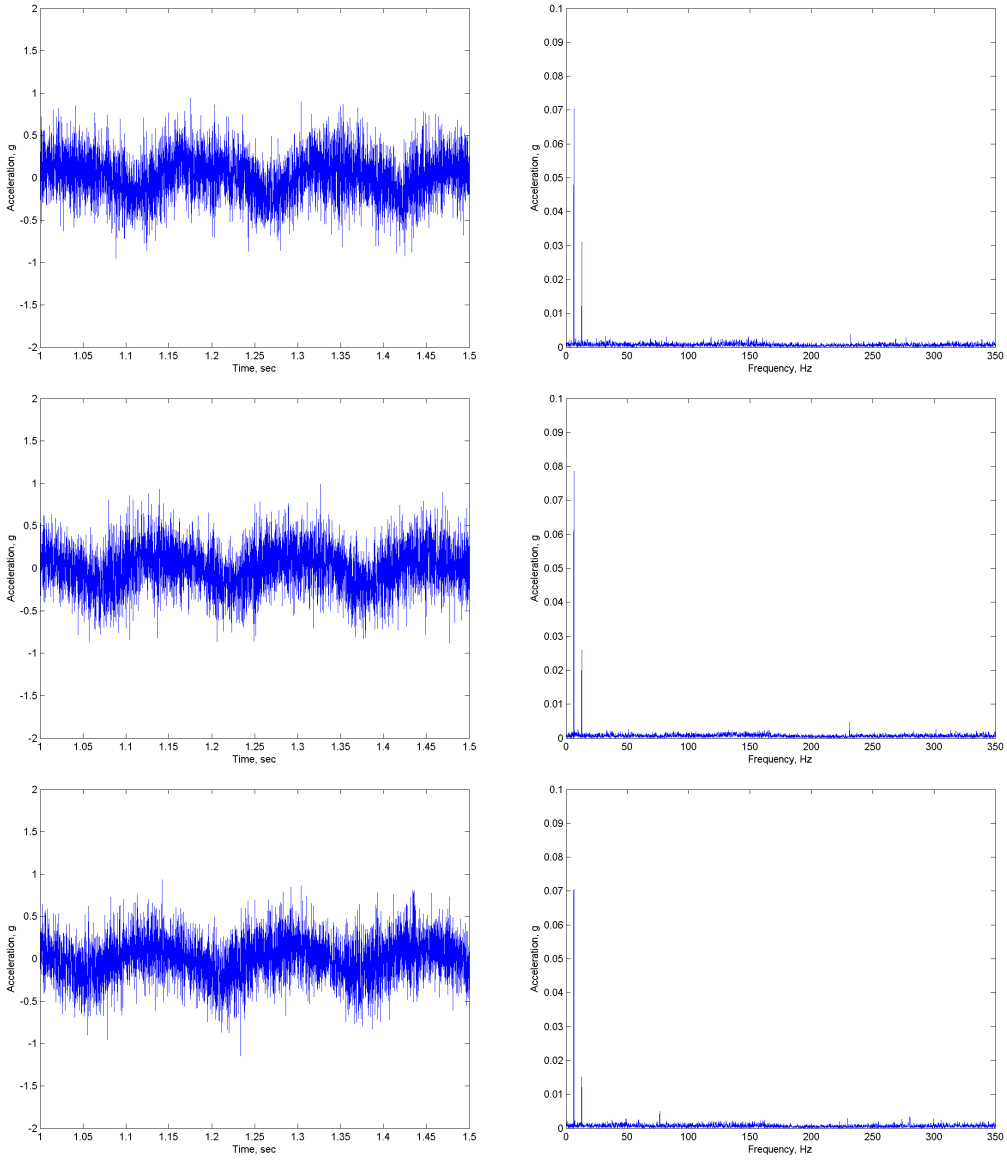

(a) Time Domain (b) Frequency Domain

Figure 5.44: Z direction frame vibration for the grooved bearing (Top: 0% Load, Middle: 50% Load, Bottom: 100% Load)

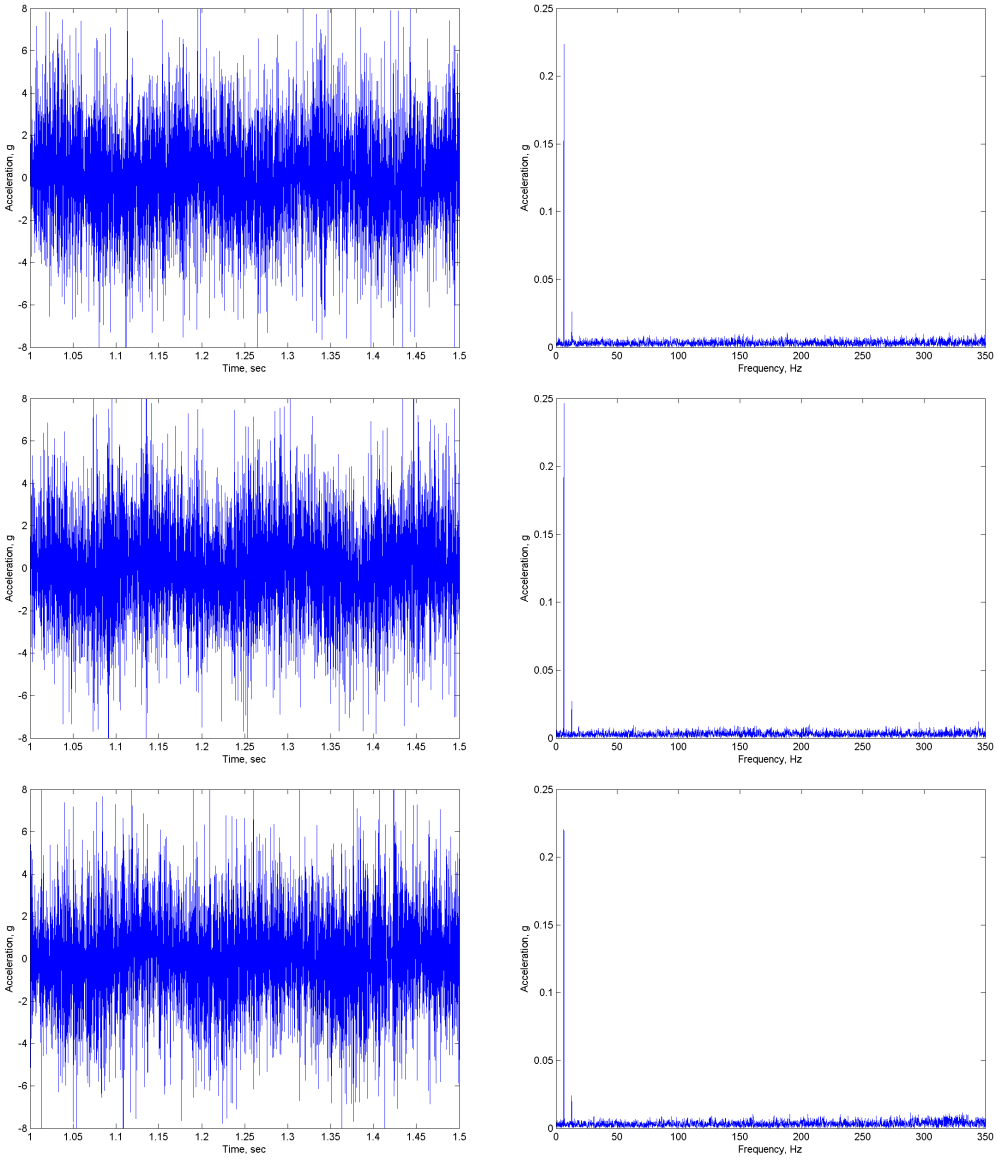

(a) Time Domain (b) Frequency Domain

Figure 5.45: X direction crankcase vibration for the grooved bearing (Top: 0% Load, Middle: 50% Load, Bottom: 100% Load)

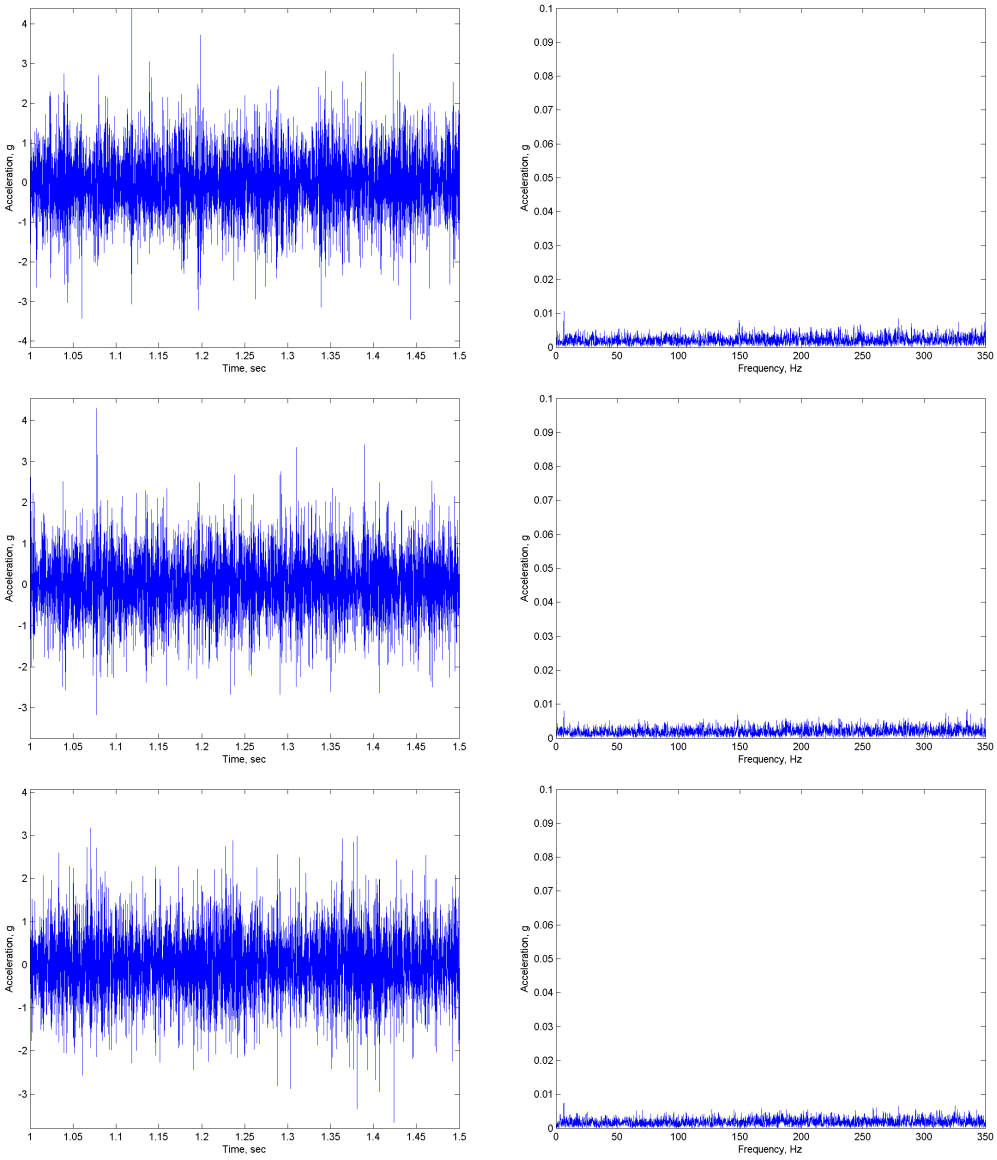

(a) Time Domain (b) Frequency Domain

Figure 5.46: Z direction crosshead vibration for the grooved bearing (Top: 0% Load, Middle: 50% Load, Bottom: 100% Load)

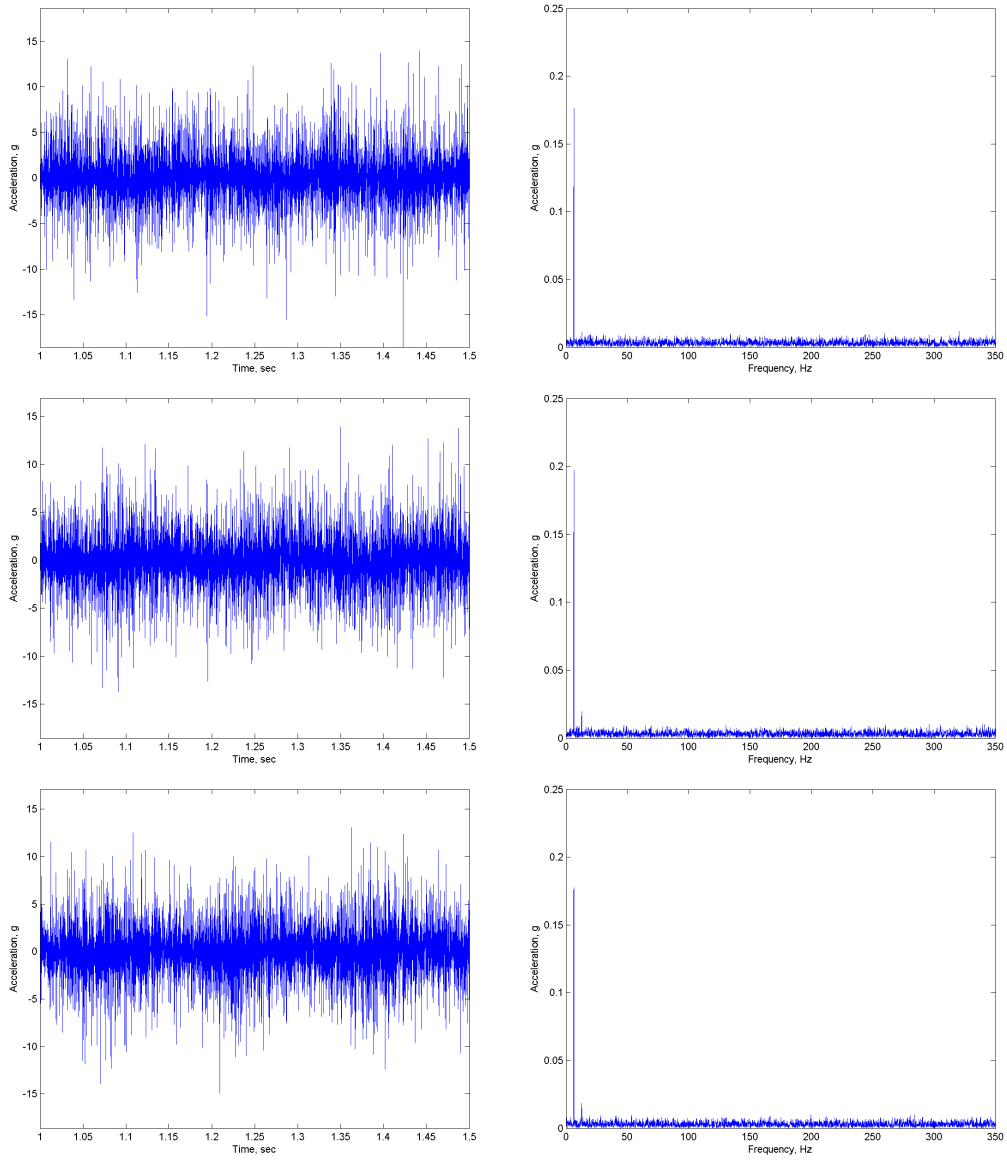

(a) Time Domain (b) Frequency Domain

Figure 5.47: Bearing housing vibration for the grooved bearing (Top: 0% Load, Middle: 50% Load, Bottom: 100% Load)

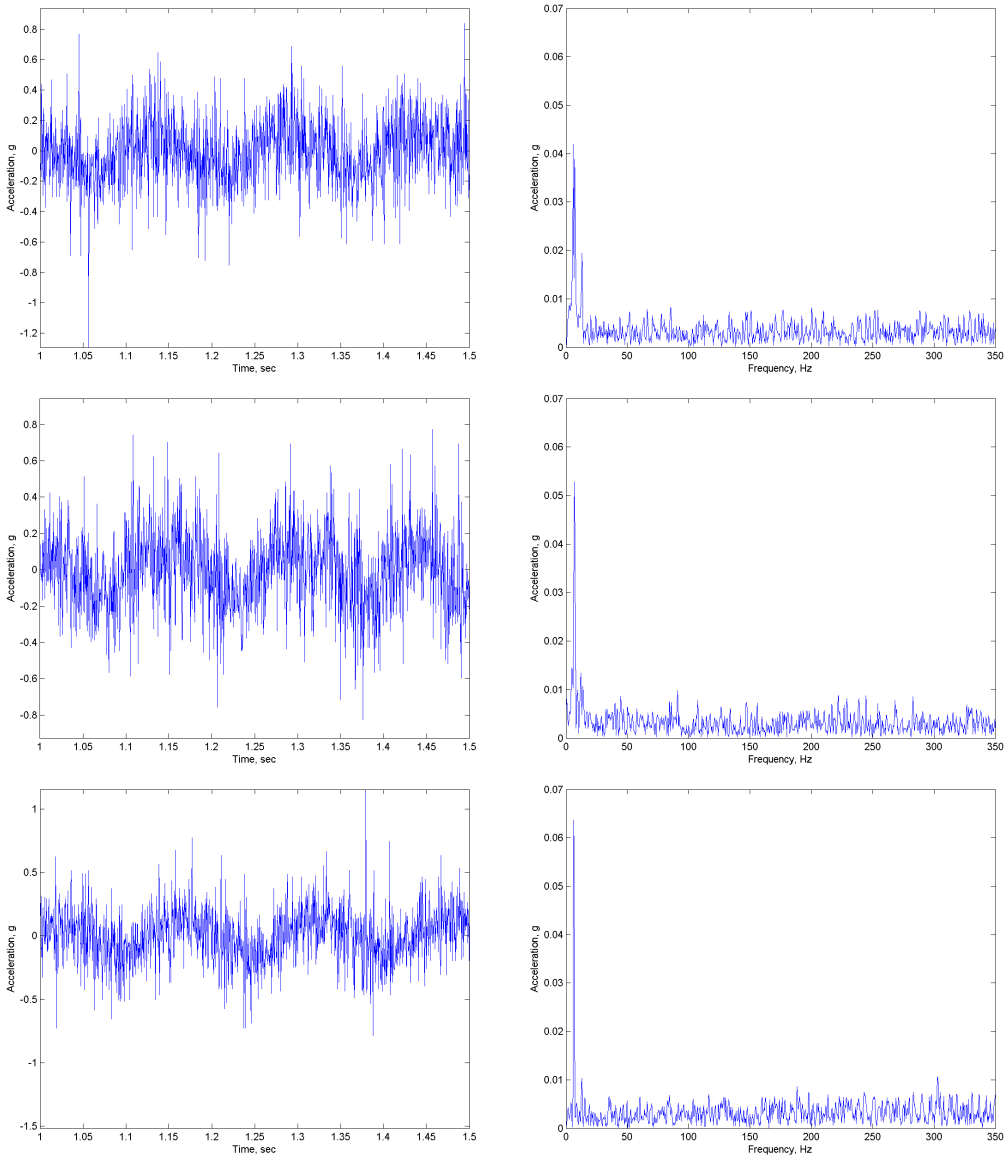

(a) Time Domain (b) Frequency Domain

Figure 5.48: Crankshaft vibration for the grooved bearing (Top: 0% Load, Middle: 50% Load, Bottom: 100% Load)

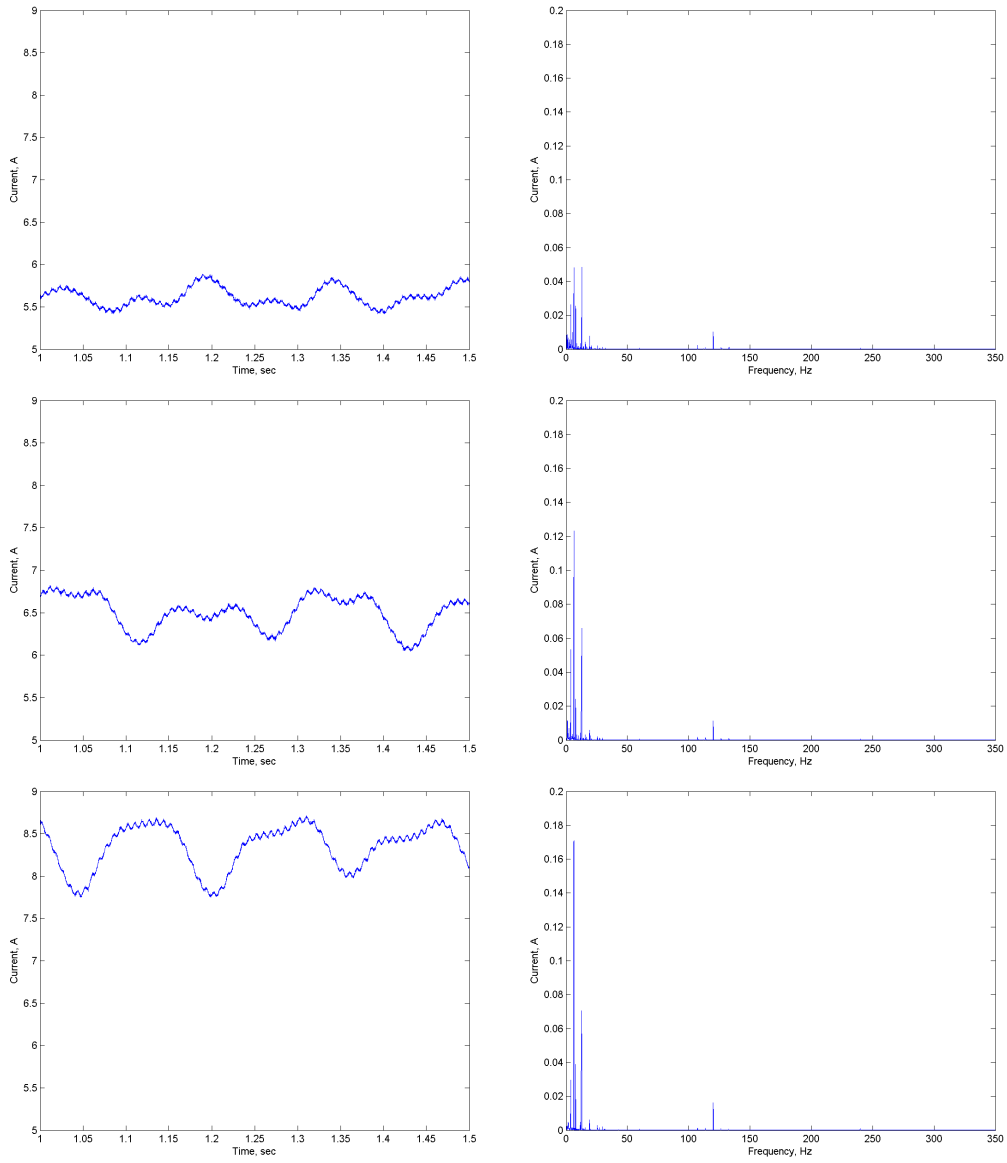

(a) Time Domain (b) Frequency Domain

Figure 5.49: Current draw for the grooved bearing (Top: 0% Load, Middle: 50% Load, Bottom: 100% Load)

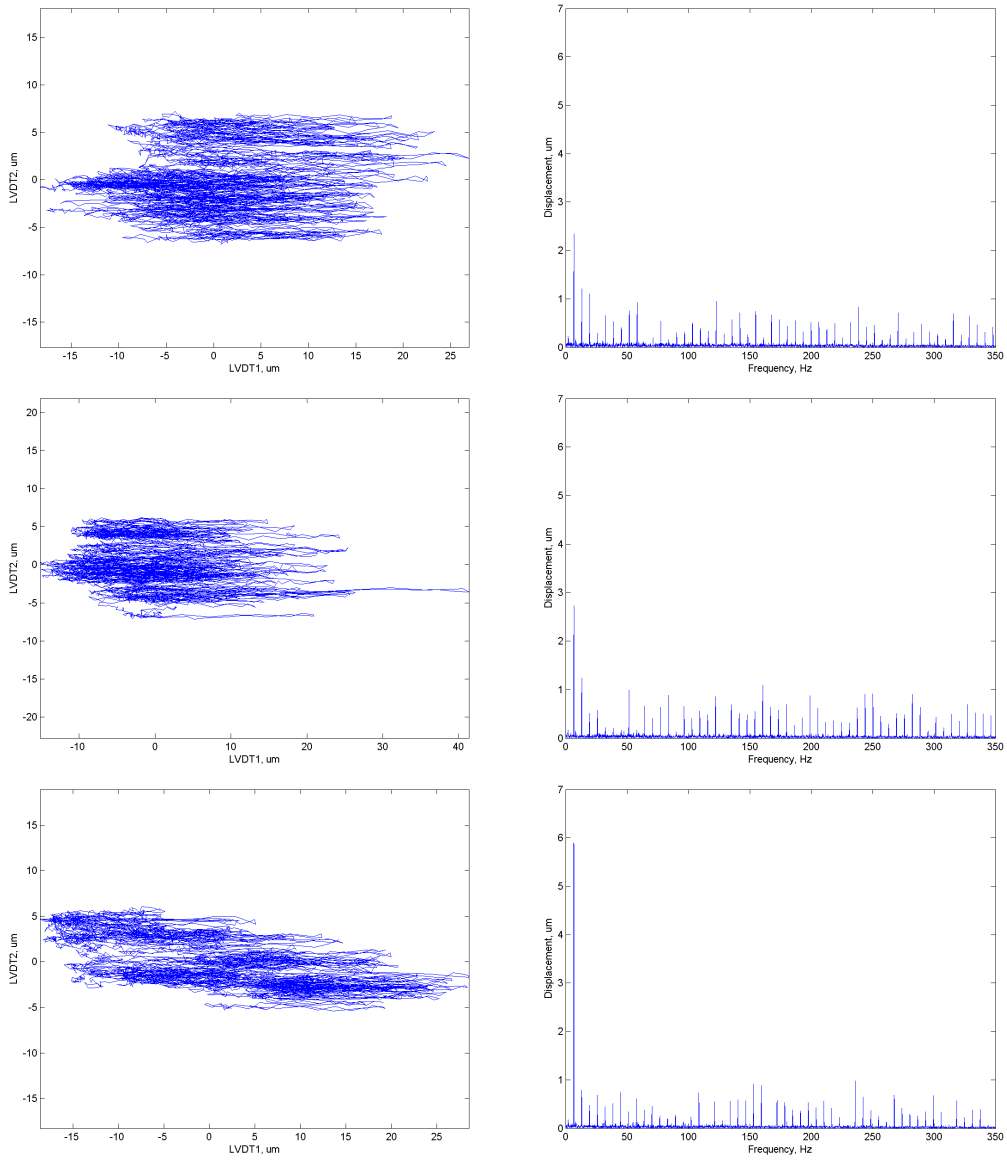

(a) Time Domain (b) Frequency Domain

Figure 5.50: Crankshaft orbit and LVDT FFT for the grooved bearing (Top: 0% Load, Middle: 50% Load, Bottom: 100% Load)

2 Grooves

The bearing with two grooves runs much better than the bearing with one groove (Fig. 5.51 through 5.58). The symmetrical layout reduces the misalignment and increases bearing performance. There are still differences visible especially in the orbit measurement which is noisier than the baseline data.

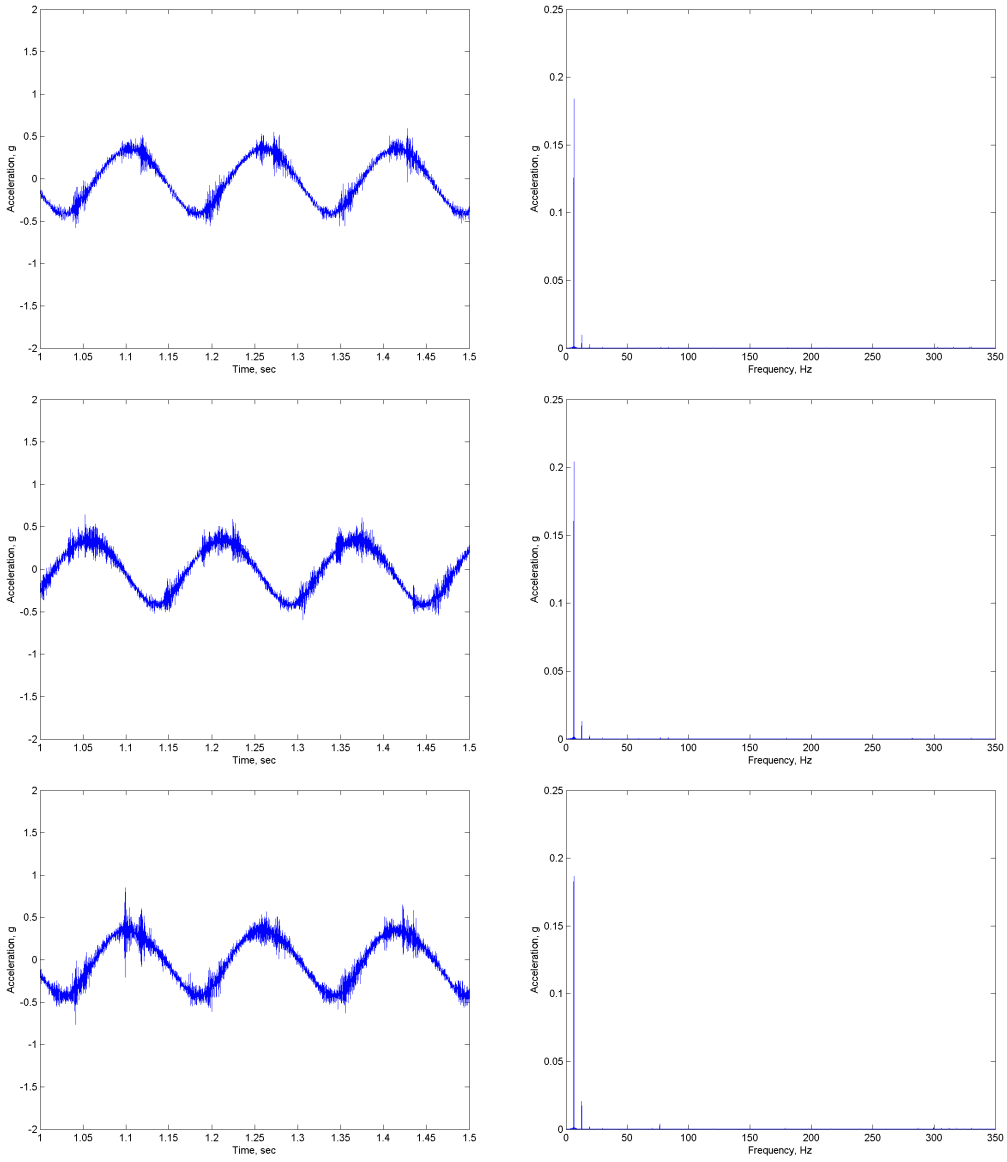

(a) Time Domain (b) Frequency Domain

Figure 5.51: X direction frame vibration for the 2 grooved bearing (Top: 0% Load, Middle: 50% Load, Bottom: 100% Load)

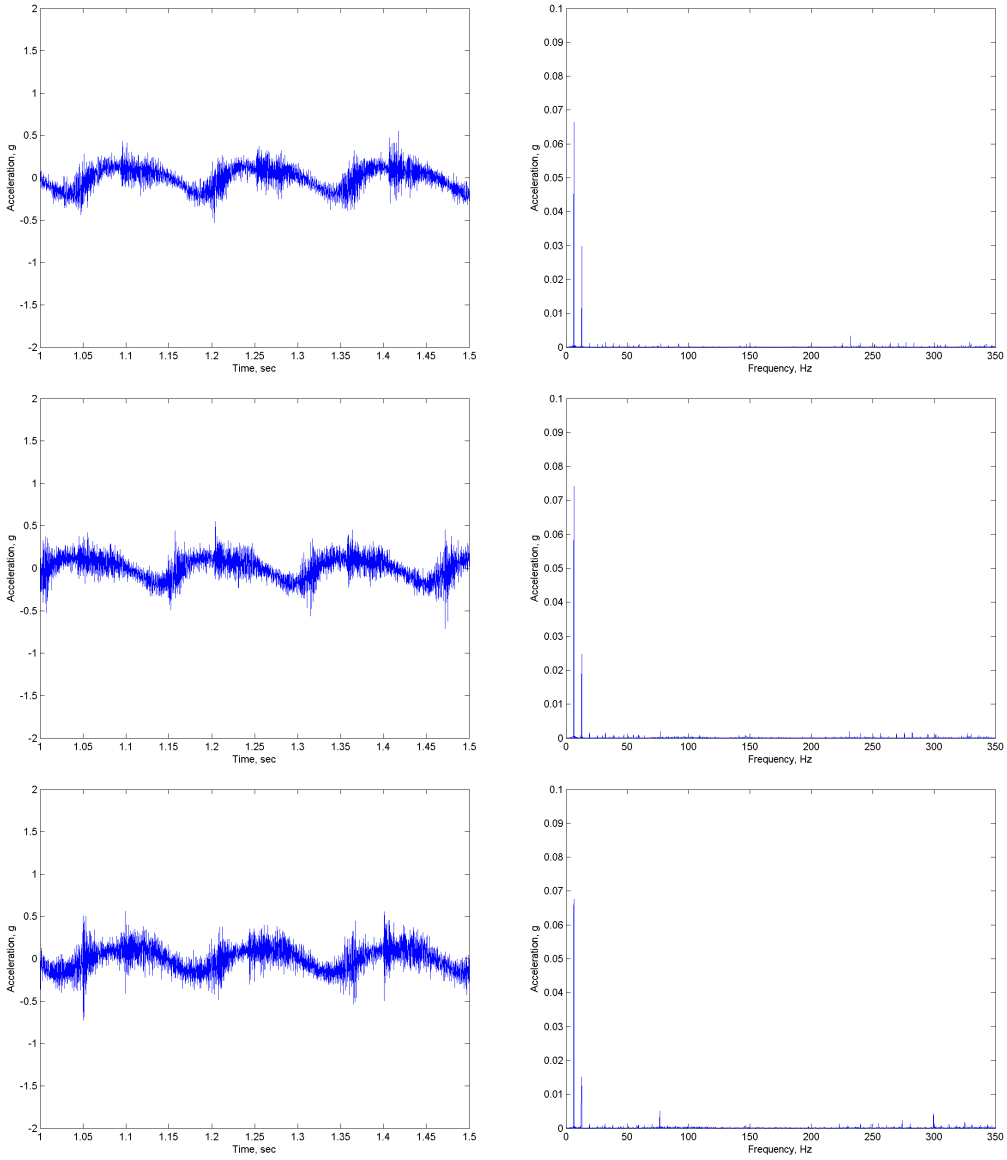

(a) Time Domain (b) Frequency Domain

Figure 5.52: Z direction frame vibration for the 2 grooved bearing (Top: 0% Load, Middle: 50% Load, Bottom: 100% Load)

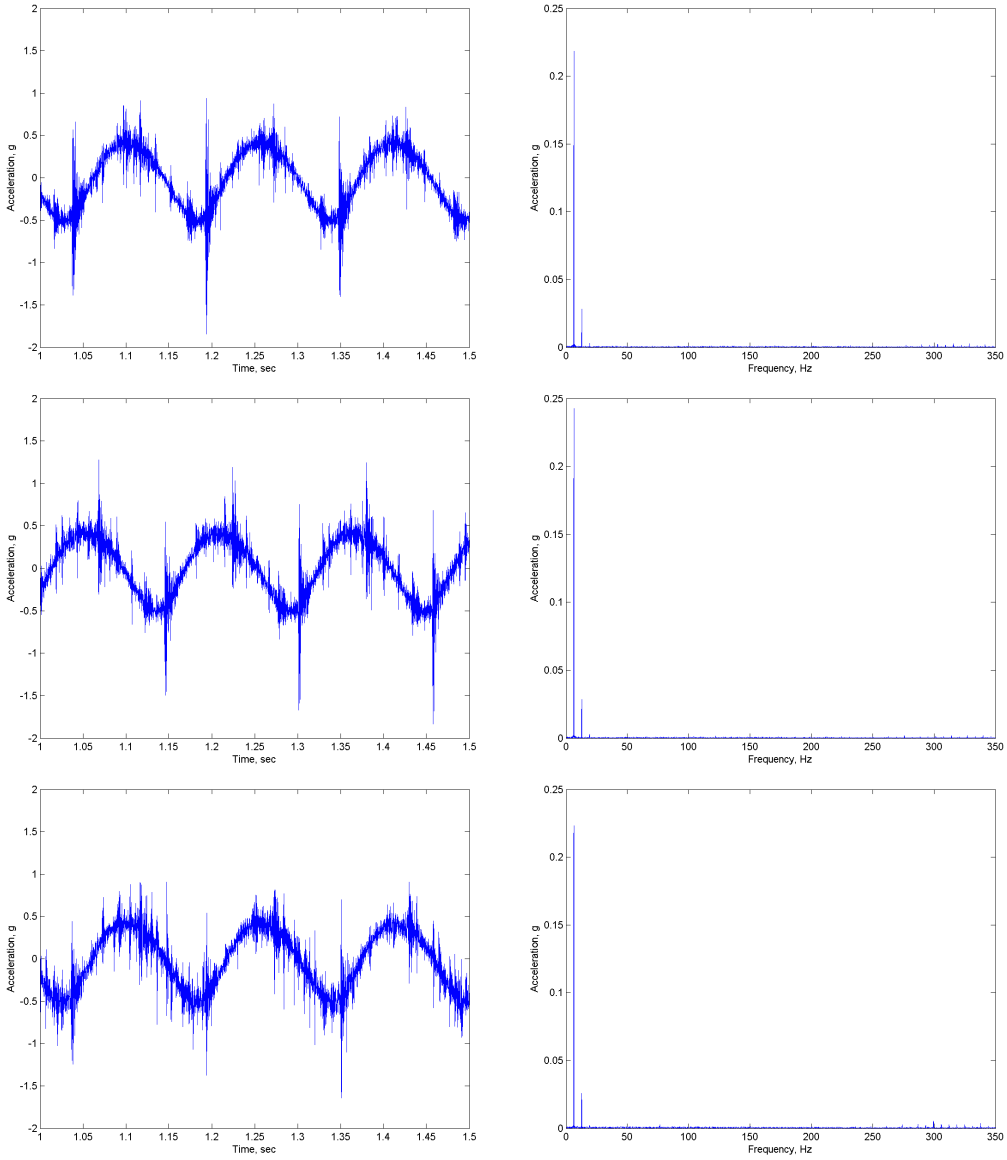

(a) Time Domain (b) Frequency Domain

Figure 5.53: X direction crankcase vibration for the 2 grooved bearing (Top: 0% Load, Middle: 50% Load, Bottom: 100% Load)

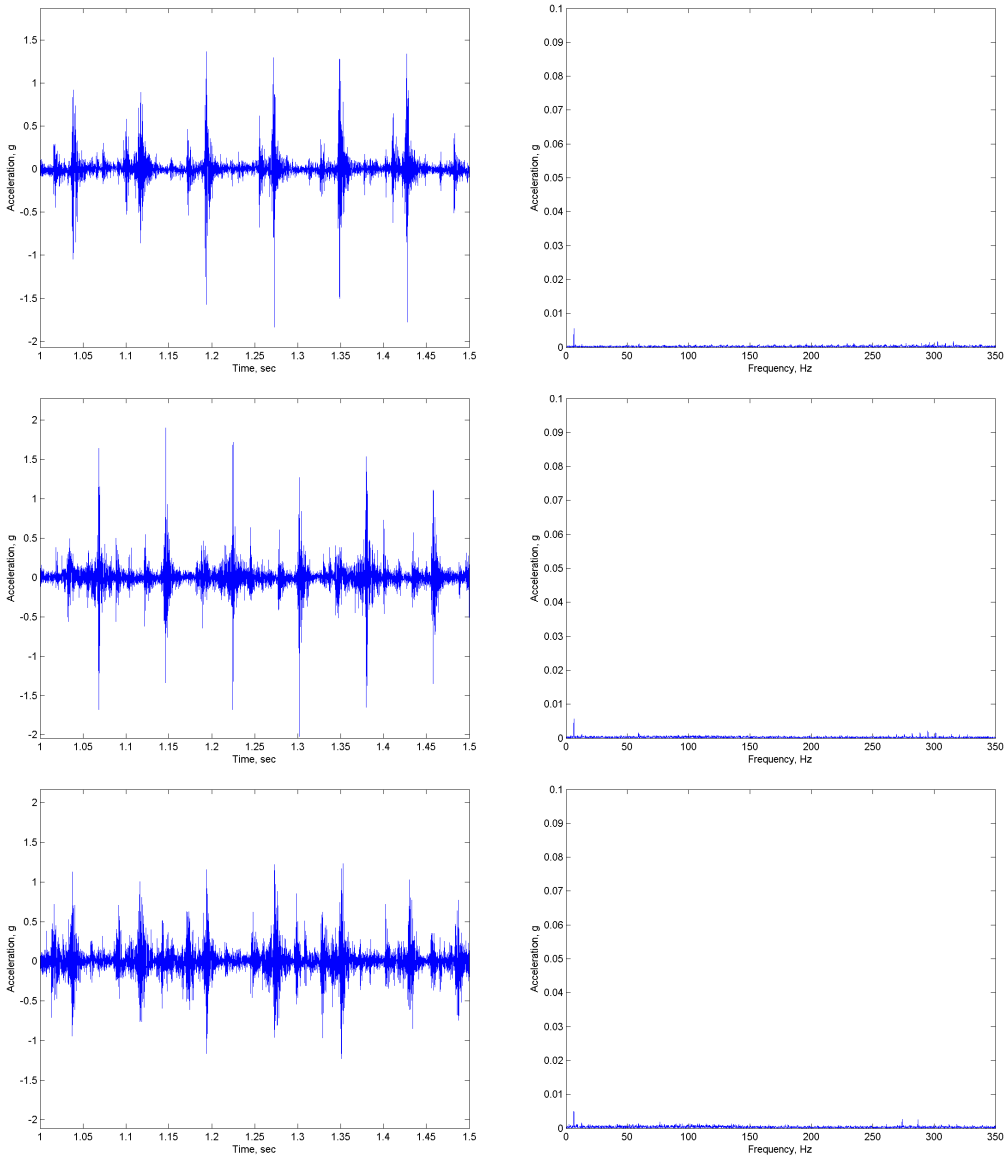

(a) Time Domain (b) Frequency Domain

Figure 5.54: Z direction crosshead vibration for the 2 grooved bearing (Top: 0% Load, Middle: 50% Load, Bottom: 100% Load)

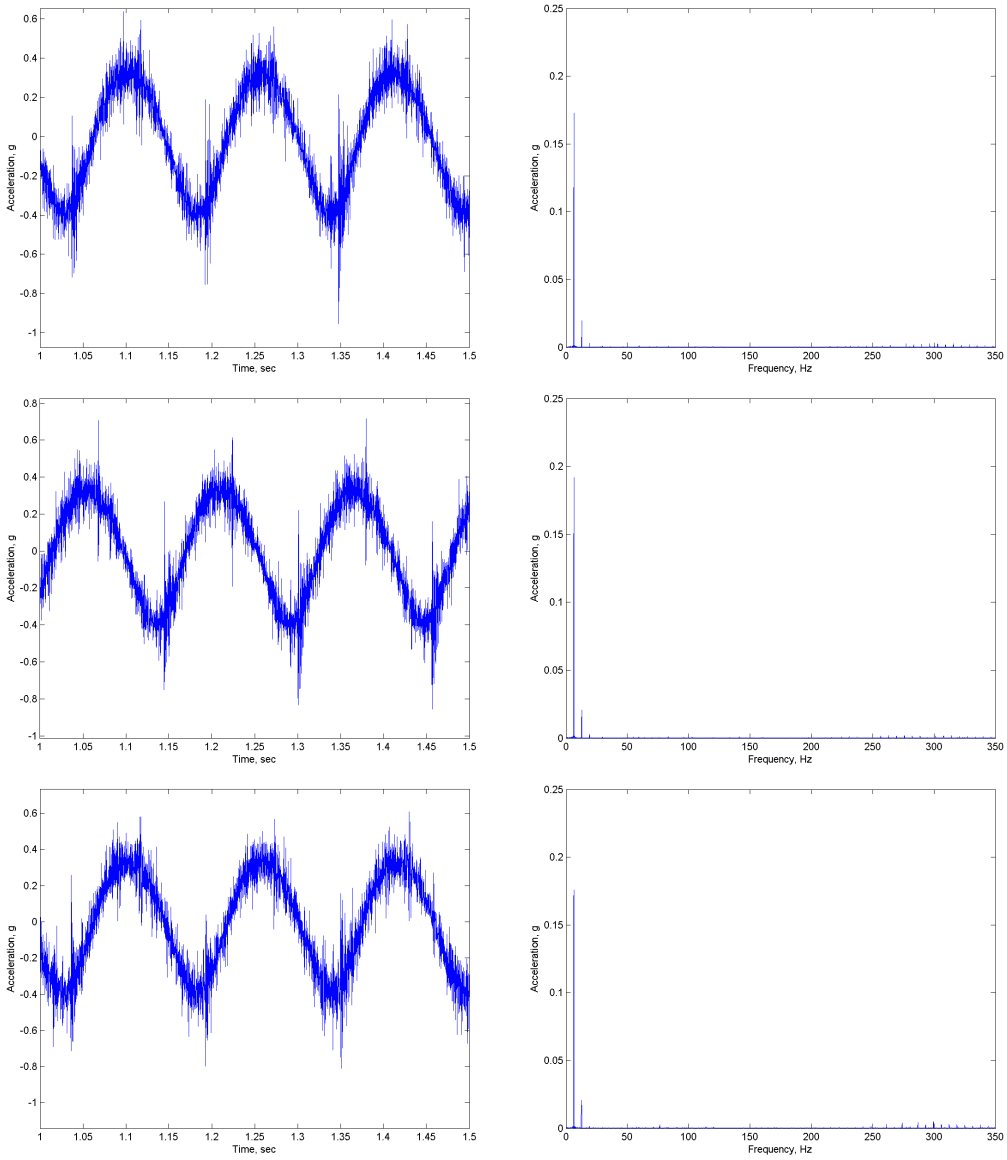

(a) Time Domain (b) Frequency Domain

Figure 5.55: Bearing housing vibration for the 2 grooved bearing (Top: 0% Load, Middle: 50% Load, Bottom: 100% Load)

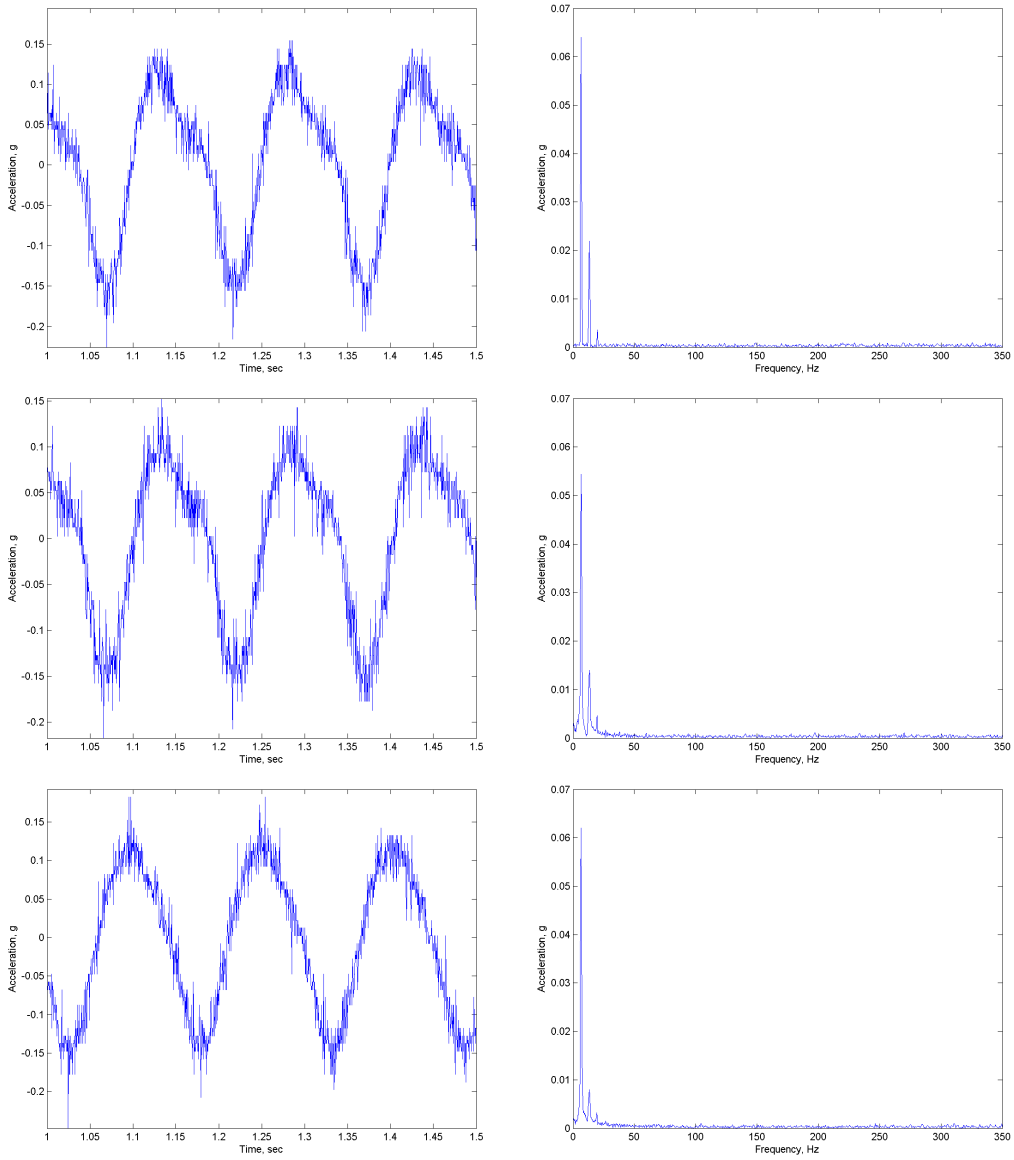

(a) Time Domain (b) Frequency Domain

Figure 5.56: Crankshaft vibration for the 2 grooved bearing (Top: 0% Load, Middle: 50% Load, Bottom: 100% Load)

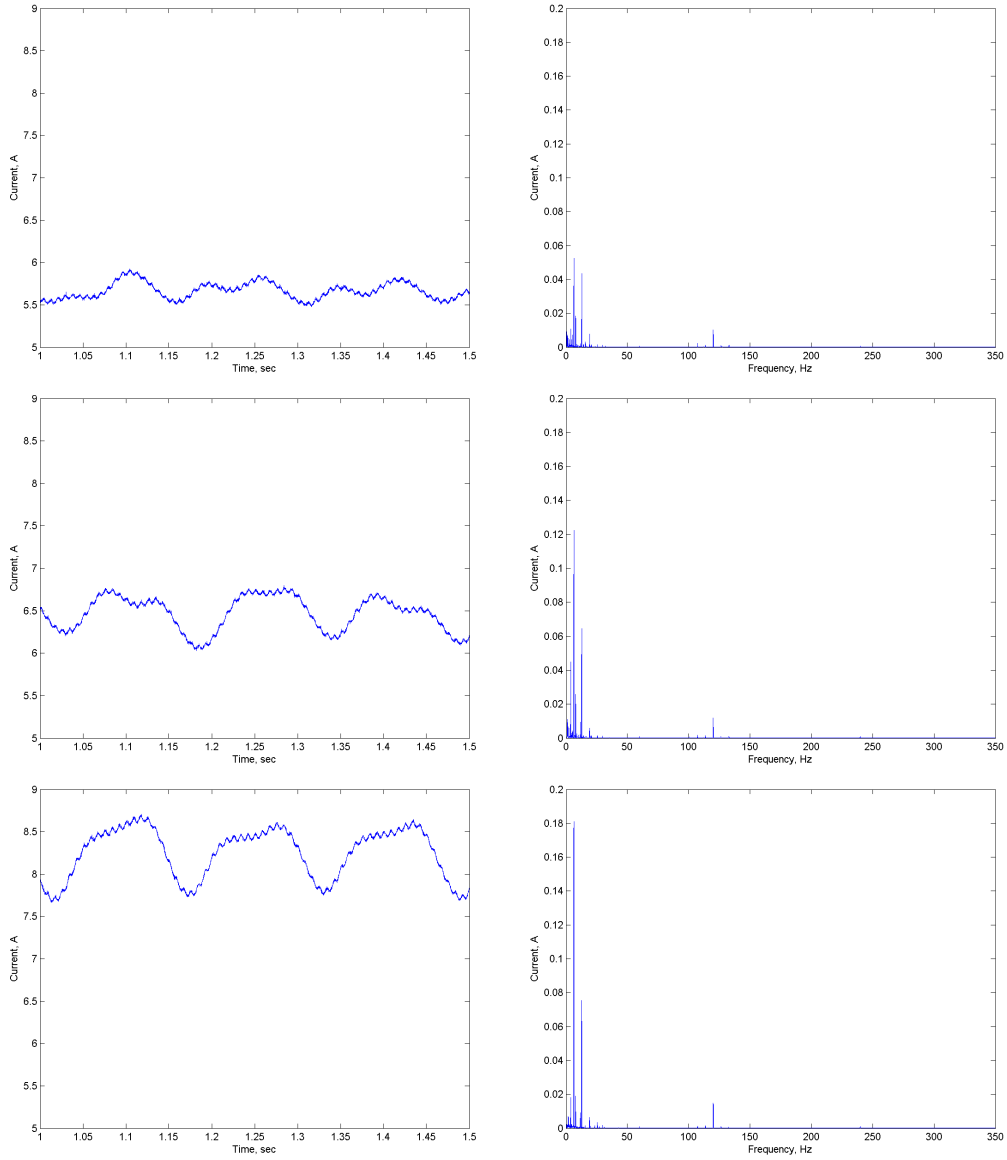

(a) Time Domain (b) Frequency Domain

Figure 5.57: Current draw for the 2 grooved bearing (Top: 0% Load, Middle: 50% Load, Bottom: 100% Load)

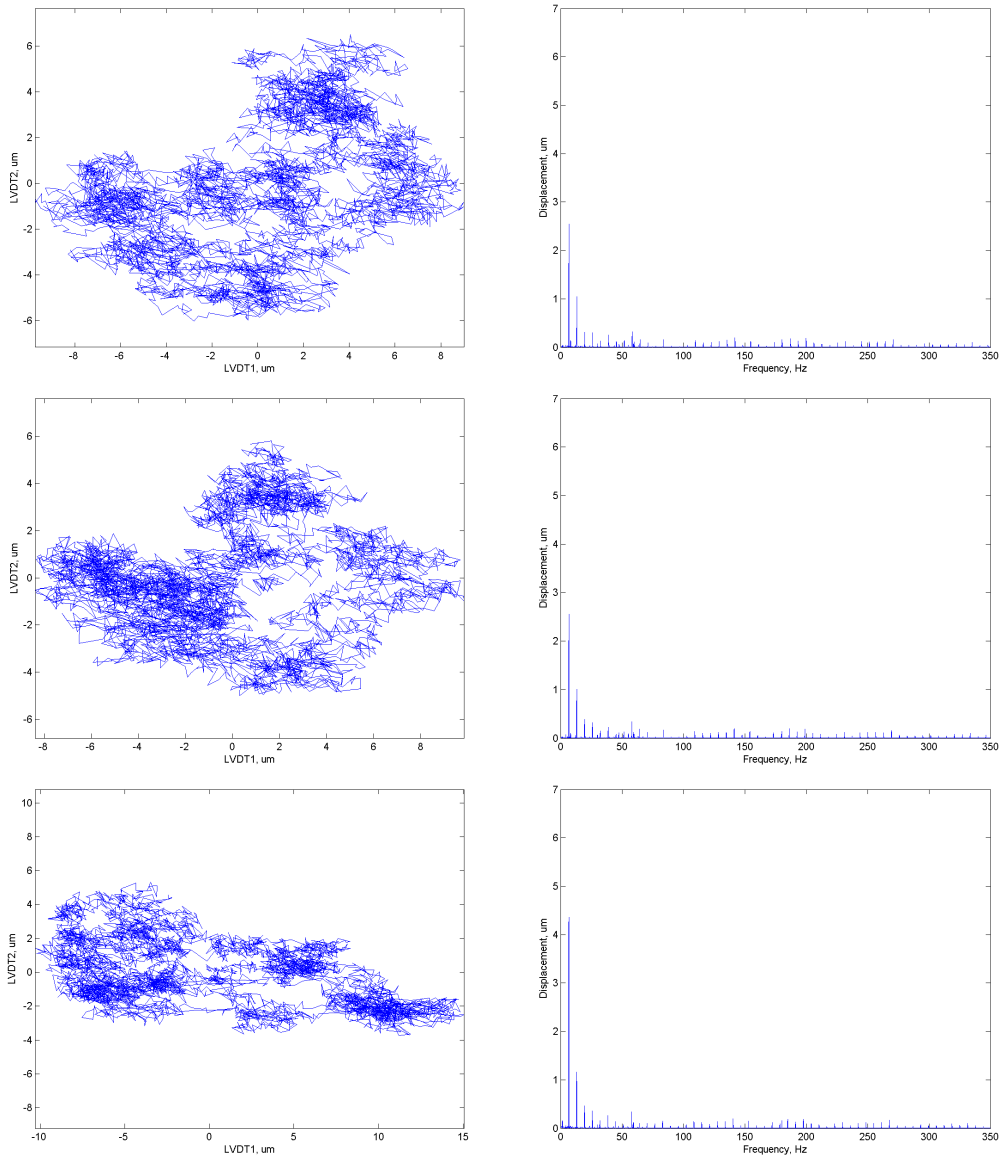

(a) Time Domain (b) Frequency Domain

Figure 5.58: Crankshaft orbit and LVDT FFT for the 2 grooved bearing (Top: 0% Load, Middle: 50% Load, Bottom: 100% Load)

5.3.6 Oil Feed Hole Obstruction

In order to partially obstruct the feed holes, epoxy is used. The holes are filled and left overnight to dry. Then the new feed hole diameter is calculated and drilled out. The same bearing is used for both cases.

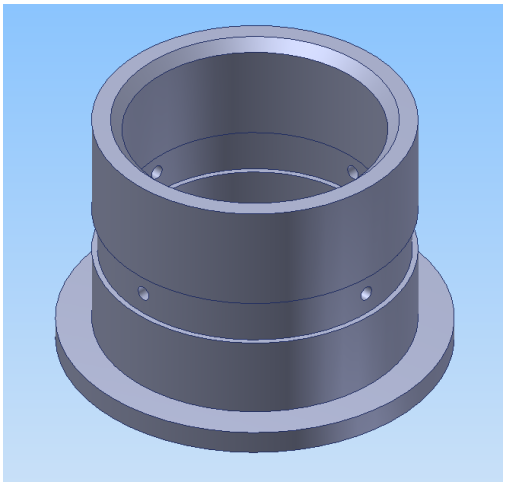

(a) 3D

(b) implementation

Figure 5.59: Bearing with 75% feed hole obstruction

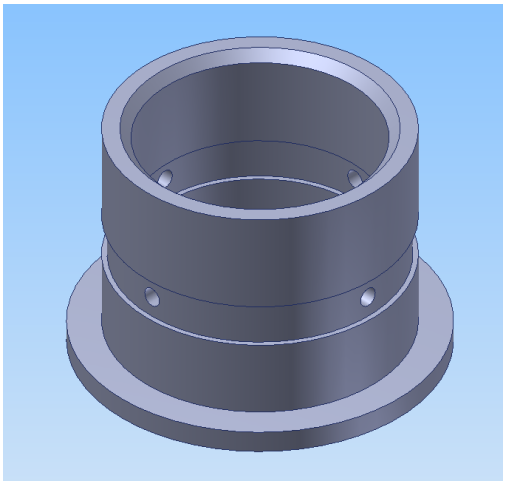

(a) 3D

(b) implementation

Figure 5.60: Bearing with 50% feed hole obstruction

75% Blocked

The bearing with the smallest oil feed hole size shows more pronounced vibration especially on the accelerometers close to the bearing. The LVDT signal is also noticeably noisier than the baseline but retains the general shape. It does show a larger orbit consistent with less oil passing through the bearing. Figures 5.61 through 5.68 show the raw data collected for this failure mode.

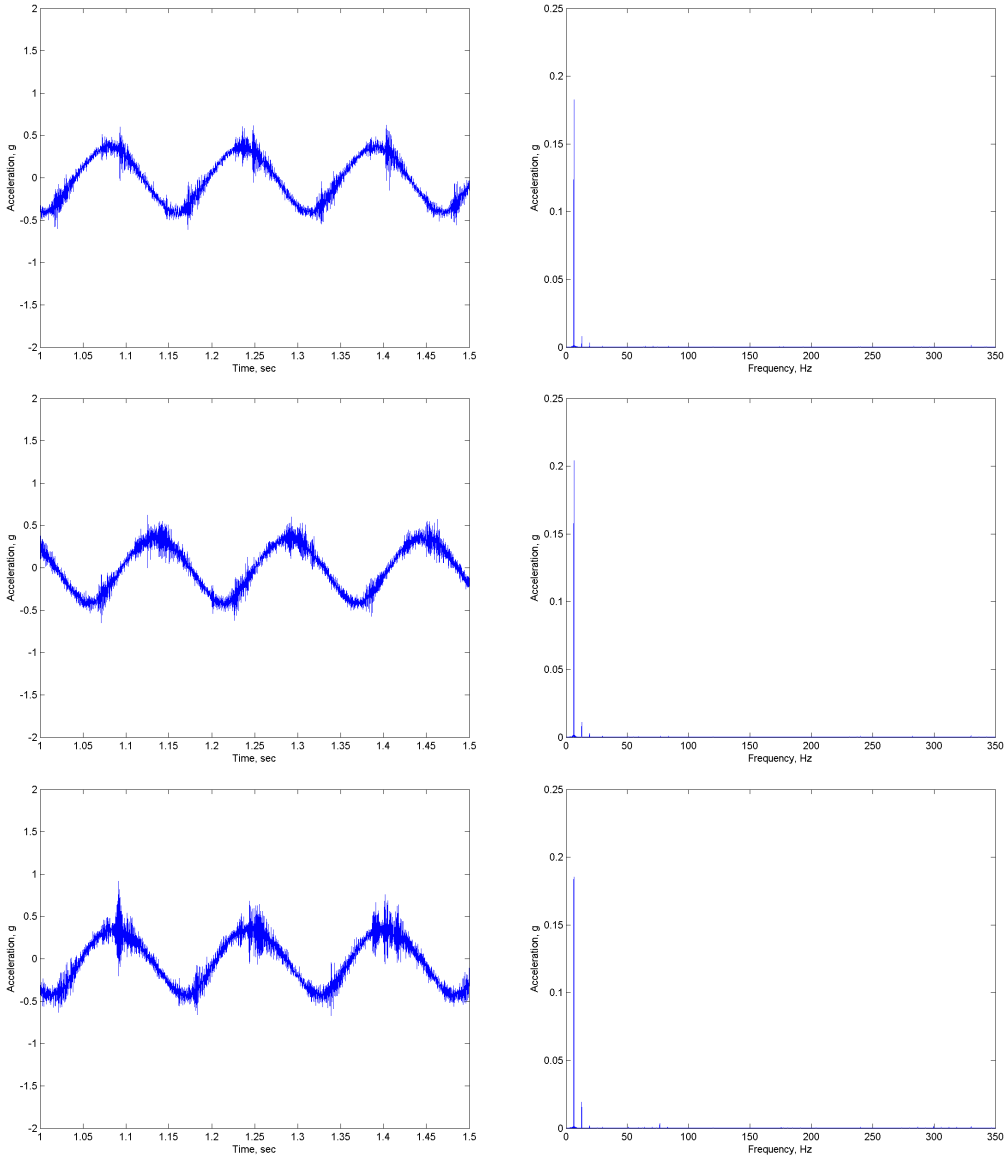

(a) Time Domain (b) Frequency Domain

Figure 5.61: X direction frame vibration for the bearing with feed hole size reduced 75% (Top: 0% Load, Middle: 50% Load, Bottom: 100% Load)

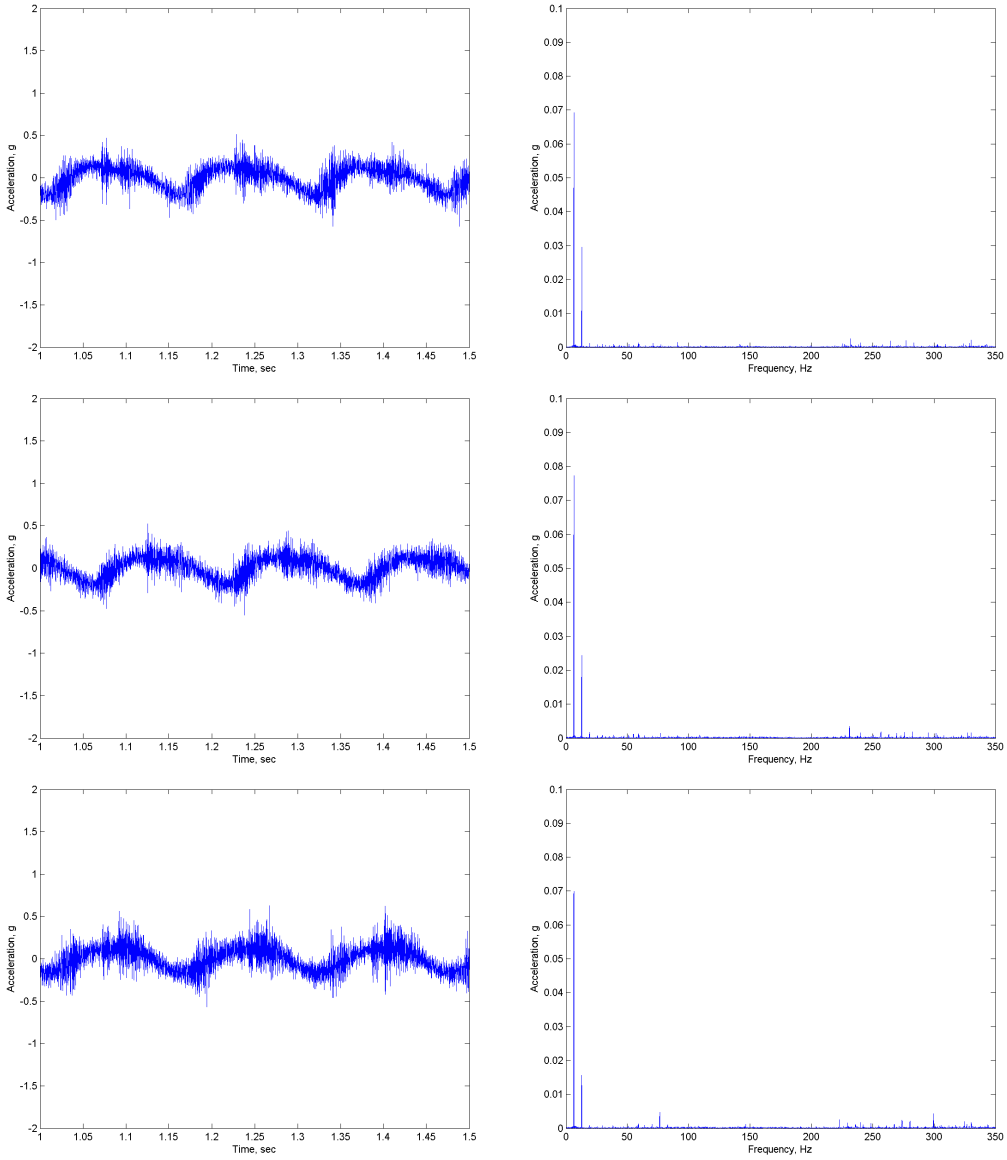

(a) Time Domain (b) Frequency Domain

Figure 5.62: Z direction frame vibration for the bearing with feed hole size reduced 75% (Top: 0% Load, Middle: 50% Load, Bottom: 100% Load)

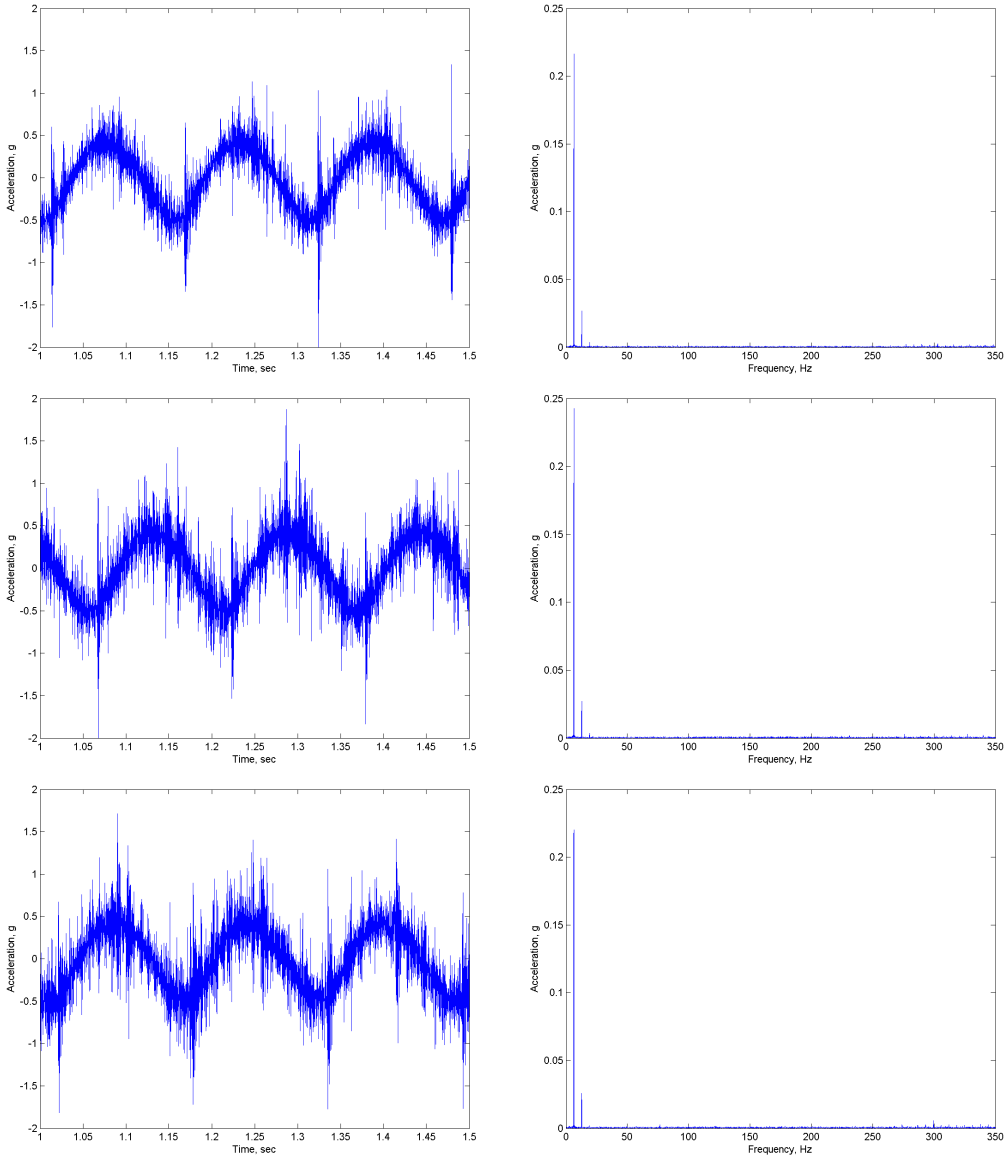

(a) Time Domain (b) Frequency Domain

Figure 5.63: X direction crankcase vibration for the bearing with feed hole size reduced 75% (Top: 0% Load, Middle: 50% Load, Bottom: 100% Load)

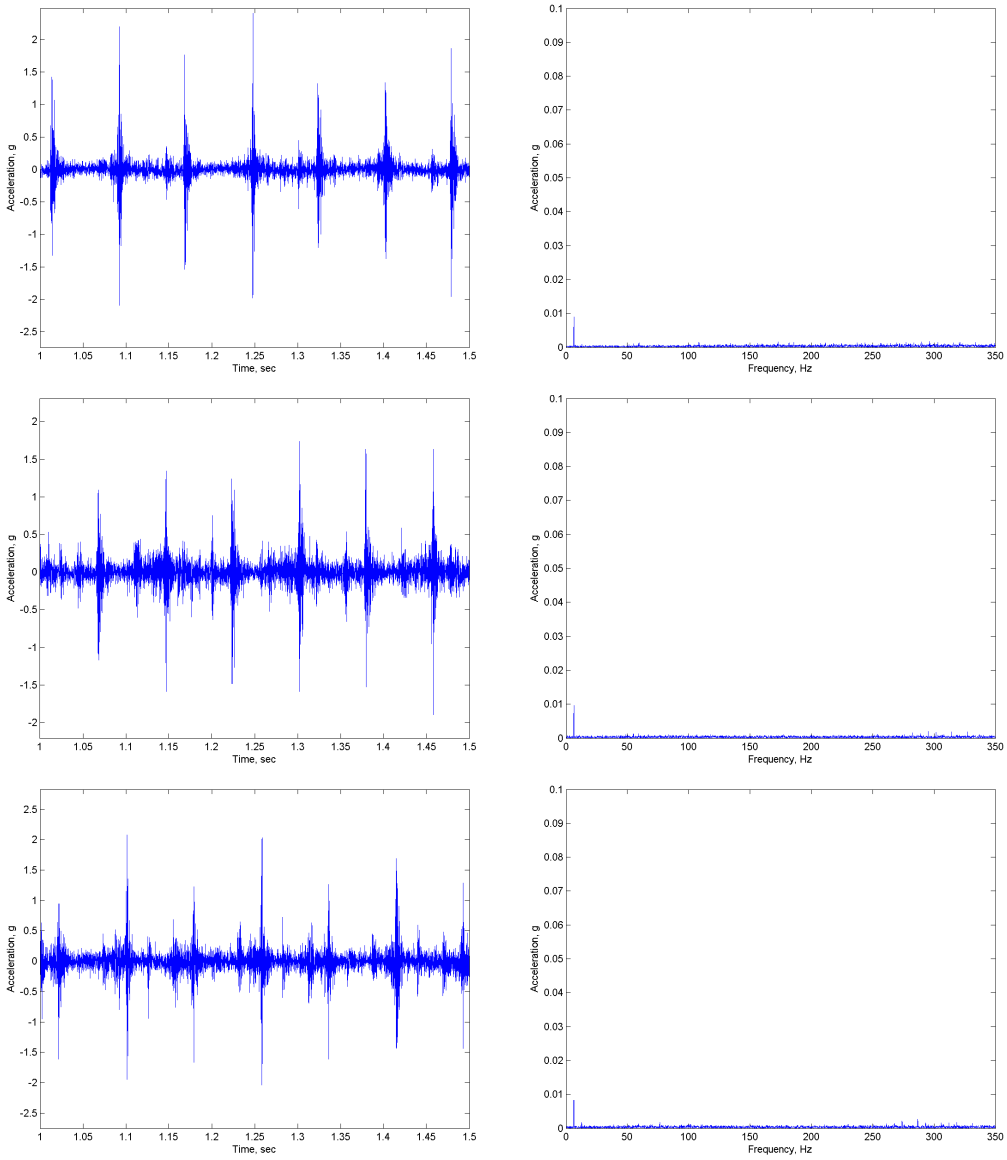

(a) Time Domain (b) Frequency Domain

Figure 5.64: Z direction crosshead vibration for the bearing with feed hole size reduced 75% (Top: 0% Load, Middle: 50% Load, Bottom: 100% Load)

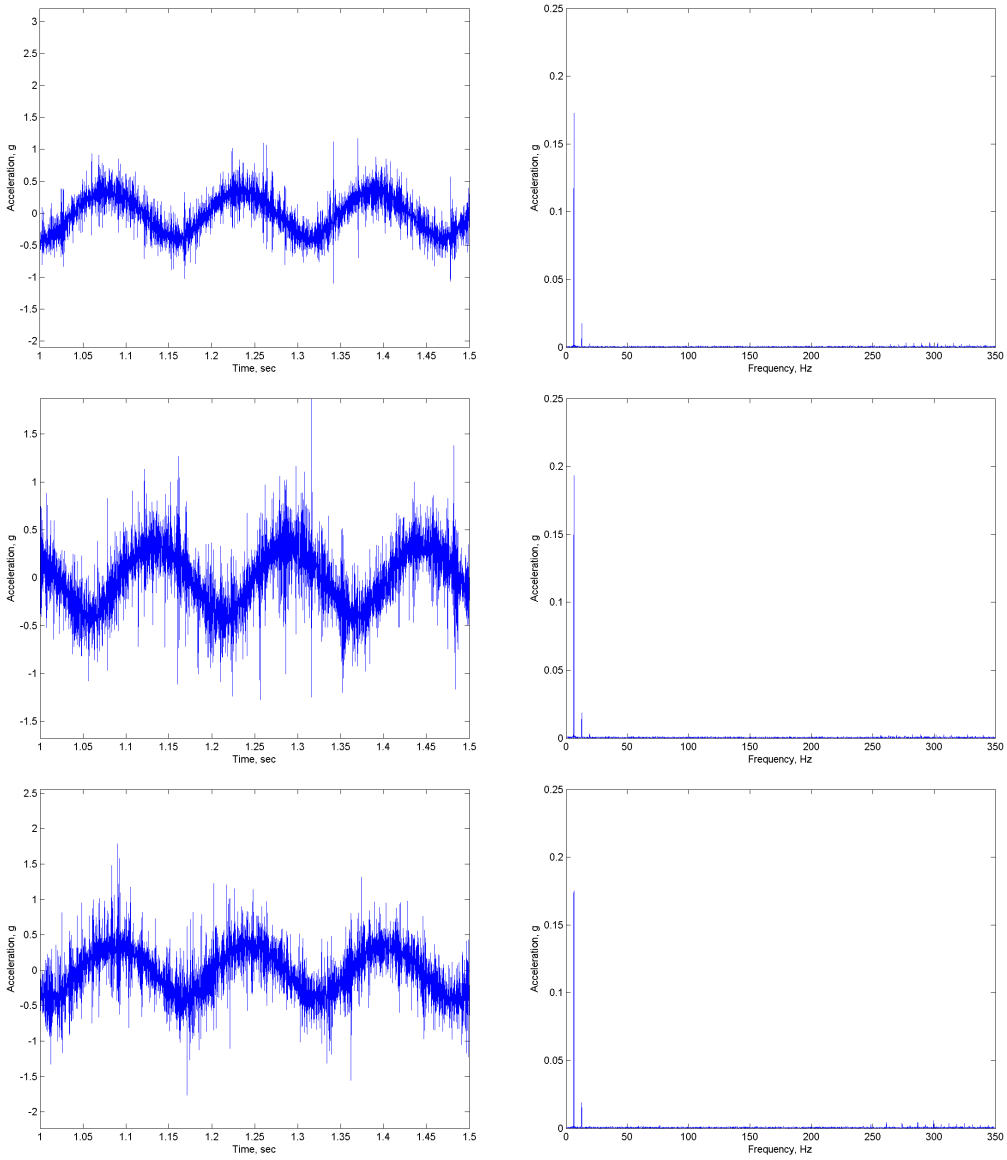

(a) Time Domain (b) Frequency Domain

Figure 5.65: Bearing housing vibration for the bearing with feed hole size reduced 75% (Top: 0% Load, Middle: 50% Load, Bottom: 100% Load)

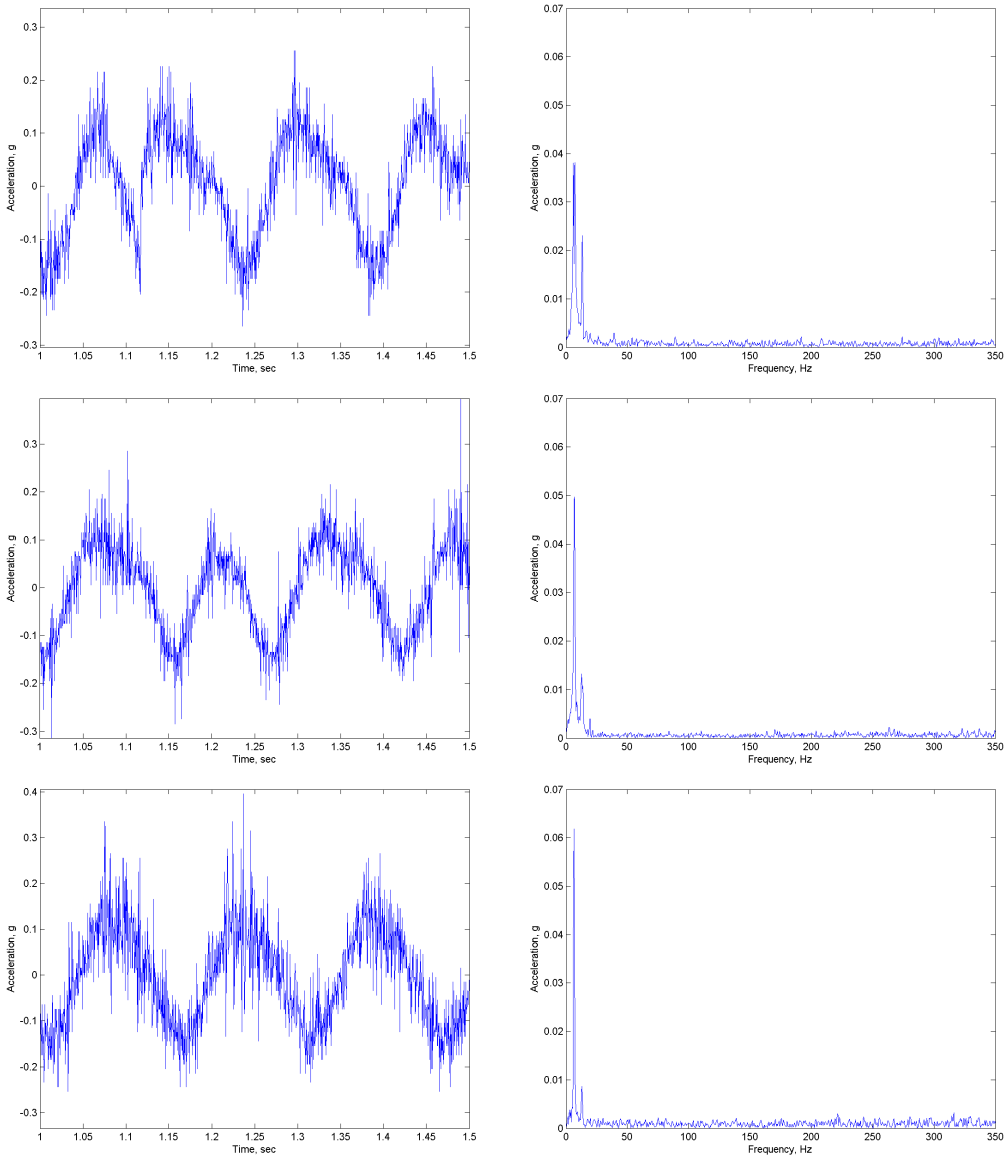

(a) Time Domain (b) Frequency Domain

Figure 5.66: Crankshaft vibration for the bearing with feed hole size reduced 75% (Top: 0% Load, Middle: 50% Load, Bottom: 100% Load)

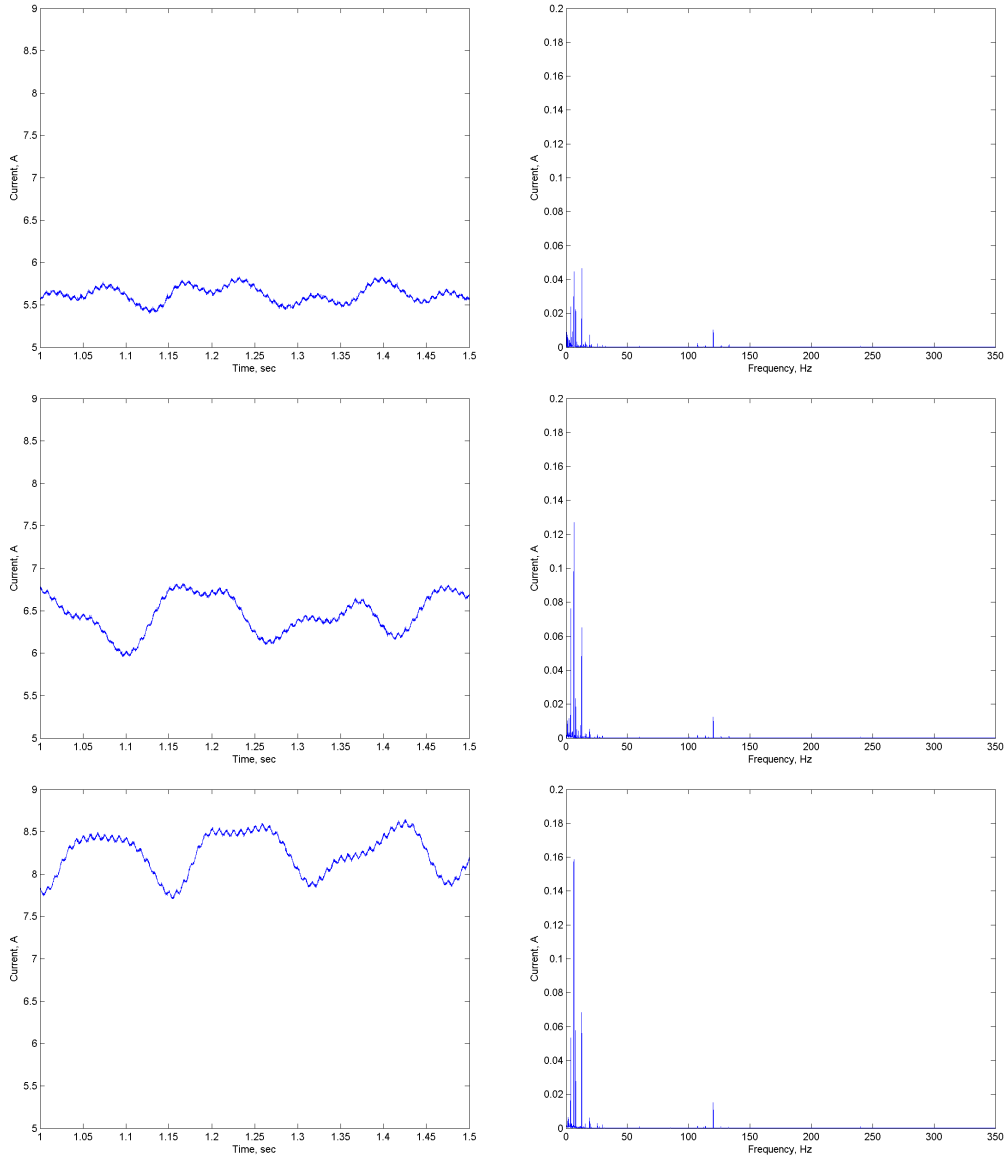

(a) Time Domain (b) Frequency Domain

Figure 5.67: Current draw for the bearing with feed hole size reduced 75% (Top: 0% Load, Middle: 50% Load, Bottom: 100% Load)

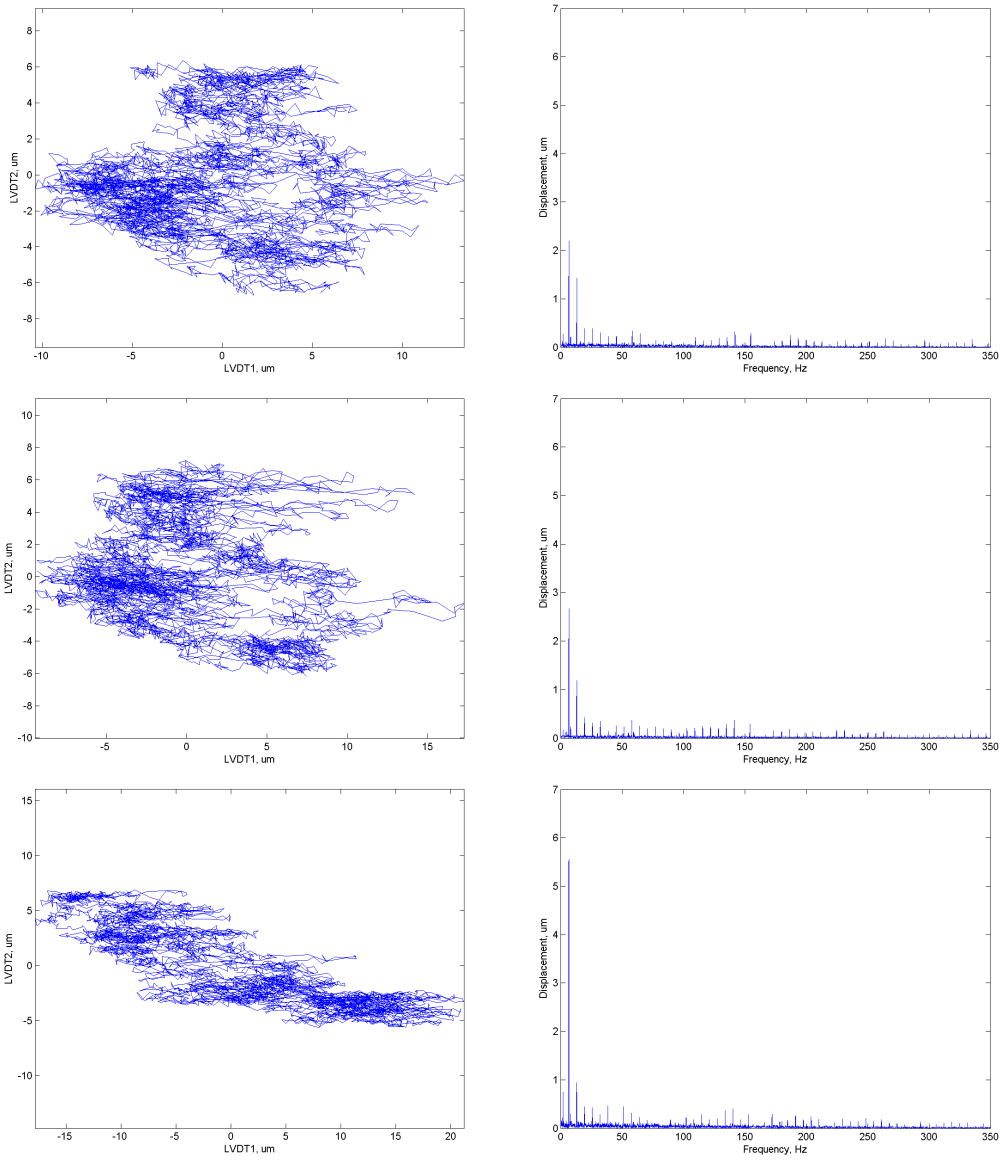

(a) Time Domain (b) Frequency Domain

Figure 5.68: Crankshaft orbit and LVDT FFT for the bearing with feed hole size reduced 75% (Top: 0% Load, Middle: 50% Load, Bottom: 100% Load)

50% Blocked

The case with the feed hole size area reduced to 50% shows the same general trends as the case with a 75% reduction. Overall the vibrations are less pronounced and the orbit shapes cleaner (Fig. 5.69 through 5.76)

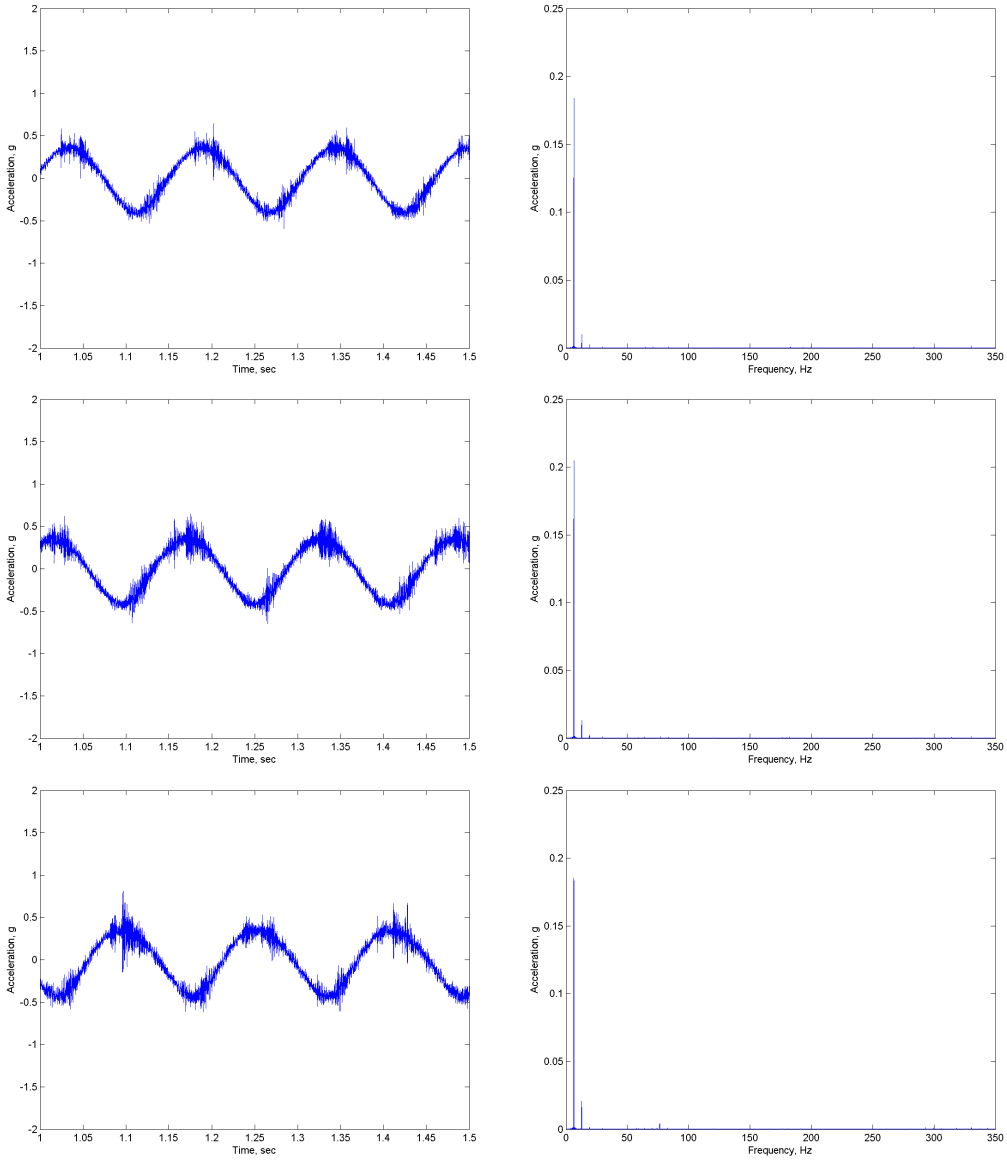

(a) Time Domain (b) Frequency Domain

Figure 5.69: X direction frame vibration for the bearing with feed hole size reduced 50% (Top: 0% Load, Middle: 50% Load, Bottom: 100% Load)

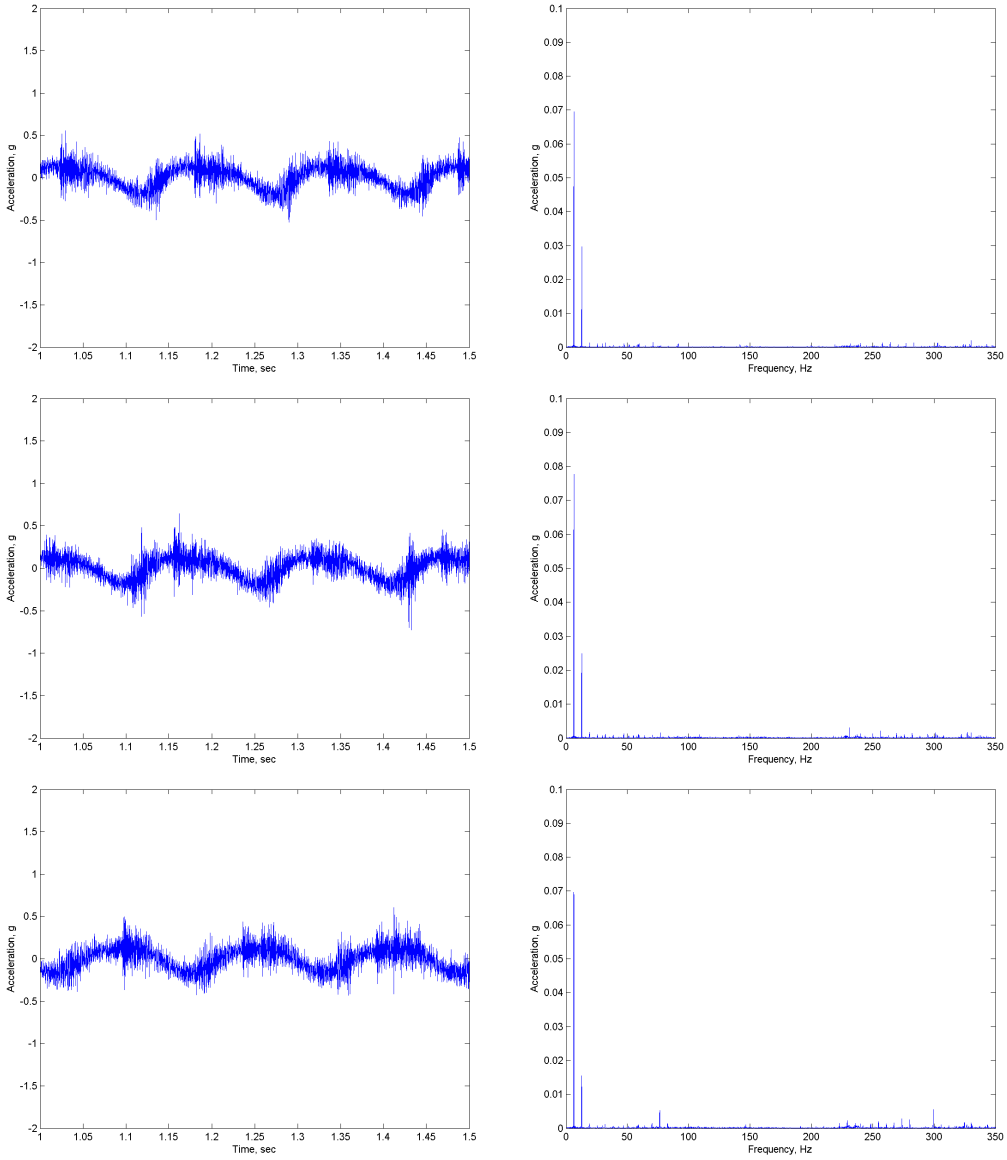

(a) Time Domain (b) Frequency Domain

Figure 5.70: Z direction frame vibration for the bearing with feed hole size reduced 50% (Top: 0% Load, Middle: 50% Load, Bottom: 100% Load)

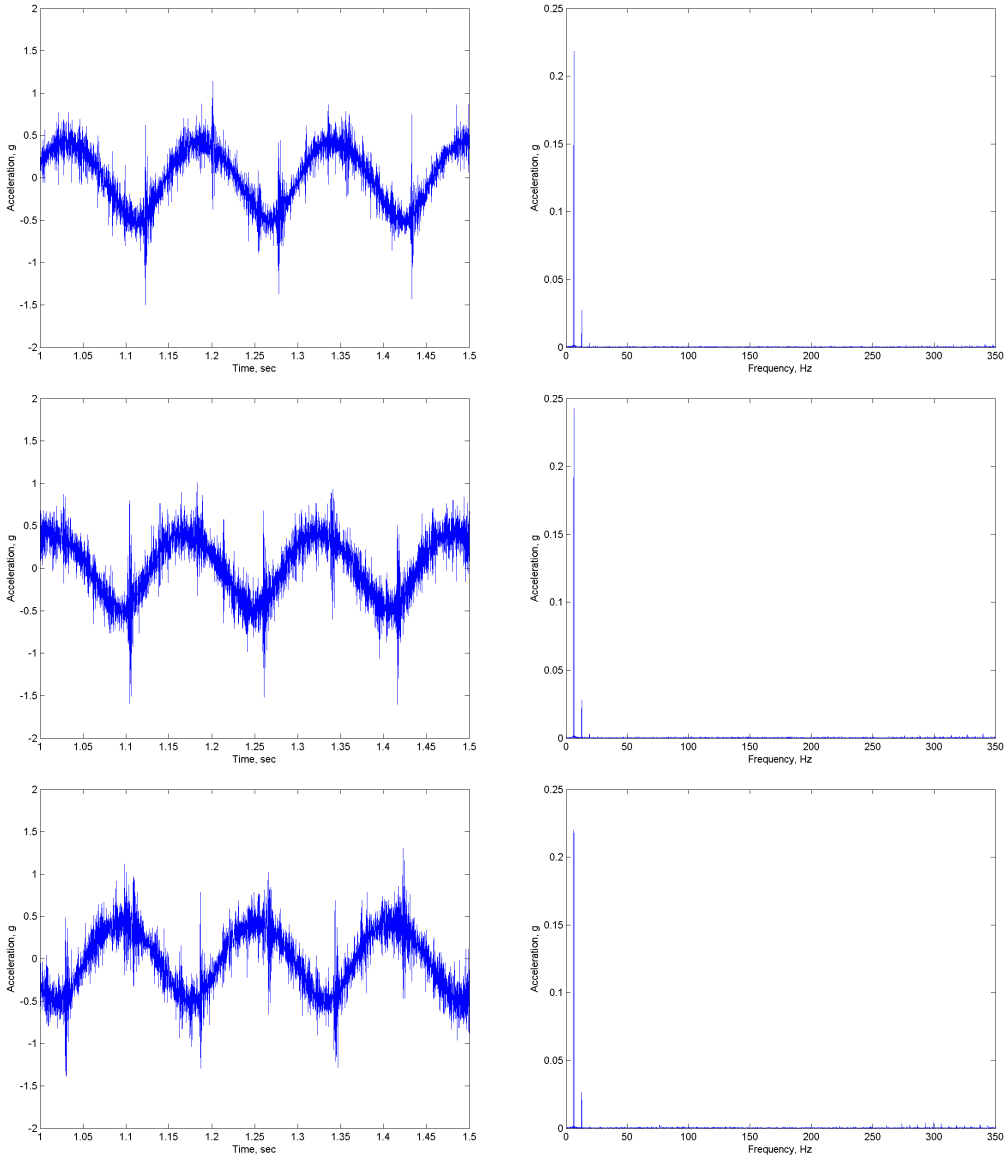

(a) Time Domain (b) Frequency Domain

Figure 5.71: X direction crankcase vibration for the bearing with feed hole size reduced 50% (Top: 0% Load, Middle: 50% Load, Bottom: 100% Load)

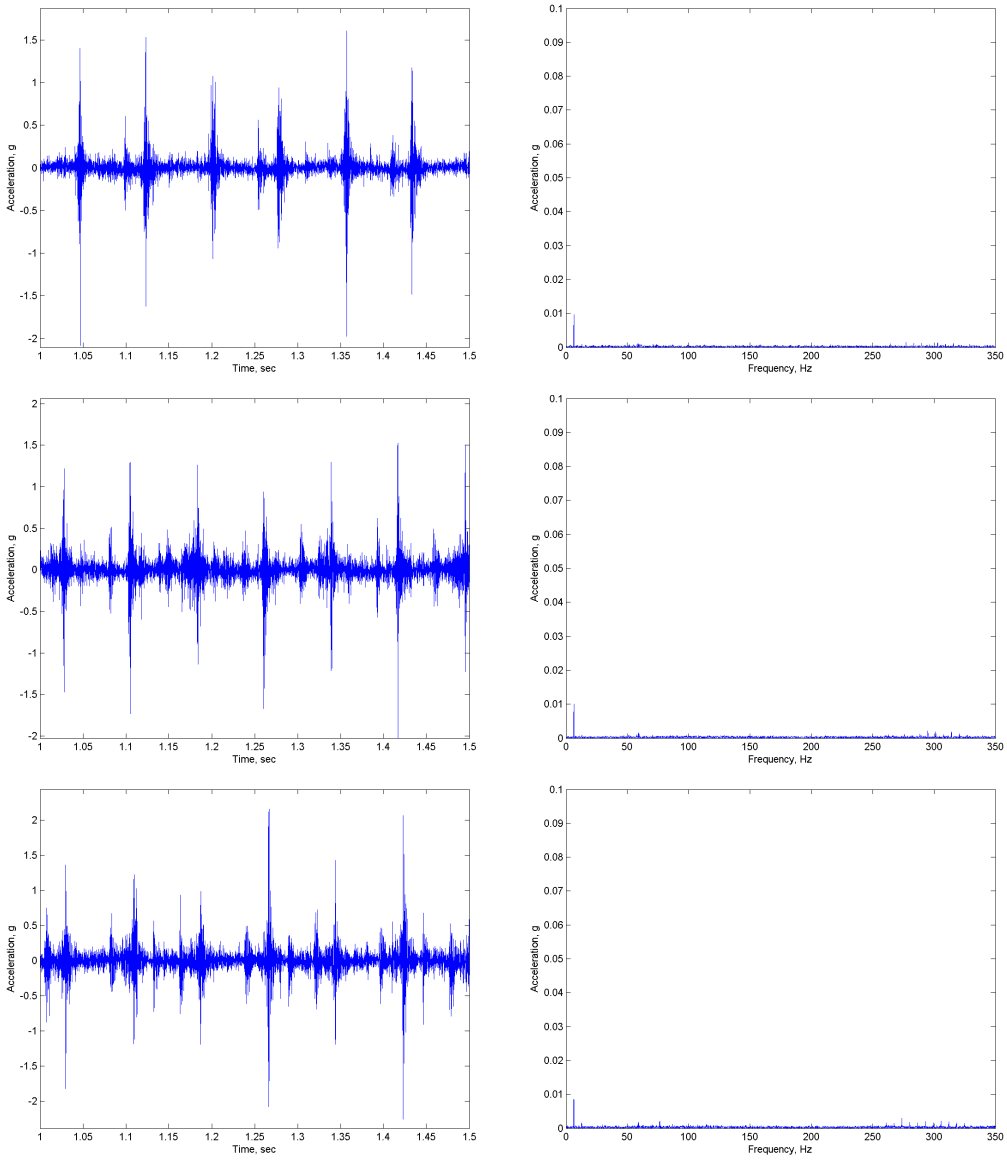

(a) Time Domain (b) Frequency Domain

Figure 5.72: Z direction crosshead vibration for the bearing with feed hole size reduced 50% (Top: 0% Load, Middle: 50% Load, Bottom: 100% Load)

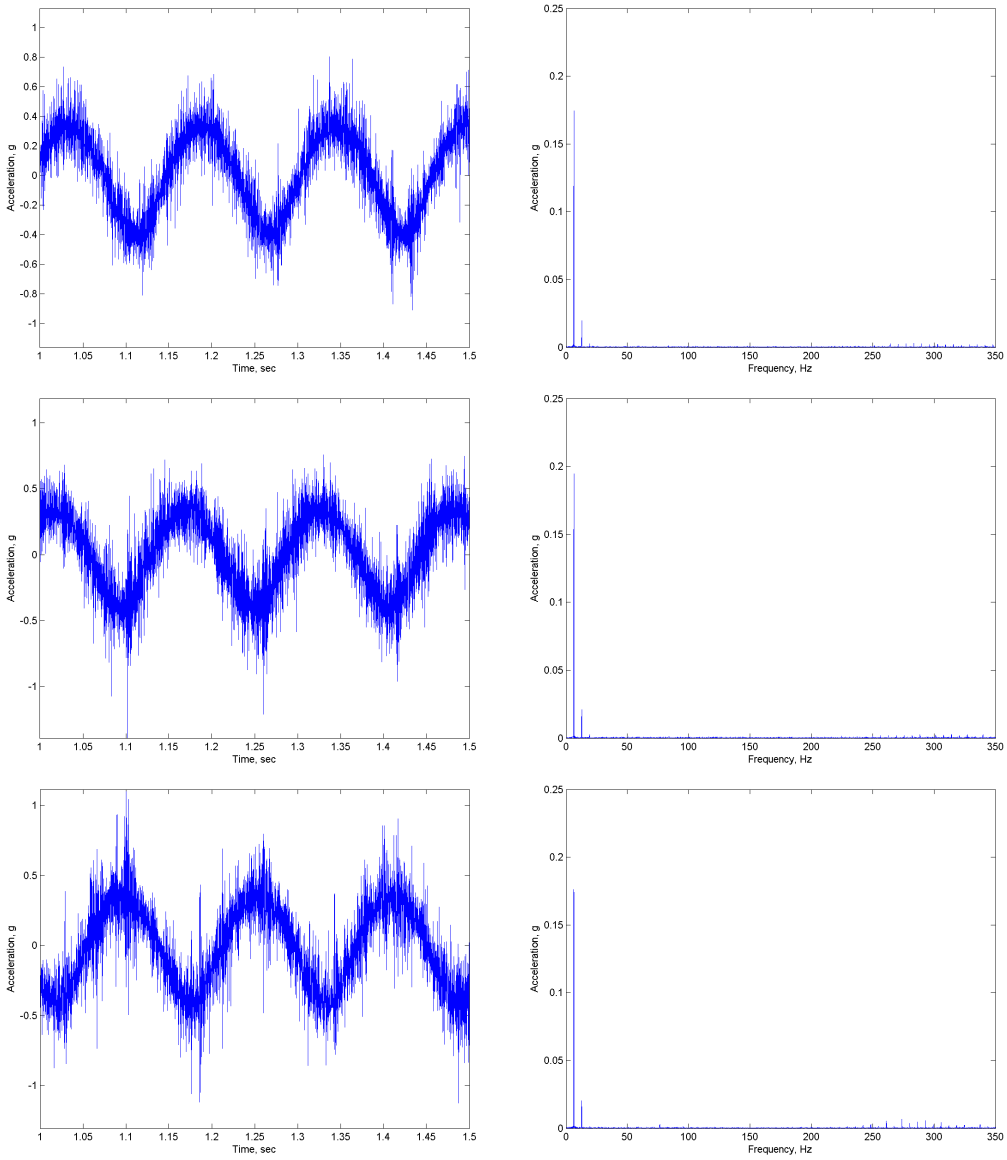

(a) Time Domain (b) Frequency Domain

Figure 5.73: Bearing housing vibration for the bearing with feed hole size reduced 50% (Top: 0% Load, Middle: 50% Load, Bottom: 100% Load)

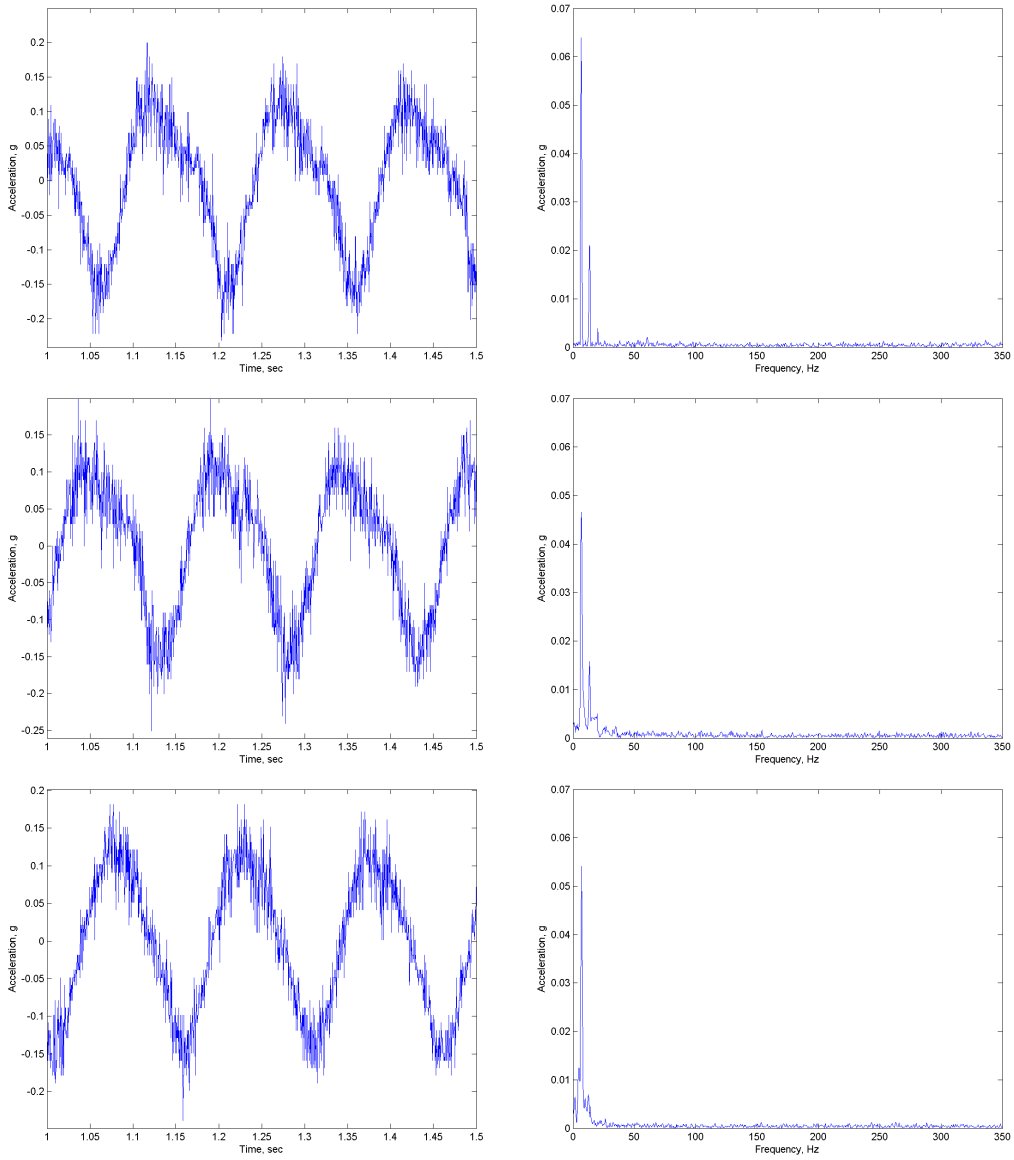

(a) Time Domain (b) Frequency Domain

Figure 5.74: Crankshaft vibration for the bearing with feed hole size reduced 50% (Top: 0% Load, Middle: 50% Load, Bottom: 100% Load)

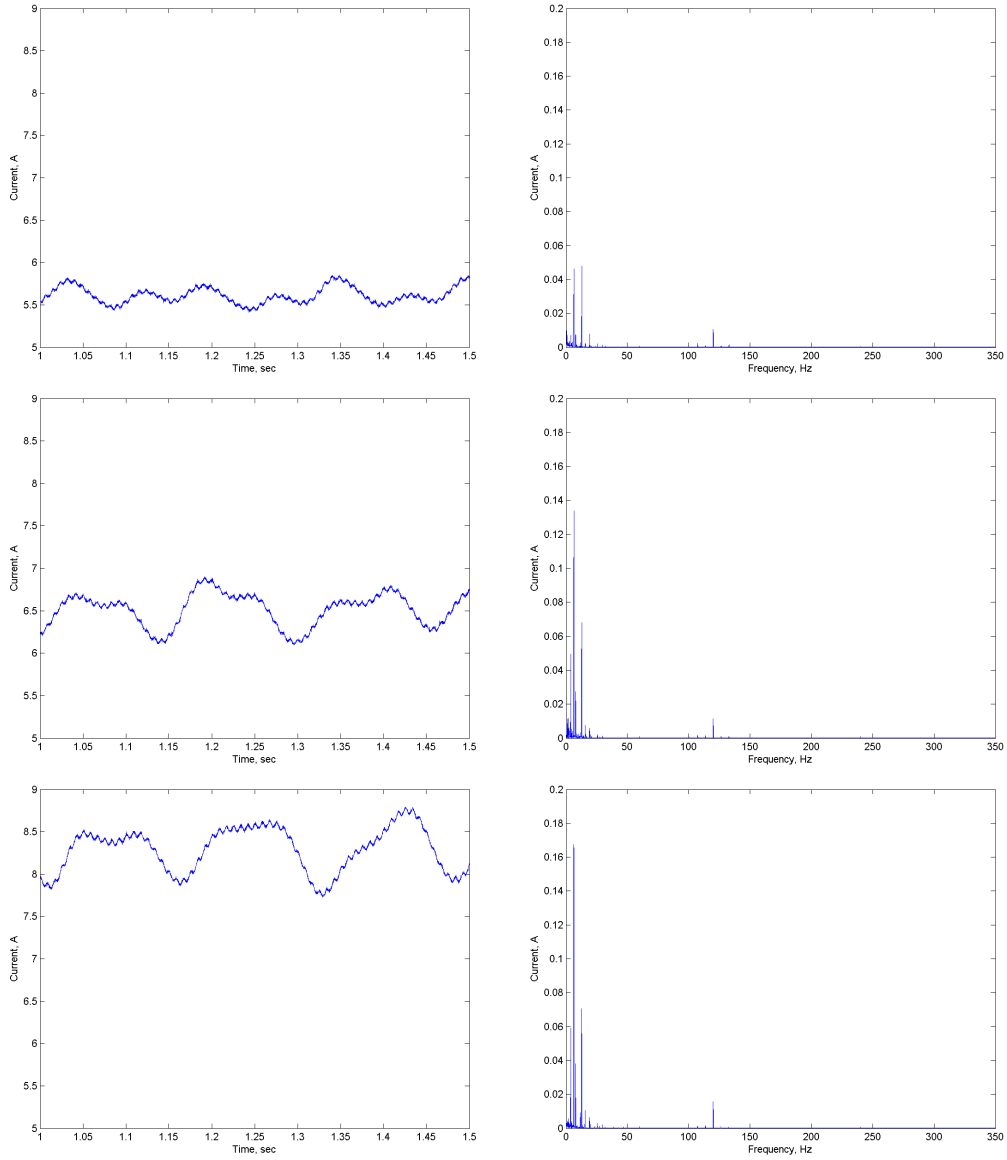

(a) Time Domain (b) Frequency Domain

Figure 5.75: Current draw for the bearing with feed hole size reduced 50% (Top: 0% Load, Middle: 50% Load, Bottom: 100% Load)

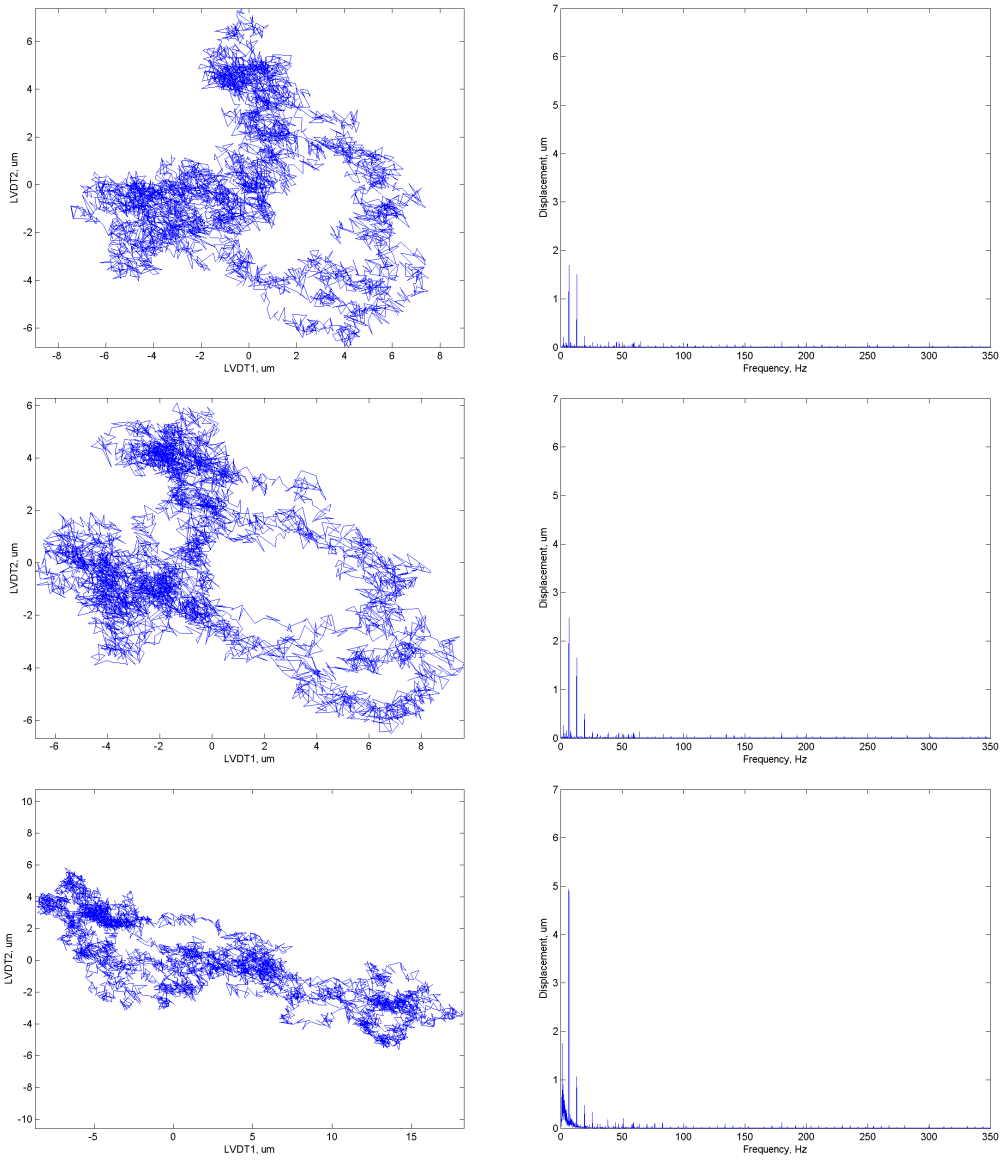

(a) Time Domain (b) Frequency Domain

Figure 5.76: Crankshaft orbit and LVDT FFT for the bearing with feed hole size reduced 50% (Top: 0% Load, Middle: 50% Load, Bottom: 100% Load)

5.3.7 Oil Viscosity Changes

Besides SAE30 oil, two different types of oil are tested to see their effect. All oil tests use the same bearing. The first was a a SAE50 oil for a heavier weight and the second type was SAE10 oil to see the effect of a lighter weight oil. During the lifetime of the oil, viscosity can change in many ways. The viscosity goes down if water or a similar substance becomes mixed with the oil. On the other hand, as the oil ages molecules can oxidize and become heavier. This can eventually lead to sludge. During this process, viscosity goes up.

SAE50

It is difficult to tell the results from the heavier oil apart from the baseline condition. Figures 5.77 through 5.84 look very similar to the results from healthy bearing. The orbit plot shows slightly smaller peak values.

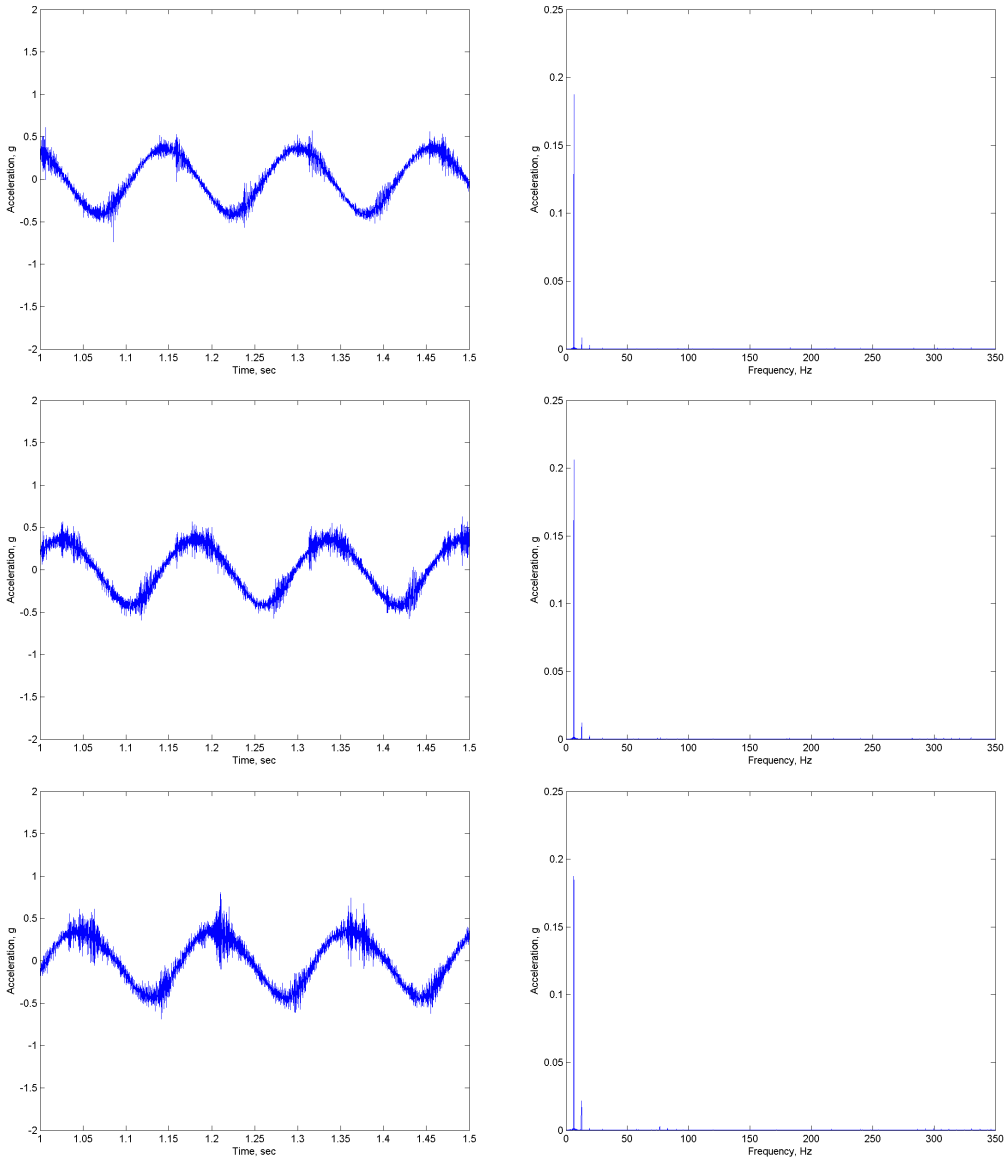

(a) Time Domain (b) Frequency Domain

Figure 5.77: X direction frame vibration for the bearing with SAE50 oil (Top: 0% Load, Middle: 50% Load, Bottom: 100% Load)

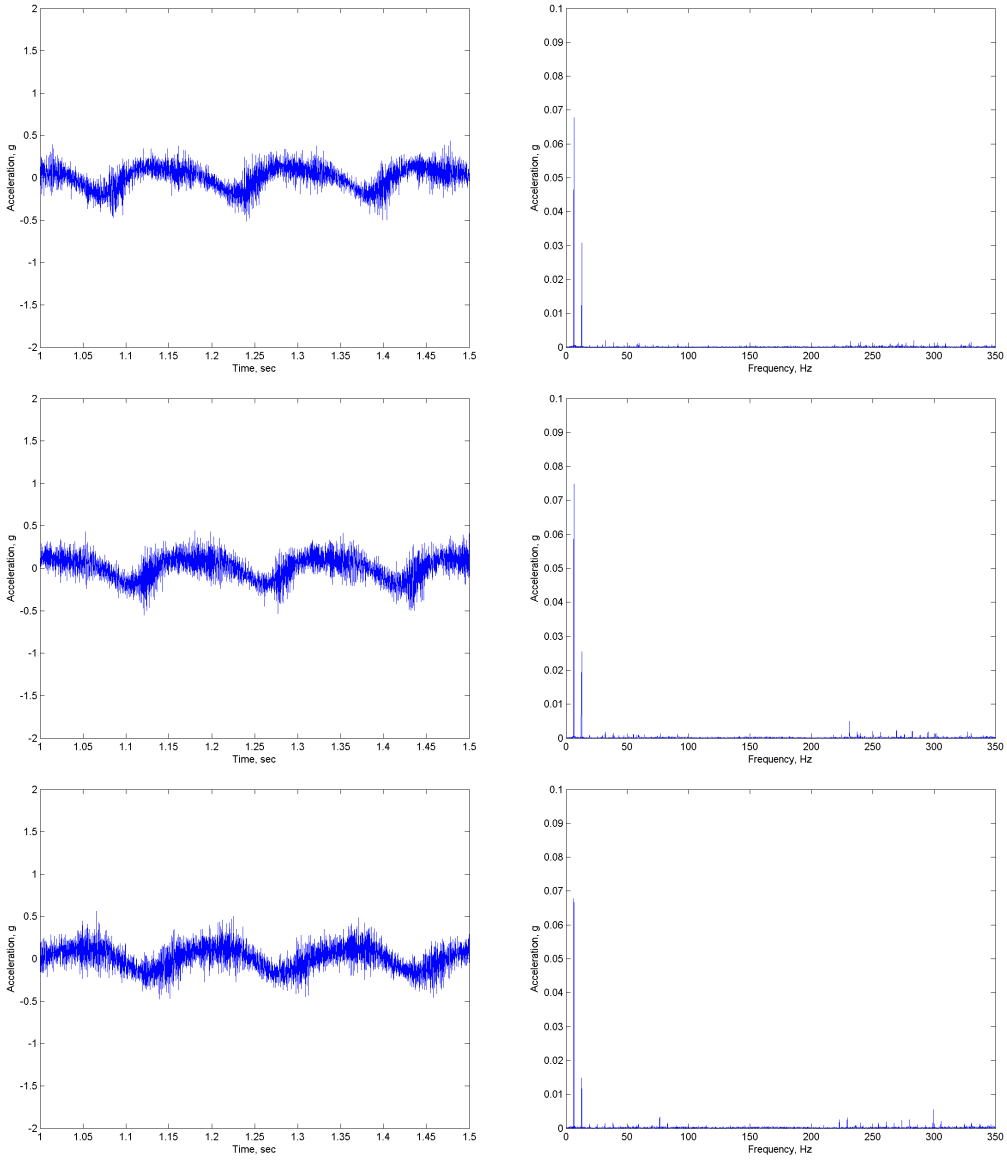

(a) Time Domain (b) Frequency Domain

Figure 5.78: Z direction frame vibration for the bearing with SAE50 oil (Top: 0% Load, Middle: 50% Load, Bottom: 100% Load)

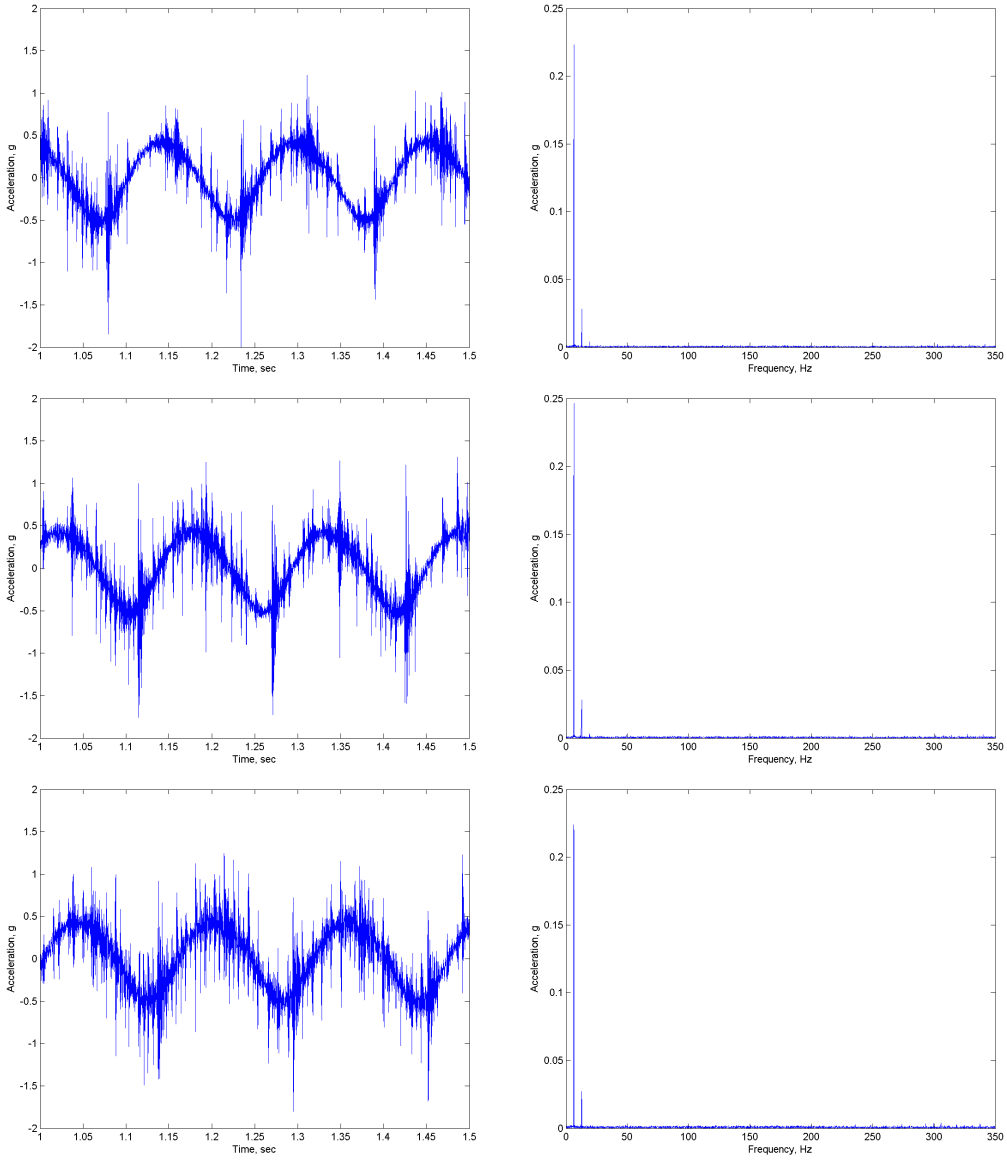

(a) Time Domain (b) Frequency Domain

Figure 5.79: X direction crankcase vibration for the bearing with SAE50 oil (Top: 0% Load, Middle: 50% Load, Bottom: 100% Load)

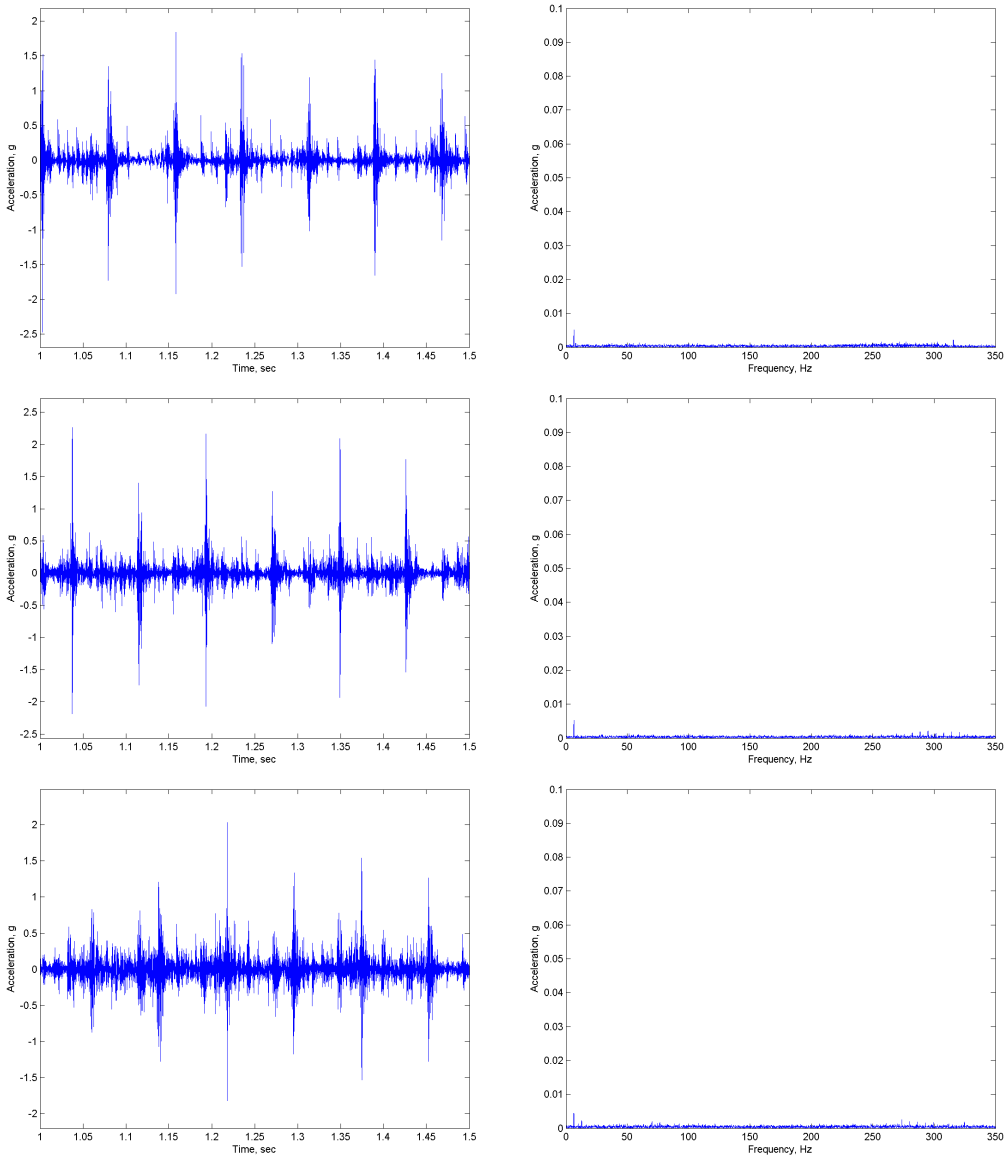

(a) Time Domain (b) Frequency Domain

Figure 5.80: Z direction crosshead vibration for the bearing with SAE50 oil (Top: 0% Load, Middle: 50% Load, Bottom: 100% Load)

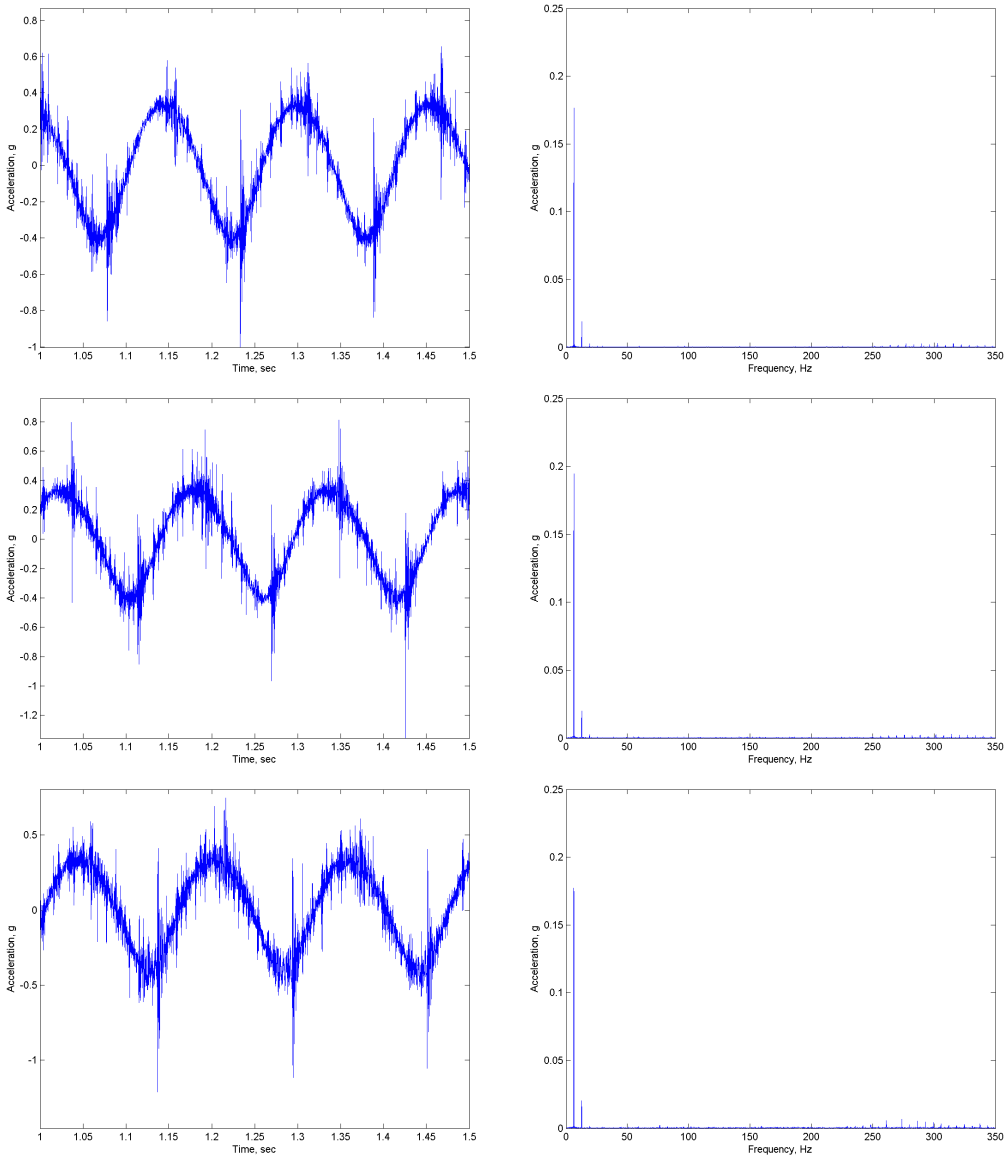

(a) Time Domain (b) Frequency Domain

Figure 5.81: Bearing housing vibration for the bearing with SAE50 oil (Top: 0% Load, Middle: 50% Load, Bottom: 100% Load)

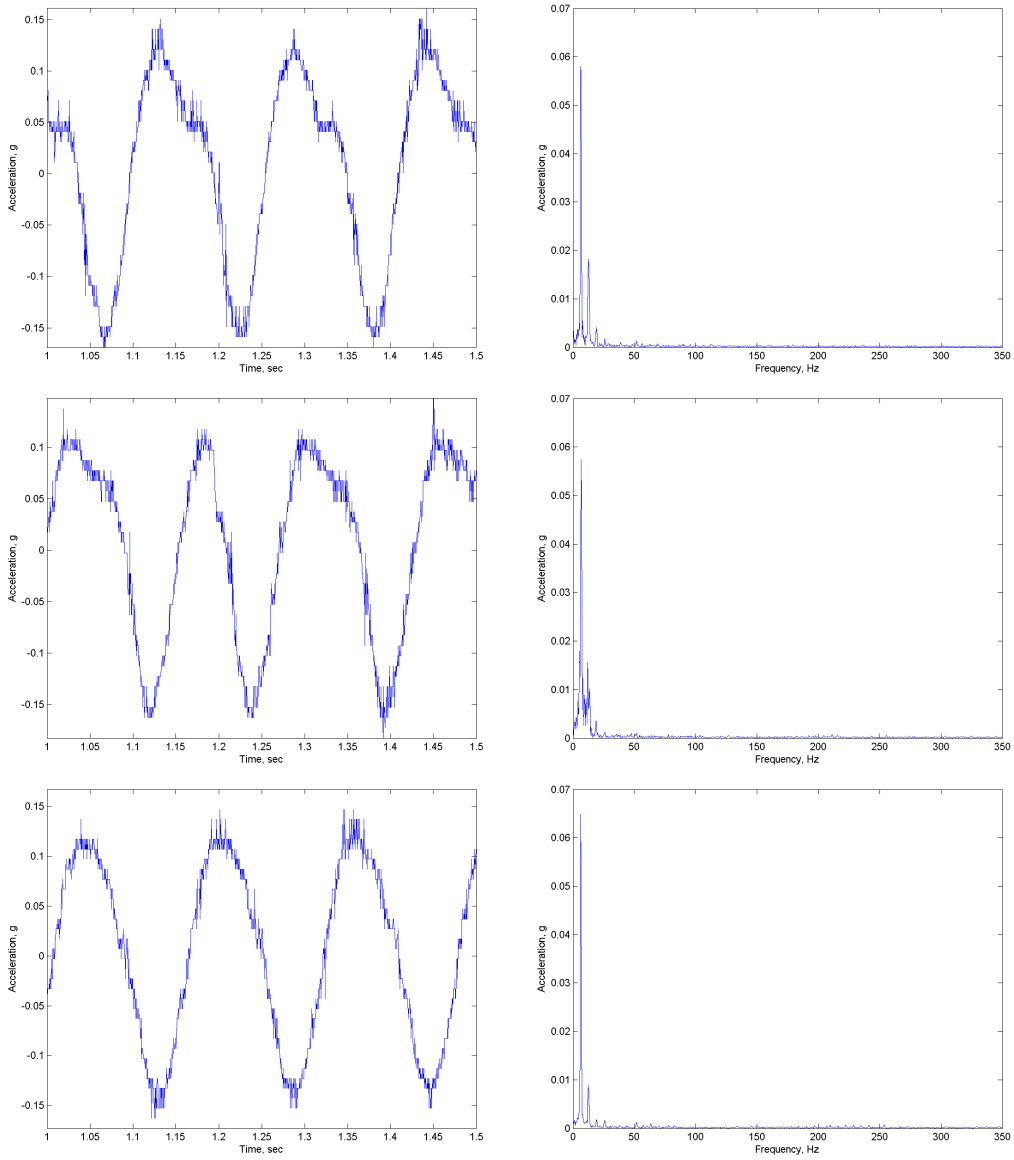

(a) Time Domain (b) Frequency Domain

Figure 5.82: Crankshaft vibration for the bearing with SAE50 oil (Top: 0% Load, Middle: 50% Load, Bottom: 100% Load)

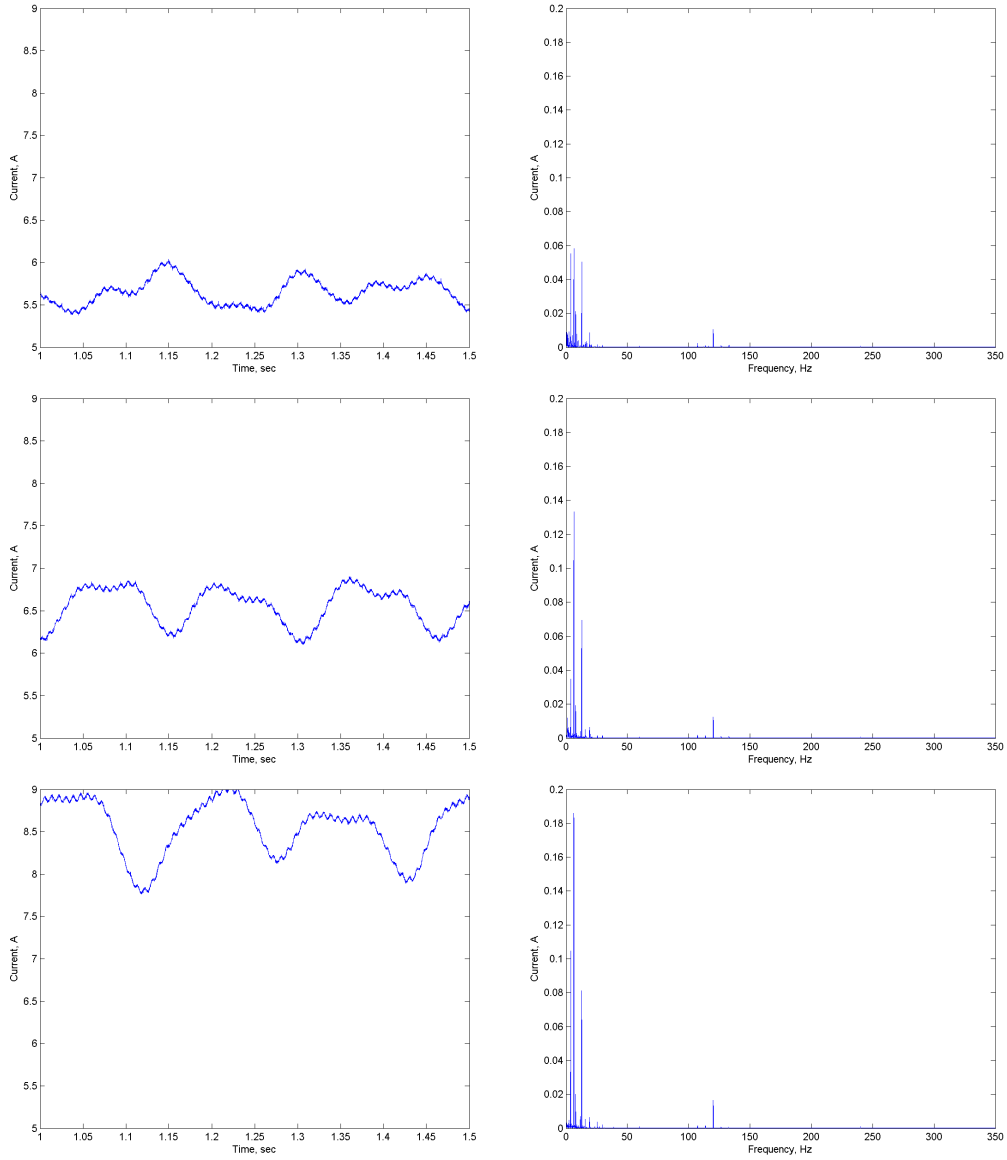

(a) Time Domain (b) Frequency Domain

Figure 5.83: Current draw for the bearing with SAE50 oil (Top: 0% Load, Middle: 50% Load, Bottom: 100% Load)

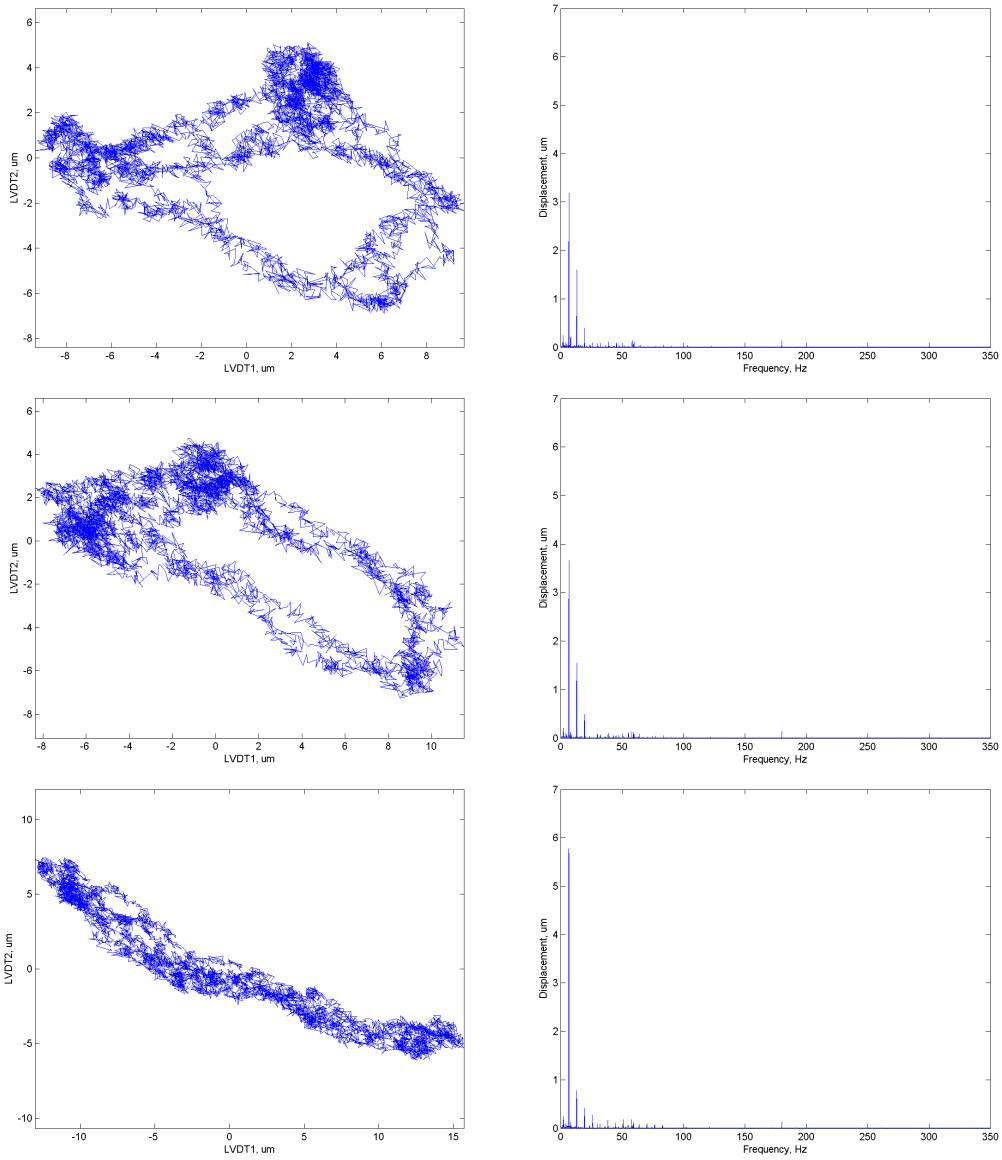

(a) Time Domain (b) Frequency Domain

Figure 5.84: Crankshaft orbit and LVDT FFT for the bearing with SAE50 oil (Top: 0% Load, Middle: 50% Load, Bottom: 100% Load)

SAE10 Oil

The results here Fig. 5.85 through 5.92) are very similar to the other two oil conditions, SAE50 and healthy. However, the orbit plot shows slightly larger values which is expected with the thinner oil.

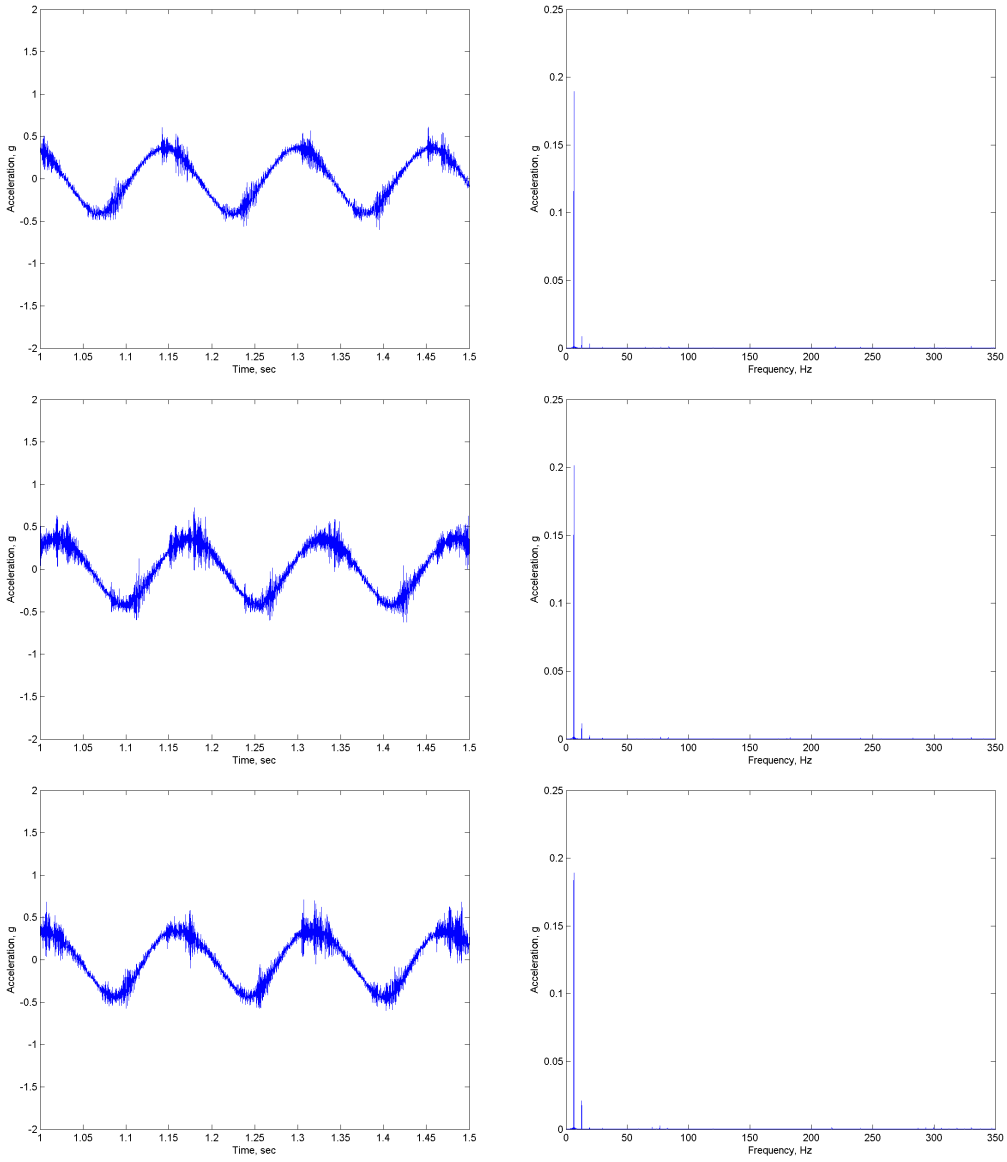

(a) Time Domain (b) Frequency Domain

Figure 5.85: X direction frame vibration for the bearing with SAE10 oil (Top: 0% Load, Middle: 50% Load, Bottom: 100% Load)

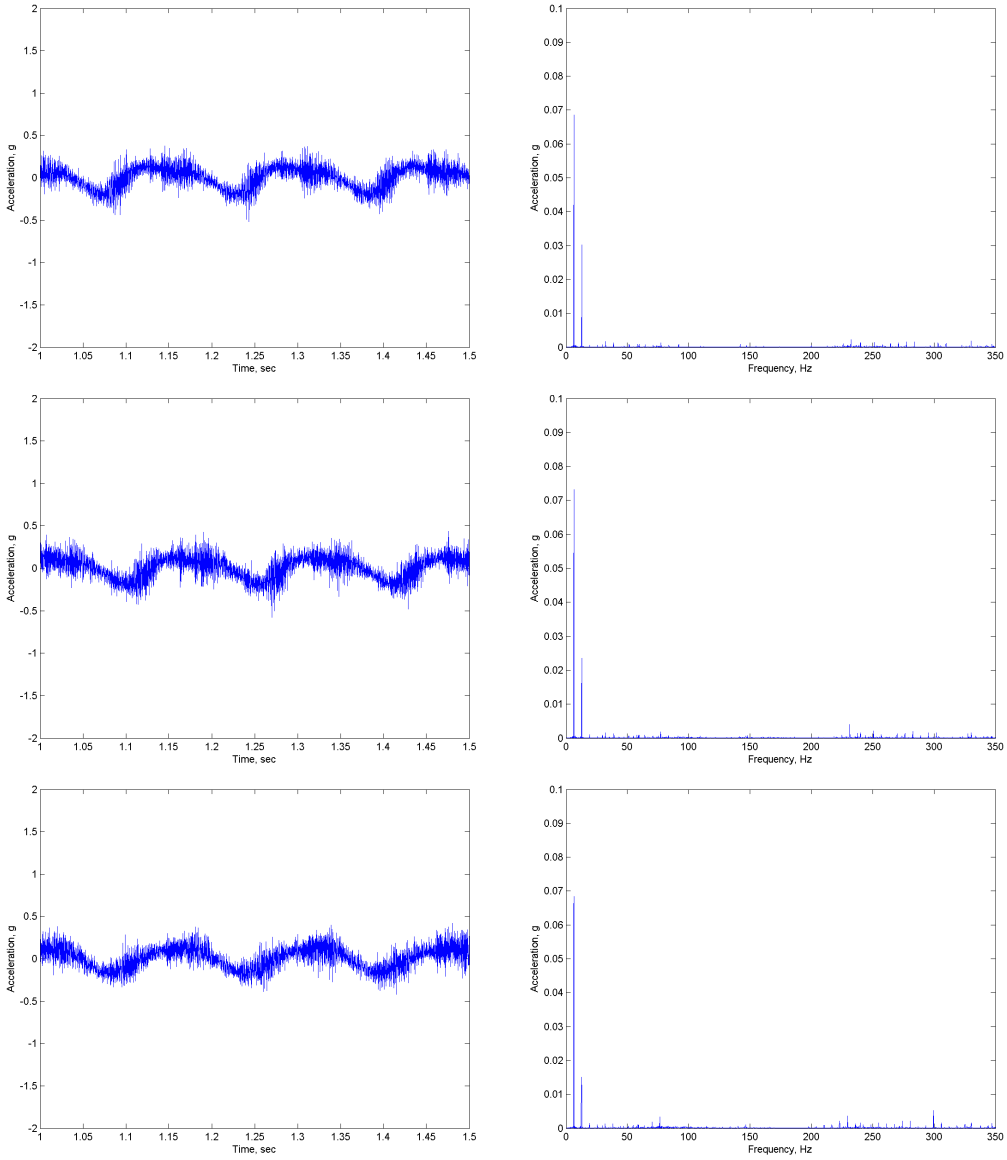

(a) Time Domain (b) Frequency Domain

Figure 5.86: Z direction frame vibration for the bearing with SAE10 oil (Top: 0% Load, Middle: 50% Load, Bottom: 100% Load)

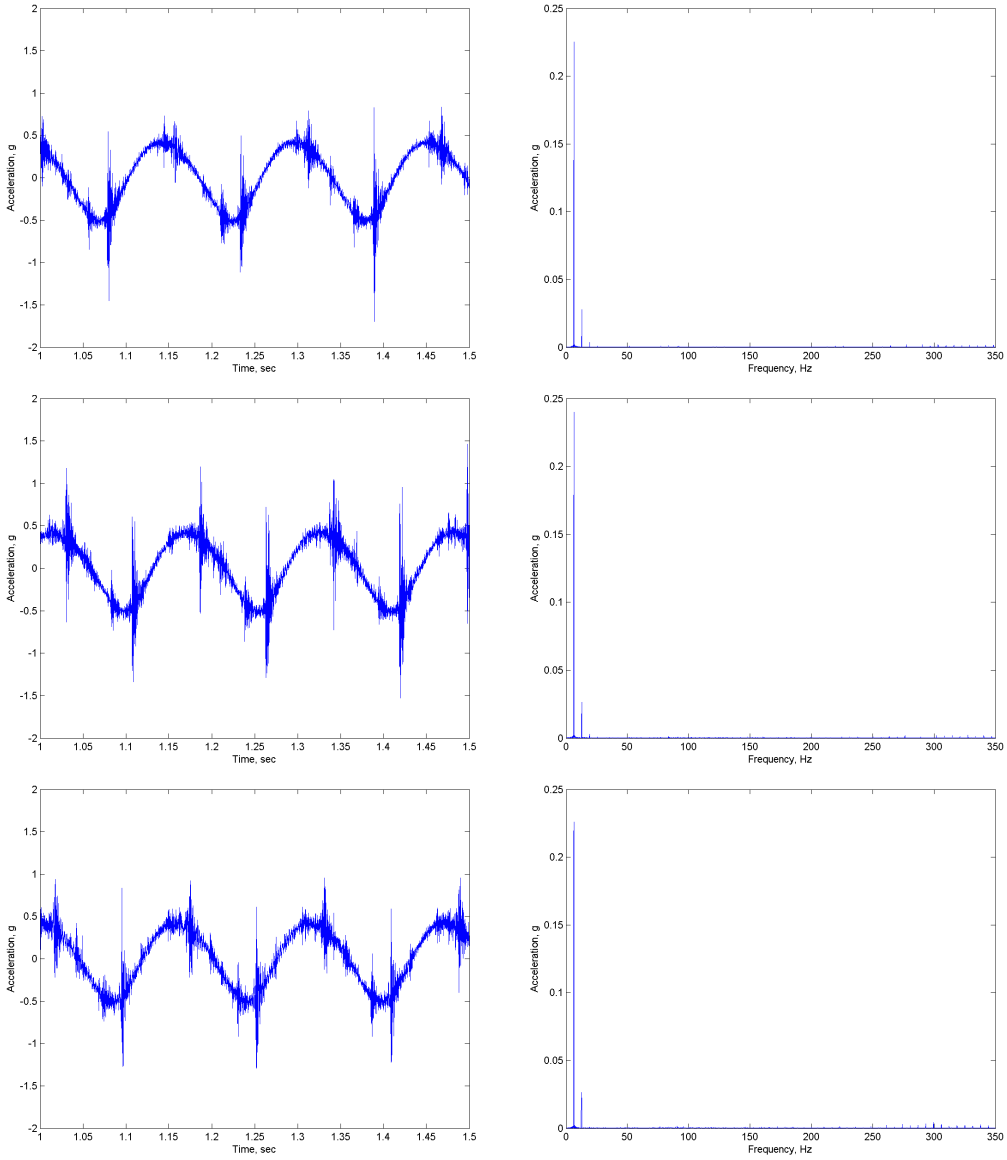

(a) Time Domain (b) Frequency Domain

Figure 5.87: X direction crankcase vibration for the bearing with SAE10 oil (Top: 0% Load, Middle: 50% Load, Bottom: 100% Load)

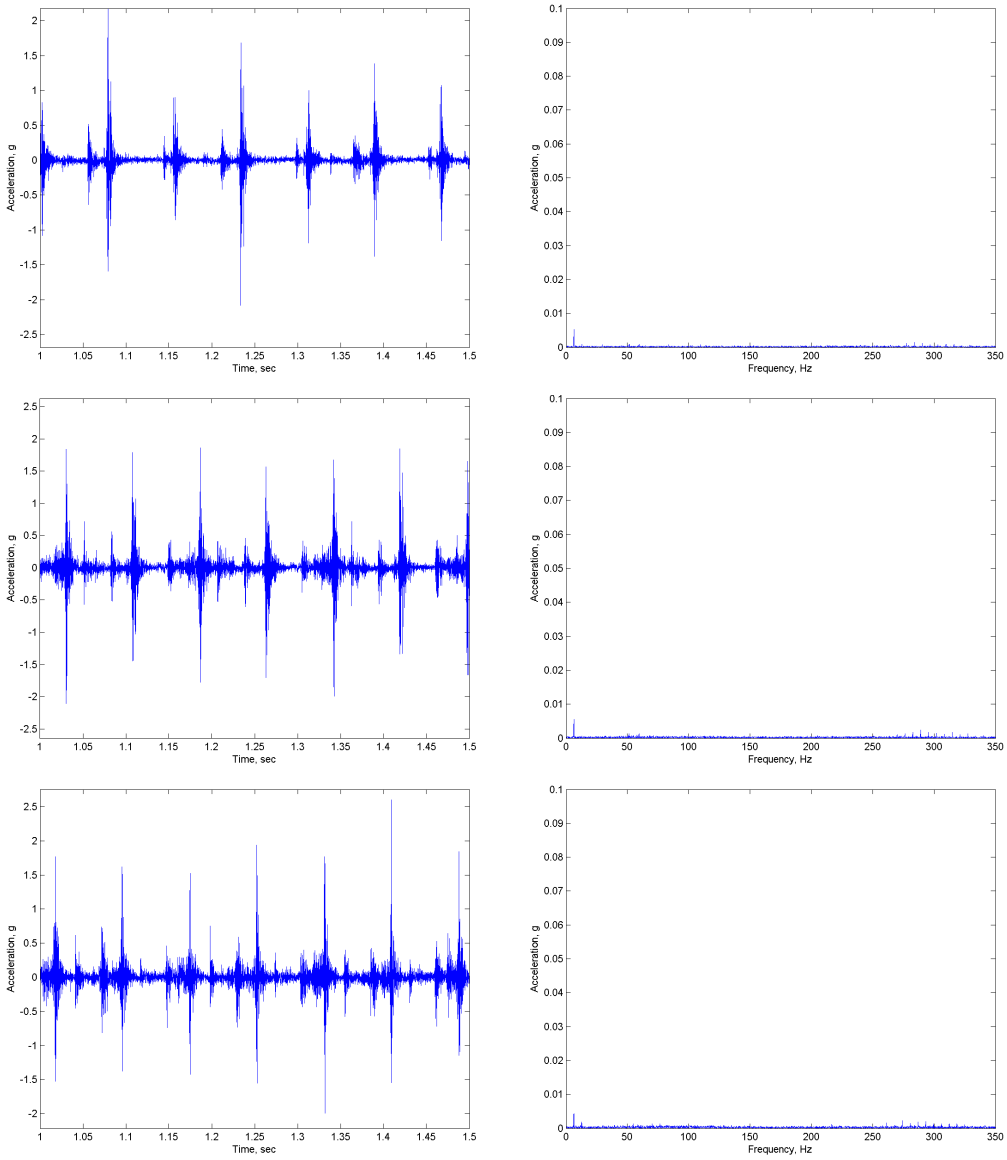

(a) Time Domain (b) Frequency Domain

Figure 5.88: Z direction crosshead vibration for the bearing with SAE10 oil (Top: 0% Load, Middle: 50% Load, Bottom: 100% Load)

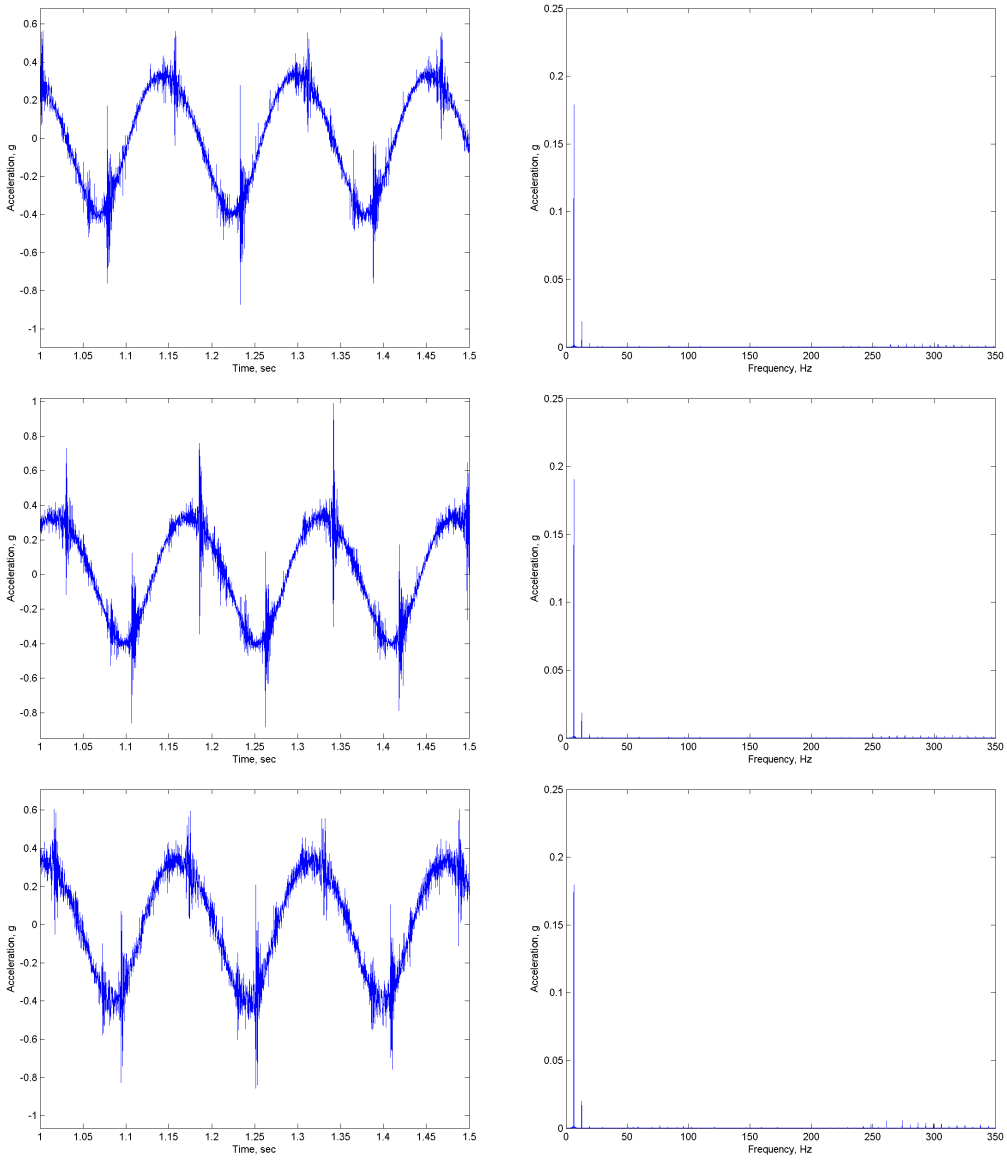

(a) Time Domain (b) Frequency Domain

Figure 5.89: Bearing housing vibration for the bearing with SAE10 oil (Top: 0% Load, Middle: 50% Load, Bottom: 100% Load)

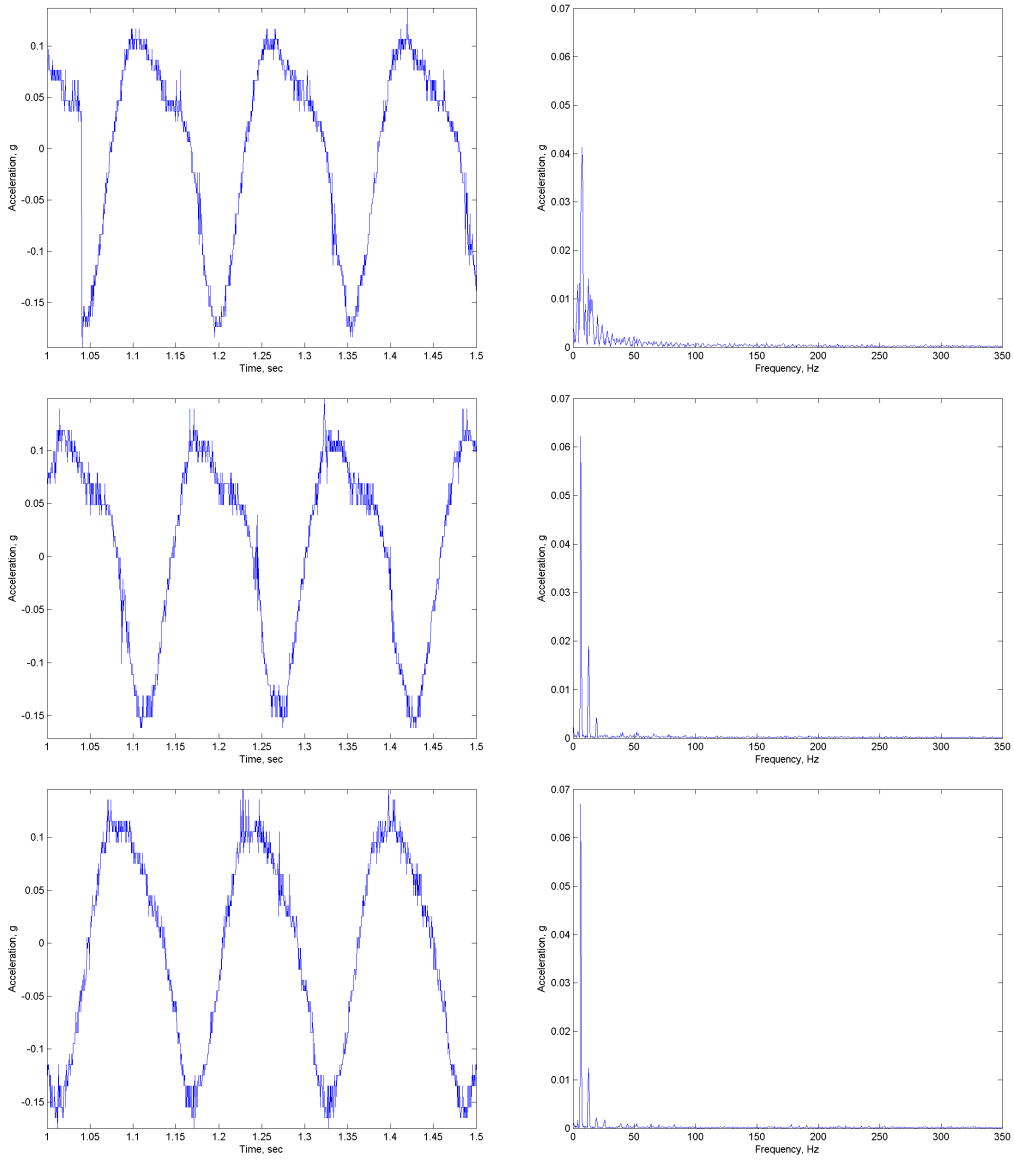

(a) Time Domain (b) Frequency Domain

Figure 5.90: Crankshaft vibration for the bearing with SAE10 oil (Top: 0% Load, Middle: 50% Load, Bottom: 100% Load)

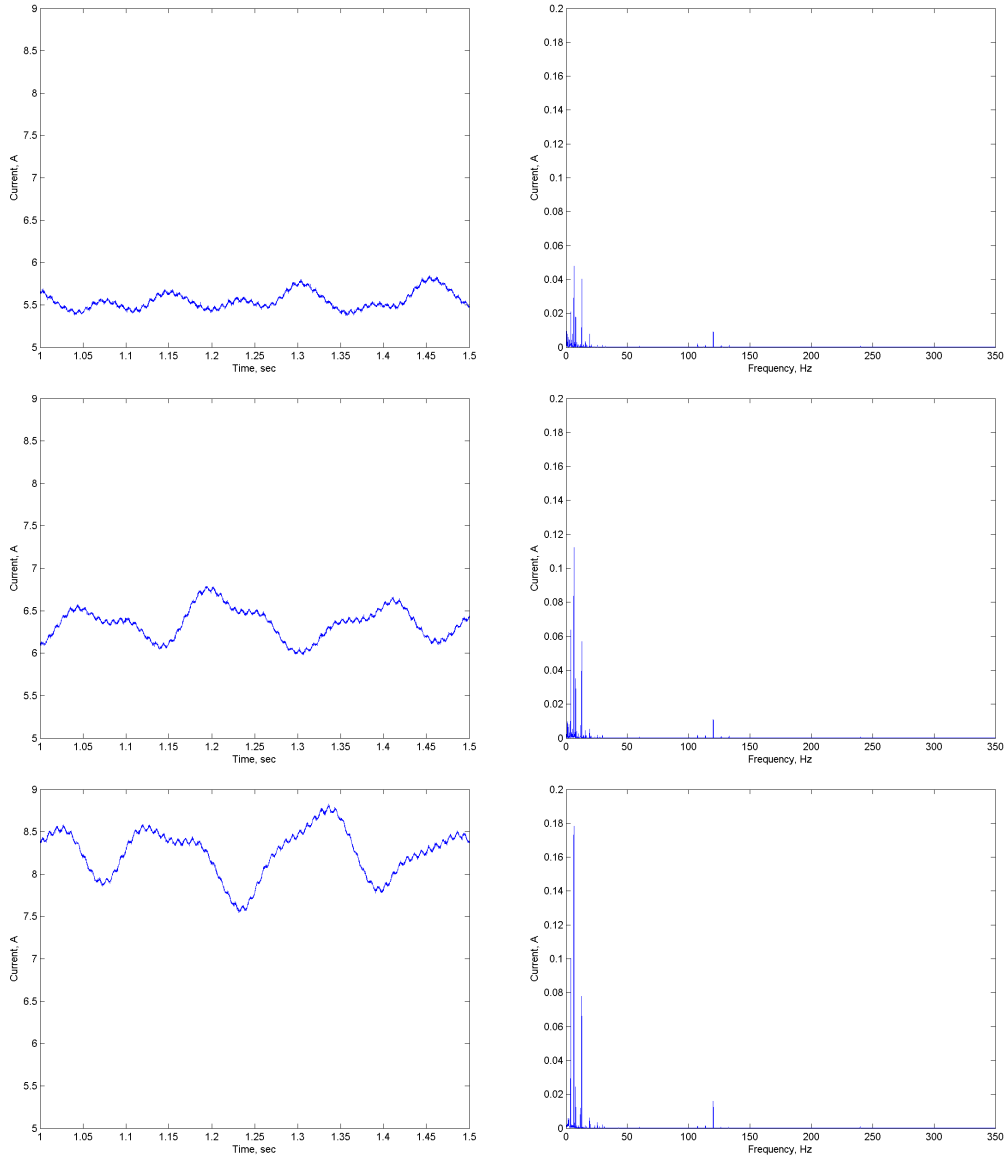

(a) Time Domain (b) Frequency Domain

Figure 5.91: Current draw for the bearing with SAE10 oil (Top: 0% Load, Middle: 50% Load, Bottom: 100% Load)

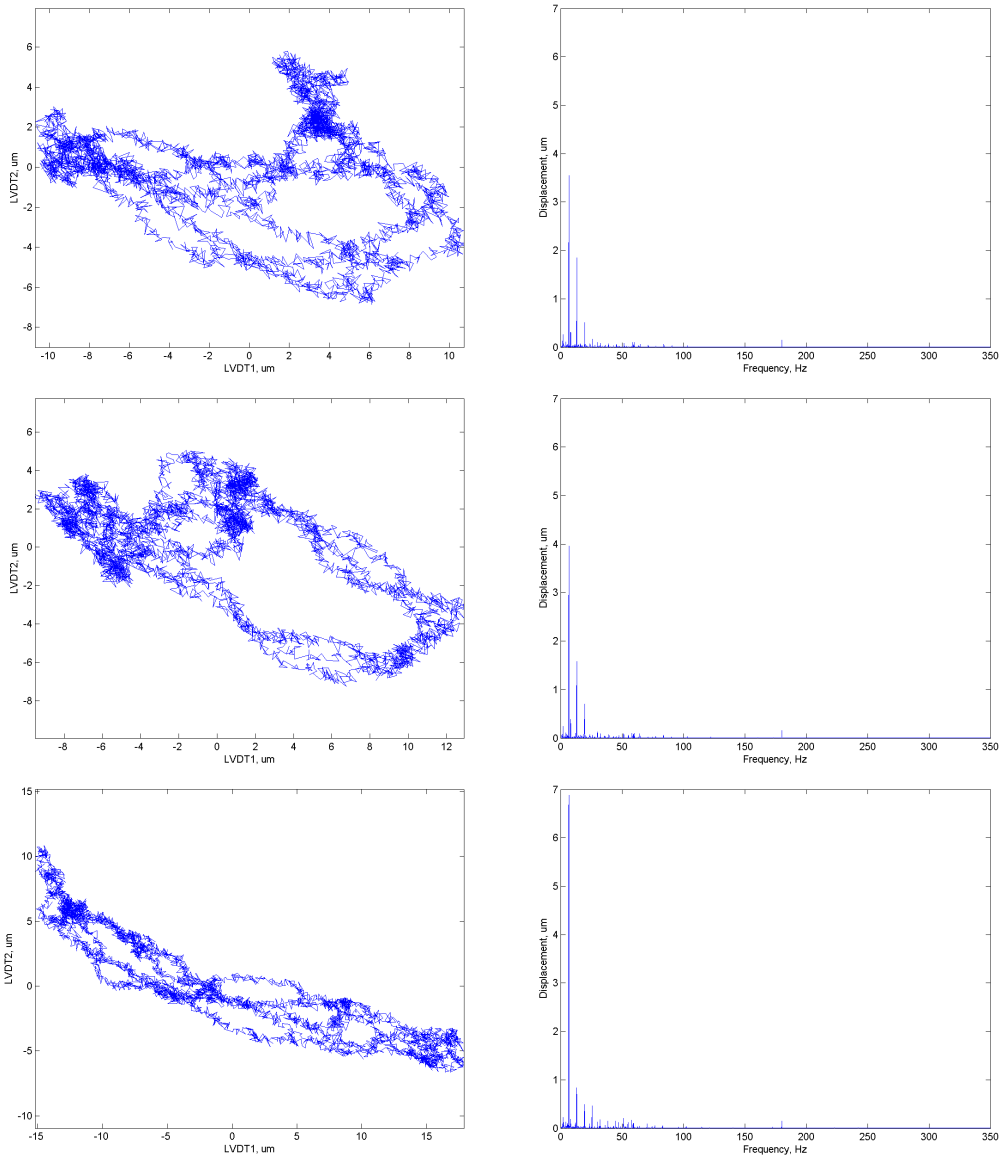

(a) Time Domain (b) Frequency Domain

Figure 5.92: Crankshaft orbit and LVDT FFT for the bearing with SAE10 oil (Top: 0% Load, Middle: 50% Load, Bottom: 100% Load)

Chapter 6

Classification Results

As part of running the compressor to steady state condition, temperature measurements of the main bearings are taken. Previous research found that temperature is not a good indicator of bearing health until just before critical failure. This is confirmed by the data taken in these experiments as all conditions show a very similar temperature profile as shown by figure 6.1. The continued small rise in temperature even after an hour of runtime cab be explained by the ambient temperature in the test cell rising.

Each fault type is analysed individually to understand the performance of different sensors for different fault types. As mentioned before, two severities of the same type are tested to investigate when the classifier started to be effective in detecting a fault. In order to test the classifier, each feature set of 50 points is split randomly into a training set of 30 points and a validation set of 20 points. The classifier performance can then be determined by comparing the assigned labels after classification to the labels prior to classification. The result is given as a range from 0 (perfect classification) to 1 (every point is misclassified). For a detailed description of the method applied to each dataset see chapter 3.

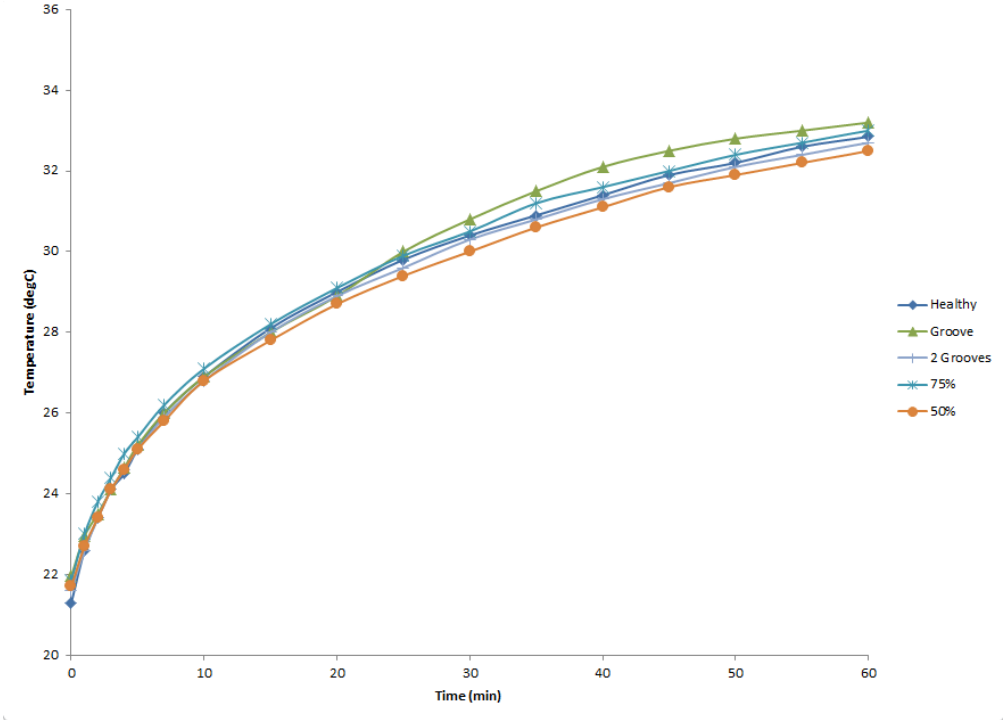

Figure 6.1: Main bearing temperature from start to steady state

6.1 Clearance Variation

In order to understand the effect of clearance variation between different bearings, the original bearing is compared to two new bearings with slightly different clearances. Table 6.1 shows the specifications of each bearing. The classification results are shown in table 6.2 and figures 6.2 through 6.4.

Legend Entry	Healthy	New 1	New 2
Inner Radial Clearance (mm)	0.035	0.010	0.005
Outer Radial Clearance (mm)	0.031	0.013	0.020
Oil Type	SAE30	SAE30	SAE30

Table 6.1: Case study details for the new bearing

Sensor	Load	T1	T2	T3	T4	T5	Avg
Bearing Housing Vibration	0	0.150	0.167	0.100	0.150	0.100	0.133
	50	0.233	0.233	0.217	0.283	0.217	0.237
	100	0.067	0.133	0.067	0.033	0.083	0.077
LVDT	0	0.000	0.000	0.000	0.000	0.000	0.000
	50	0.000	0.000	0.000	0.000	0.000	0.000
	100	0.000	0.000	0.000	0.000	0.000	0.000
Wireless Accelerometer	0	0.517	0.483	0.567	0.350	0.600	0.503
	50	0.617	0.567	0.550	0.500	0.550	0.557
	100	0.567	0.583	0.550	0.667	0.600	0.593

Table 6.2: Classifier performance for the new bearing given various sensors and loading conditions

The bearing housing accelerometer separates the different bearings into individual clouds and the classifier returns good results. The small axis scale indicates that the vibrations from the different bearings are very similar in nature. With increasing loading condition the separation between the points increases as seen by the axis scales.

The LVDT has a perfect classification results. This can be expected as clearance has the most significant impact on journal orbit. The experimental results shows similar trends to the simulated results. The agreement is especially good in the case of a 100% loading. The larger clearance bearing has the larger absolute value for feature one compared to the smaller clearance bearing. This agrees with the larger orbit associated with the larger clearance.

The wireless accelerometer can not classify different bearing clearances indicating that different clearances do not affect the crankshaft. Overall, these results are very similar to the different oil viscosities also tested. This is expected as different viscosities have a similar impact on bearing orbit as clearance.

As clearance has such an impact on the classification, the following case studies are performed comparing bearings with identical or similar clearance. This ensures the classification is due to the seeded fault and not just due to a variance in the clearance.

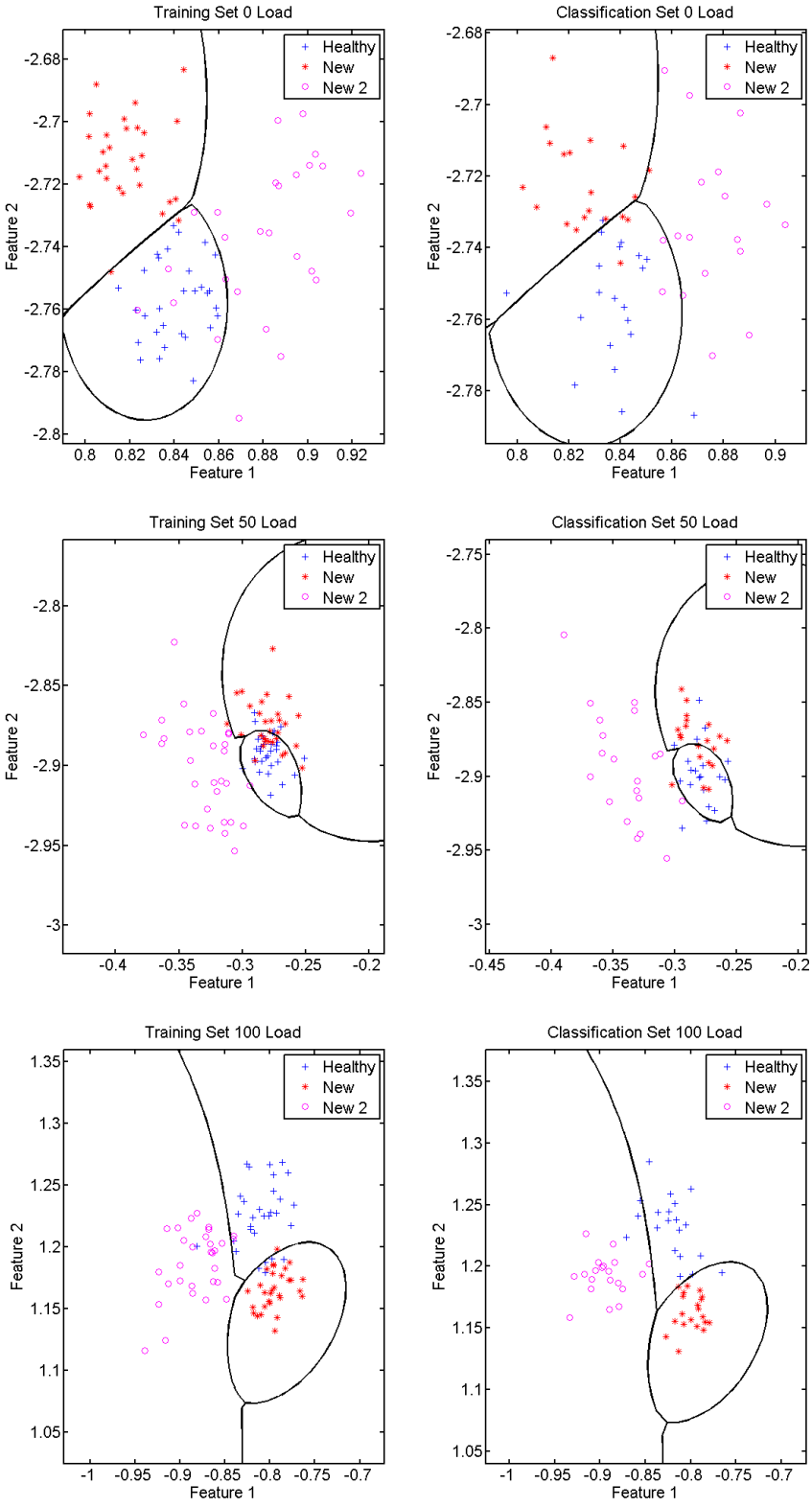

Figure 6.2: Classification training and validation sets for the new bearing from the bearing housing accelerometer (Top: 0% Load, Middle: 50% Load, Bottom: 100% Load)

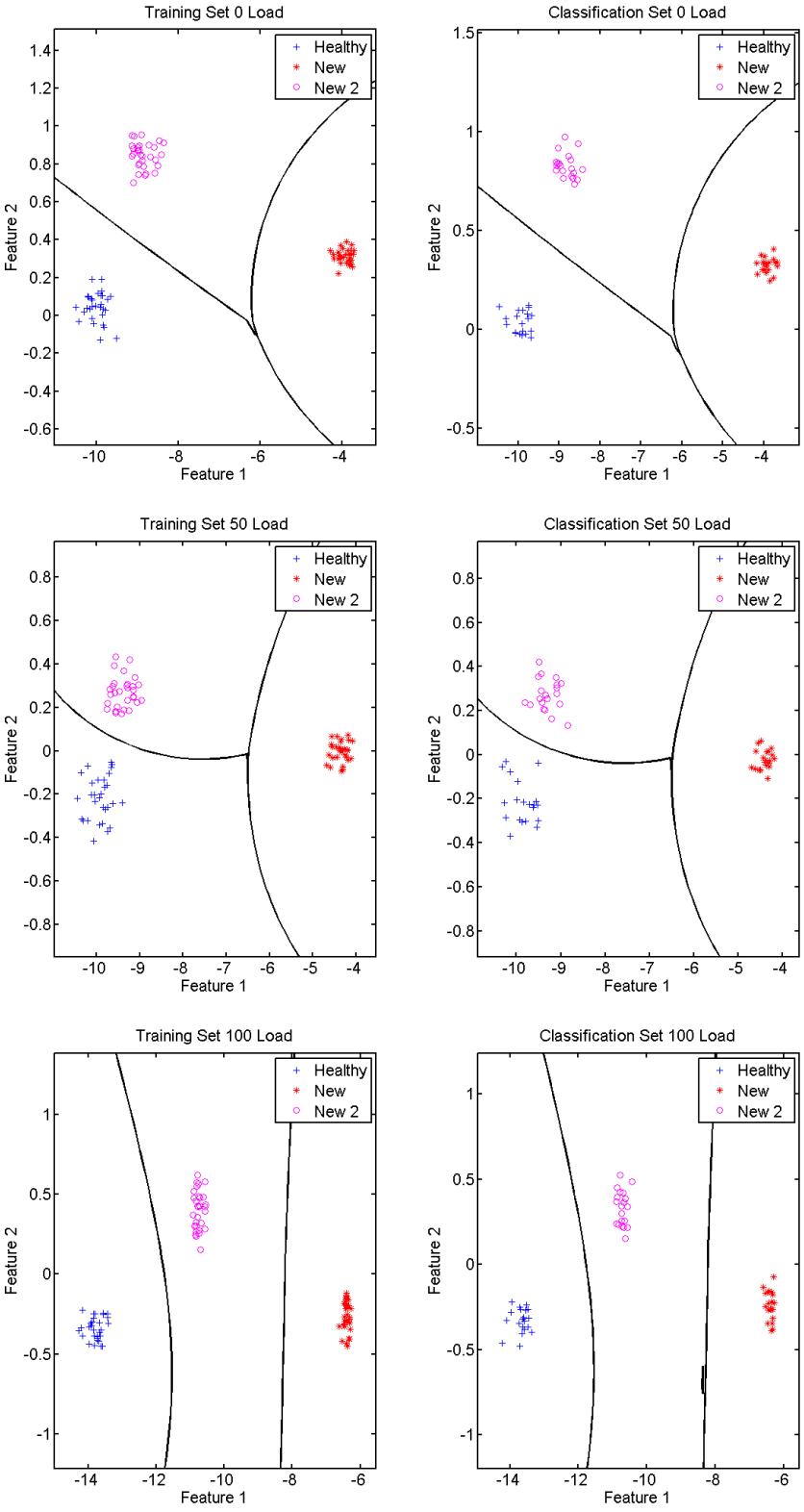

Figure 6.3: Classification training and validation sets for the new bearing from the LVDT (Top: 0% Load, Middle: 50% Load, Bottom: 100% Load)

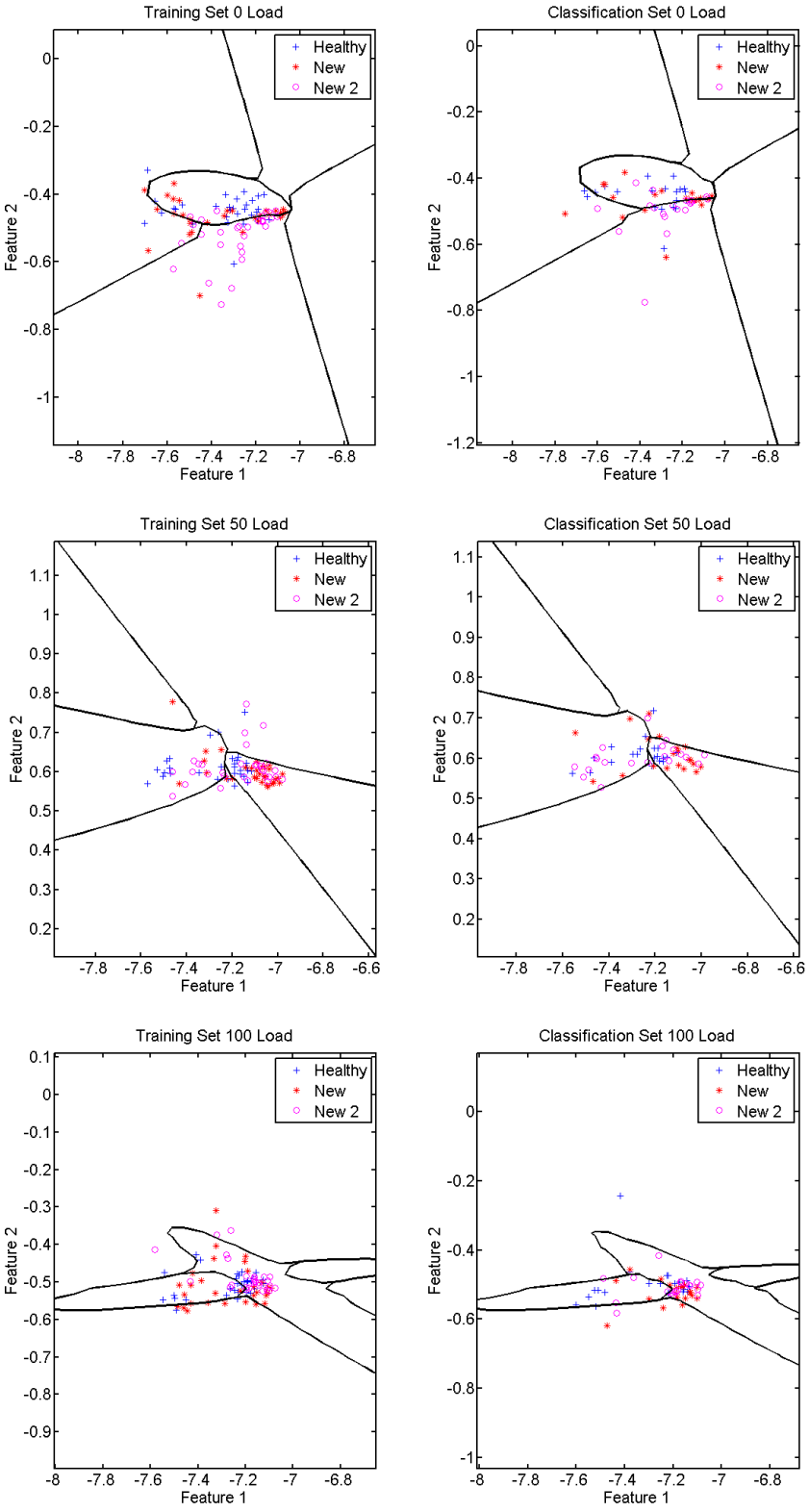

Figure 6.4: Classification training and validation sets for the new bearing from the wireless accelerometer (Top: 0% Load, Middle: 50% Load, Bottom: 100% Load)

6.2 Grooved Bearing

Table 6.3 shows the bearing details for the grooved bearing fault. Figures 6.5 through 6.8 show the results of classification for the groove failure mode. Both a single groove and double grooves are classified. The results from several sensors are shown with a quantitative comparison in table 6.4.

Legend Entry	Healthy	1 Groove	2 Grooves
Inner Radial Clearance (mm)	0.010	0.012	0.012
Outer Radial Clearance (mm)	0.013	0.017	0.017
Oil Type	SAE30	SAE30	SAE30

Table 6.3: Case study details for grooved bearing seeded fault

Sensor	Load	T1	T2	T3	T4	T5	Avg
Bearing Housing Vibration	0	0.150	0.233	0.217	0.200	0.233	0.207
	50	0.150	0.183	0.200	0.233	0.183	0.190
	100	0.233	0.200	0.150	0.217	0.217	0.203
LVDT	0	0.000	0.000	0.000	0.000	0.000	0.000
	50	0.000	0.000	0.000	0.000	0.000	0.000
	100	0.000	0.000	0.000	0.000	0.000	0.000
Wireless Accelerometer	0	0.267	0.200	0.250	0.200	0.250	0.233
	50	0.300	0.367	0.267	0.217	0.283	0.287
	100	0.167	0.233	0.300	0.233	0.267	0.240

Table 6.4: Classifier performance for the grooved bearing given various sensors and loading conditions

Figures 6.5 shows the results based on the bearing housing vibration sensor. The single groove bearing is very well separated from the healthy case. The bearing with two grooves is harder to classify. Figure 6.6 shows how closely the double grooved bearing matches the healthy bearing. Even though the displayed decision boundaries look different, both plots use the same classifier. The difference in display is a plotting issue from the small axis scale. It also shows that the all misclassification is between the healthy bearing and the bearing with two grooves. The bearing with a single groove is detected correctly in every case.

Figures 6.7 shows the results from the LVDT. One can see much better separation between the results. This classifier returns 0% error for this fault type. The LVDT is much more sensitive to changes in motion compared to the accelerometers and can detect the small change from the bearing with two grooves.

Figures 6.8 shows the results from the wireless accelerometer installed on the crankshaft. The results show better separation compared to the bearing housing accelerometer. However, the overlap between healthy and single groove are enough so that the numerical performance is similar.

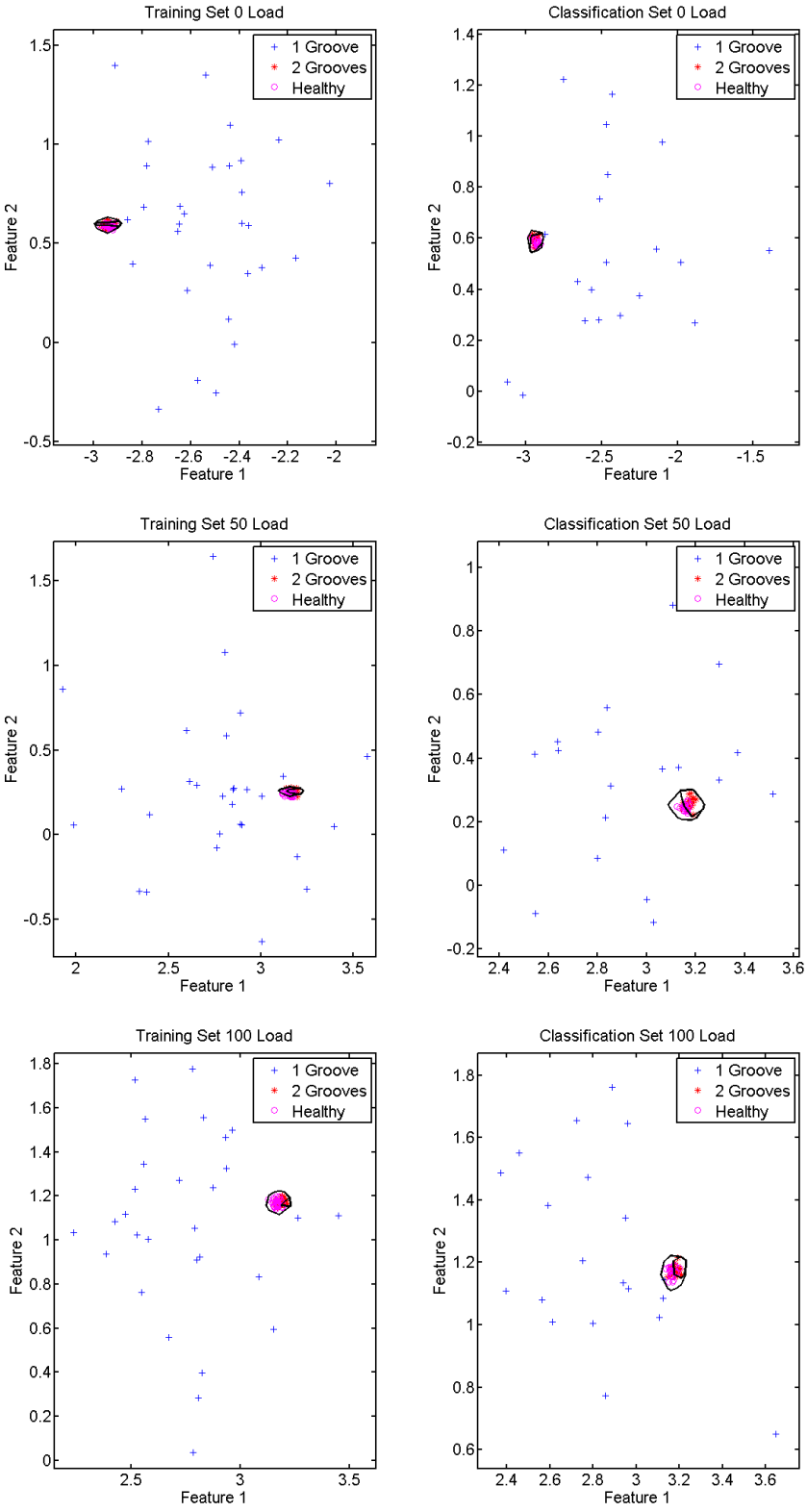

Figure 6.5: Classification training and validation sets for the grooved bearing from the bearing housing accelerometer (Top: 0% Load, Middle: 50% Load, Bottom: 100% Load)

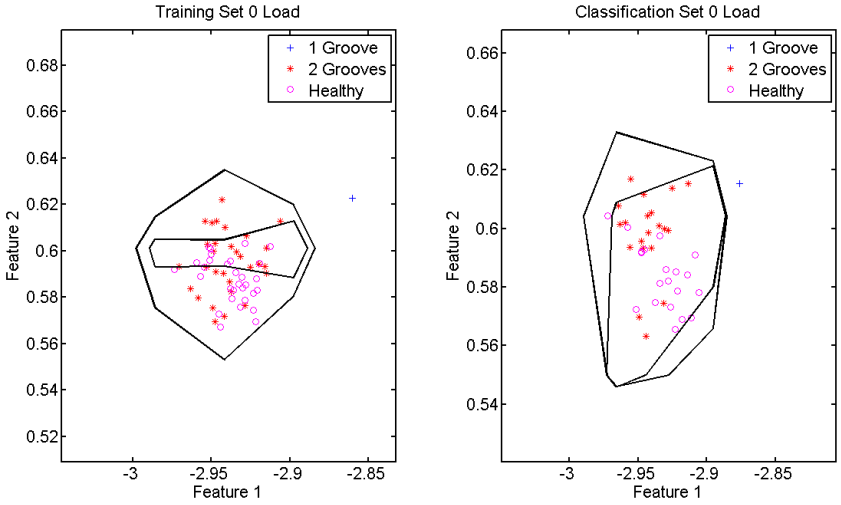

Figure 6.6: Enlarged view of the healthy and single grooved bearing features from the bearing housing accelerometer

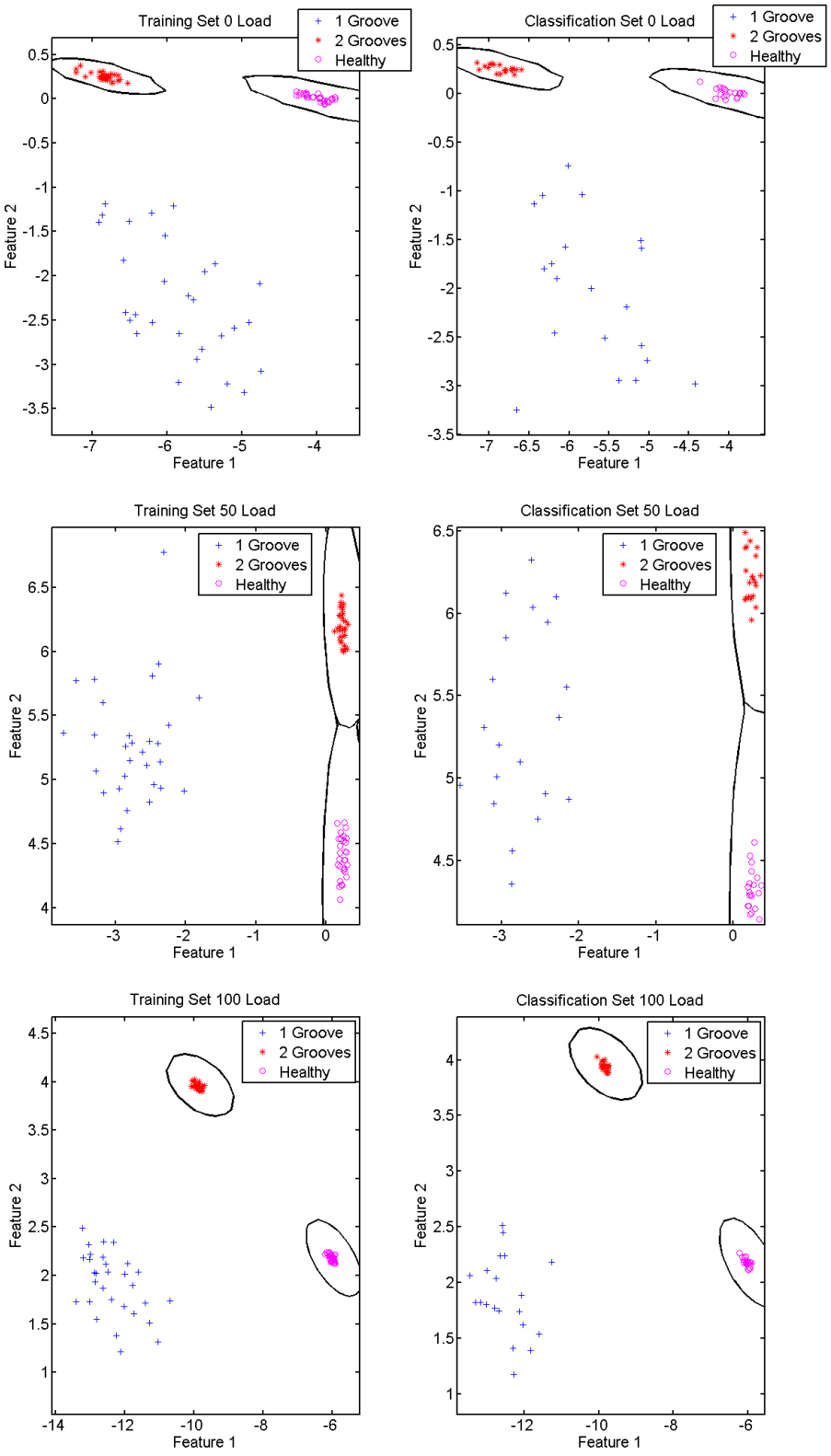

Figure 6.7: Classification training and validation sets for the grooved bearing from the LVDT (Top: 0% Load, Middle: 50% Load, Bottom: 100% Load)

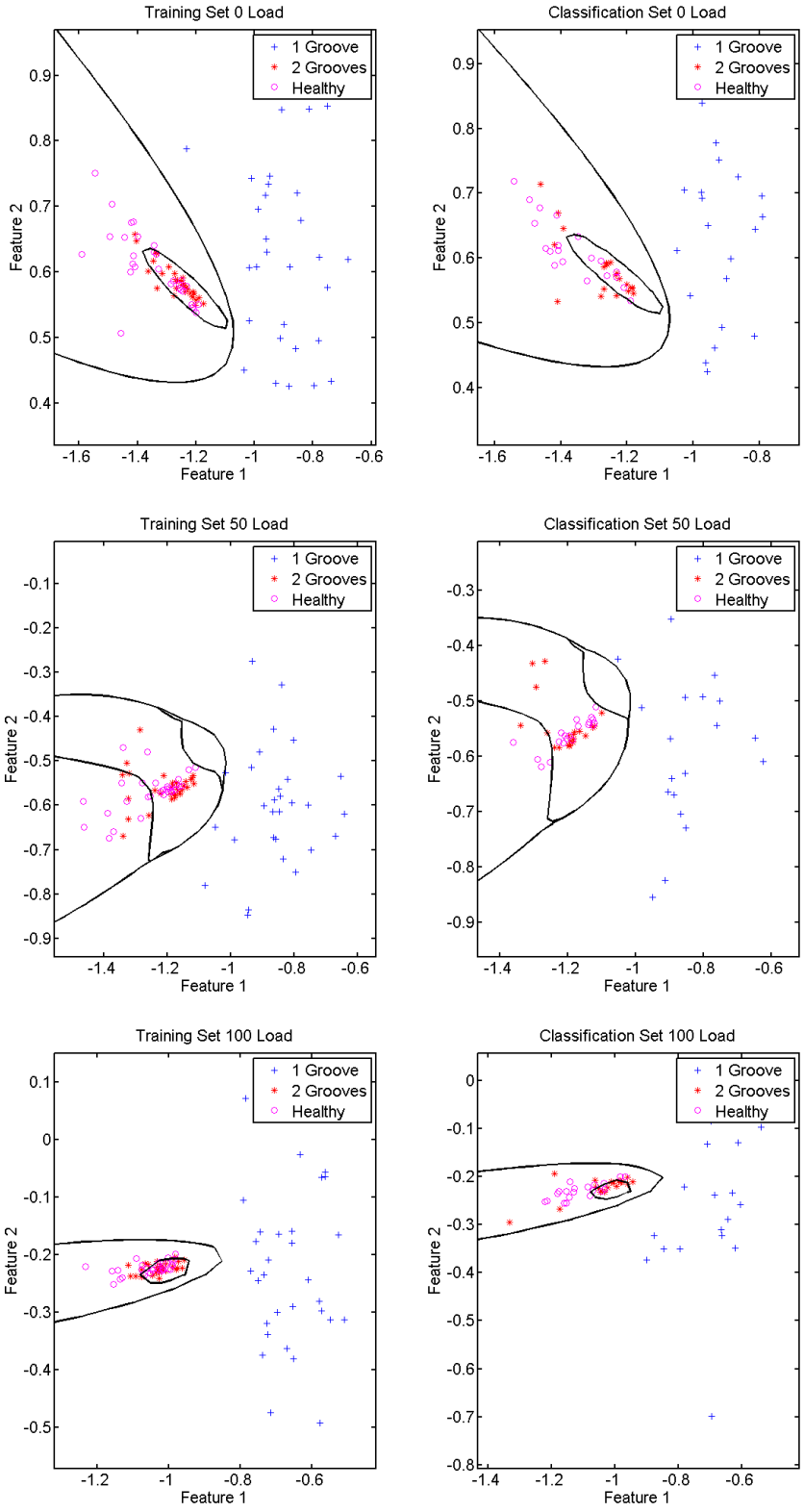

Figure 6.8: Classification training and validation sets for the grooved bearing from the wireless crankshaft accelerometer (Top: 0% Load, Middle: 50% Load, Bottom: 100% Load)

6.3 Obstructed Oil Holes

Table 6.5 shows the bearing details for the obstructed oil feed hole fault. Table 6.6 shows the classifier results for the bearing with obstructed oil feed holes. Again, the LVDT shows the best results with near perfect classification for all loading conditions.

Legend Entry	Healthy	Holes 50% Obstructed	Holes 75% Obstructed
Inner Radial Clearance (mm)	0.005	0.005	0.005
Outer Radial Clearance (mm)	0.020	0.020	0.020
Oil Type	SAE30	SAE30	SAE30

Table 6.5: Case study details for oil feed hole obstruction seeded fault

Sensor	Load	T1	T2	T3	T4	T5	Avg
Bearing Housing Accelerometer	0	0.317	0.300	0.267	0.400	0.367	0.330
	50	0.350	0.417	0.367	0.367	0.267	0.353
	100	0.217	0.183	0.167	0.150	0.167	0.177
LVDT	0	0.000	0.000	0.017	0.000	0.000	0.003
	50	0.000	0.000	0.000	0.000	0.000	0.000
	100	0.000	0.000	0.000	0.000	0.000	0.000
Wireless Accelerometer	0	0.317	0.500	0.317	0.283	0.300	0.343
	50	0.400	0.400	0.300	0.350	0.350	0.360
	100	0.317	0.300	0.333	0.317	0.267	0.267

Table 6.6: Classifier performance for the bearing with obstructed oil feed holes given various sensors and loading conditions

Figure 6.9 shows the decision boundaries for the bearing housing accelerometer. One can see that the more severe case of 75% obstruction is more easily identified. This is similar to the previous fault type of a grooved bearing.

Figure 6.10 shows the decision boundaries for the LVDT. It is easy to see the clear separation between different classes. It is interesting to note that for the all loading condition, the classes of healthy and 50% obstructed have a similar shape and spread. However, the spread of the 75% obstructed class is much larger.

The wireless accelerometer results (Fig. 6.11) are similar in nature to the bearing housing accelerometer. There is some misclassification between the two fault classes. Separation between healthy and faulty is good with only a few points data points in the wrong class.

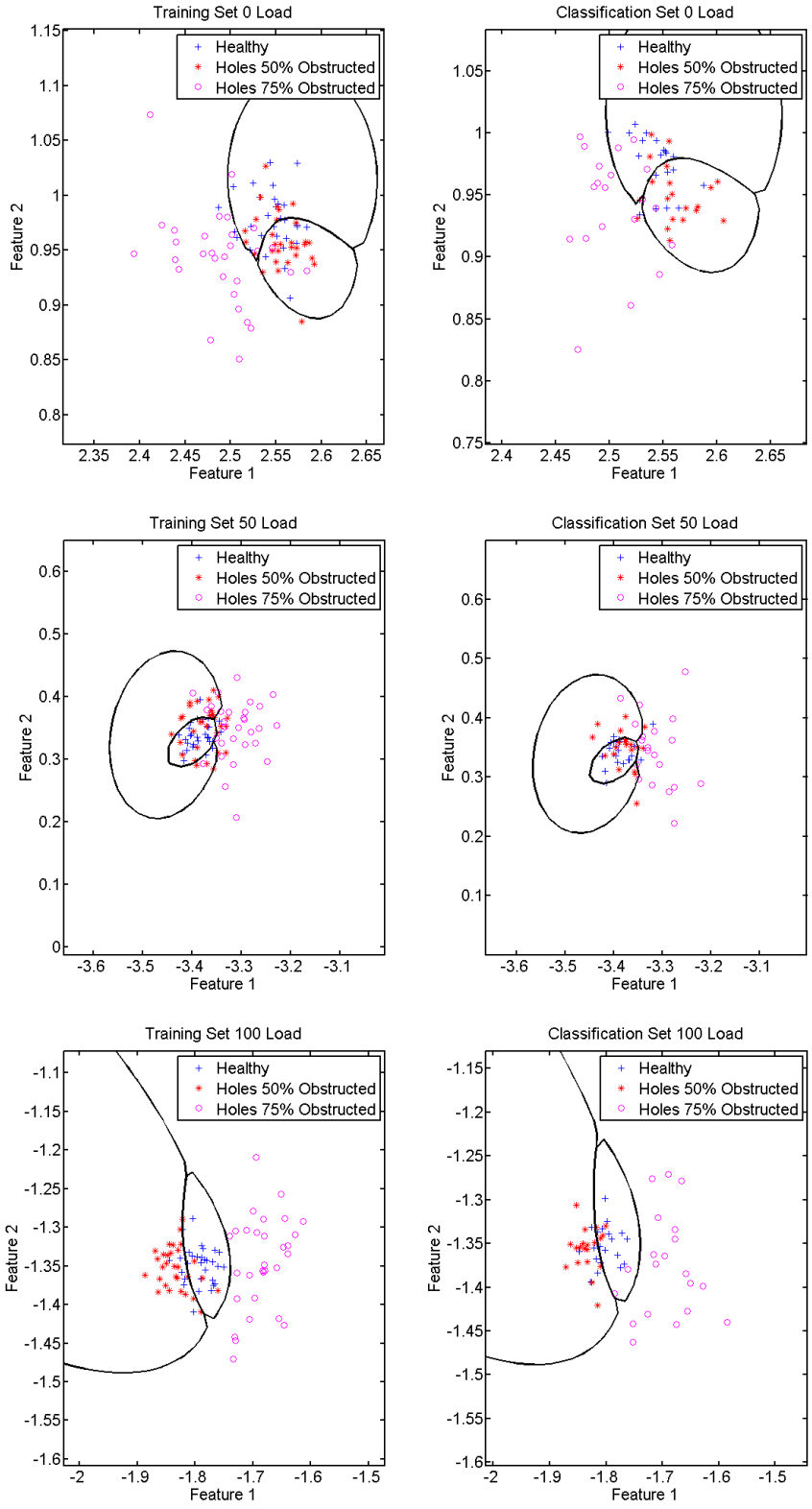

Figure 6.9: Classification training and validation sets for the bearing with obstructed oil feed holes from the bearing housing accelerometer (Top: 0% Load, Middle: 50% Load, Bottom: 100% Load)

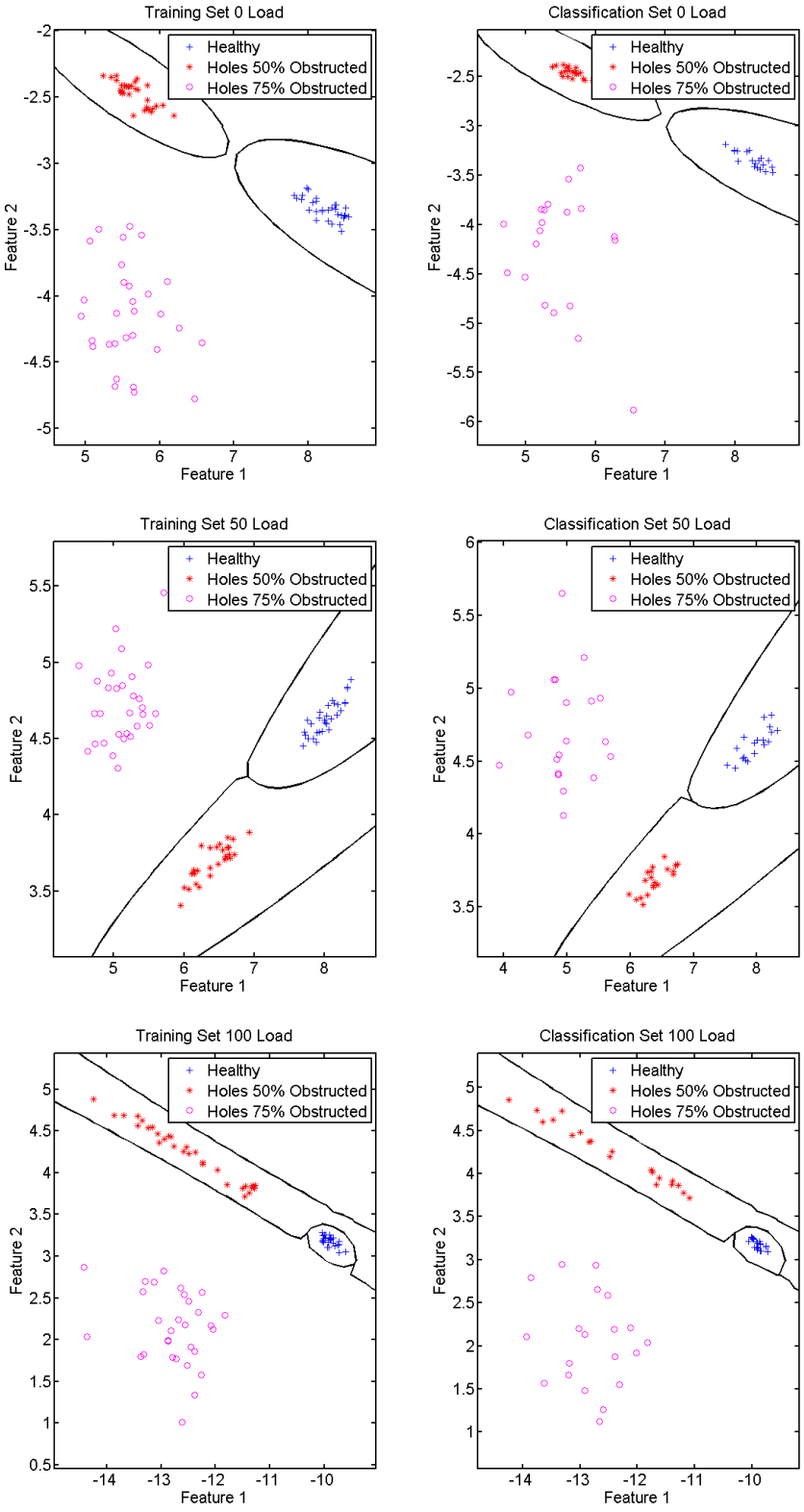

Figure 6.10: Classification training and validation sets for the bearing with obstructed oil feed holes from the bearing housing accelerometer (Top: 0% Load, Middle: 50% Load, Bottom: 100% Load)

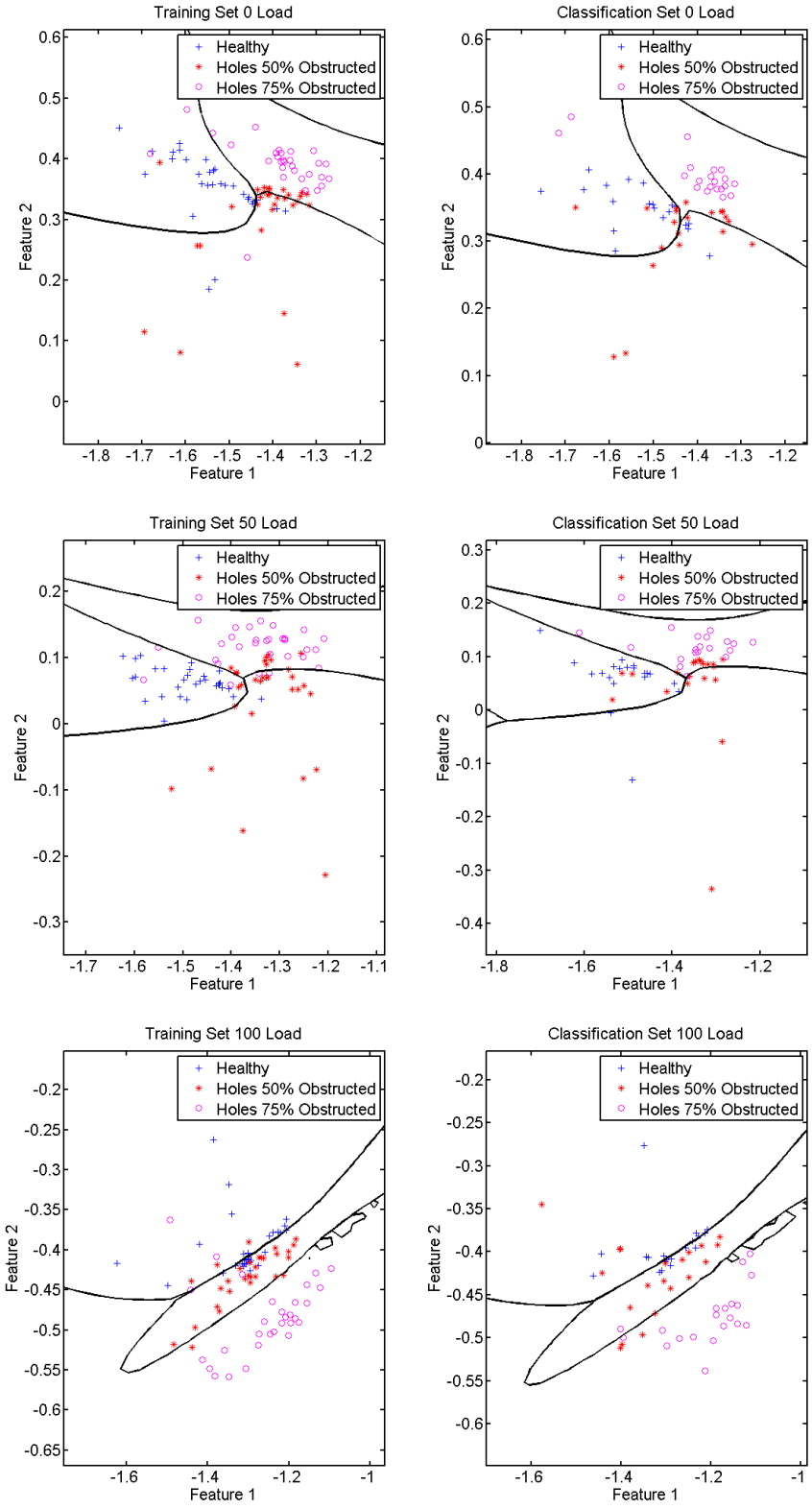

Figure 6.11: Classification training and validation sets for the bearing with obstructed oil feed holes from the wireless accelerometer (Top: 0% Load, Middle: 50% Load, Bottom: 100% Load)

6.4 Oil Viscosity Changes

Table 6.7 shows the bearing details for the viscosity change seeded fault. Table 6.6 shows the classifier results for different oil viscosities. Again, the LVDT shows the best results but not with the same accuracy as the other fault types. The bearing housing accelerometer gives similar results while the wireless accelerometer cannot distinguish between the viscosities.

Legend Entry	Healthy	SAE10	SAE50
Inner Radial Clearance (mm)	0.035	0.035	0.035
Outer Radial Clearance (mm)	0.031	0.031	0.031
Oil Type	SAE30	SAE10	SAE50

Table 6.7: Case study details for the viscosity change seeded fault

Sensor	Load	T1	T2	T3	T4	T5	Avg
Bearing Housing Accelerometer	0	0.117	0.200	0.150	0.117	0.133	0.143
	50	0.183	0.217	0.200	0.183	0.167	0.190
	100	0.017	0.017	0.033	0.017	0.017	0.020
LVDT	0	0.067	0.133	0.133	0.183	0.117	0.127
	50	0.233	0.200	0.167	0.117	0.150	0.173
	100	0.083	0.067	0.050	0.033	0.067	0.060
Wireless Accelerometer	0	0.467	0.567	0.550	0.533	0.517	0.527
	50	0.650	0.717	0.617	0.667	0.600	0.650
	100	0.500	0.400	0.500	0.483	0.517	0.480

Table 6.8: Classifier performance for various viscosities given various sensors and loading conditions

All three loading conditions show the same general behaviour from the bearing housing accelerometer with increasing separation as loading increases (Fig. 6.12). This leads to very good classification for the 100% loading condition (98% correct)

The results from the LVDT show very good trends (Fig. 6.13) and matches closely with the simulated results. As viscosity increases, the motion becomes smaller and vice versa. These trends are reflected in the results with the SAE50 oil data points on the right, then the healthy or SAE30 oil data points, and the SAE10 oil data points on the far left. This is consistent with the simulated example show in figure 3.8. This trend can also be seen in the raw data presentation from the smaller orbit shape in figure **??** compared to figure **??** For both the bearing housing accelerometer and the LVDT it is more successful to differentiate between healthy and the lower viscosity of the SAE10 oil than it is to differentiate between healthy and the higher viscosity of SAE50 oil. This is a good trend for bearing wear as lower viscosity can lead to thinner lubrication films which in turn can lead to increased wear.

The poor performance of the wireless sensor regarding viscosity is obvious when looking at the feature plot (Fig. 6.14). All points are mixed in a single cloud with no obvious trends of separation. Overall, these results match the results for different bearing clearances very closely. This is expected due to the similar effect of viscosity and clearance on bearing orbit.

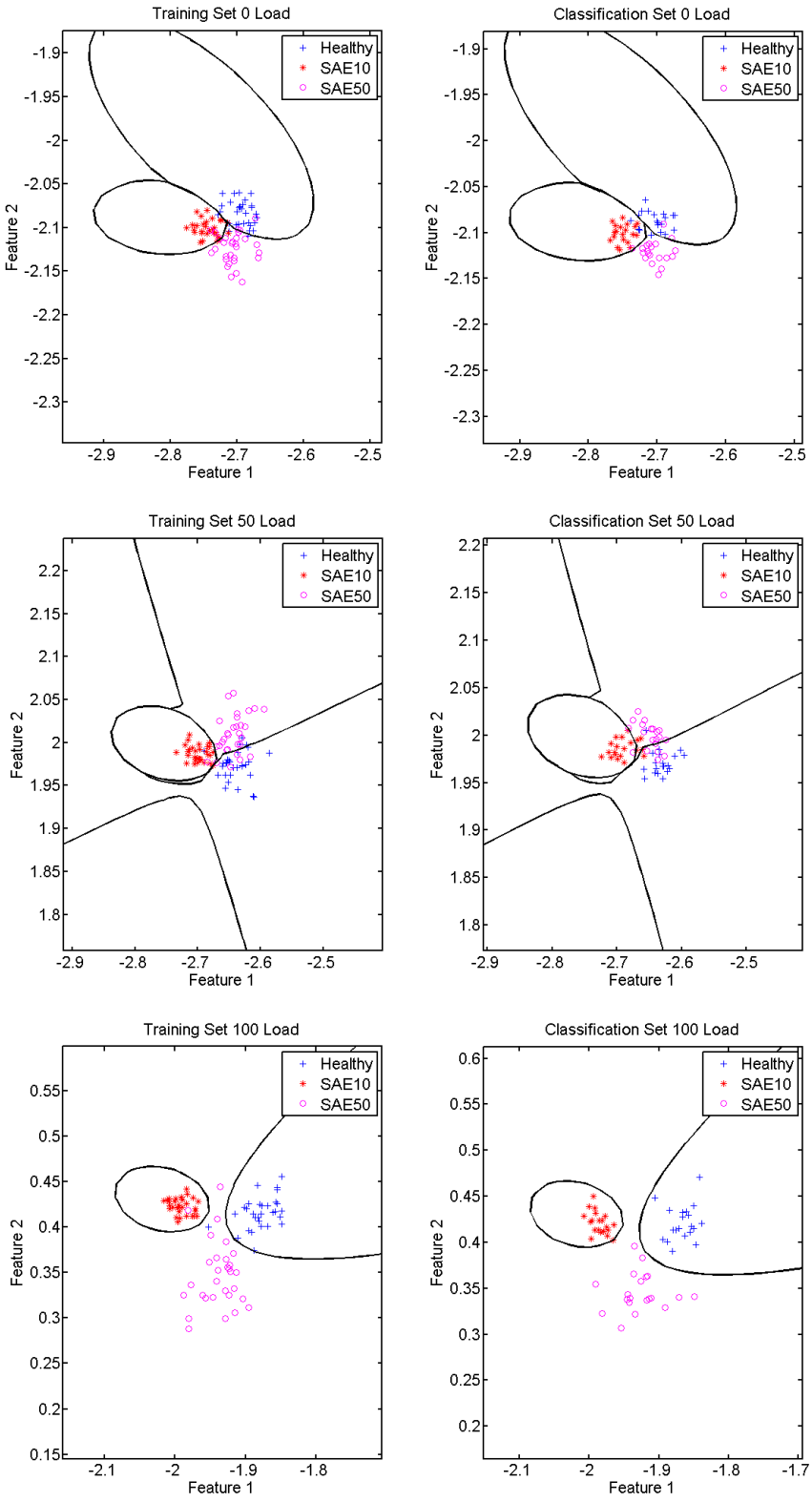

Figure 6.12: Classification training and validation sets for various viscosities from the bearing housing accelerometer (Top: 0% Load, Middle: 50% Load, Bottom: 100% Load)

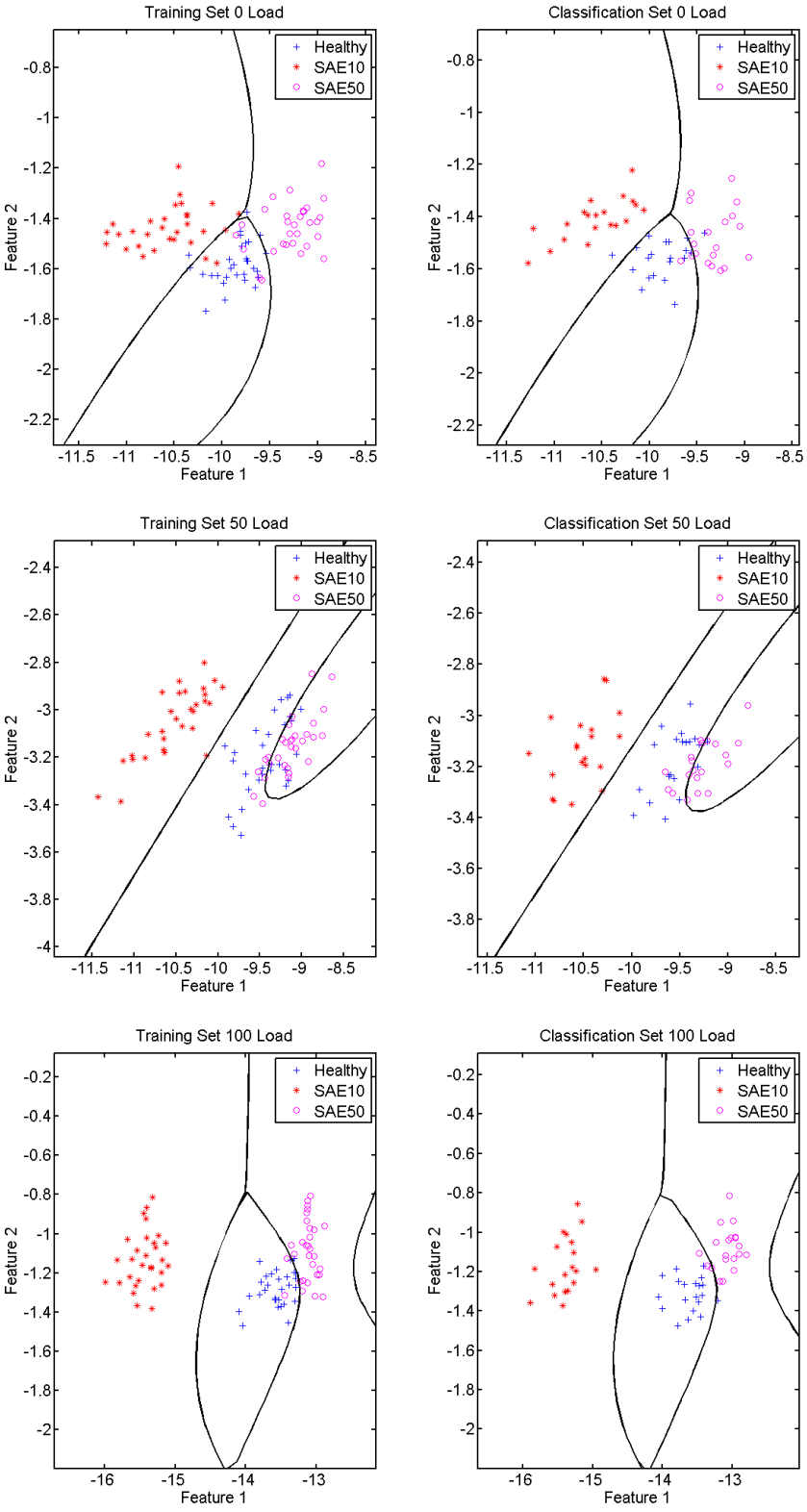

Figure 6.13: Classification training and validation sets for various viscosities from the LVDT (Top: 0% Load, Middle: 50% Load, Bottom: 100% Load)

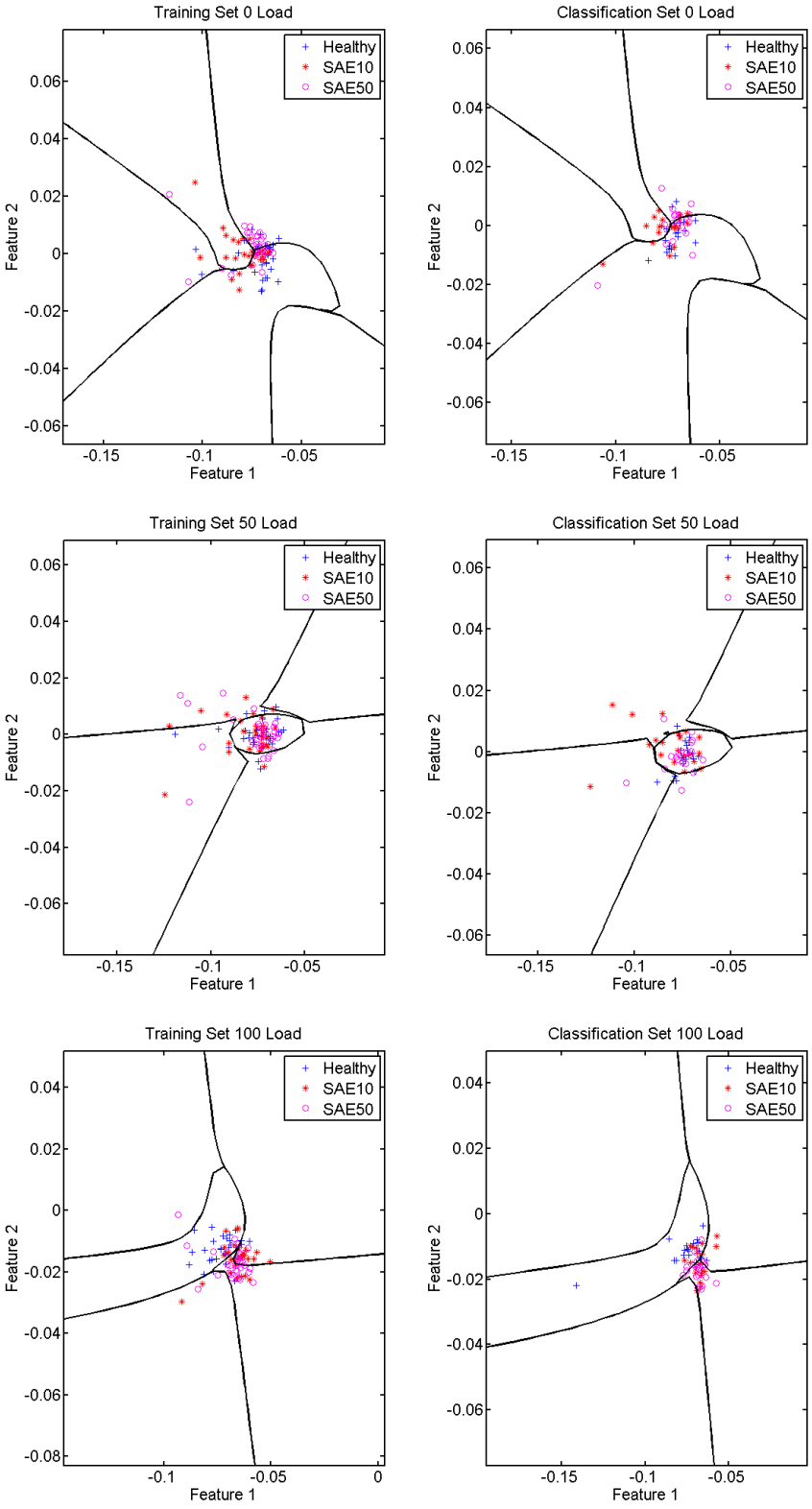

Figure 6.14: Classification training and validation sets for various viscosities from the wireless accelerometer (Top: 0% Load, Middle: 50% Load, Bottom: 100% Load)

Chapter 7

Conclusions

7.1 Summary of Research

This research successfully accomplishes the goals in its scope. The first step is to develop a model for the main bearings of the reciprocating compressor. Based on a mix of theoretical and empirical data, a full dynamic model of the forces acting on the main bearings is derived. This information is then used to calculate the bearing orbit based on a modified version of the mobility method that allows one to solve fully floating ring bearing problems. The model can be easily modified to show the difference in operation for several fault types such as too high or too low lubricant viscosity, wide clearance, or grooving in the form of reduced L/D ratio.

Secondly, a low cost method of measuring bearing motion is developed and put into practice. It follows the conventional format of using two position probes oriented at a ninety degree angle to measure position in two dimensions are calculating the position of the shaft center. However, instead of measuring inside the bearing directly, which would only give the position of the ring and no information about the journal, the crankshaft is measured at a position offset from the bearing. This is considerably easier to install than a sensor within the bearing since there are no concerns about a hazardous operating environment or modification of precision machined surfaces. While bearing motion is not measured directly in this case, it gives an overarching look at the bearing performance.

Thirdly, three separate fault types with two cases in each type are investigated through seeded fault testing. Steady state operating characteristics are measured by a wide array of sensors for each case. The sensors include several accelerometers in two directions as well as an accelerometer directly mounted to the bearing housing as well as a novel positioning directly on the crankshaft with a wireless transmission to the recording interface. Additional sensor include the LVDTs used to measure the crankshaft orbit and a current sensor to monitor the power draw of the drive motor. Temperature data was also taken to monitor each bearing as the compressor approached steady state condition.

The data from the seeded fault testing is then used to develop a classification algorithm based on binned FFTs principle component analysis. Three different sensors aree compared to each other to determine the most effective one. The conventional accelerometer on the bearing housing served as a baseline to the novel sensor placements of an LVDT measuring the crankshaft motion and the accelerometer on the crankshaft.

7.2 Key Results

The wireless accelerometer showed similar results to the conventional accelerometer installed on the bearing housing. It has the benefit of not needing additional signal conditioning hardware and connecting straight to the computer through USB. The most successful sensor however was found to be the LVDT measuring shaft motion. Applying the outlined methodology to a single LVDT resulted in a 100% correct classification for five out of six conditions for the grooved bearing and reduced oil feed hole size bearing. The sensor also achieved the best classification for different oil viscosities with a very good detection of a viscosity too low for safe operation. It is noteworthy that the trends in the classification agree between the simulated results

and experimental results.

The fact that a single position sensor can be used to monitor bearing condition instead of the typical requirement of at least two should be highlighted here as it has the potential to reduce costs greatly.

7.3 Future Work

This research successfully demonstrates the feasibility of applying statistics-based classification to monitor the condition of journal main bearings. However, a limited time was spent tuning the parameters of the feature extraction as well as the classifier itself. By spending more time and performing a thorough investigation into the effects of various parameters on classifier performance, the results will most likely improve even further.

Another aspect that should be investigated is the replacement of the contact LVDT with a non-contact probe as there were issues detected with wear both on the crankshaft as well the sensor tip. This was after about ten hours of test time, so for continuous operation a non contact option needs to be developed.

Lastly, research should be done into part to part variation with an increased sample size for different fault types. A brief investigation was performed with two "new" bearings compared to the original bearing which served as the "healthy" condition in the seeded fault testing. Figure 7.1 shows the result of applying the classification algorithm to this dataset. Typically, one would expect that all bearings that meet the tolerance specifications from the factory would be classified as the same type, i.e. the data shown here should be represented in an indistinguishable cloud. However when measuring the individual bearings it was found that the brand new bearings have much tighter radial clearances which lead to much tighter bearing orbits. This shows that some run-in occurs during the first hours of operation of a new bearing. This is picked up by the position sensor and represented in the classification results. This run-in period should be investigated and the classifier modified accordingly. Testing faults on several bearings will also give a better idea of the repeatability of the results and this method of feature extraction in general.

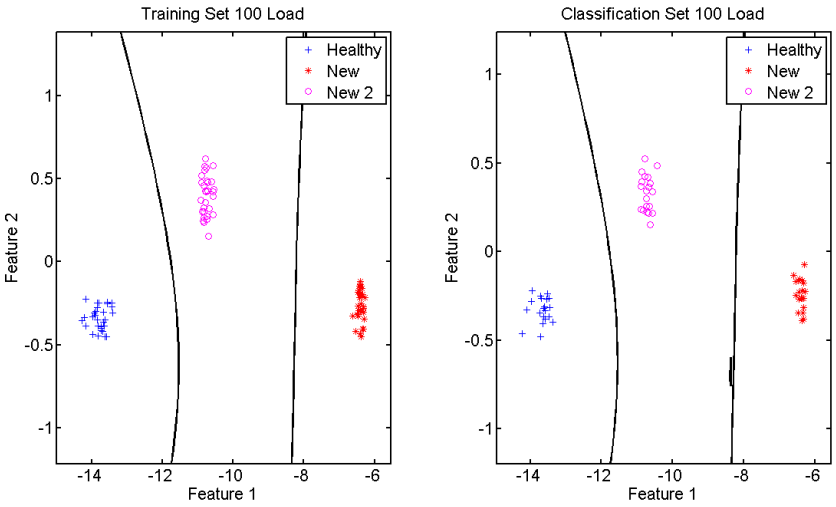

Figure 7.1: Classifier results of the "healthy" baseline bearing versus two brand new bearings

7.4 Final Comments

This research shows that is possible to develop a data driven classifier for the main bearings of a reciprocating compressor. It also shows the applicability of this method of feature extraction in this case and expands the application in the field of rotating machinery.

Appendix A

Technical Drawings

Figures A.1 and A.2 show the details of the modifications made to the bearing for the seeded fault testing.

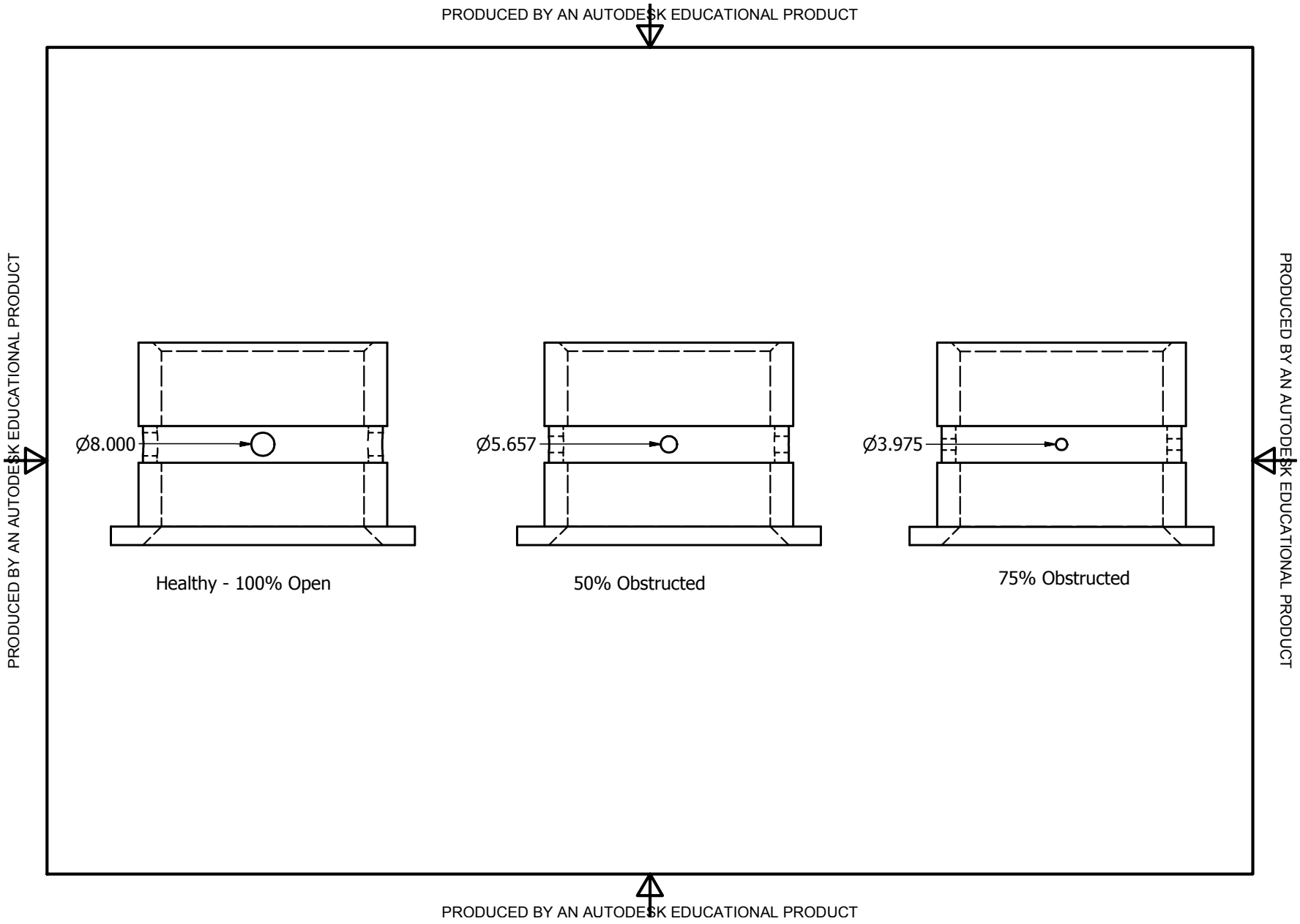

Figure A.1: Dimensions for the oil feed hole obstruction seeded fault in mm

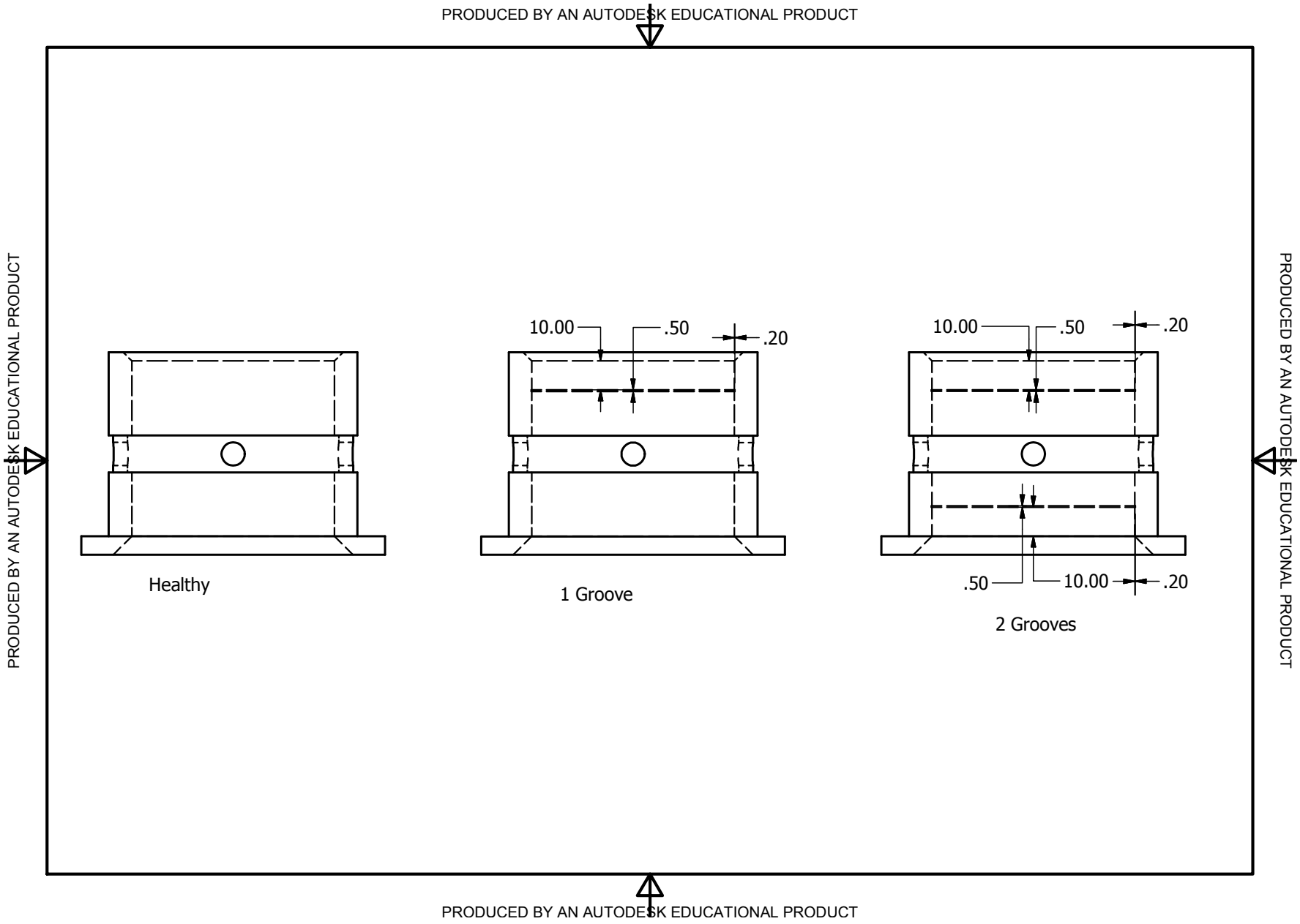

Figure A.2: Dimensions for the grooved bearing seeded fault in mm

Appendix B

Load History

Table B.1: Load history for one land of the flywheel side main crankshaft bearing

theta (deg)	fx (N)	fy (N)	theta (deg)	fx (N)	fy (N)	theta (deg)	fx (N)	fy (N)
0	4212	1109	120	-2491	1525	240	-1270	795
1	4207	1093	121	-2534	1529	241	-1235	797
2	4196	1077	122	-2544	1526	242	-1184	803
3	4178	1061	123	-2569	1526	243	-1145	806
4	4185	1045	124	-2656	1538	244	-1096	812
5	4135	1030	125	-2674	1536	245	-1104	805
6	4164	1014	126	-2703	1536	246	-992	826
7	4112	999	127	-2761	1542	247	-981	824
8	4073	985	128	-2786	1540	248	-888	841
9	4073	969	129	-2803	1537	249	-829	850
10	4043	954	130	-2884	1546	250	-795	854
11	4014	940	131	-2874	1537	251	-763	858
12	3999	925	132	-2936	1542	252	-695	870
13	3947	912	133	-2961	1539	253	-640	880
14	3922	898	134	-2942	1528	254	-600	886
15	3876	886	135	-3020	1535	255	-559	892
16	3825	874	136	-3072	1536	256	-482	908
17	3761	864	137	-3123	1536	257	-421	920
18	3787	847	138	-3118	1527	258	-376	927
19	3717	837	139	-3201	1533	259	-332	935
20	3651	828	140	-3224	1527	260	-260	951
21	3624	816	141	-3242	1521	261	-250	950
22	3583	806	142	-3262	1515	262	-146	974
23	3533	796	143	-3330	1516	263	-94	984
24	3504	785	144	-3374	1513	264	-42	995
25	3448	777	145	-3375	1504	265	8	1005
26	3353	774	146	-3419	1500	266	131	1034
27	3294	767	147	-3469	1497	267	132	1032
28	3264	758	148	-3445	1483	268	197	1046
29	3201	752	149	-3465	1475	269	238	1054
30	3170	744	150	-3506	1470	270	316	1072
31	3036	748	151	-3487	1457	271	323	1072
32	3005	740	152	-3456	1442	272	415	1093
33	2925	739	153	-3514	1438	273	495	1111
34	2885	733	154	-3465	1422	274	467	1102

Table B.1: Load history for one land of the flywheel side main crankshaft bearing

theta (deg)	fx (N)	fy (N)	theta (deg)	fx (N)	fy (N)	theta (deg)	fx (N)	fy (N)
35	2889	721	155	-3471	1411	275	569	1126
36	2790	724	156	-3483	1401	276	606	1134
37	2588	743	157	-3480	1390	277	692	1153
38	2619	728	158	-3462	1377	278	763	1169
39	2559	727	159	-3471	1366	279	808	1179
40	2455	733	160	-3419	1351	280	848	1187
41	2384	735	161	-3349	1334	281	915	1201
42	2339	733	162	-3434	1329	282	972	1213
43	2231	742	163	-3425	1317	283	1002	1219
44	2206	738	164	-3483	1309	284	1087	1238
45	2110	746	165	-3413	1293	285	1185	1259
46	2016	754	166	-3376	1279	286	1197	1260
47	1974	754	167	-3368	1267	287	1284	1279
48	1849	769	168	-3368	1255	288	1341	1290
49	1756	779	169	-3371	1243	289	1405	1303
50	1724	778	170	-3366	1231	290	1466	1315
51	1648	785	171	-3392	1220	291	1543	1331
52	1591	790	172	-3343	1207	292	1585	1338
53	1504	800	173	-3292	1193	293	1704	1363
54	1432	808	174	-3342	1183	294	1679	1354
55	1280	833	175	-3331	1170	295	1791	1377
56	1276	828	176	-3349	1159	296	1835	1383
57	1151	849	177	-3326	1146	297	1924	1400
58	1142	845	178	-3333	1134	298	2025	1419
59	1001	871	179	-3368	1122	299	2033	1417
60	966	873	180	-3365	1109	300	2139	1436
61	912	880	181	-3312	1097	301	2205	1446
62	807	899	182	-3295	1084	302	2322	1466
63	758	905	183	-3263	1072	303	2499	1499
64	678	919	184	-3241	1060	304	2450	1483
65	663	918	185	-3222	1049	305	2525	1494
66	518	948	186	-3189	1037	306	2565	1496
67	486	952	187	-3073	1028	307	2679	1513
68	334	983	188	-3170	1013	308	2737	1519
69	301	988	189	-3169	1001	309	2798	1525
70	202	1008	190	-3182	988	310	2871	1532
71	185	1009	191	-3133	978	311	2921	1535
72	100	1026	192	-3068	969	312	3058	1553
73	25	1042	193	-3113	955	313	3105	1554
74	-29	1052	194	-3121	942	314	3155	1556
75	-107	1068	195	-3053	934	315	3234	1561
76	-187	1085	196	-3098	919	316	3288	1563
77	-210	1088	197	-3042	911	317	3336	1562
78	-282	1104	198	-3079	896	318	3411	1566
79	-423	1136	199	-3001	890	319	3451	1563
80	-485	1149	200	-2978	880	320	3549	1570
81	-514	1155	201	-2972	868	321	3603	1568
82	-578	1169	202	-2965	857	322	3660	1567
83	-714	1200	203	-2919	849	323	3724	1566
84	-769	1212	204	-2883	841	324	3802	1567
85	-848	1230	205	-2859	832	325	3878	1566

Table B.1: Load history for one land of the flywheel side main crankshaft bearing

theta (deg)	fx (N)	fy (N)	theta (deg)	fx (N)	fy (N)	theta (deg)	fx (N)	fy (N)
86	-906	1243	206	-2854	821	326	3855	1552
87	-959	1254	207	-2792	817	327	3899	1546
88	-1021	1268	208	-2766	808	328	3933	1539
89	-1073	1279	209	-2774	796	329	3934	1527
90	-1165	1300	210	-2761	786	330	3995	1522
91	-1237	1316	211	-2661	788	331	4007	1511
92	-1238	1314	212	-2607	784	332	4024	1501
93	-1326	1335	213	-2576	778	333	4123	1499
94	-1335	1335	214	-2519	775	334	4100	1483
95	-1412	1352	215	-2527	764	335	4097	1470
96	-1494	1370	216	-2420	769	336	4090	1456
97	-1472	1363	217	-2411	760	337	4089	1442
98	-1595	1391	218	-2405	752	338	4033	1424
99	-1635	1398	219	-2199	774	339	4104	1417
100	-1636	1396	220	-2214	762	340	4145	1406
101	-1805	1435	221	-2154	763	341	4234	1399
102	-1788	1428	222	-2093	764	342	4187	1381
103	-1809	1431	223	-2092	756	343	4183	1367
104	-1881	1446	224	-2070	751	344	4219	1355
105	-1918	1452	225	-1983	758	345	4262	1343
106	-2010	1471	226	-1939	757	346	4283	1329
107	-2003	1466	227	-1923	752	347	4307	1315
108	-2021	1467	228	-1876	753	348	4298	1299
109	-2176	1500	229	-1800	759	349	4294	1284
110	-2134	1487	230	-1822	748	350	4289	1268
111	-2165	1490	231	-1733	757	351	4252	1251
112	-2193	1493	232	-1655	765	352	4318	1238
113	-2150	1479	233	-1619	766	353	4244	1220
114	-2254	1499	234	-1606	761	354	4283	1205
115	-2334	1513	235	-1529	770	355	4242	1188
116	-2292	1499	236	-1459	778	356	4243	1173
117	-2364	1511	237	-1356	794	357	4199	1156
118	-2404	1515	238	-1400	778	358	4224	1141
119	-2475	1526	239	-1377	777	359	4206	1125

Bibliography

[1] Freudenrich, Ph.D., Craig. "How Oil Refining Works" 04 January 2001. HowStuffWorks.com. ¡http://science.howstuffworks.com/environmental/energy/oil-refining.htm¿ 04 December 2012.

[2] Diab, S., and Howard, B., "Reciprocating Compressor Management Systems Provide Solid Return on Investment."

[3] Schultheis, S. M., Lickteig, C. A., and Parchewsky, R., 2007, "Reciprocating Compressor Condition Monitoring," Proc. Turbomachinery Symposium, pp. 107-113.

[4] Sela, U., 2000, "Reciprocating Compressor Condition Monitoring," Hydrocarbon Processing, 59(2).

[5] Yang, B.-S., Han, T., An, J.-L., Kim, H.-C., and Ahn, B.-H., 2004, "Technical Note: A Condition Classification System for Reciprocating Compressors," Structural Health Monitoring, 3(3), pp. 277-284.

[6] Ahmed, M., Gu, F., and Ball, A., 2011, "Feature Selection and Fault Classification of Reciprocating Compressors Using a Genetic Algorithm and Probabilistic Neural Network," Journal of Physics, Conference Series 305

[7] Jiang, X., 2011, "Air Compressor Wear Condition Monitoring Based on Oil Analysis Technology," Applied mechanics and materials, 66, pp. 498-503.

[8] Sandy, J., 1988, "Monitoring and Diagnostics for Rolling Element Bearings," Sound and Vibration, pp. 5.

[9] Kaewkongka, T., Joe Au, Y. H., Rakowski, R. T., and Jones, B. E., 2003, "A Comparative Study of Short Time Fourier Transform and Continuous Wavelet Transform for Bearing Condition Monitoring," International Journal of COMADEM, 6(1), pp. 41-48.

[10] Luo, G. Y., Osypiw, D., and Irle, M., 2003, "On-Line Vibration Analysis with Fast Continuous Wavelet Algorithm for Condition Monitoring of Bearing," Journal of Vibration and Control, 9,pp. 931-947.

[11] Parnelli, V. L., Boedo, S., Kempski, M. H., Kochersberger, K. B., and Haselkorn, M. H., 2007, "Health Monitoring of Lav Planet Gear Bushings Using Vibration Signature Analysis Techniques."

[12] Yang, D.-M., Stronach, A. F., Macconnell, P., and Penman, J., 2002, "Third-Order Spectral Techniques for the Diagnosis of Motor Bearing Condition Using Artificial Neural Networks", Mechanical Systems and Signal Processing, 16(2-3), pp. 391-411.

[13] N. Tandon and A. Parey, 2006, "Condition Monitoring of Rotary Machines", L. Whang and R. Gao, Condition Monitoring and Control for Intelligent Manufacturing, Springer London, 109-136, 5, Springer Series in Advanced Manufacturing

[14] Chen, Y.D., Du, R., Qu, L.S., 1995, "Fault Features of Large Rotating Machinery and Diagnosis using Sensor Fusion", Journal of Sound and Vibration, 188(2), pp. 227-242

[15] Boedo ,S., 1986, "Dynamics of Engine Bearing Systems", M.S. Thesis, Cornell University, Ithaca, NY.

[16] Boedo, S., 2010, "Practical Tribological Issues in Big End Bearings", Tribology and Dynamics of Engine and Powertrain, Cambridge, pp. 615-635

[17] Boedo, S., Booker, J.F., 1989, "Transient Dynamics of Engine Bearing Systems", Tribological Design of Machine Elements, Elsevier, pp. 323-332

[18] Goenka, P.K., 1984, "Analytical Curve Fits for Solution Parameters of Dynamically Loaded Journal Bearings", Journal of Tribology, 106, pp 421-427

[19] Booker, J. F., 1971, "Dynamically-Loaded Journal Bearings: Numerical Application of the Mobility Method", Transactions of the ASME, pp. 168-176.

[20] Rohdem S.M., Ezzat, H.A., 1980, "Analysis of Dynamically Loaded Floating-Ring Bearings for Automotive Applications", Journal of Lubrication Technology, 102, pp. 271-276

[21] Miba Bearing Group, "Bearing Damage"

[22] Chirico, A. and Kolodziej, J., "Fault Detection and Isolation for Electro-Mechanical Actuators Using a Data-Driven Bayesian Classification," SAE Int. J. Aerosp. 5(2):494-502, 2012, doi:10.4271/2012-01-2215.

[23] De Boe, P. and Golinval, J-C., "Principle Component Analysis of a Piezosensor Array for Damage Localization", Structural Health Monitoring, June 2003 2: 137-144

[24] Smith, Lindsay I, 2002, "A Tutorial on Principal Component Analysis"

[25] Van Der Heijden, F., Duin, R. P. W., De Ridder, D., and Tax, D. M. J., 2004, Classification, Parameter Estimation and State Estimation - an Engineering Approach Using Matlab, John Wiley & Sons, Ltd.

[26] Jeon, S., Ahn, H.F., Han, D.C., Chang, I.B., 2001, "New Design of Cylindrical Capacitive Sensor for On-Line Precision Control of AMB Spindle", IEEE Transactions on Instrumentation and Measurement, 50(3), pp 757-763

[27] Macro Sensors, 2003, "LVDT Basics", Technical Bulletin 0103